A ROBOTIC TELESCOPE FOR OPTICAL FOLLOW-UP OBSERVATIONS OF GAMMA-RAY BURSTS

John French

UCD School of Physics
College of Mathematical, Engineering and Physical Sciences
University College Dublin

Submitted in fulfilment of the
requirements for the degree of
Doctor of Philosophy

Head of Dept.: Prof. G. O'Sullivan

Supervisor: Prof. L. Hanlon

July 7, 2008

Contents

Abstract

γ–ray bursts (GRBs) are brief, highly energetic pulses of γ–ray radiation which were accidentally discovered in the late 1960's by the *Vela* satellites while they were monitoring for violations of the US–Soviet Nuclear Test Ban Treaty. With isotropic energies of $\sim 10^{53}$ ergs, they are the most luminous objects in the universe. Initially, the lack of observed counterparts at other wavelengths was a significant obstacle in understanding the progenitors and underlying physics of GRBs. The unpredicable and transient nature of the events, together with the inherent technological difficulty in accurately localising sources at γ–ray energies, inhibited multi–wavelength follow–up observations. The breakthrough came in 1997, when the Italian–Dutch BeppoSAX satellite detected a long–lived GRB afterglow at X–ray energies. This was soon followed by the detection of counterparts at optical and radio wavelengths by ground–based telescopes. It is now known that GRBs can give rise to long–lived emission at X–ray, UV, optical, infrared, and radio wavelengths.

Robotic optical telescopes are particularly well suited to the study of GRBs. The unpredictable and transient nature of these events precludes the scheduling of observations and demands automated responses on the shortest possible timescales. Small (< 1 m) telescopes are sensitive enough to detect the optical emission in many cases, particularly since they can carry out observations at very early times when an optical counterpart will be at its brightest. Since the landmark detection of an optical flash from GRB 990123 by ROTSE–I, robotic telescopes have made significant contributions to the study of GRBs. Such instruments have become particularly relevant in the *Swift* era when accurate GRB localisations are being made available with unprecedented speed and regularity. The enhanced quality of observations in the *Swift* era has revealed unexpected complexity and variety in the optical behaviour of GRBs, and has allowed the early–time regime to be explored in greater detail than was previously possible. The complexity of optical light curves in the *Swift* era and the unexpectedly large fraction of bursts for which no optical

counterpart has been detected raises new questions which will require a large sample of well–observed bursts to address.

Watcher is a 40 cm robotic optical telescope dedicated to GRB follow–up observations. The system has been operating fully robotically at Boyden Observatory in South Africa since April 2006, and has carried out extensive observations in response to GRB alerts generated by *Swift* and other missions. This thesis describes the development, installation and operation of the system and summarises the GRB follow–up observations that have been performed to date. The highlight of Watcher's GRB observations so far has been the earliest detection of optical emission from GRB 060526, which Watcher began observing 36 s after the burst was detected by the *Swift* satellite. The well–sampled light curve obtained by Watcher reveals a complex light curve with a number of features. Watcher's data set was combined with late–time multi–wavelength data from a number of larger instruments and successfully modelled with several episodes of energy injection.

List of Figures

List of Tables

Chapter 1

Introduction to GRBs

1.1 Introduction

γ–ray bursts (GRBs) are brief, highly energetic pulses of γ–ray radiation which were accidentally discovered in the late 1960's (Klebesadel et al., 1973) by the *Vela* satellites while they were monitoring for violations of the US–Soviet Nuclear Test Ban Treaty. With isotropic energies of $\sim 10^{53}$ ergs, they are the most luminous objects in the universe. Progress in understanding these unusual astrophysical sources was hampered in the early years by a lack of observations, which led to the development of a plethora of theoretical models, many of which were based on Galactic neutron stars (see review in Harding, 1991). Their origins, distances, and energies remained a mystery until the launch of the Compton Gamma–Ray Observatory (CGRO) in 1991. The Burst And Transient Source Experiment (BATSE, Fishman et al., 1989a), the dedicated GRB instrument on–board CGRO, observed more than 2700 bursts over its nine year lifespan, establishing an all–sky rate of ~ 2 per day for these events. The isotropic sky distribution (Fig. 1.1) and inhomogeneous intensity distribution (Fig. 1.2) revealed by the BATSE observations (Meegan et al., 1992), were strongly suggestive of a cosmological origin for GRBs, and hinted at the huge energies involved. BATSE also provided solid evidence for two distinct classes, short and long bursts, separated in duration at ~ 2 s (§1.3).

The lack of observed counterparts at other wavelengths was a significant obstacle in understanding the progenitors and underlying physics of GRBs. The unpredicable and transient nature of GRBs, together with the inherent technological difficulty in accurately localising sources at γ–ray energies, inhibited multi–wavelength follow–up observations.

The breakthrough came in 1997, when the Italian–Dutch BeppoSAX satellite (Boella et al., 1997) detected a long–lived GRB afterglow at X–ray energies (Costa et al., 1997). This was soon followed by the detection of counterparts at optical and radio wavelengths by ground–based telescopes, thanks to the accurate and relatively prompt localisations provided by BeppoSAX. Spectroscopy of an optical counterpart provided the first redshift determination and finally confirmed the cosmological origin of GRBs (§2.2.1).

Observations of the host galaxies of long GRBs (§1.8), and strong evidence for an association with supernovae (§1.7), suggests that this class of GRBs is caused by the collapse of a massive star to a black hole. Short GRBs are thought to be produced in compact object mergers (§1.6). This class of burst has proved elusive, not having been observed outside the γ–ray band until the first short burst afterglows were detected in 2005 (§2.3.4).

Recent GRB research has been dominated by NASA's *Swift* mission, a multi–wavelength observatory dedicated to the study of GRBs (§3.4.1). The greater sensitivity of *Swift* compared to previous missions, together with its ability to perform very early follow–up observations at X–ray and optical wavelengths, has produced a significant contribution to our knowledge of GRB physics, progenitors, and environments, and has raised many new questions.

1.2 Classes of GRBs

A key step in the study of GRBs was determining if there were different classes of bursts with inherently different properties, which could provide clues as to the nature of the progenitors. Studies of the extensive catalog of bursts observed by BATSE revealed a clear bimodal distribution based on duration (Kouveliotou et al., 1993). The duration distribution of BATSE bursts strongly suggested two distincts groupings separated at ~ 2 s (Figure 1.2). This classification was further reinforced by studies of spectral hardness, denoted as the ratio of background–subtracted counts between two different energy bands in the detector. Short bursts tend to be hard while long bursts are somewhat softer (Figure 1.2), leading to a classification scheme being adopted in the literature comprising two distinct groups: "short–hard" GRBs and "long-soft" GRBs. Studies of GRB prompt emission has also revealed that the spectral lag (the difference in arrival time between lower energy emission and higher energy emission) in short GRBs is negligible compared to that

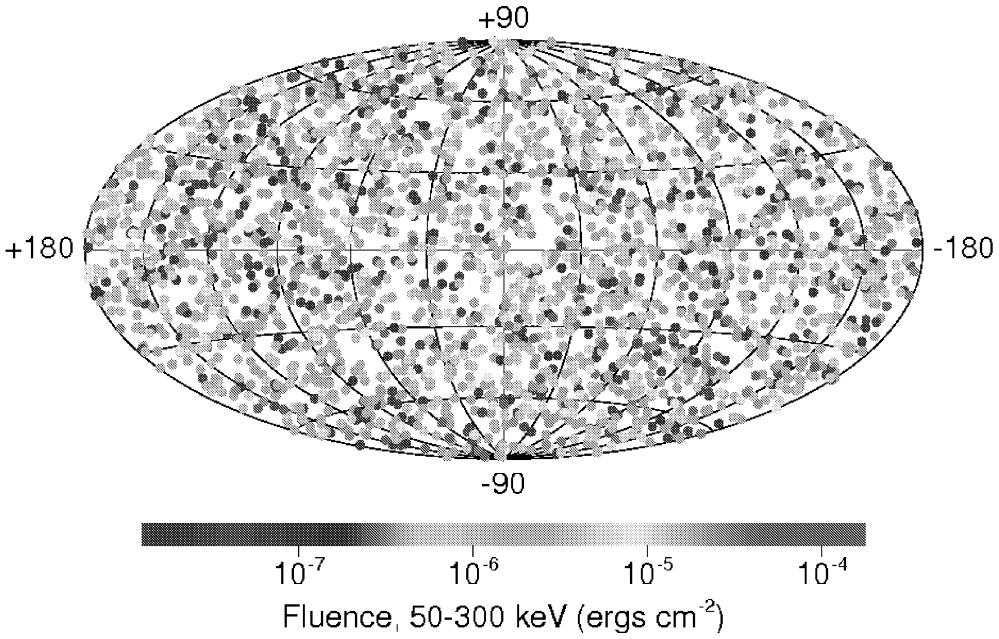

Figure 1.1: The spatial distribution of the 2704 GRBs observed by BATSE. Burst locations are color–coded based on fluence, with long duration, bright bursts shown in red, and short, weak bursts shown in purple. Grey is used for bursts for which the fluence cannot be calculated due to incomplete data. *From http://www.batse.msfc.nasa.gov/batse/grb/skymap/*

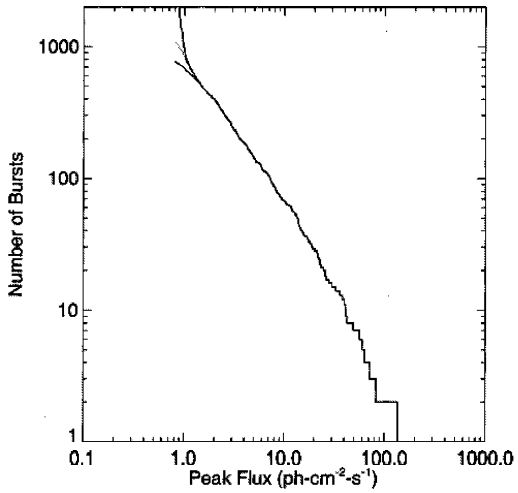

Figure 1.2: The peak flux distribution of BATSE GRBs, plotted as the cumulative distribution of the flux (S) (photons cm^{-2} s^{-1}) at the peak of the light curve versus the log of the number of bursts (N). This results in a $-3/2$ power-law slope at high fluxes, as expected in a homogeneous Euclidean model. However a shallower distribution at lower flux regimes deviates from this simple model implying a relative under-abundance of faint sources. *From (Paciesas et al., 1999).*

measured for long GRBs (Norris and Bonnell, 2006; Yi et al., 2006). Afterglow (§2) and host galaxy (§1.8) observations of GRBs further strengthened the short–hard/long–soft taxonomy and offered physical clues as to the nature of the different types of progenitors responsible.

Recent studies suggest that modifications to this simple classification scheme may be required. Donaghy et al. (2006) suggest that the dividing line in the duration distribution should be at 5 s, while a third, intermediate, class of GRBs has also been proposed (e.g. Horváth et al., 2006). A significant number of short GRBs may be incorrectly classified. About 1/3 of short GRBs exhibit softer, extended emission lasting tens of seconds after the initial spike–like emission (Norris and Bonnell, 2006), complicating their classification. The most significant challenge lies in the very well–discussed case of GRB 060614: a bright, relatively nearby ($z = 0.125$) event, whose long duration suggests it belongs to the class of long bursts. Surprisingly, no associated supernova was detected, despite deep observations (Fynbo et al., 2006b). The spectral lag and peak luminosity of this burst are consistent with short GRBs, all of which indicate that this burst belongs in the short sub–class (Gehrels et al., 2006). These apparent contradictions suggest that a third class, spanning the long–short divide, may be required.

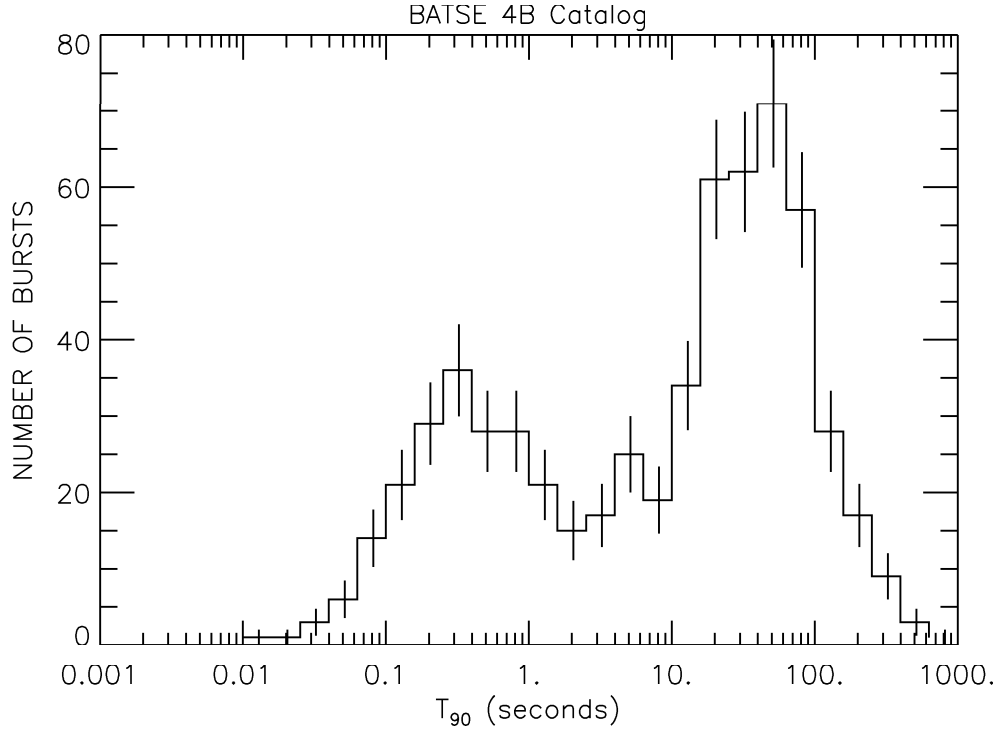

Figure 1.3: The bimodal duration distribution of BATSE GRBs. *From Kouveliotou et al. (1993)*

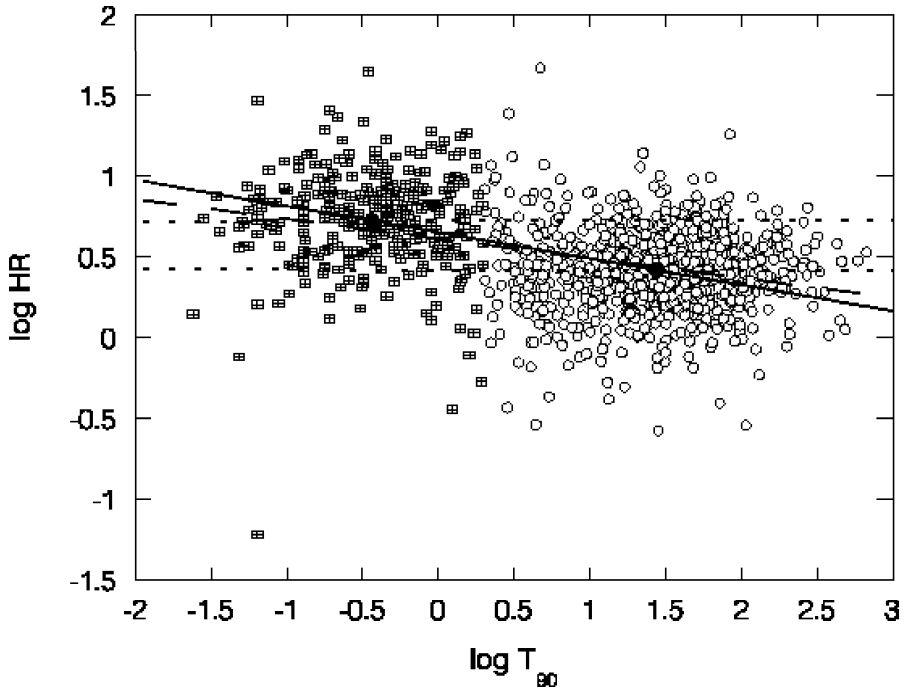

Figure 1.4: The hardness–duration correlation for BATSE bursts. HR is the ratio of fluence between BATSE channels 3 (100 keV – 300 keV) and 2 (50 keV – 100 keV). Squares represent short bursts and circles long bursts. The solid line is a regression line for the whole sample. The two dotted lines are the regression lines for the short and long samples respectively. *From Qin et al. (2000).*

1.3 Temporal Properties

GRB durations are usually described by the quantity T_{90}, which corresponds to the time over which 5% to 95% of the burst's fluence is observed. The duration distribution spans 5 orders of magnitude from 10^{-2} s – 10^{2} s or more, with typical values of T_{90} for long and short bursts of ~ 20 s and ~ 0.2 s respectively (Fig. 1.2).

The majority of GRB light curves are highly variable, with flux variations of up to 100% on time scales as short as milliseconds (Figure 1.5). Some light curves are smooth, typically with a fast rise exponential decay (FRED) structure, while others are composed of distinct, well–separated emission episodes. The variability time scale δt (determined by the width of individual pulses) is much shorter than the overall duration of the burst, and variability on a time scale of milliseconds has been observed (e.g. McBreen et al., 2001). Individual pulses tend to be asymmetric, with the leading edge steeper than the

trailing edge.

A correlation between temporal variability and absolute luminosity, which finds smooth bursts to be less luminous, has been reported by Fenimore and Ramirez-Ruiz (2000) (see also Reichart et al. (2001)). Norris et al. (1996) compared the arrival times of peaks in the 4 BATSE energy channels and found that the low–energy emission is delayed with respect to the high–energy emission in long GRBs. The spectral lags are found to be anti–correlated with the luminosity of the bursts (Norris et al., 2000). These two relations are among several empirical correlations which may be used to infer luminosities of GRBs from parameters measured solely at γ–ray energies in order to use GRBs as standard candles to constrain cosmological models (§1.9).

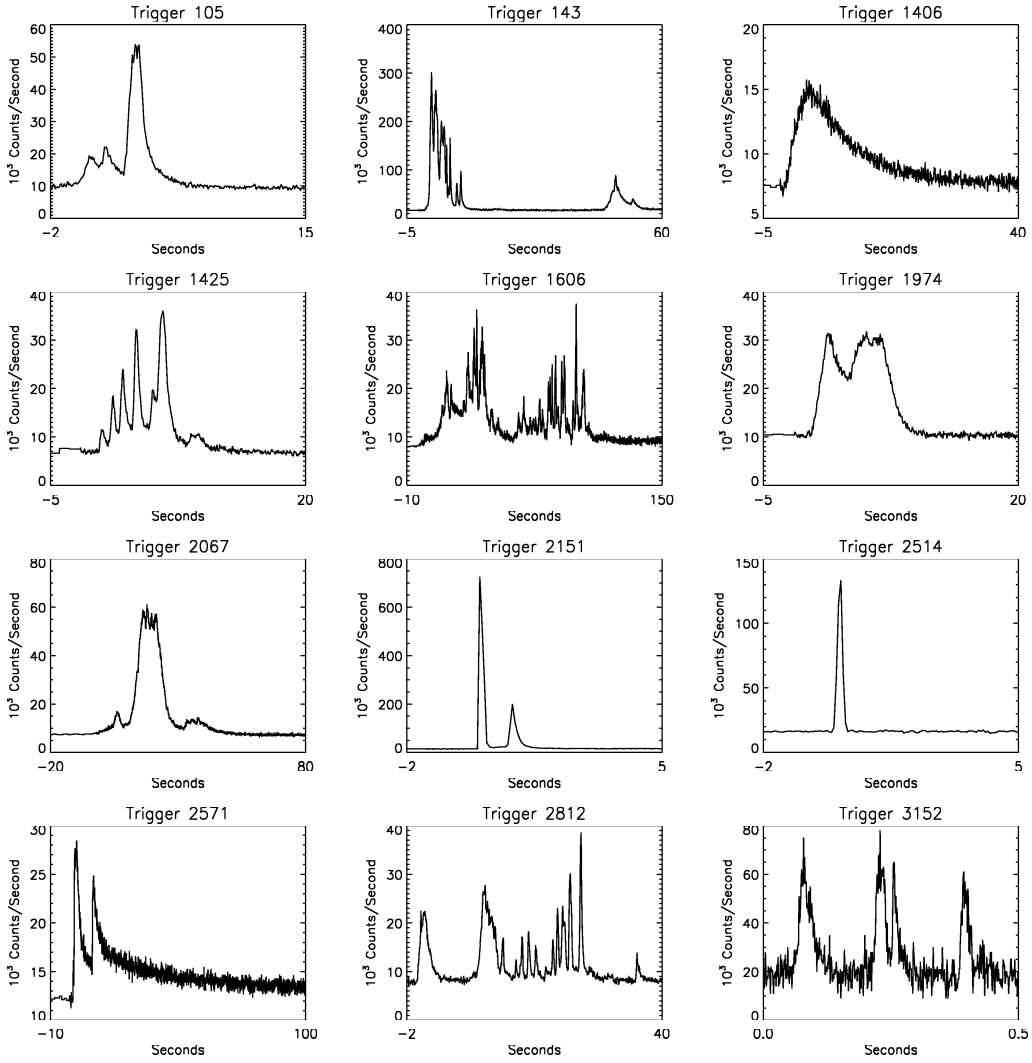

Figure 1.5: Sample of the diverse temporal profiles of BATSE GRBs. *From Mészáros (2006)*

1.4 Spectral Properties

GRBs have non–thermal spectra spanning a broad energy range. Though spectra vary widely from one burst to another, many bursts can be well described by an empirical broken power–law function (Band et al., 1993) with three independent spectral parameters: a low energy photon index (α); a high energy photon index (β); and the break energy (E_0). The peak energy (E_p), at which the burst's power output is at a maximum, is often used as a measure of spectral hardness. E_p is the peak in a νF_ν logarithmic plot of the spectrum, and is given by $E_p = (2 + \alpha)E_0$, where $\beta > -2$. This spectral shape is valid both for integrated emission over the whole burst duration, and for the emission during a shorter temporal segment of the burst. A sample broadband spectrum of GRB 990123 is shown in Figure 1.6.

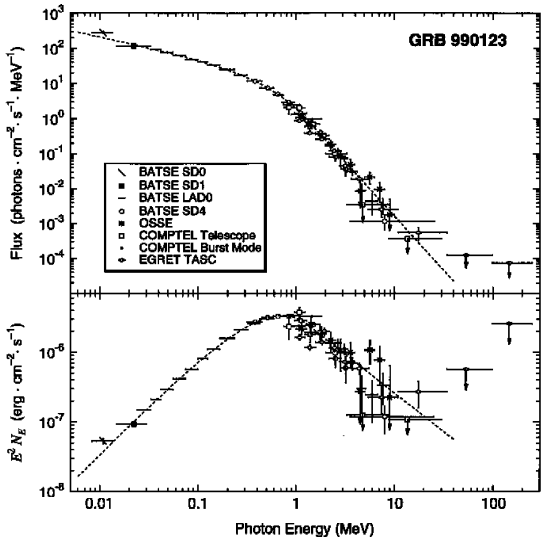

Figure 1.6: The upper panel shows the differential photon spectrum and the lower panel the νF_ν spectrum for the intense burst GRB 990123 detected by all the Compton Gamma–Ray Observatory instruments. *From Briggs et al. (1999)*

A study of 156 bright BATSE bursts (Preece et al., 2000; Kaneko et al., 2006), yielding 5500 spectra, determined typical values and ranges for the spectral indices to be $\alpha \sim -1 \pm 1$ and $\beta \sim -2^{+1}_{-2}$, with E_p distributed lognormally around ~ 250 keV with a range of less than a decade in energy (Figure 1.7). The distributions of α and β are wide enough to accommodate faint and bright GRBs, whereas the distribution of E_p is remarkably narrow. The small number of bursts peaking at lower energies ($\sim$ 10's keV) is likely to be a selection effect due to the lower sensitivity of BATSE in this energy range, especially

since a group of X–ray transient events called X–ray flashes (XRFs) were discovered (Heise et al., 2001; Kippen et al., 2002) which have similar temporal profiles to GRBs but with peak energies around or below 40 keV. However, at the high energy end, studies by Harris and Share (1998) indicate that the paucity of spectrally hard bursts is due to an inherent deficiency of bursts peaking above 3 MeV.

High energy GRB emission ranging from 100 MeV to 18 GeV has been observed by *EGRET* (Dingus, 2001) and the Solar Maximum Mission (SMM) (Harris and Share, 1998). While most of these spectra were consistent with the Band model up to high energies, tentative evidence exists for a distinct high energy component in some bursts (e.g. Hurley et al., 2004; González et al., 2003), and a possible detection of TeV emission has been reported in one burst (Atkins et al., 2000). The *GLAST* mission (§9.2.3.1) will allow GRB high energy emission to be studied in much greater detail.

Patterns of spectral variability and evolution are a common feature of GRB prompt emission and much effort has been devoted to searching for empirical relations and correlations between the observable quantities. Spectral hardness, as measured by the quantity E_p (or in the case of Golenetskii et al. (1983), the temperature from thermal spectral fits) has been found to be correlated with intensity during the temporal evolution of individual pulses. This observation has given rise to two empirical relations, the Hardness–Intensity Correlation (Golenetskii et al., 1983) and the Hardness–Fluence Correlation (Liang and Kargatis, 1996). Ford et al. (1995) found evidence for hard–to–soft spectral evolution in bursts with multiple pulses, where later pulses have softer peak energies than earlier ones. For long bursts, E_p is found to be correlated with E_{iso}, the total isotropic energy radiated in γ–rays (Amati et al., 2002), a relation which has proved to be quite robust in light of *Swift* observations (Amati, 2006).

1.5 Theoretical Models

1.5.1 The Fireball Model

The generic fireball model has become the standard theoretical framework for the interpretation of GRBs due to its success in predicting and incorporating the observed properties of GRB prompt and afterglow emission. Its component physical processes are discussed below.

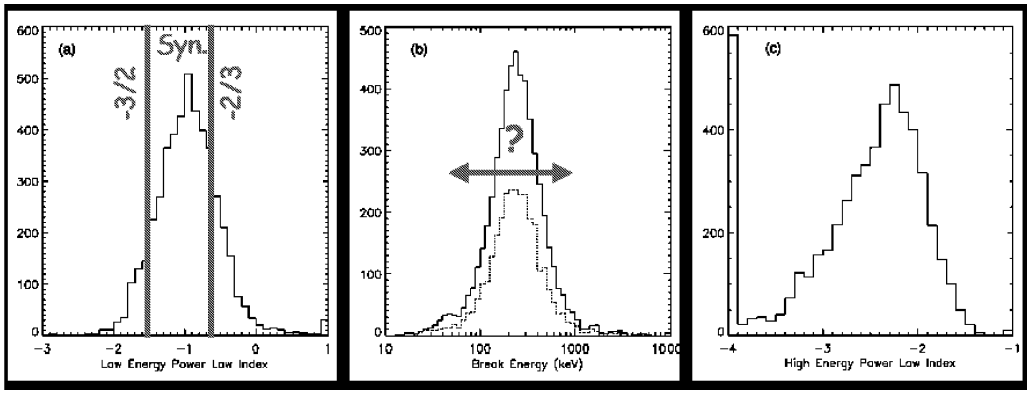

Figure 1.7: Distribution of the low–energy power–law index (α), break energy (E_0), and high–energy power–law index (β) in GRB spectral fits. The vertical lines in (a) indicate the region of the distribution which can be accounted for by synchrotron radiation. The arrows in (b) highlight the narrowness of the break energy distribution. *From Preece et al. (2000).*

1.5.1.1 The Compactness Problem

The first basic ingredient of the fireball model involves the release of $\sim 10^{52}$ ergs over a short time in a small volume of space. The short time scale variability observed in GRB light curves requires that the energy be deposited in a compact region. However, this produces a large optical depth to typical γ–ray photons of ~ 1 MeV due to $\gamma\gamma$ interactions which lead to e^+ e^- pair production. This difficulty, known as the compactness problem, can be resolved by invoking relativistic expansion of the burst (e.g. Paczynski, 1986; Goodman, 1986), the second basic ingredient of the fireball model.

If the emission site is moving towards the observer with a Lorentz factor Γ then the optical depth is affected in two ways. The first effect is that the emission site may be a factor of Γ^2 larger and still produce the same short time scale variability. This is because not all the source from a relativistically moving object is visible. Relativistic beaming confines the view to $\frac{1}{\Gamma}$. The second effect is that the photons in the local frame are softer by a factor of Γ. This means that a smaller fraction of the photons are energetic enough to create pairs and contribute to opacity. The combined effect is a reduction of the opacity by $\Gamma^{\sim 6.5}$ where the exact value of the index depends on the precise burst spectrum (Lithwick and Sari, 2001). The compactness problem is eliminated if $\Gamma > 100$. Such relativistic expansion can be produced by radiation pressure if the baryonic contamination is low, typically $< 10^{-5}$ $M_\odot$, since the presence of more baryons will cause the energy of the flow to be converted to kinetic energy of the baryons and the flow will no longer be relativistic

(Mészáros and Rees, 1993).

1.5.1.2 Internal – External Shocks

In order to produce the observed γ–ray and afterglow emission, the kinetic energy of the relativistic flow must be dissipated in an efficient manner, producing the observed non–thermal spectra (§1.4). The leading mechanism proposed for this dissipation is shocks, which can accelerate particles to ultra–relativistic energies via the Fermi process. In this process, charged particles gain velocity in repeated reflections from moving magnetic field inhomogenities in a shock wave, resulting in a power–law electron energy distribution $N(\gamma) \propto \gamma^{-p}$ with $p \geq 2$ (Kobayashi et al., 1997). The accelerated electrons can then emit non-thermal radiation through various processes (§1.5.1.3).

Internal shocks are expected to occur in a baryonic outflow (Narayan et al., 1992; Paczynski and Xu, 1994). These are caused by velocity variations in the outflow which result in material moving at higher Lorentz factors catching up with material moving with lower Γ values. The shells collide, producing a pair of shocks propagating in both forward and reverse directions that heat and accelerate electrons. The shocks take place at a radius $r_{dec} \sim 10^{14}$ cm where the plasma has become optically thin, so that the propagation of the accelerated electrons in the plasma magnetic field produces the observed prompt emission. Due to the low plasma density required for the flow to be optically thin, the internal shocks are thought to be collisionless, i.e. dominated by the interaction of chaotic electric and magnetic fields. Collisionless shocks are believed to efficiently accelerate particles to relativistic velocities, and have been extensively studied in other astrophysical contexts, e.g. solar flares, supernova remnants, and AGN jets. It has been shown that internal shocks can easily reproduce the rapid, high amplitude variability seen in GRB light curves (Rees and Mészáros, 1994a).

The relativistic ejecta are eventually decelerated by the ambient medium generating an external shock (Mészáros and Rees, 1992; Rees and Mészáros, 1992) which has two main components: a forward shock (or blast wave) propagating into the external medium, and a reverse shock propagating back into the ejecta (Mészáros and Rees, 1993). The ambient medium may be the interstellar medium (ISM), or the stellar wind ejected from the progenitor before the collapse. The forward shock component of the external shock produces the long–lived multi–wavelength afterglow (§2, Mészáros and Rees, 1997). It has been suggested that a forward shock propagating into an ambient medium composed

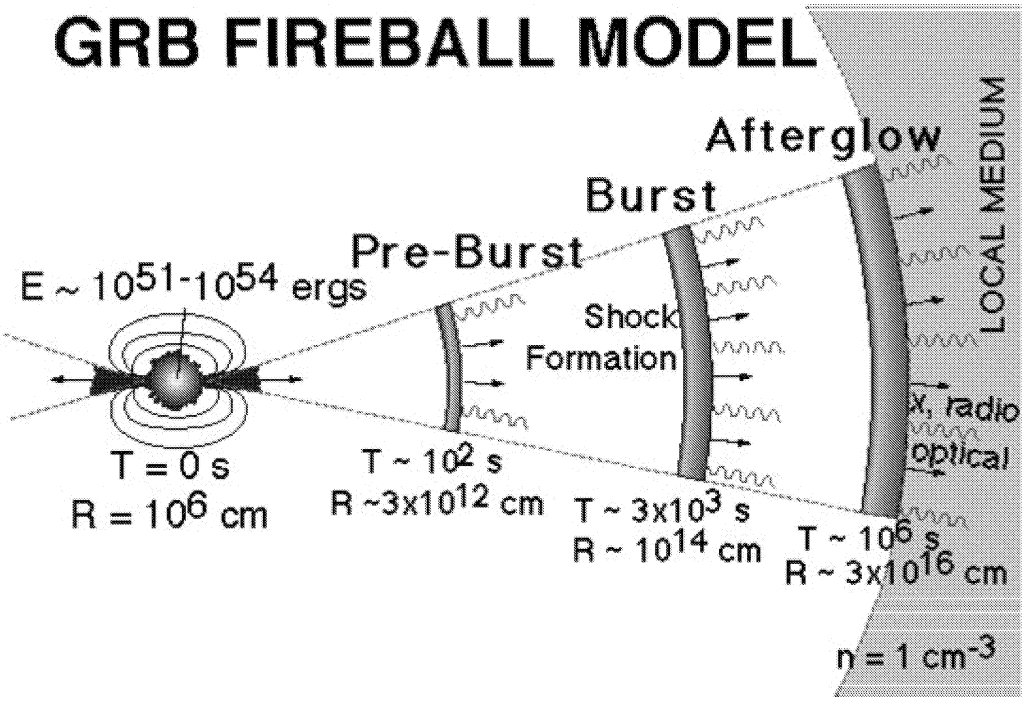

Figure 1.8: Cartoon of the GRB fireball model. *Credit: NASA*

of a large number of small dense clouds can produce highly variable γ–ray emission (Dermer and Mitman, 1999; Mészáros and Rees, 1993), though Sari and Piran (1997) argue that only internal shocks can produce such variability, while Piran (2005) shows that external shocks can only produce smooth burst profiles.

This general picture, illustrated in Figure 1.8, has become known as the internal–external shock scenario (Piran and Sari, 1998). Its main drawback lies in the low radiative efficiency of the internal shocks, since only a small fraction of the bulk kinetic energy is converted into radiation. High efficiency is required by the fact that the energy emitted in γ–rays is of the same order as or greater than the afterglow energy (Frail et al., 2001; Panaitescu and Kumar, 2001). Several solutions to this efficiency problem have been proposed, e.g. very large differences in Lorentz factors between shells (Beloborodov, 2000), and repeated shocks from reflections between shells (Kobayashi and Sari, 2001).

1.5.1.3 Emission Mechanisms

Synchrotron radiation (photons emitted by relativistic electrons in a magnetic field) is currently considered to be the dominant emission mechanism in GRBs. The synchrotron nature of the afterglow has been well established (§2.1), however the origin of the prompt emission is still highly debated. Polarisation of the optical afterglow, a characteristic

feature of synchrotron radiation, has been detected in several bursts (Lazzati, 2006). The synchtron shock model of Tavani (1996) predicted an optically–thin synchrotron spectrum from a power–law electron energy distribution with a sharp minimum energy cutoff and an isotropic pitch angle distribution which provided a good fit to many observed spectra. However, modifications to the simple synchrotron spectrum are required to explain some features in the low–energy spectra of GRBs observed by BATSE (Preece et al., 2000). Lloyd and Petrosian (2000) showed that a combination of a smooth low–energy cutoff in the electron energy distribution, an anisotropic pitch angle distribution, and synchrotron self–absorption at the lower end of the BATSE energy range could produce a whole range of low–energy spectral behaviour in the synchrotron spectrum.

Several authors invoke Compton processes to account for some of the observed spectral features. The inverse Compton process involves a relativistic electron giving up a fraction of its energy to a photon in a collision, thereby increasing the energy of the photon. In the direct Compton process, a photon scatters off a non–relativistic electron and transfers some of its energy to the electron. Panaitescu and Mészáros (2000) show that inverse Compton upscattering of synchrotron emission can produce the types of spectra observed in GRBs. Stern and Poutanen (2004) examine inverse Compton scattering in a partially self–absorbed regime, and show that the first Compton scattering radiation from nearly monoenergetic electrons can reproduce the hardness of most of the observed GRB spectra. The second Compton peak should be observed at higher energies, and may be responsible for the high energy emission observed in some GRBs (§1.4).

Some authors propose the synchrotron–self–Compton (SSC) process as an alternative to the simple synchrotron model (e.g. Kumar and McMahon, 2008), and as a possible source of high energy γ–rays (Mészáros and Rees, 1994). In the SSC process, photons created by the synchrotron mechamism are scattered to higher energies by the same electrons initially responsible for their creation. Another theory proposed by Medvedev (2006) is the jitter radiation mechanism from small–scale shock–generated magnetic fields. This model can explain the hard–to–soft evolution and rapid spectral variability observed in GRBs, as well as the presence of a soft X–ray component in some GRBs, and the peak in the low energy spectral index distribution at $\alpha \approx -1$ (Preece et al., 2000).

1.5.2 Alternative Models

1.5.2.1 Poynting dominated flows

The main alternative to the standard fireball model involves strong magnetic fields, where the fireball is Poynting flux dominated, i.e. a large fraction of its energy is contained in electromagnetic fields as opposed to the kinetic energy of the matter. There are several reasons to consider strong magnetic fields in the context of GRBs. A GRB fireball typically requires a very small baryon loading in order to achieve the high Lorentz factors needed to solve the compactness problem, and a Poynting flux is an effective way to transport a large amount of energy without carrying many baryons (Levinson and Eichler, 2003). The presence of strong magnetic fields is predicted in some progenitor models (§1.6). Magnetic fields can collimate the outflow (Vlahakis and Königl, 2003), and can help alleviate the problem of inefficiency in internal shocks (Spruit et al., 2001).

However, since strong shocks cannot develop in highly magnetised outflows (Kennel and Coroniti, 1984), an alternative energy dissipation mechanism is required. Magnetic reconnection has been suggested by Spruit et al. (2001). Usov (1994) proposes particles accelerated by electromagnetic waves to $\Gamma \sim 10^6$ generating synchro–Compton radiation at ~ 1 MeV, with a possible high energy tail up to $\sim 10^4$ MeV. Relativistic Alfvén turbulence in the MHD wind may cause quasi–thermal emission from the fireball's photosphere to be Compton upscattered to γ–ray energies (Thompson, 1994). However the development of GRB models involving magnetic fields is at a relatively early stage, and a standard framework has yet to be developed.

1.5.2.2 Cannonball Model

The cannonball model (Dar and de Rújula, 2004) suggests that long GRBs and their afterglows are produced when discrete balls of matter are ejected at relativistic velocities in ordinary core–collapse supernovae. The γ–ray emission is produced by inverse Compton scattering of photons in the immediate environment of the supernova by electrons in the cannonball's plasma, with each individual pulse in the GRB light curve produced by a single cannonball's motion through the ambient light. The afterglow is explained as synchrotron radiation from electrons swept up by, and accelerated within, the cannonball. A key problem with this model is a lack of understanding surrounding the cannonball's formation and acceleration to relativistic velocities. It is also a more exotic process than

that of shocks within plasma outflows, which are known to exist in other well–observed systems and have been extensively studied theoretically.

1.6 Progenitors

Several features of GRBs have been used to infer properties of the central engine, the energy source producing the ultrarelativistic flows described by the fireball model (§1.5.1). The variability time scale δt of the GRB prompt emission can be as short as 1 ms, which requires a compact object. The typical overall duration is much longer than the variability time scale, suggesting prolonged central engine activity which can be explained by accretion. The large total energy release ($\sim 10^{51}$ ergs) requires a massive ($\sim 0.1\,M_{\odot}$) accretion disk. Since the relativistic outflow is thought to be collimated (§2.1.2), the central engine must produce relativistic outflows in the form of jets.

Most central engine models involve accretion of a massive disk onto a compact object, most likely a newborn black hole. The black hole accretion disk system extracts energy and converts it into a relativistic fireball. The energy is provided either by the binding energy of the torus or by the rotational energy of the black hole itself. Energy may be extracted from the system by neutrino emission from the hot accretion disk (e.g. MacFadyen and Woosley, 1999), or the Blandford–Znajek mechanism (Blandford and Znajek, 1977), in which the black hole/torus system is engulfed in a magnetic field and the rotational energy of the black hole is extracted via this magnetic field.

Observations of relativistic jets in active galactic nuclei, which are powered by accretion onto black holes, support the black–hole/accretion disk scenario for GRBs. An alternative to the accretion mechanism, proposed by Usov (1992), involves a Poynting flux dominated relativistic flow driven by the strong magnetic and rotational energy of a newborn neutron star (§1.6.1.3). Salient features of a selection of more specific progenitor models based on these general frameworks are discussed below (see also discussion in Piran (2005)).

1.6.1 Long GRBs

1.6.1.1 Collapsars

The collapsar model is one of the leading central engine models for long GRBs. According to this model, the iron core of a rapidly rotating massive star of mass $M > 30\,M_{\odot}$collapses to form a black hole surrounded by an accretion disk of mass $\sim 0.1\,M_{\odot}$(Woosley, 1993). Accretion of the disk onto the black hole takes place within several dozen seconds and powers the GRB. The collimated outflows produced by the accretion process are further collimated by their passage through the stellar mantle. The flows attain high Lorentz factors as they emerge from the stellar surface, and after traversing several stellar radii produce a GRB and an afterglow by internal and external shocks respectively (Rees and Mészáros, 1994b; Paczynski and Xu, 1994; Rees and Mészáros, 1992; Mészáros and Rees, 1993). The collapsar model is often referred to as a "failed" Type Ib supernova because the core collapse does not result in ejection of the stellar envelope (Aloy et al., 2000). The collapsar model predicts that GRBs will predominantly occur in star–forming regions with circumburst media consistent with a Wolf–Rayet star at the end of its life. An asymmetric Type I supernova is expected to accompany each GRB.

Studies of GRB host galaxies have found that long GRBs occur exclusively in regions of active star–formation within star–forming galaxies (§1.8). The association of long–duration GRBs with stellar collapse is now secure (§1.7), especially since the observations of the afterglow of GRB 030329 and the spectroscopic discovery of its associated supernova SN 2003dh (Hjorth et al., 2003b; Stanek et al., 2003). The discovery of X–ray lines in several GRBs eg GRB 011211 (Reeves et al., 2002) similarly point to the supernova connection. Modelling indicates that this scenario can produce lines reported in bursts (Kallman et al., 2003). Further observational support is provided by evidence of GRBs in wind–blown environments (eg Greiner et al., 2003a; Li and Chevalier, 2001; Jaunsen et al., 2001), and of a possible shell nebula around a Wolf–Rayet star in the case of GRB 021004 (Mirabal et al., 2003). These observations strongly suggest that most, if not all, long GRBs are produced by collapsars. However, Zhang et al. (2003b) speculates that the breakout of a relativistic jet and its collision with the stellar wind can produce a brief transient with properties similar to those short GRBs.

1.6.1.2 Supranovae

The supranova model also involves the collapse of a massive star in a supernova explosion (Vietri and Stella, 1998, 1999). In contrast to the collapsar model, in which a black–hole/accretion disk system is formed directly, the supranova model involves an intermediate stage in which a "supramassive" neutron star (SMNS) is formed in the supernova explosion. The SMNS is ""supramassive" in the sense that its mass exceeds the maximum cold nonrotating neutron star mass, i.e. without the supporting centrifugal force provided by its rotation it would collapse to a black hole. This collapse does eventually occur, on a time scale of weeks to months, as angular momentum is lost via gravitational radiation and magnetic braking. When the SMNS loses so much angular momentum that the centrifugal support against self gravity becomes impossible, the star experiences a period of runaway deformation and gravitational radiation before collapsing into a black hole. A disk of $\sim 1\,M_\odot$ is assumed to remain, which accretes onto the black hole to power the burst like the neutron star merger model (§ 1.6.2.1).

The supranova model offers a promising interpretation of the X–ray line emission and absorption features observed in GRBs. If the supernova shell or some remnant was ejected by the progenitor days or months before the final collapse and moved at a velocity $\sim 0.1\,c$ it would be located at a distance of $10^{15} - 10^{17}$ cm. This remnant would provide a large mass of heavy elements for the inferred photoionization and recombination that produce a strong iron emission line (Lazzati et al., 1999; Böttcher, 2000; Vietri et al., 2001). These effects are thought to be responsible for many of the discrete X–ray features detected in several GRBs (Amati et al., 2000; Piro et al., 2000; Reeves et al., 2002). Detection of low Z elements such as calcium, sodium and sulphur has also been reported (Reeves et al., 2002; Watson et al., 2003). However, these lines may also be explained by the collapsar model (§1.6.1.1). A strong pulsar wind may develop after the supernova and before the final collapse (Königl and Granot, 2002). This wind would produce a denser, highly magnetised medium into which the GRB jet propagates, thus providing the strong magnetic field required for the synchrotron afterglow model.

While both the collapsar and supranova involve supernova–type events, there are key differences. Contrary to the collapsar model, a supernova bump is not expected to be observed in the afterglow light curve in the supranova model, unless the time delay between collapses is a few days. The supranova model more readily explains how the iron required to produce the iron X–ray lines reaches the implied large distances, since the su-

pernova shell is ejected several weeks to months before the GRB. Though the association of GRB 030329 with SN 2003dh has been interpreted as supporting the collapsar model, proponents of the supranova model argue that there may be a wide distribution of delay times between the first and second collapses which may account for observed supernova associations.

1.6.1.3 Millisecond Magnetars

The millisecond magnetar model proposes that GRBs can arise as a massive star collapses to form a rapidly rotating neutron star with an extremely powerful magnetic field (Usov, 1992). The magnetic field, having already been strengthened dramatically during the stellar collapse, can reach values of $\sim 10^{15} - 10^{17}$ G as a result of the dynamo process (Thompson and Duncan, 1993). The highly magnetised neutron star, or magnetar, loses its rotational kinetic energy (up to 10^{52} ergs) catastrophically, on a time scale of seconds or less, by a variation of the pulsar spin down mechanism involving magnetic braking (Duncan and Thompson, 1992). Rotation of the magnetic field creates a strong electric field and hence an electron–positron plasma which is optically thick and in quasi–thermodynamic equilibrium. This plasma flows away from the neutron star at relativistic speeds, and X–ray and γ–ray emission at the photosphere of this relativistic wind may then reproduce the observational characteristics of a GRB.

The magnetar at the heart of this model has already been successfully used to explain the observed properties of soft γ–ray repeaters (SGRs) and anomalous X–ray pulsars (AXPs). Attractive features of this model include the association with known objects such as massive stars and supernovae events. Furthermore, collimation of the outflow arises naturally in this model.

1.6.2 Short GRBs

1.6.2.1 Neutron Star Mergers

Neutron–star binary mergers, which also produce a black–hole/accretion disk system, are popular progenitor candidates for short GRBs. Merger events occur when binary stars coalesce as their orbits decay due to the emission of gravitational radiation, as observed in the binary pulsar PSR 1913+16 (Taylor and Weisberg, 1982). Binary mergers are expected to take $\sim 10^6 - 10^7$ years (Narayan et al., 1992), and occur at a rate of $\approx 10^{-6}$

events per year per galaxy (Narayan et al., 1991). These mergers are expected to occur far from their birth–site, due to their long orbital decay times and the high spatial velocities provided by supernova "kicks" during their evolution (Hansen and Phinney, 1997; Brandt and Podsiadlowski, 1995). However, an alternative channel of formation may produce short–lived binaries with very close orbits and lifetimes of $\sim 10^5$ yr (e.g. Belczynski et al., 2002), so that mergers may take place closer to the birth–site.

A close binary system is formed from a massive X–ray binary which evolves into a neutron binary after the companions undergo supernova explosions (Clark et al., 1979). Both stars must have initially been in the mass range $\sim 8\,M_\odot - 25\,M_\odot$to form neutron stars. Depending on the initial masses, other possible binaries such as neutron star–black hole (NS–BH, §1.6.2.2) and neutron star–white dwarf (NS–WD) may be formed. Provided the binary system remains bound and is not disrupted by the supernova, a merger eventually occurs following gravitational damping of the orbits. The outcome of the merger is expected to be a $\sim 2.4\,M_\odot$ black hole surrounded by a neutron rich accretion disk of $\sim 0.1\,M_\odot - 0.2\,M_\odot$. The compact binary is rotating rapidly when it merges, resulting in a black hole with the necessary angular momentum to form an accretion disk (eg Ruffert and Janka, 2003; Rosswog et al., 2003) .

Though most of the $\sim 5 \times 10^{53}$ ergs released by the merger is in the form of low–energy neutrinos and gravitational waves, just a fraction of this energy ($\sim 10^{52}$ ergs) is required to power the burst (Rees, 1999). The relativistic outflow required by the fireball model may be driven by $\nu\bar{\nu}$ annihilation (Eichler et al., 1989), though this mechanism may not be sufficiently energetic. Ruffert and Janka (1999) found that $\nu\bar{\nu}$ annihilation can provide sufficient energy to power a GRB. The simulations of Rosswog and Davies (2002) generate the required energy from $\nu\bar{\nu}$ annihilation if the outflow is beamed to a solid angle of $< 1\%$. This collimation may be produced by the energetic neutrino–driven wind that accompanies the merger. The differential rotation process may allow the central object to remain stable for a short period (~ 20 ms to 100 s) before collapsing to a black hole (Rosswog and Davies, 2002). Alternatively, a large–scale dynamo process can wind the magnetic field up to large values of $\sim 10^{16}$ G (Thompson and Duncan, 1993), enough to power a GRB, before collapsing to a black hole. The spin–down time scale of ~ 0.2 s matches the typical time scale of short GRBs, but is not long enough to account for GRBs with durations > 2 s.

1.6.2.2 Neutron Star – Black Hole Mergers

Another compact object merger considered a promising progenitor for short GRBs is the merger of a neutron star and a black hole (Blinnikov et al., 1984; Eichler et al., 1989; Paczynski, 1991; Narayan et al., 1991; Fryer et al., 1999). No neutron star–black hole (NS–BH) binaries have so far been observed in nature, but they are believed to exist. They can evolve from two massive stars in a binary system when one forms a neutron star and its companion collapses to a black hole. The initial mass of the former should be $\sim 8\,M_\odot - 25\,M_\odot$ and the mass of the latter must exceed $25\,M_\odot$. If the system remains bound a NS–BH binary is formed. Neutron star binary observations have shown that this is possible, since the supernova explosion leading to the formation of the compact star does not always destroy the companion or disrupt the binary. Estimates put the rate of these events at one every $10^5 - 10^6$ years in a galaxy (eg Lattimer and Schramm, 1976; Bethe and Brown, 1998). An asymmetric merger of a NS and BH is expected to yield a more massive torus around the black hole than the NS–NS merger. The black hole is already formed and no mass needs to be lost from the neutron star for its formation (Janka et al., 1999). This makes a deeper gravitational potential, which may facilitate more accretion and may spin up the black hole leading to an increased source of energy (Popham et al., 1999). Similar to NS–NS mergers, the release of just a fraction of the gravitational energy of the system into a relativistic fireball is required to power the burst.

1.7 The GRB – Supernova Connection

Even before GRBs were discovered, their existence and association with supernovae was predicted by Colgate (1968), leading the original discoverers (Klebesadel et al., 1973) to search for SN–GRB coincidences, without success. In general, however, it was thought that the two phenomena were unrelated, particularly since the uncertainty regarding the GRB distance scale meant that the energies of these events were unknown and thus could not be compared to core–collapse supernovae. Once the cosmological origin of long GRBs was firmly established (Metzger et al., 1997b), the total isotropic energy in γ–rays was determined to be $\sim 10^{51}$ erg, comparable to the total kinetic energy in a supernova explosion. The association of long GRBs with active star–formation (§1.8) indicated massive stellar death as a likely progenitor, further hinting at a supernova connection.

The first strong evidence for such an association came with the detection of the highly

unusual supernova SN 1998bw (Galama et al., 1998a), spatially and temporally coincident with GRB 980425. This low redshift burst ($z = 0.0085$), at a distance of ~ 35 Mpc, was very underluminous, with an isotropic γ–ray energy of $8.5 \pm 0.1 \times 10^{47}$ erg, more than three orders of magnitude fainter than typical long bursts. The unusual optical spectrum of SN 1998bw showed an absence of H lines (Lidman et al., 1998), suggesting it was not of the Type II class, but otherwise defied simple classification, leading to suggestions that it should be classified as a "peculiar Type Ic" (e.g. Patat and Piemonte, 1998). Using this burst as a template, other possible associations have been claimed by identifying reddened late–time bumps in the optical light curves, thought to be signatures of contributions from underlying Type I SNe. The best examples are GRB 970228 (Reichart, 1999) and GRB 980326 (Bloom and Kulkarni, 1998).

GRB 030329 and its associated highly energetic supernova (or "hypernova") SN 2003dh provided the first concrete evidence for the GRB–SN connection. The bright, slowly fading afterglow ($R \sim 13$ mag) and low redshift ($z = 0.1685$, Greiner et al., 2003b) of the burst made it well suited to extensive spectroscopic follow–ups. Spectra of the afterglow several days after the burst showed a deviation from a pure power–law and the emergence of broad SN spectral features (e.g. Hjorth et al., 2003c). As the afterglow faded, a red supernova bump became prominent, showing remarkable similarity to SN 1998bw (see review in Della Valle, 2005). Several other GRBs have been reported to be associated with SNe, based on spectroscopic as well as light curve signatures, including GRB 031203 (Bailyn et al., 2003; Malesani et al., 2004), GRB 021211 (Della Valle et al., 2003), and GRB 050525 (Della Valle et al., 2006b).

Several observational biases which serve to lower the probability of detecting GRB–related SNe have been identified (see discussion in Woosley and Bloom, 2006). Extinction due to dust will be significant when the GRB is located near the line of sight through our own galaxy, or in particularly dusty regions of their hosts. Essentially no optical flux is expected to be observable from SNe at $z \gtrsim 1.2$, due to the effects of metal absorption and unfavourable k corrections at optical wavelengths at higher redshifts. The host galaxy contribution can drown out the signature of a supernova whose peak magnitude is close to that of its host. However, the detection of SN spectra in the four nearest GRBs and the detection of bumps consistent with SNe in the lightcurves of most low–redshift bursts (Zeh et al., 2004) seems to confirm the association of GRBs with SNe.

This paradigm has been brought into question recently by the non–detection of SNe

in two nearby GRBs, GRB 060505 at $z = 0.089$ (Fynbo et al., 2006b; Ofek et al., 2007) and GRB 060614 at $z = 0.125$ (Fynbo et al., 2006b; Gal-Yam et al., 2006; Della Valle et al., 2006a). Due to their proximity and apparent membership of the long duration class (T_{90} of 4 ± 1 s and 102 ± 1 s respectively (Hullinger et al., 2006; Barthelmy et al., 2006)), SN searches were initiated by many observers, which failed to detect a SN down to limits ~ 100 times fainter than the prototypical SN1998bw. The durations, host galaxy properties, and in the case of GRB 060505 the location within the host galaxy, all imply a massive stellar origin for these bursts. The lack of an associated SN to such deep limits may be evidence for a new phenomenological type of massive stellar death.

1.8 Host Galaxies

Studies of the host galaxies of GRBs, in particular the morphology of the hosts and the burst locations with respect to the hosts, can shed light on the validity of the proposed progenitors (Bloom et al., 2002). Since the most massive stars explode soon ($\lesssim 10^7$ yr) after zero–age main sequence (ZAMS, the beginning of the star's life as a hydrogen burning object), then we expect GRBs from collapsars to be observed in galaxies undergoing vigorous star formation (e.g. late–type, irregular, and starburst galaxies), but not in early–type galaxies. However, GRBs from compact object mergers could occur in early–type galaxies, since compact binary systems require a median time of $\sim (2-10) \times 10^8$ yr from ZAMS to coalesce (e.g. Phinney, 1991; Bloom et al., 1999). Massive stars which end their lives as collapsars do so quite young and therefore near to the site of their birth, so GRBs produced by these events would be expected to occur in star forming regions in the host galaxy. The evolution of the objects in a compact binary system involves at least one, and possibly both of them undergoing a supernova explosion. This imparts a significant "kick" to the system (Hansen and Phinney, 1997; Brandt and Podsiadlowski, 1995), causing it to be ejected from the birth site. Therefore GRBs from such progenitors are not expected to be found in star forming regions.

The accurate GRB localisations achieved by *Swift*, in particular at X–ray and optical wavelengths, allow for subsequent searches for the underlying host galaxy. In practically all cases in which *HST* observations were performed of a GRB field, a host galaxy has been detected at the position of the early afterglow. Long GRBs are found exclusively in star forming galaxies, predominantly irregular dwarf (Fruchter et al., 2006). Their

hosts tend to be extremely blue (Le Floc'h et al., 2003), with strong emission lines (e.g. Vreeswijk et al., 2001), indicating a significant abundance of young, very massive stars. This strengthens the case for collapsars as progenitors of the long class of GRBs . Long GRBs are expected be found in environments similar to core–collapse supernovae. However, Fruchter et al. (2006) has shown that GRBs are more concentrated on the very brightest regions of their hosts than core–collapse supernovae, and that their host galaxies are significantly fainter and more irregular, which suggests that GRBs are produced by only the most massive stars, and that they may be restricted to galaxies of limited chemical evolution. Only a small fraction of long bursts are found in spiral galaxies, even at $z < 1$, where spirals are much more common.

The breakthrough discovery of short GRB afterglows has allowed their hosts to be studied for the first time. At least some short GRBs are found on the outskirts of elliptical galaxies, e.g. GRB 050509 (Gehrels et al., 2005), and GRB 050724 (Barthelmy et al., 2005b). Short GRBs have also been found in actively star–forming galaxies, e.g. GRB 050709 (Fox et al., 2005), and GRB 051221A (Soderberg et al., 2006), however, the star–formation activity in these host galaxies was found to be less intense than is typical in long GRB hosts. Both hosts also contain a significant population of old stars (~ 1 Gyr), and the bursts are thought to have been located among this population and not in the star–forming regions. These results support the compact object merger progenitor that has been proposed for short–hard GRBs. Examples of host galaxies of long and short GRBs are shown in Fig. 1.9.

It is still unclear whether GRB host galaxies are in some way special. A comparison of GRB–selected high–redshift (up to $z \sim 3$) galaxies with the field population at comparable redshift carried out by Conselice et al. (2005) indicates that the type of galaxies in which GRBs are found varies with redshift, such that at higher redshifts GRB hosts may be more massive than typical field galaxies, unlike lower redshift ($z \leq 1$) GRB hosts which tend to be small, low mass galaxies. Studies of the environments of GRB 030323 (Vreeswijk et al., 2004) and GRB 020124 (Hjorth et al., 2003a) reveal a low–metallicity environment and a high column density of neutral hydrogen in the region around the burst. These results suggest that GRB host galaxies may be largely dust free systems. Alternatively, the intense energy of the burst may destroy any nearby dust (e.g. Galama et al., 2003; Savaglio and Fall, 2004).

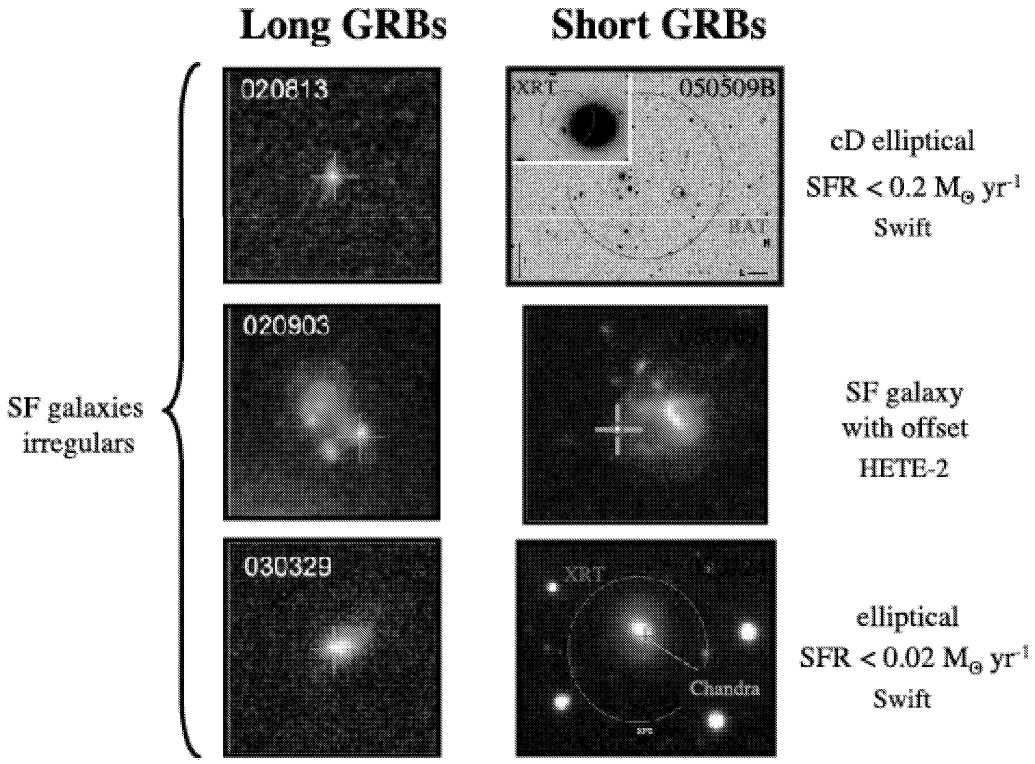

Figure 1.9: Typical host galaxies of long and short GRBs. *From Gehrels et al. (2007).*

1.9 GRBs and Cosmology

The greatly increased number of redshift determinations made possible by Swift has revealed the vast distance scale spanned by GRBs, from $z = 0.0086 - 6.30$ (Figure 1.10), with the highest mean redshift ($z = 2.8$) of any class of celestial object (Jakobsson et al., 2006). The extremely high luminosities of GRBs make them detectable, in theory, out to $z \sim 20$ (Lamb and Reichart, 2000). Unlike galaxies and quasars, which fade rapidly with increasing redshift due to increased luminosity distance, infrared and near–IR afterglows of GRBs are detectable out to very high redshifts due to cosmological time–stretching of the afterglow transient (Ciardi and Loeb, 2000) Given that GRBs are expected to occur out to $z \geq 10$, they provide a unique means to probe the high redshift universe.

Studies of GRB host galaxies suggest that long GRBs occur in star–forming regions in star–forming galaxies (e.g. Bloom et al., 1998; Holland and Hjorth, 1999) and so trace some fraction of massive star–formation. As their initial detection in γ–rays and subsequent localisation in X–rays is essentially unaffected by intervening dust, GRBs can provide an unobscured tracer of the history of cosmic star–formation (Blain and Natarajan, 2000). Galaxies may be selected independent of their emission properties, such as dust

obscuration and, uniquely, the brightness of the host galaxy at any wavelength. However, the extent to which GRB properties depend on redshift and metallicity (e.g. Salvaterra and Chincarini, 2007) are not yet fully understood.

With their featureless, bright continua, afterglows are also superb in situ probes of star–forming regions throughout the universe, permitting absorption studies of the host in a manner akin to quasar absorption, but with major advantages over quasar absorption studies for analysing star–formation (Bromm and Loeb, 2007). Such absorption studies are not limited to the near–infrared/optical/UV regime as they usually are for quasar absorbers, but as GRB afterglows are often incredibly bright in X–rays, absorption spectroscopy is also frequently performed at high energies, and may in principle be done in the mid–infrared.

Another benefit is that GRB afterglows produce no proximity effects on intergalactic distances scales, and have simple power–law spectra with no emission lines. Thus GRBs are clean probes of the intergalactic medium (IGM) and can be used to study its metal enrichment (Li, 2007; Fynbo et al., 2006a) and ionisation states (Lamb and Reichart, 2000) at high redshifts, particularly during the epoch of reionisation. Simply by detecting GRBs at very high redshifts, they may also shed light on the formation of the first stars (known as Population III), expected to have formed around $z \sim 20$, provided that such metal–free stars were capable of creating GRBs (Bromm and Loeb, 2006).

Much work has been done on the use of GRBs as standard candles in order to extend measurement of the universe into the high–redshift regime, beyond what is currently possible with Type Ia SNe. Several empirical correlations (e.g. Norris et al., 2000; Fenimore and Ramirez-Ruiz, 2000; Amati et al., 2002) have been used to infer luminosities, and hence distances, for GRBs with independently measured redshifts. Schaefer (2007) used 69 GRBs and various luminosity indicators to construct a GRB Hubble Diagram to $z > 6$ (Figure 1.11). Fits to a variety of cosmological models favour the concordance model, where dark energy is a cosmological constant which doesn't vary with time.

However, many difficulties in the use of GRBs as standard candles remain (see discussion in Zhang, 2007). Perhaps most importantly, the underlying physics is poorly understood in comparison to SNe: no physical basis has yet been determined for any of the empirical relations used as luminosity indicators. Calibration problems may also exist, particularly in using a low–z population of GRBs to calibrate a standard candle, since they may belong to a different population to most other GRBs, which occur at high–z. There

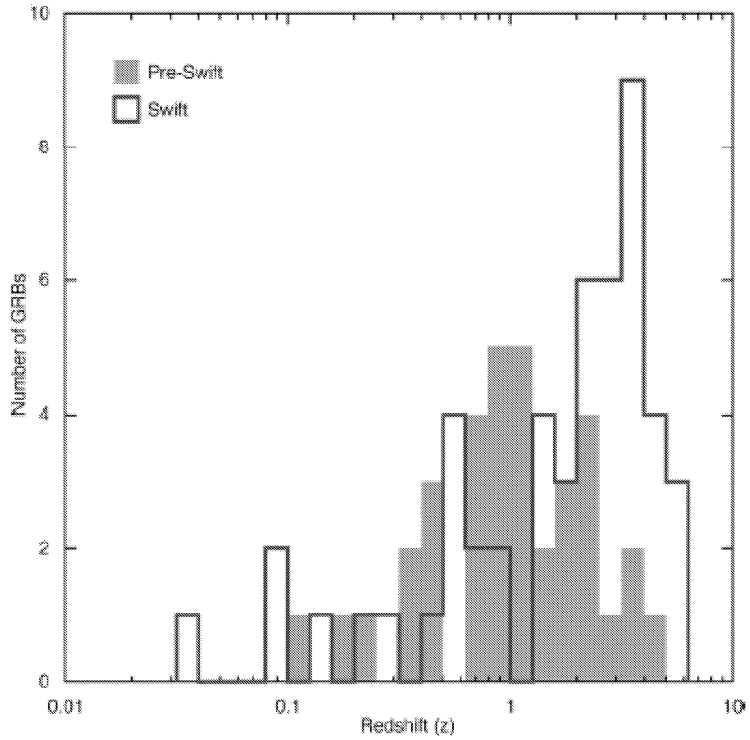

Figure 1.10: The redshift distribution of GRBs detected by *Swift* compared to the pre–*Swift* sample. *From Gehrels et al. (2007)*

may also be inherent selection effects, e.g. the Malmquist bias, whereby an increase in average luminosity with distance is observed in flux–limited sources.

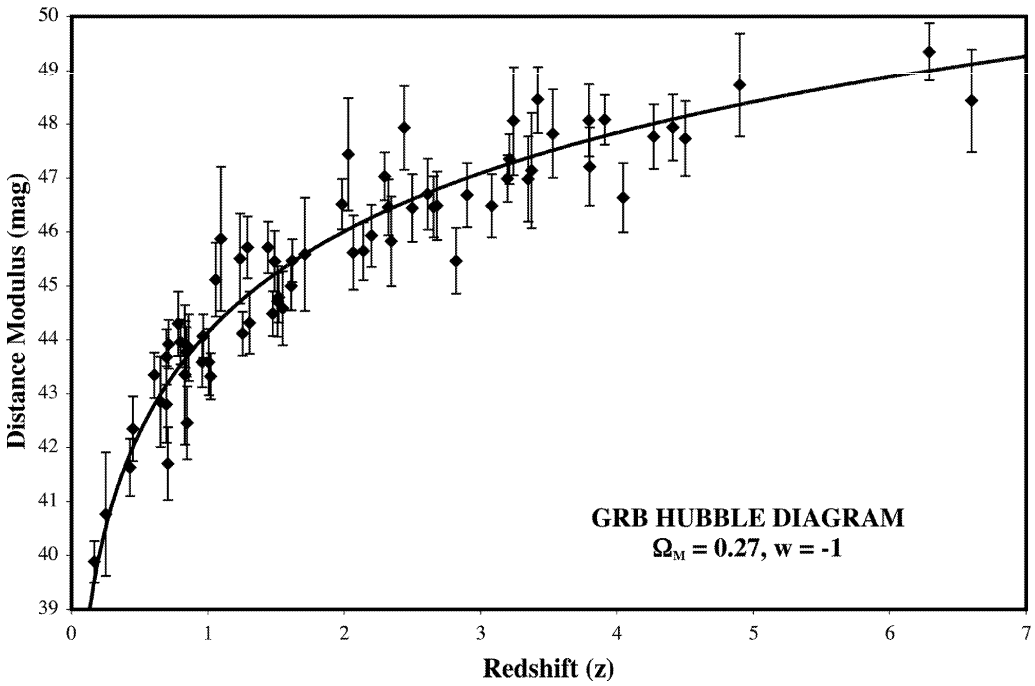

Figure 1.11: The GRB Hubble Diagram fit with the concordance cosmology (for a flat universe with $\Omega_M = 0.27$ and $\omega = -1$). The quality of the fit suggests that dark energy is unchanging with time. *From Schaefer (2007)*

Chapter 2

GRB Afterglows

2.1 Afterglow Theory

2.1.1 Simple Afterglow Model

In the context of the fireball model of GRBs (§1.5.1), the relativistic fireball with initial bulk Lorentz factor Γ_0 is decelerated as it sweeps up a large quantity of the ambient medium. The resulting forward shock propagates into the ambient medium, generating the long–lived multi–wavelength afterglow, while a short–lived reverse shock propagates back into the ejecta (§2.1.3). Most of the fireball kinetic energy is transferred into the shocked external medium. The fireball Lorentz factor evolves with radius r and with observer's time t as:

$$\Gamma \propto r^{-3/2} \propto t^{-3/8}, \quad r \propto t^{1/4}$$
$$\Gamma \propto r^{-3} \propto t^{-3/7}, \quad r \propto t^{1/7}$$

The first case describes adiabatic fireball evolution in which the energy is constant, which is generally valid at late times ($\sim$ hours). The second case describes radiative evolution, in which a significant fraction of the kinetic energy is lost due to radiative processes (Rees and Mészáros, 1992; Mészáros et al., 1998). This phase is thought to apply to the prompt emission and early afterglow.

The dynamics of the forward shock are based on the theory of relativistic blast waves described by Blandford and McKee (1976), which is the relativistic counterpart to the Sedov–Taylor solution for blast waves in the Newtonian regime, applicable to supernova

remnants. In the simple afterglow model (Mészáros and Rees, 1997; Sari et al., 1998), electrons in the external medium are shock–accelerated to a power–law distribution of Lorentz factors given by $N(\gamma_e) \propto \gamma_e^{-p}$, for $\gamma_e > \gamma_{e,min}$, the minimum Lorentz factor of the distribution. The electrons radiate via the synchrotron process to produce the afterglow spectrum shown in Fig. 2.1. The spectrum is composed of a series of broken power–laws connected at the characteristic frequencies ν_a, ν_m, and ν_c. At frequencies below the self–absorption frequency ν_a, the flux undergoes synchrotron self–absorption and is described by the Rayleigh–Jeans part of the blackbody spectrum. The typical synchrotron frequency ν_m corresponds to the typical electron Lorentz factor, which is determined by the mimimum Lorentz factor $\gamma_{e,min}$. Since electrons cool on timescales $\propto \gamma_e^{-1}$, electrons with $\gamma_e > \gamma_c$ (corresponding to ν_c, the cooling frequency) cool very rapidly. This results in two types of spectra: fast–cooling, where $\nu_m > \nu_c$ (at early times); and slow–cooling, where $\nu_m < \nu_c$ (at late times). The transition from fast to slow cooling occurs at a time t_0 when $\nu_m = \nu_c$. For a given observed frequency, either $t_0 > t_m > t_c$ (typical for high frequencies), or $t_0 < t_m < t_c$, where t_m and t_c are the times when the break frequencies ν_m and ν_c cross the observed frequency ν.

Given values for the isotropic equivalent energy of the initial explosion and the microphysical parameters (p, ϵ_e, ϵ_B, and ζ_e), and for a certain fireball Lorentz factor evolution (i.e. adiabatic or radiative), the temporal evolution of the characteristic frequencies can be determined. The observed light curve at a specific frequency (in the observer frame) can then be described by the temporal variation of the characteristic frequencies and of $F_{\nu,max}$, the peak flux (Fig. 2.2). The flux at a given frequency ν can be expressed as $F_\nu(t,\nu) \propto t^\alpha \nu^\beta$, where α and β are the temporal and spectral decay indices (Sari et al., 1998).

This simple afterglow model is based on certain assumptions. The fireball is taken to be isotropic, resulting from an impulsive injection of energy from the central engine, and the density of the external medium into which the forward shock propagates is assumed to be constant. Constraints are also placed on the microphysical parameters associated with the shock. A fraction ζ_e (generally taken to be $\lesssim 1$) of the total electrons in the shocked external medium are accelerated, resulting in an electron energy distribution with spectral index $p > 2$. The maximum electron energy, $\gamma_{e,max} >> \gamma_{e,min}$, and the electrons are assumed to radiate via the synchrotron process. The energy density in the magnetic field and relativistic electrons are a fixed fraction, ϵ_B and ϵ_e respectively, of the total energy density

in the shock. Finally, it is assumed that no evolution of the microphysical parameters occurs.

2.1.2 Modified Afterglow Models

The assumptions in the basic afterglow model serve to simplify the analysis, and are not expected to be realistic in all cases, though they work remarkably well for many events. Many authors have proposed modifications to the simple afterglow model by considering cases in which the first–order assumptions are not satisfied. Some of the main modifications are discussed below (for further details, see Zhang and Mészáros (2004), and references therein). Table 2.1 shows the expected temporal and spectral indices corresponding to the forward shock spectral regimes in the simple afterglow model, and also presents values for some of the modified cases discussed below, as well as cases where the electron power–law index $1 < p < 2$ (e.g. Dai and Cheng, 2001).

Jets

The assumption that the fireball is isotropic is unlikely to be realistic, and several authors have studied the effects of modifying the simple afterglow model by introducing a collimated relativistic outflow i.e. a jet (e.g. Panaitescu et al., 1998; Rhoads, 1999). The geometric beaming factor θ_j introduced by a simple jet model is the opening angle of the jet. This is entirely separate from the relativistic beaming factor which causes emission from an object moving with Lorentz factor Γ to be beamed into a cone with opening angle $1/\Gamma$. However, the interaction of these two effects can produce measurable changes in the afterglow light curve.

Initially the outflow is highly relativistic and therefore highly beamed, so that $1/\Gamma < \theta_j$. An observer along the line of sight can only detect emission from within this relativistic cone, so the observed dynamical evolution of the fireball is equivalent to the isotropic case, i.e. the simple model. As the jet slows down, the relativistic beaming effects decrease and the cone expands until it eventually becomes wider than the collimation angle, i.e. $1/\Gamma > \theta_j$. The fireball evolution, which had been equivalent to the isotropic case where Γ declined as a power–law of radius r, now qualitatively changes so that Γ declines as an exponent of radius, i.e.

$$\Gamma \propto exp(-r/l) \propto t^{-1/2}, r \propto t^0$$

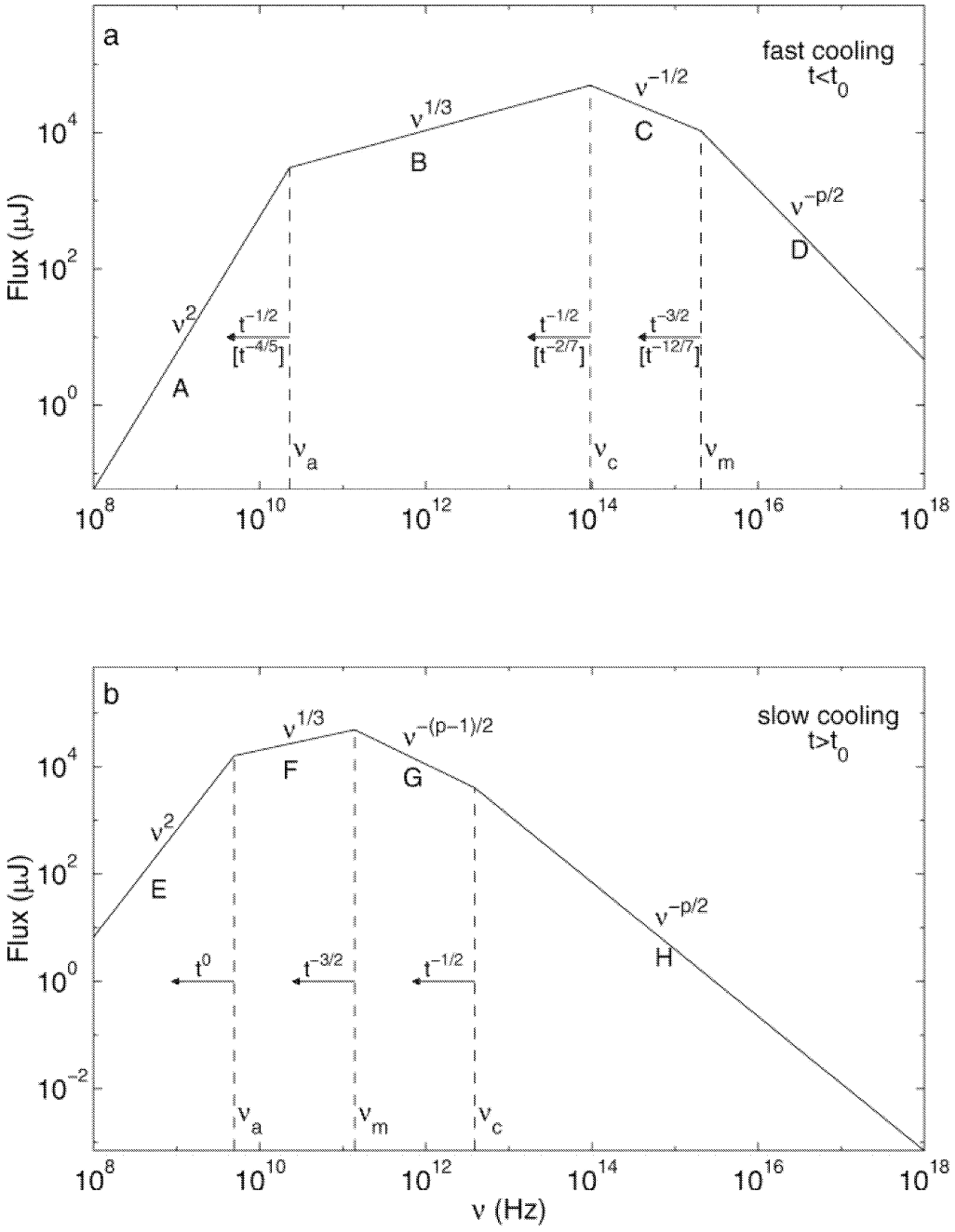

Figure 2.1: Synchrotron spectrum of a relativistic shock with a power–law electron energy distribution. (a) Fast cooling, which is expected at early times ($t < t_0$). The spectrum consists of four segments, identified as A, B, C, and D. Self–absorption is important below ν_a. The frequencies ν_m, ν_c, and ν_a decrease with time as indicated; the scalings above the arrows correspond to an adiabatic evolution, and the scalings below, in square brackets, correspond to a fully radiative evolution. (b) Slow cooling, which is expected at late times ($t > t_0$). The evolution in this case is always adiabatic. The four segments are identified as E, F, G, and H. *From Sari et al. (1998)*

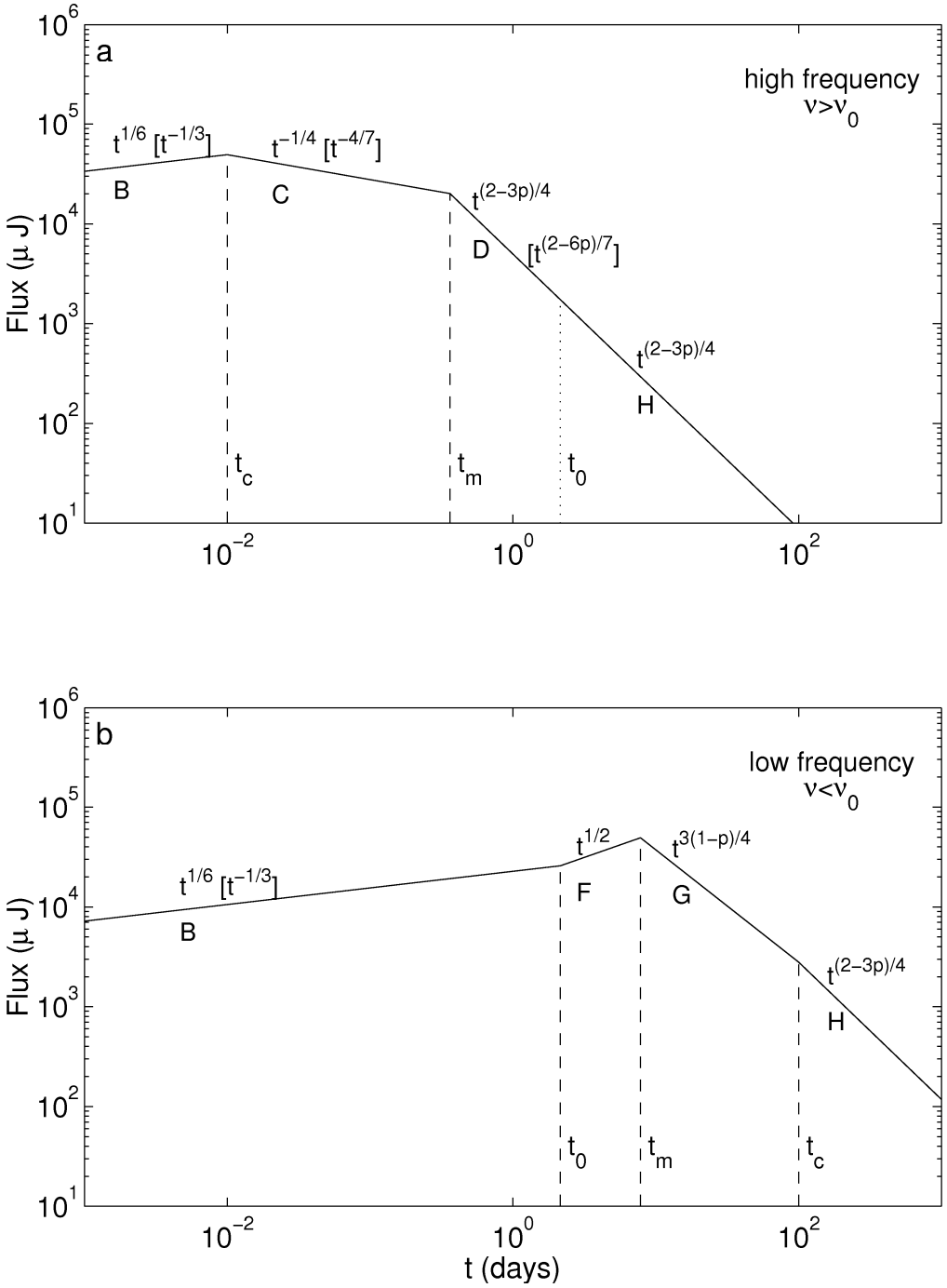

Figure 2.2: Afterglow light curves corresponding to the synchtron spectrum shown in Fig. 2.1. (a) illustrates the high–frequency case ($\nu > \nu_0$), while the low–frequency case ($\nu < \nu_0$) is shown in (b). The critical frequency ν_0 is defined as the frequency at time t_0 when the transition from fast to slow cooling occurs, i.e. $\nu_0 = \nu_c(t_0) = \nu_m(t_0)$. The scalings within square brackets are for radiative evolution (which is restricted to $t < t_0$), while the others are for adiabatic evolution. *From Sari et al. (1998)*

	β	α ($p > 2$, $p \sim 2.3$)	$\alpha(\beta)$	α ($1 < p < 2$, $p \sim 1.5$)	$\alpha(\beta)$
ISM, slow cooling					
$\nu < \nu_a$	2	$\frac{1}{2}$		$\frac{17p-26}{16(p-1)} \sim -0.06$	
$\nu_a < \nu < \nu_m$	$\frac{1}{3}$	$\frac{1}{2}$	$\alpha = \frac{3\beta}{2}$	$\frac{p+2}{8(p-1)} \sim 0.9$	
$\nu_m < \nu < \nu_c$	$-\frac{p-1}{2}$	$\frac{3(1-p)}{4} \sim -1.0$	$\alpha = \frac{3\beta}{2}$	$-\frac{3(p+2)}{16} \sim -0.7$	$\alpha = \frac{3(2\beta-3)}{16}$
$\nu > \nu_c$	$-\frac{p}{2}$	$\frac{2-3p}{4} \sim -1.2$	$\alpha = \frac{3\beta+1}{2}$	$-\frac{3p+10}{16} \sim -0.9$	$\alpha = \frac{3\beta-5}{8}$
ISM, fast cooling					
$\nu < \nu_a$	2	1		1	
$\nu_a < \nu < \nu_c$	$\frac{1}{3}$	$\frac{1}{6}$	$\alpha = \frac{\beta}{2}$	$\frac{1}{6}$	$\alpha = \frac{\beta}{2}$
$\nu_c < \nu < \nu_m$	$-\frac{1}{2}$	$-\frac{1}{4}$	$\alpha = \frac{\beta}{2}$	$-\frac{1}{4}$	$\alpha = \frac{\beta}{2}$
$\nu > \nu_m$	$-\frac{p}{2}$	$\frac{2-3p}{4} \sim -1.2$	$\alpha = \frac{3\beta+1}{2}$	$-\frac{3p+10}{16} \sim -0.9$	$\alpha = \frac{3\beta-5}{8}$
Wind, slow cooling					
$\nu < \nu_a$	2	1		$\frac{13p-18}{8(p-1)} \sim 0.4$	
$\nu_a < \nu < \nu_m$	$\frac{1}{3}$	0	$\alpha = \frac{3\beta-1}{2}$	$\frac{5(2-p)}{12(p-1)} \sim 0.4$	
$\nu_m < \nu < \nu_c$	$-\frac{p-1}{2}$	$\frac{1-3p}{4} \sim -1.5$	$\alpha = \frac{3\beta-1}{2}$	$-\frac{p+8}{8} \sim -1.2$	$\alpha = \frac{2\beta-9}{8}$
$\nu > \nu_c$	$-\frac{p}{2}$	$\frac{2-3p}{4} \sim -1.2$	$\alpha = \frac{3\beta+1}{2}$	$-\frac{p+6}{8} \sim -0.9$	$\alpha = \frac{\beta-3}{4}$
Wind, fast cooling					
$\nu < \nu_a$	2	2		2	
$\nu_a < \nu < \nu_c$	$\frac{1}{3}$	-$\frac{2}{3}$	$\alpha = -\frac{\beta+1}{2}$	-$\frac{2}{3}$	$\alpha = -\frac{\beta+1}{2}$
$\nu_c < \nu < \nu_m$	$-\frac{1}{2}$	$-\frac{1}{4}$	$\alpha = -\frac{\beta+1}{2}$	$-\frac{1}{4}$	$\alpha = -\frac{\beta+1}{2}$
$\nu > \nu_m$	$-\frac{p}{2}$	$\frac{2-3p}{4} \sim -1.2$	$\alpha = \frac{3\beta+1}{2}$	$-\frac{p+6}{8} \sim -0.9$	$\alpha = \frac{\beta-3}{4}$
Jet, slow cooling					
$\nu < \nu_a$	2	0		$\frac{3(p-2)}{4(p-1)} \sim -0.8$	
$\nu_a < \nu < \nu_m$	$\frac{1}{3}$	$-\frac{1}{3}$	$\alpha = 2\beta - 1$	$\frac{8-5p}{6(p-1)} \sim 0.2$	
$\nu_m < \nu < \nu_c$	$-\frac{p-1}{2}$	$-p \sim -2.3$	$\alpha = 2\beta - 1$	$-\frac{p+6}{4} \sim -1.9$	$\alpha = \frac{2\beta-7}{4}$
$\nu > \nu_c$	$-\frac{p}{2}$	$-p \sim -2.3$	$\alpha = 2\beta$	$-\frac{p+6}{4} \sim -1.9$	$\alpha = \frac{\beta-3}{2}$

Table 2.1: Predicted temporal and spectral indices α and β from various afterglow models, following the convention $F_\nu \propto t^\alpha \nu^\beta$. The assumption $\nu_a < \min(\nu_m, \nu_c)$ is made. *From Zhang and Mészáros (2004)*

This change results in a break in the power–law light curve, where the late–time decay is $\propto t^{-p} \sim t^{-2}$, much faster than that expected for the isotropic case ($\propto t^{-1}$) (Sari et al., 1999). Since this is a purely hydrodynamical effect, the temporal break should occur simultaneously across all wavelengths. Similarly, the shock microphysics should remain unaffected. The time at which the jet break occurs can be used as a measure of the opening angle of the jet, θ_j, which in turn can be used to infer the geometrically corrected total energy budget of the burst.

Wind Medium

The simple afterglow model assumes that the forward shock propagates into a constant density ISM. However, the massive star progenitor which has been proposed for long GRBs suggests that the ambient medium may be a stellar wind environment, as seen in Wolf–Rayet stars. The density profile of such an environment is $\rho \propto r^{-2}$, which changes the fireball evolution to

$$\Gamma \propto r^{-1/2} \propto t^{-1/4}, \quad r \propto t^{1/2}2 \tag{2.1}$$

The optical afterglow in this case is expected to decline more steeply (Chevalier and Li, 1999, 2000). Concurrent X–ray, optical, and radio afterglow observations are particularly useful for distinguishing between the wind and ISM environments.

Energy Injections

If the central engine is still active when the fireball is decelerated (the onset of the afterglow), or if the ejecta shells have a range of bulk Lorentz factors, then shells emitted later or with lower Lorentz factors can catch up and refresh the forward shock (Rees and Mészáros, 1998). Generally, a total injection energy comparable to that of the impulsive energy in the initial fireball is required to make a detectable signature in the afterglow light curves (Zhang and Mészáros, 2002). Energy injections can produce a variety of signatures in afterglow light curves, including flattening, bumps, and temporal breaks on cessation of energy injection.

2.1.3 Reverse Shocks

When the fireball ejecta (in the form of a relativistic shell) are decelerated by the ambient medium, a reverse shock is generated which propagates back into the ejecta (Mészáros and Rees, 1997; Sari and Piran, 1999b). As the shock crosses the shell, electrons are accelerated to a power–law energy distribution and emit radiation according to the synchrotron spectrum described by Sari et al. (1998). As it crosses the shell, the reverse shock carries a comparable amount of energy to the forward shock, but with a much lower Lorentz factor, so that significant flux is expected at the typical synchrotron frequency which lies in the

optical regime (Sari and Piran, 1999b).

The appearance of the light curve at a given frequency depends on the temporal evolution of the peak flux $F_{\nu,max}$, and the break frequencies ν_m and ν_c in the synchrotron spectrum (the self–absorption frequency, ν_a, can be neglected since it falls well below the peak frequency which is in the optical). For values of $\Gamma \approx 1000$'s, the spectrum is slow–cooling throughout its evolution, i.e. $\nu_m < \nu_c$, so that the evolution of the shell can be treated as being adiabatic (Kobayashi, 2000). A third key frequency, ν_{cut}, can be defined, above which no flux is observed. Once the shock has crossed the shell, no new electrons are accelerated, so that there is no longer emission above ν_{cut}.

The hydrodynamical analysis of the reverse shock evolution requires that high and low density shells are treated separately (Sari and Piran, 1995). If the shell density is high, the reverse shock is Newtownian and is too weak to effectively decelerate the shocked shell (the thin–shell case). If the shell density is low, the shock is relativistic and causes considerable deceleration in the shell. Shells have high densities when ejected, but expansion causes the density to decrease, so that the shock may become relativistic as it crosses the shell. According to the internal shock model, the duration of a GRB is given by the shell width Δ_0/c, where Δ_0 is the shell width in the laboratory frame. The reverse shock crosses a thick shell at $T \sim \Delta_0/c$, so the peak of the emission is comparable to the GRB duration. In the thin shell case, the reverse shock crosses at t_γ, where $\Delta_0/c < t_\gamma$. Therefore a delay is expected between the GRB and the peak of the reverse shock emission (Kobayashi, 2000).

Predicted light curves for the reverse shock emission in the slow–cooling phase for both the thick and thin–shell cases, as calculated by Kobayashi (2000), are shown in Fig. 2.3. The light curves peak at the reverse shock crossing times T (thick–shell) and t_γ (thin–shell). While the temporal power–law indices of the rise to the peak are different in each case, the power–law decay indices after the peak are ~ -2 in both cases (for typical values of $p \sim 2.2 - 2.5$), corresponding to adiabatic cooling of the accelerated electrons after the shock has crossed the shell.

Zhang et al. (2003a) analysed a sample of early optical afterglows as a combination of reverse and forward shock emission. The light curve for optical emission from the forward shock is well described by the low–frequency case of Sari et al. (1998) (Fig. 2.2), characterised by a turnover of the temporal indices from $1/2$ to ~ -1 at the peak time $t_{p,f}$, at which the typical synchrotron frequency of the forward shock $\nu_{m,f}$ crosses

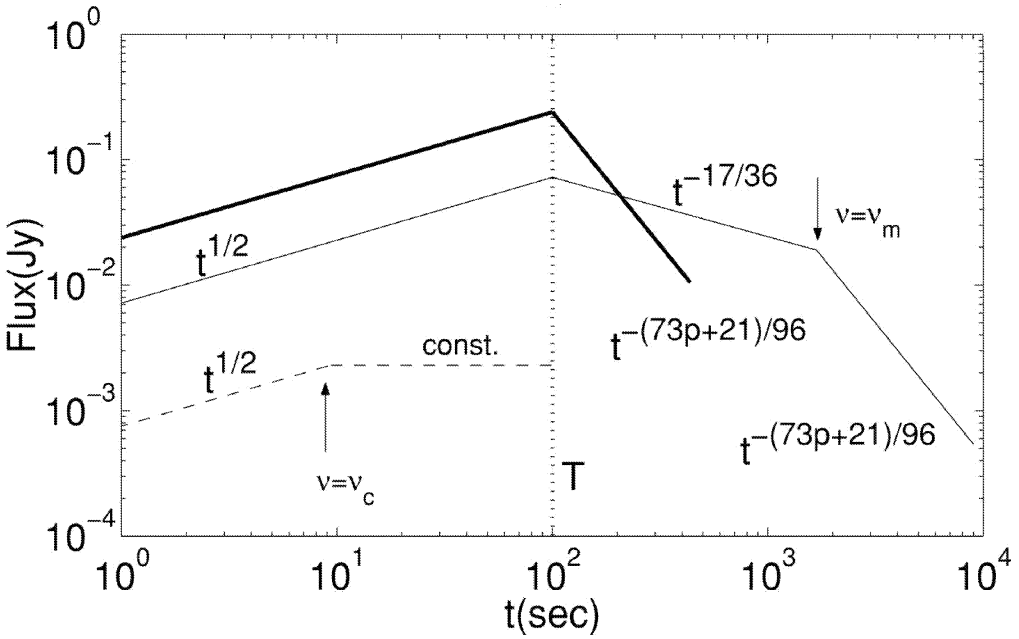

(a) Thick shell case. The observed frequency ν is $\nu = 10^{13}$ Hz $< \nu_m(T)$ (thin solid line), $\nu_m(T) < \nu = 10^{15}$ Hz $< \nu_c(T)$ (thick solid line), and $\nu = 10^{17}$ Hz $> \nu_c(T)$ (dashed line).

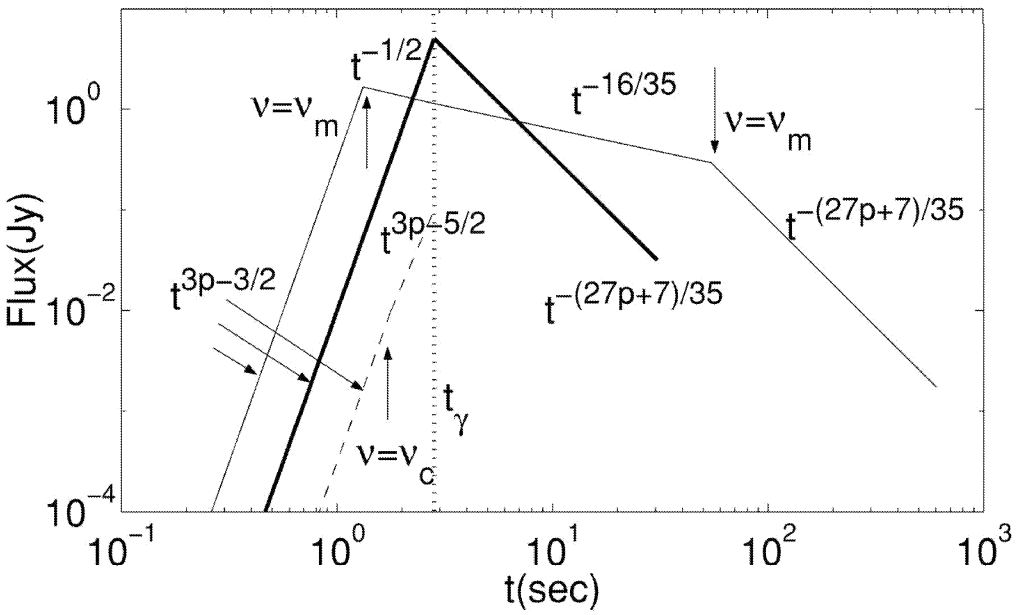

(b) Thin shell case. The observed frequency ν is $\nu = 10^{13}$ Hz $< \nu_m(t_\gamma)$ (thin solid line), $\nu_m(t_\gamma) < \nu = 10^{15}$ Hz $< \nu_c(t_\gamma)$ (thick solid line), and $\nu = 10^{17}$ Hz $> \nu_c(t_\gamma)$ (dashed line).

Figure 2.3: Predicted typical light curves of reverse shock emission in the slow–cooling phase for three frequency regimes separated by the two key frequencies ν_m and ν_c at time T for the thick shell case (a), and t_γ for the thin–shell case (b). Optical emission ($\nu = 10^{15}$Hz), is represented by the thick solid lines. *From Kobayashi (2000).*

the observational band (the typical R–band frequency ν_R). The reverse shock light curve is more complicated, depending on whether the shell is thin or thick, and on how the observed frequency compares with the typical synchrotron frequency of the reverse shock, $\nu_{m,r}$. Two types of early optical light curve were identified (Fig. 2.4):

Type I (Rebrightening): The reverse shock component meets the forward shock component before the forward shock peak time.

Type II (Flattening): The reverse shock component meets the forward shock component after the forward shock peak time.

Zhang et al. (2003a) also propose a method to constrain the initial fireball Lorentz factor by measuring the peak times of the reverse and forward shock emission, and the rapid temporal decay index after the reverse shock. The advantage of this method over previous approaches (e.g. Sari and Piran, 1999a) is that it reduces the dependance on the poorly known shock microphysics parameters.

2.2 Observational Highlights

2.2.1 First Afterglow Detections

The launch of the Italian–Dutch BeppoSAX mission in 1996 (§3.3.2) paved the way for the first detections of GRB counterparts at longer wavelengths. The breakthrough discovery occurred after hard X–rays from GRB 970228 were detected by one of the WFCs on BeppoSAX. Pointed observations carried out by the satellite's Narrow Field Monitor (NFI) ~ 8 hours later revealed the presence of an unknown soft X–ray point source. Observations four days later showed the flux of this source to have decreased by a factor of ~ 20 (Fig. 2.5), thus confirming the first detection of a GRB X–ray afterglow (Costa et al., 1997). This landmark burst was also the first for which an optical afterglow was detected, when a fading 21 magnitude source was detected in images taken 21 hours and 4 weeks after the burst (Fig. 2.6) with the William Herschel and Isaac Newton Telescopes at La Palma (van Paradijs et al., 1997). Subsequent deep imaging with various instruments, including the HST (e.g. Sahu et al., 1997; Fruchter et al., 1999), discovered a decaying source at the edge of an extended object, which was determined to be the host galaxy of GRB 970228 at a redshift of $z = 0.695$ (Djorgovski et al., 1999).

The slopes (α_{opt} and α_X) of the optical and X–ray temporal power–law decays, and the

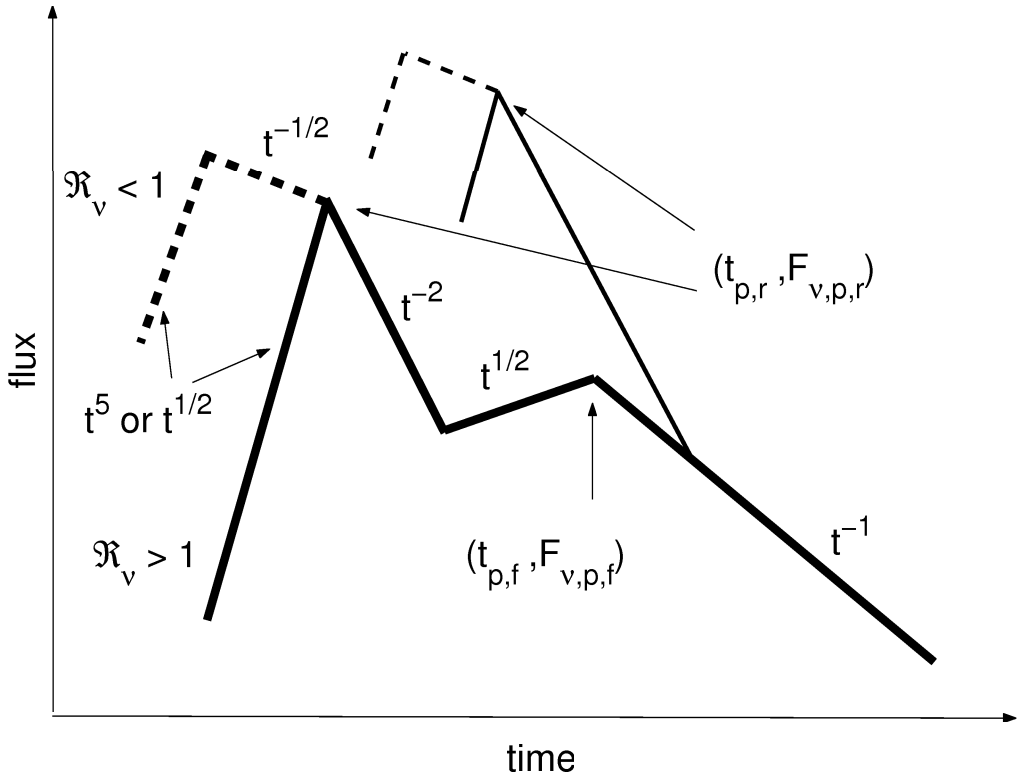

Figure 2.4: Typical lightcurves of the reverse–forward shock emission combinations for the homogeneous ISM case. The thick lines depict a typical "rebrightening" (type I) lightcurve, while thin lines indicate a typical "flattening" (type II) lightcurve. The forward shock peak $(t_{p,f}, F_{\nu,m,p})$ is defined at the transition point of the $\propto t^{1/2}$ to $\propto t^{-1}$ lightcurves. The reverse shock peak $(t_{p,r}, F_{\nu,m,r})$ is defined at the beginning of the $\propto t^{-2}$ segment for the reverse shock emission. Before this point, the lightcurve is $\propto t^5$ (thin shell) or $\propto t^{1/2}$ (thick shell) for $\mathcal{R}_\nu \equiv \nu_R/\nu_{m,r}(t_\times) > 1$ (usually the case), and $\propto t^{-1/2}$ for $\mathcal{R}_\nu < 1$. *From Zhang et al. (2003a)*

slopes (β_X and β_{X-opt}) of the (assumed) power–law afterglow spectrum in the X–ray and X–ray to optical wavebands were determined. The relation between α and β was in good agreement with predictions from the simple fireball model, although after subtracting a suspected SN contribution to the late–time (1–2 weeks) optical light curve, it may be better fit by a blast wave propagating in a stellar wind (Chevalier and Li, 1999).

Further progress was made with the detection of the optical afterglow of GRB 970508 (Bond, 1997), which rebrightened to a peak of $R \simeq 19.8$ two days after the burst before commencing a slow power–law decline which could be followed for several hundred days (e.g. Djorgovski et al., 1997). Spectroscopic observations of the optical transient revealed the presence of absorption lines of Mg II, Fe II, amd Mg I at a redshift $z = 0.835$ (Metzger et al., 1997a). This result firmly established that GRBs occur at cosmological distances,

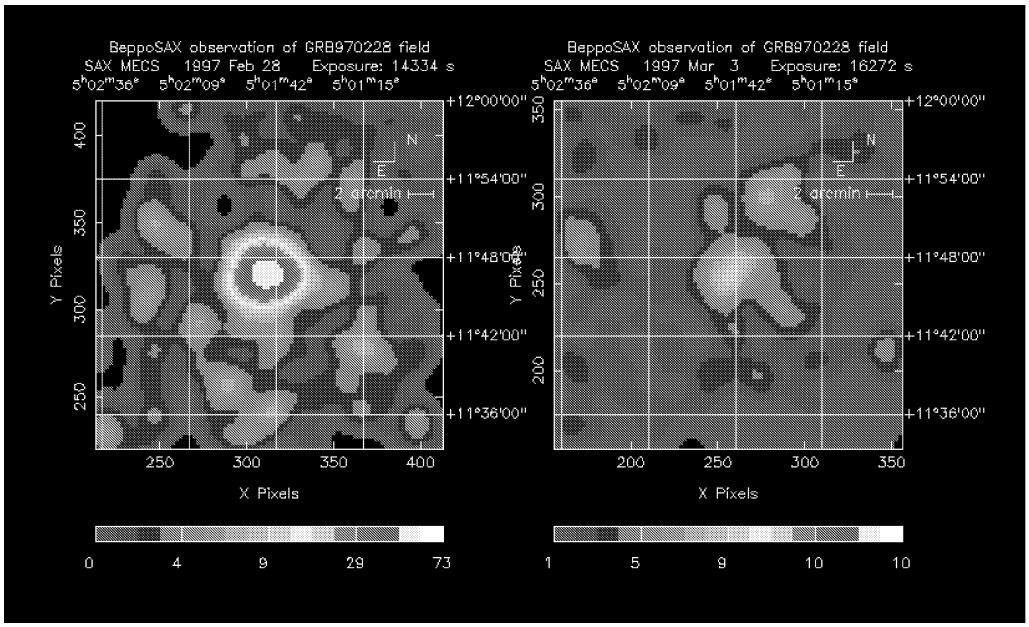

Figure 2.5: The X–ray afterglow of GRB 970228, as observed by the NFI instrument on BeppoSAX. *From Costa et al. (1997)*

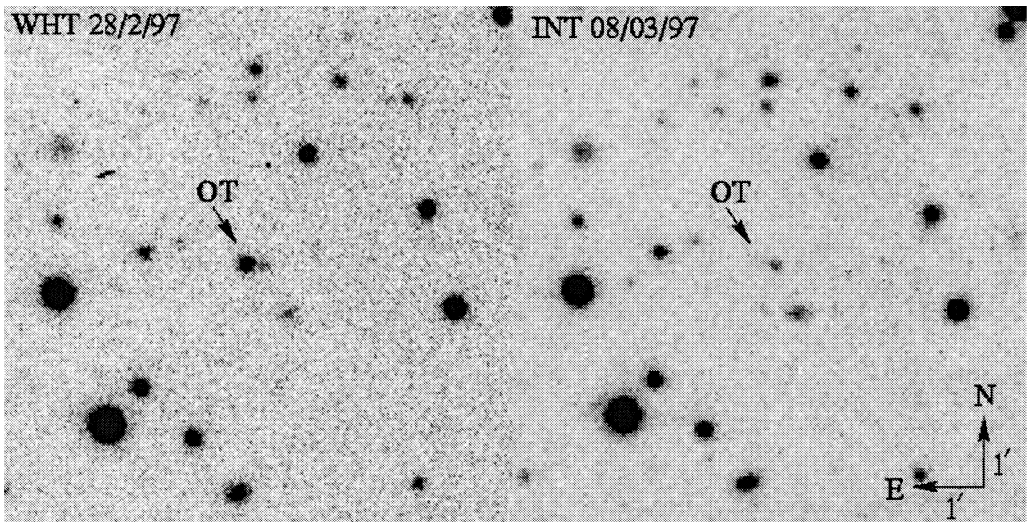

Figure 2.6: The optical afterglow of GRB 970228, as observed by the William Herschel and Isaac Newton Telescopes at La Palma. *From van Paradijs et al. (1997)*

and so resolved the debate over the distance scale.

Radio observations of the field of GRB 970508 by Frail et al. (1997) led to the first detection of a GRB counterpart at radio wavelengths. Strong variations in the radio flux which damped out after a month were observed, and interpreted as interstellar scintillation in our galaxy, damped by the increasing size of the emitting region. By inferring a value for the source size when variations ceased it could be determined that the radio source had expanded relativistically, as predicted by the fireball model.

GRB 970508 was the first GRB whose afterglow was observed from X–ray wavelengths to optical/near–IR, sub–mm, and low–frequency radio, allowing the broadband spectrum to be reconstructed by Galama et al. (1998b), at 12.1 days after the burst. This spectrum was well described by a model of an adiabatically expanding blast wave emitting synchrotron radiation, strongly supporting the relativistic shock model of GRB afterglows.

2.2.2 Early Optical Observations

In 1999, the ROTSE–I ground–based optical telescope (Marshall et al., 1997) detected, for the first time, optical emission from a GRB contemporaneous with the γ–ray emission. At 09:46:56 on January 23, BATSE detected an extremely bright burst with $T_{90} = 63.30 \pm 0.26$ s (Kippen, 1999). The ROTSE–I instrument rapidly responded to the GCN alert, producing its first useful image of the BATSE error box 22 s after the onset of the burst. A bright optical transient was detected (Fig. 2.7), which increased in brightness from $m_v = 11.7$ mag to 8.9 mag in the following 25 seconds, before beginning a smooth power–law decline (Akerlof et al., 1999). Spectroscopic observations of the optical transient later determined a redshift of $z = 1.6$ (Kelson et al., 1999). From the optical and γ–ray light curves shown in the insert of Fig. 2.8, it is clear that the prompt optical and γ–ray emission are uncorrelated, and so are likely produced in different emitting regions in the fireball (Sari and Piran, 1999a). This result confirmed predictions by Sari and Piran (1999b), who postulated that, in the context of the internal–external shock scenario, a strong optical flash brighter than 15^{th} mag would be produced by a reverse shock propagating into the relativistic ejecta (§2.1.3). Further support for the reverse shock scenario was provided by detection of a flare in the radio afterglow of GRB 990123, which was interpreted as a signature of reverse shock emission (Kulkarni et al., 1999).

Evidence for a reverse shock was also seen in the early optical emission from GRB 021211, a bright long–duration (~5 s) burst detected by HETE–2 (Crew et al., 2002). Rapid

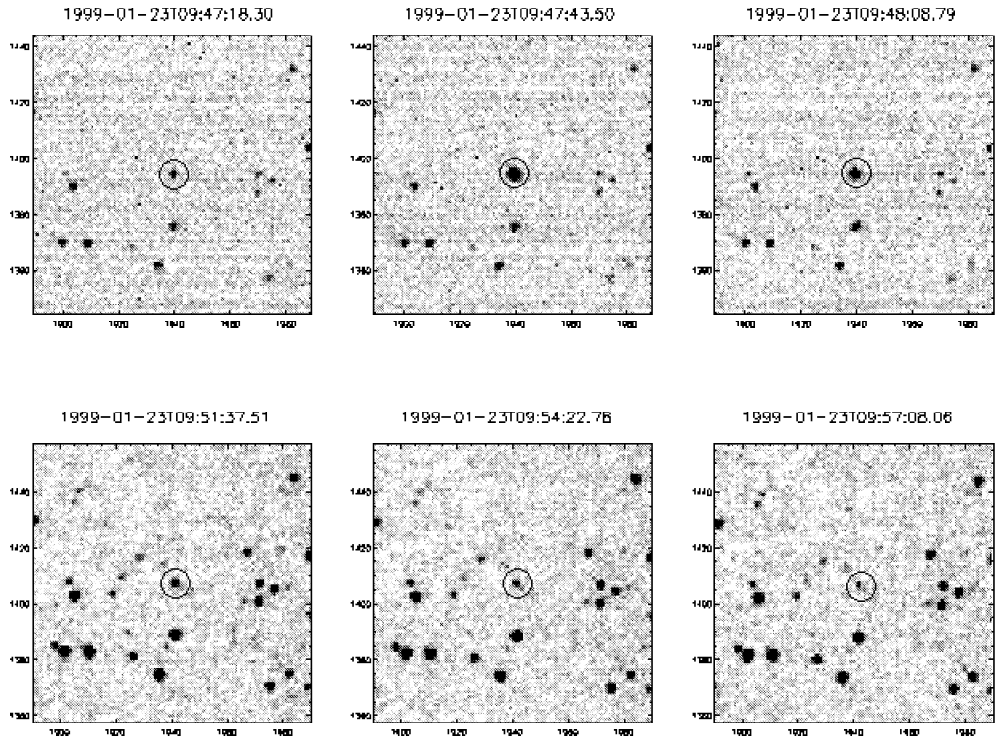

Figure 2.7: Prompt ROTSE–I images of the optical counterpart of GRB 990123, 3×5 s exposures (top) and 3×75 s exposures (bottom). The OT is clearly detected in all images, and can be seen to rebrighten from the first to the second frame before beginning to decay Each image is $24' \times 24'$, which comprises 6×10^{-4} of the ROTSE–I field of view. *From Akerlof et al. (1999).*

follow–up observations were performed by several instruments, the earliest at T_0 +65 s by RAPTOR, which detected an optical transient with $R_c = 14.06 \pm 0.08$ mag (Wozniak et al., 2002). The optical afterglow displayed a similar temporal evolution to that of GRB 990123, though fainter by ∼3 mag at similar epochs (Li et al., 2003). While GRB 990123 was observed from optical through infra–red, sub–mm to mm, and radio wavelengths (Galama et al., 1999), GRB 021211 was detected only in the optical and infrared. It is significant that the γ–ray fluence of GRB 990123 place it among the top 0.3% of BATSE bursts, while that of GRB 021211 is typical of the HETE–2 bursts reported by Barraud et al. (2003). The intrinsic faintness of the afterglow of GRB 021211, together with its fast decline, suggest that the lack of afterglow detections in at least some of the so–called "dark bursts" (§2.3.2) may be due to the intrinsic faintness of the afterglow, which has rapidly declined below instrumental detection limits by the time it is observed.

Early optical emission was observed for another GRB in 2002: GRB 021004, a long

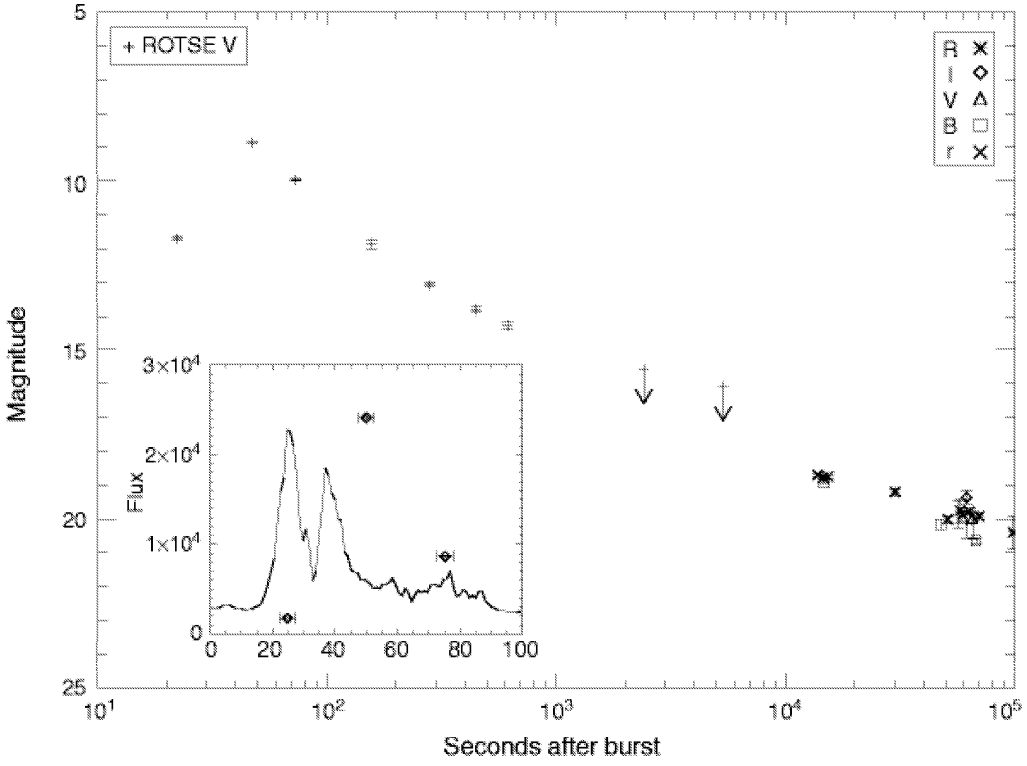

Figure 2.8: The combined optical light curve of GRB 990123, with prompt ROTSE–I observations and afterglow data taken from the GCN. The inset shows the first three ROTSE–I data points (in arbitrary units) plotted with the BATSE 100–300keV γ–ray light curve. *From Akerlof et al. (1999).*

(T_{90} ~ 100 s) burst detected by HETE–2 (Shirasaki et al., 2002). The 30′ radius error circle was observed by several ground–based instruments, beginning at T_0 + 193 s, and a bright optical transient was detected, with initial brightness of 15.45 mag (Fox, 2003). The brightness and early detection of the optical afterglow allowed for extensive follow–up observations by observers worldwide, leading to a high–quality, densely sampled afterglow light curve in wavelengths from blue into the near–IR and radio (Berger et al., 2002). The early decay of the optical light curve was unexpectedly shallow and displayed a major rebrightening at ~ 0.1 days, along with short timescale variability at various times from ~ 1 days. Kobayashi and Zhang (2003) explained the slow decline, rebrightening and subsequent decay in the context of the fireball model as the initial rise of the forward shock emission as the typical synchrotron frequency crossed the optical band, together with a component from reverse shock emission. Fox (2003) interpreted the subsequent variability as possible evidence for central engine activity continuing well beyond T_{GRB}. Similar variability was also observed in the light curve of GRB 030329 (Lipkin et al.,

2004).

Following ROTSE's breakthrough observations of GRB 990123, optical emission contemporaneous with γ–ray activity was not observed in another GRB until GRB 041219a. This very bright burst, detected by both *INTEGRAL* and *Swift* (McBreen et al., 2006; Gotz et al., 2004; Barthelmy et al., 2004), was one of the longest bursts ever detected, with T_{90} = 520 s. Transient counterparts were detected in the optical by RAPTOR at T_0 + 115 s (Vestrand et al., 2005), and in the infra–red by PAIRITEL at T_0 + 7.2 mins (Blake et al., 2005). The γ–ray lightcurve of GRB 041219a was remarkably similar to that of GRB 990123 (Fig. 2.9), given a temporal scaling factor to account for the significant duration differences. However, in contrast to the optical behaviour of GRB 990123, an optical–IR flash was observed from GRB 041219a which tracked the γ–ray light curve. Vestrand et al. (2005) found that by scaling the γ–ray emission by a constant optical to high–energy flux ratio, the predicted light curve was a close match to their observations, indicating that the optical and γ–ray emission were correlated. Fan et al. (2005) successfully modelled the optical and infra–red lightcurves with emission from internal shocks in a neutron–rich GRB outflow during the prompt phase, and a superposition of reverse and forward shock components thereafter (similar to the work by Kobayashi and Zhang (2003) on GRB 021004). Based on the new optical properties displayed by GRB 041219a, Vestrand et al. (2005) proposed a new taxonomy of GRB optical emission types and mechanisms:

- prompt optical emission correlated with γ–ray emission, produced by internal shocks in the relativistic ejecta
- early afterglow emission due to a reverse shock
- late afterglow from forward external shocks driven into the circumburst medium

2.2.3 Jet Breaks

Afterglow observations in the pre–*Swift* era were generally carried out at late times in optical and radio bands, and were focused on identifying temporal breaks in the light curves in order to confirm the collimation of the GRB outflow (§2.1.2). Steepening of the temporal decay indices consistent with theoretical predictions for jet breaks were observed in many cases (see compilation of pre–*Swift* afterglow data in Zeh et al., 2006),

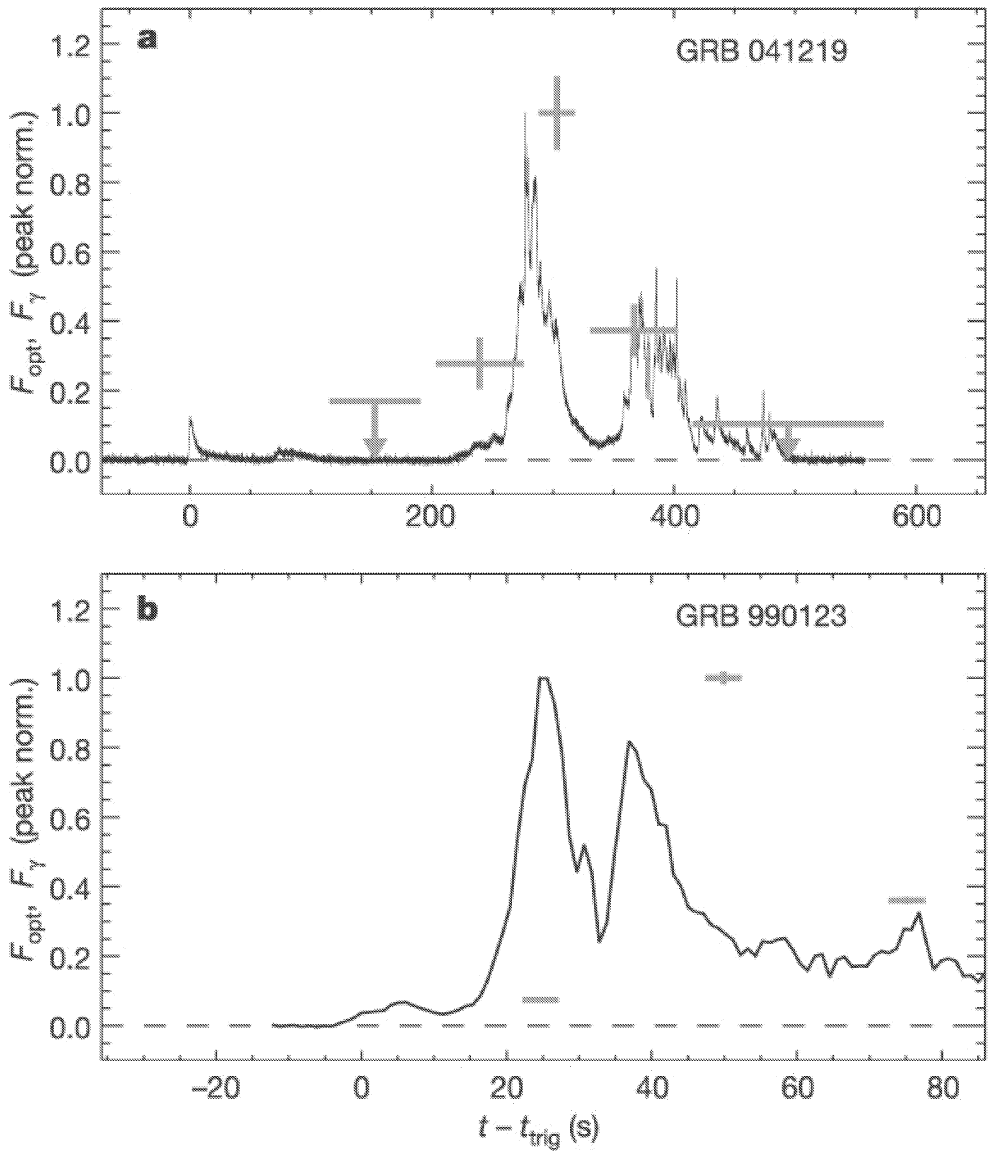

Figure 2.9: Comparison of the γ–ray and and prompt optical light curves for GRB 041219a and GRB 990123. *From Vestrand et al. (2005).*

with the prototypical GRB 990510 being the best example (Harrison et al., 1999). By interpreting these temporal breaks as jet breaks, the jet opening angle, and therefore the geometrically corrected γ–ray energy, could be inferred from the time of the break. This alleviated the energy budget problem encountered in some GRBs if their emission was assumed to be isotropic (e.g. GRB 990123, Kulkarni et al., 1999). An empirical relation was found whereby the beaming–corrected γ–ray energy is essentially constant at $\sim 5\times10^{50}$ ergs (Frail et al., 2001; Bloom et al., 2003). The jet break interpretation became generally accepted in the pre–*Swift* era, though some authors cast doubts on whether the

observed breaks could be explained by a jet model (e.g. Wei and Lu, 2002).

2.3 The *Swift* Era

The quality of GRB afterglow observations has dramatically improved in the *Swift* era. The *Swift* mission (§3.4.1) combines improved sensitivity to GRBs with multi–wavelength instruments and, crucially, rapid localisation and slewing capabilities, which has led to routine observations of GRBs at X–ray and UV/optical wavelengths ∼100 s from the trigger. These capabilities have allowed the prompt and early afterglow phases to be explored in far greater detail than was previously possible. *Swift* also provides GRB positions with unprecedented speed and accuracy, which has greatly assisted ground–based follow–up observations with robotic optical/IR telescopes, a significant number of which have come online in recent years.

2.3.1 Optical Afterglows

Observations of optical afterglows in the *Swift* era have revealed early faintness to be more the norm than the exception, contrary to pre–*Swift* expectations. Reverse shock optical flashes have been much less common than had been suggested by early optical observations pre–*Swift*, while optical afterglow behaviour in general has been unexpectedly complex and varied. Surprisingly, a sizeable fraction of GRBs have no detectable afterglows at optical wavelengths (the so–called "dark bursts" problem, §2.3.2).

A comparison of the luminosities of optical afterglows in the *Swift* and pre–*Swift* eras by Kann et al. (2007) finds no statistically significant difference between the samples, suggesting that the faintness of *Swift*–era afterglows may be attributed to their higher mean redshift (§1.9), though several selection effects apply. The study also confirms the bimodal distribution of optical afterglow luminosities found previously (Nardini et al., 2007; Liang and Zhang, 2006; Kann et al., 2006). A majority of afterglows belong to the brighter of the two populations, while low redshift afterglows are, on average, less luminous than more distant ones, providing possible evidence for the existence of a nearby, sub–luminous population as proposed by several authors (e.g. Norris, 2002; Soderberg et al., 2004; Foley et al., 2008). The luminosity distribution at early times (10^{-3} days at $z = 1$) is very broad, yet exhibits strong clustering around 13 mag. (Fig. 2.10). Kann et al. (2007) suggest that

the clustered afterglows are those which are dominated by forward shock emission at early times, while the even brighter ones are dominated by additional emission components.

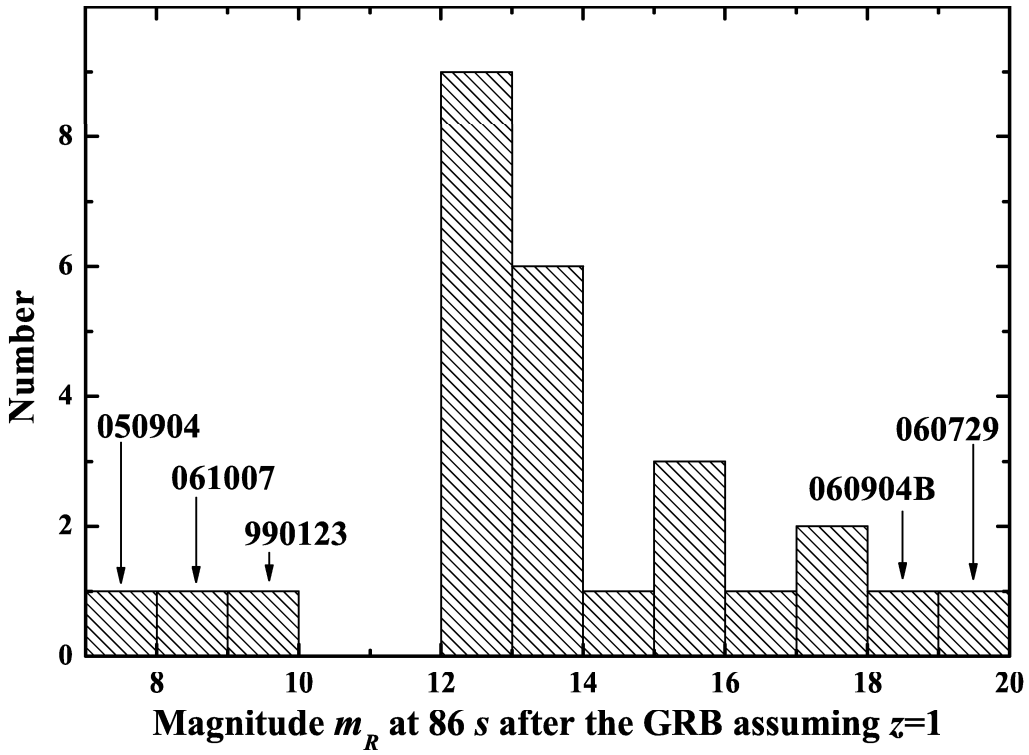

Figure 2.10: Distribution of optical afterglow magnitudes at 86 s (10^{-3} days) from the trigger, having shifted all afterglows to $z = 1$. *From Kann et al. (2007).*

2.3.1.1 Reverse Shock Emission

Though rare, optical flashes similar to GRB 990123 have been observed. GRB 060111b was a bright, double–peaked burst detected by *Swift* (Perri et al., 2006), with $T_{90} = 59 \pm 1$ s. A $\sim 13^{th}$ mag, rapidly decaying, optical transient was detected at $\sim T_0 + 29$ s by both the ROTSE–III and TAROT robotic telescopes (Yost et al., 2006b; Klotz et al., 2006a). The high–time resolution light curve obtained by TAROT revealed a lack of fine time structure during the decay of the optical flare, while the γ–ray light curve showed a peak during the same time interval. The clear anti–correlation between the optical and γ–ray flux rules out a common emission mechanism, and the rapid ($\alpha = 2.4$) decay of the optical afterglow unambiguously identifies the reverse shock as the source of the prompt optical emission (Klotz et al., 2006b).

GRB 060117 was an extremely intense burst detected by *Swift* (Campana et al., 2006a), with $T_{90} = 16 \pm 1$ s. Observations by the robotic telescope FRAM, beginning at T_0

+ 124 s, detected a very bright optical transient at $R = 10.1$ mag (Kubanek et al., 2006; Jelinek et al., 2006), one of the brightest GRB optical counterparts yet observed. The early optical emission decayed rapidly, and later observations by other instruments failed to detect an optical or radio transient (Nysewander et al., 2006; Schmidt et al., 2006), setting strong limits on the fluxes which indicated an unexpectedly rapid further decay. Jelínek et al. (2006) interpreted the light curve as a transition between reverse and forward shock emission, with a relatively steep electron–distribution index $p \simeq 3.0$. Evidence for a transition from the reverse shock to forward shock phase was also present in the optical emission from GRB 050525a (Shao and Dai, 2005), the first bright, low–redshift burst to be observed by both the narrow field instruments on *Swift*, resulting in one of the most comprehensive multiwavelength descriptions of the early evolution of a GRB afterglow (Fig. 2.11).

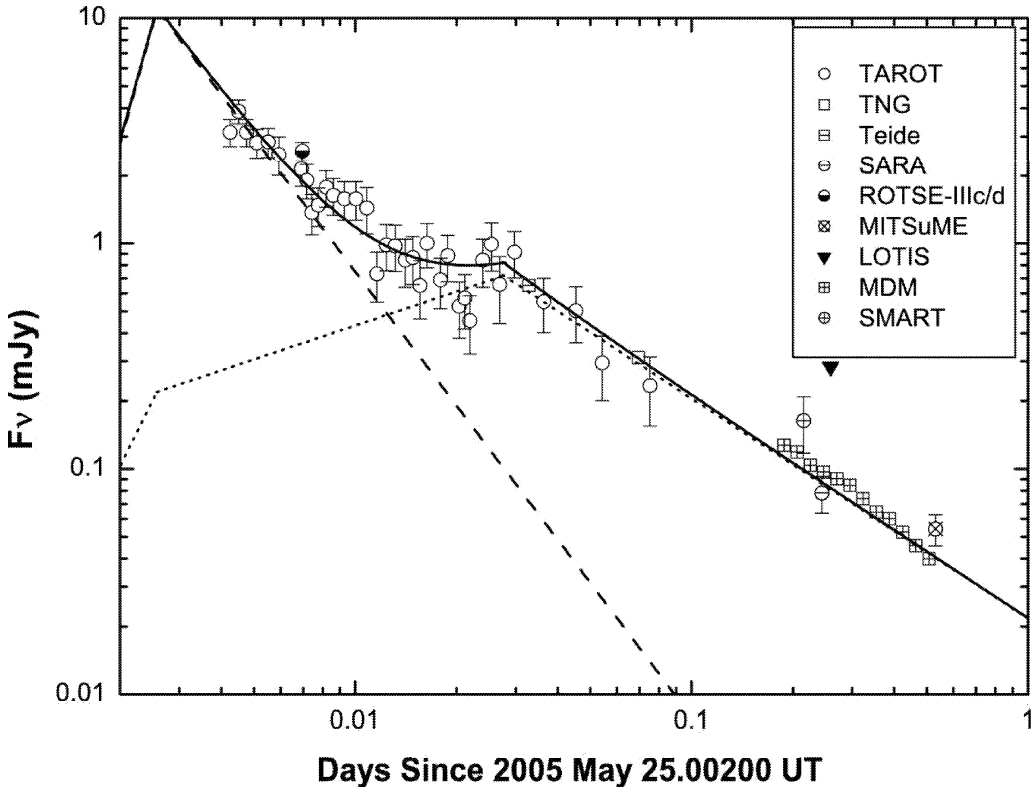

Figure 2.11: R–band light curve of GRB 050525a. The fitting curve (*solid line*) is generated by superposition of the forward shock emission (*dotted line*) and reverse shock emission (*dashed line*). *From Shao and Dai (2005).*

Several bursts for which early optical data is available have displayed no evidence of reverse shock emission. The ROTSE–IIIa robotic telescope detected prompt optical emission from GRB 050401, 33 s after its detection by *Swift* (Barbier et al., 2005). After

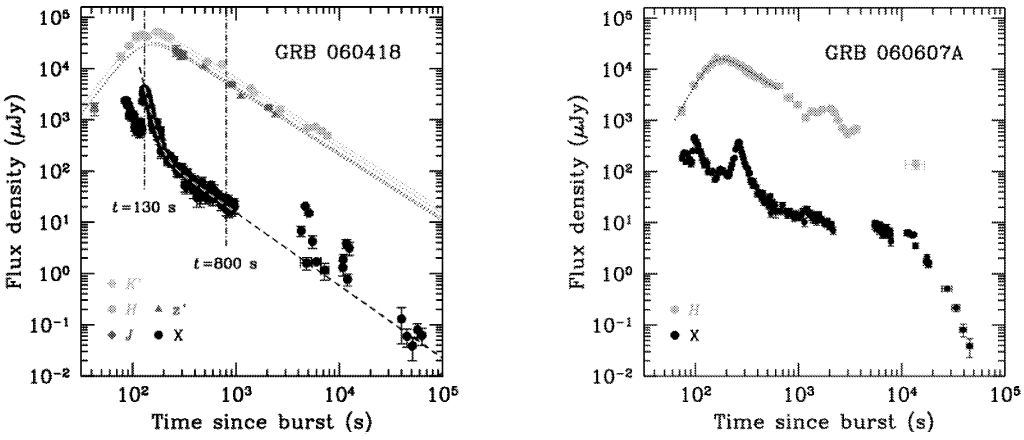

(a) (b)

Figure 2.12: NIR and X–ray light curves of GRB 060418 (a) and GRB 060607a (b). The dotted lines show the fit of a broken power–law model to the NIR data. *From Molinari et al. (2007).*

the prompt optical detections of GRB 990123 and GRB 041219a, this was just the third GRB that had been detected optically while still active in γ–rays, and the first detection for a burst of average duration and luminosity. The early optical behaviour showed no similarity to that of either GRB 990123 or GRB 041219a. No correlation with the γ–ray emission was observed, and the prompt optical emission was well fitted by a backward extrapolation of the afterglow at late times, indicating a very rapid rise of the forward shock emission, and a negligible contribution from internal shocks (Rykoff et al., 2005b). Early dominance of the forward shock emission was also suggested by the simple power–law decay observed from very early times in GRB 061007 (Mundell et al., 2007), which reached a peak magnitude of $R \sim 10.3$. The well–sampled early optical light curves of GRB 060418 and GRB 060607a were clearly shaped by the forward shock only (Fig. 2.12), and by determining the time at which the afterglow peaked, Molinari et al. (2007) could infer the original Lorentz factor of the fireball to be ~400.

2.3.1.2 Emission from Internal Shocks

An alternative to the reverse shock interpretation was proposed for the bright optical flare observed from GRB 050904. This exceptional burst had a spectroscopically measured redshift of 6.29 ± 0.01 (Kawai et al., 2005), making it the most distant GRB ever detected and the 2^{nd} most distant source yet observed. Even more remarkable was that a bright optical counterpart was detected during the γ–ray emission in unfiltered observations by

TAROT, a robotic telescope of just 25 cm aperture (Boër et al., 2006), beginning 86 s after the trigger. The 30 cm BOOTES telescope failed to detect an optical counterpart at early times in its R–band observations (Jelinek et al., 2005), since the high redshift placed the Lyα cutoff redward of the R–band. GRB 050904 was similar to GRB 990123 in that it had a large isotropic equivalent energy, high intrinsic peak energy, and displayed similar optical behaviour. Unlike GRB 990123 however, an X–ray flare was observed contemporaneous with the optical flare. While the optical flare can be accounted for in the context of the reverse shock model, this emission process is expected to have a negligible contribution in the X–ray band. Wei et al. (2006) suggest that, with the proper parameters, both the optical and X–ray flashes can be explained by the late internal shock model, first proposed by Fan et al. (2005) to interpret the prompt emission from GRB 041219a.

Further confirmation of a link between prompt emission at γ–ray and optical wavelengths was discovered in GRB 050820a. This burst was composed of an initial period of γ–ray emission from T_0 -17 to T_0 $+22$ s (Page et al., 2005), followed by a second, larger episode of emission from T_0 $+217$ to T_0 $+270$ s, and was detected by both *Swift* (Cummings et al., 2005) and KONUS–Wind (Pal'shin and Frederiks, 2005). The RAPTOR robotic telescope responded to the GCN alert based on the initial BAT trigger, and subsequently detected optical emission contemporaneous with the main outburst of energy in γ–rays . These observations reveal faint optical emission that suddenly flares and varies erratically, tracking the γ–ray emission, before fading over the course of the next hour (Vestrand et al., 2006). Comparison of the optical and γ–ray lightcurves allowed the determination of the temporal relationship and relative strength of the two optical components, one which tracks the γ–ray lightcurve and one from the external shock emission (Fig. 2.13).

2.3.1.3 Complex Light Curves

The simple power–law decaying light curve predicted by the most basic version of the afterglow model has rarely been observed in the *Swift* era, where improved early time optical coverage suggests that "anomalous" light curves are more likely to be the norm (Stanek et al., 2007). Rebrightenings and short time scale variability, similar to those seen in GRB 021004 and GRB 030329 (§2.2.2), have been observed in several *Swift* bursts. RAPTOR observations of GRB 060206 revealed a slow early decay followed by a major rebrightening of $\sim$1 mag. after 1 hour (Fig. 2.14), the first time such dramatic late–time

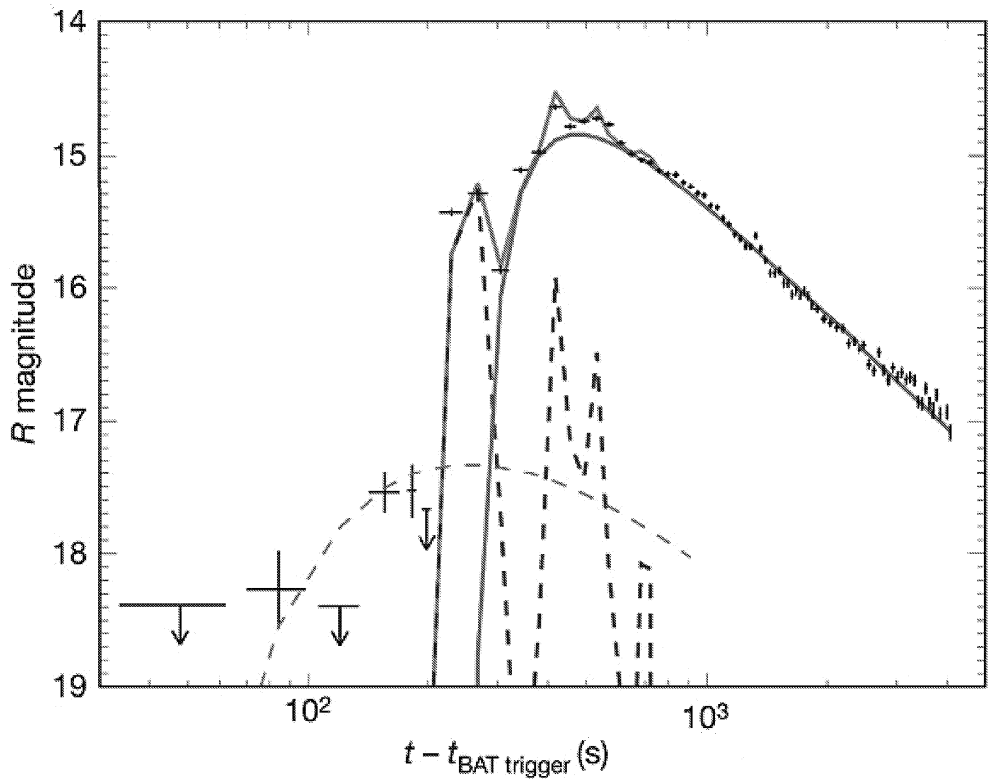

Figure 2.13: RAPTOR observations of GRB 050820a (black crosses). The blue dashed line shows the predicted prompt optical component obtained by scaling the KONUS–Wind γ–ray flux measurements, after re–binning to the same time intervals as the RAPTOR measurements, by a factor $F_{opt}/F_{\gamma} = 7.4 \times 10^{-6}$ and converting to the R–band equivalent magnitude. The solid red line shows the model early afterglow component, with a reference time t_0 set to the start of the second, more intense γ–ray pulse. The green trace shows the sum of these prompt and early afterglow components. The dashed red line shows an afterglow component with the same flux–rise timescale as the dominant afterglow, but with a reference time set to the onset of the precursor pulse, and an amplitude given by the ratio of the γ–ray fluence for the precursor pulse to that of the main pulse. *From Vestrand et al. (2006).*

activity had ever been observed (Woźniak et al., 2006). The light curve subsequently followed a typical broken power–law decay, with small amplitude ($\sim$ 10%) variations superimposed. Multiple rebrightening episodes were observed in GRB 060607a (Nysewander et al., 2007), and at late times in GRB 070311 (Guidorzi et al., 2007).

The ROTSE–IIIc telescope detected the optical counterpart of GRB 050801 just 21.8 s from the *Swift* trigger, the earliest detection of a GRB optical counterpart to date. The light curve did not fade or brighten significantly over the first $\sim$ 250 s, after which it decayed in typical power–law fashion (Rykoff et al., 2006a). The light curve of GRB 060210 displayed a similar plateau phase (Stanek et al., 2007, Fig. 2.14), while the early afterglow

of GRB 050319 showed an unusually slow decline (Woźniak et al., 2005).

Several physical scenarios have been proposed to explain these features. In the patchy shell model (Kumar and Piran, 2000), variations in the energy density of the outflow produce bumps in the light curve which are expected to decrease in amplitude with time. The forward shock can be reenergised by delayed shocks or the continued activity of a long–lived central engine (§2.1.2), which is expected to produce plateaux or slow decline phases in afterglows, as well as bumps. Density enhancements in the circumburst medium can also be expected to produce sharp flux increases (Wang and Loeb, 2000). Further observations at both low and high energy are required to further explore the various mechanisms proposed.

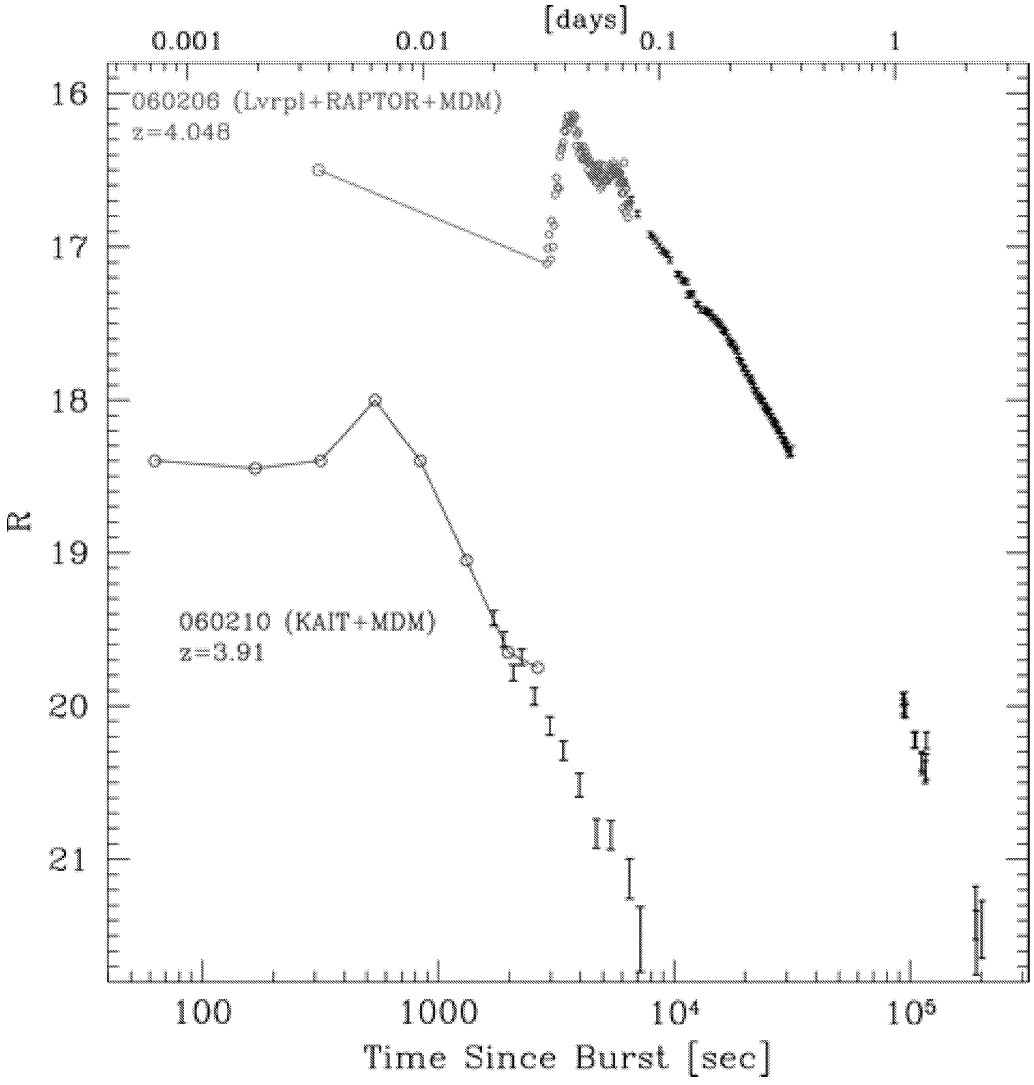

Figure 2.14: R–Band light curves of GRB 060206 and GRB 060210. *From Stanek et al. (2007).*

2.3.2 Dark Bursts

Of the 307 GRBs detected by *Swift* (to March 20^{th} 2008), 248 have been observed by UVOT, resulting in just 87 UV/optical detections. When ground–based follow–ups are included, the number of UV/optical/IR detections rises to 177, or ~58% of *Swift* GRBs[1]. Though a high–redshift, resulting in a Lyα cutoff redward of the UVOT's band, can account for the discrepancy between the number of UVOT and ground–based detections, there remains a significant number of "dark bursts", far greater than was expected in the pre–*Swift* era (Roming et al., 2006a).

Several explanations have been proposed to account for the paucity of optical/IR detections. The most obvious is the lack of a sufficiently deep detection limit due to adverse observing conditions, e.g. excessive sky brightness due to twilight or the moon, or the field's proximity to nearby bright stars or the moon. Optical emission may have been present, but decayed rapidly to below detectable limits by the time observations began (e.g Groot et al., 1998; Li et al., 2003; Berger et al., 2002), or may have been intrinsically faint to begin with (e.g. Li et al., 2003). Optical photons may be absorbed by local dust in the host galaxy (e.g. Piro et al., 2002; Fynbo et al., 2001). This idea is supported by the detections of radio transients without optical transients (Hurley et al., 2002), and by the association of GRBs with star–forming regions, which are dusty, optically–thick environments. Since GRBs are at cosmological distances, there may also be significant foreground extinction due to the ISM (Paczynski, 1998), as well as Galactic dust along the line of sight. A low–density ambient medium can result in a sub–luminous afterglow (Groot et al., 1998), since the afterglow peak flux depends on the square root of the density of the ambient medium, leading to reduction of the afterglow peak flux by several magnitudes with respect to bursts that occur in higher density regions (Mészáros and Rees, 1997). Some fraction of bursts are expected to be located beyond $z \gtrsim 5$, so that the UV band, which is heavily affected by absorption in the Lyα forest, is redshifted to optical wavelengths (Fynbo et al., 2001; Jakobsson et al., 2004). If the burst ejecta are Poynting–dominated, a significant suppression of the reverse shock would be expected (Zhang and Kobayashi, 2005), though a Poynting flow is not necessarily required since the strength of the optical emission from some reverse shocks may be weaker than previously calculated (e.g. Nakar and Piran, 2004)

The variety of factors that may lead to a non–detection makes the classification of

[1] Statistics were obtained from the *Swift* GRB table: http://swift.gsfc.nasa.gov/docs/swift/archive/grb_table.html

dark bursts problematic. Several authors have proposed quantitative schemes for classifying dark bursts. Jakobsson et al. (2004) proposed a definition that could serve as a quick diagnostic tool for identifying dark bursts based on limited information. The optical–to–X–ray spectral index β_{OX} is used to define a dark burst as one having $\beta_{OX} < 0.5$, i.e. optically subluminous in the context of the fireball model. Bursts falling in the range $0.50 < \beta_{OX} < 0.55$ are classified as potentially dark. In the ULAF method, Rol et al. (2005) use the X–ray temporal and spectral indices to extrapolate the X–ray flux to the epoch and frequency of the optical/IR upper limit, based on eight different scenarios within the standard afterglow model, and define any burst whose upper limit falls below the minimum predicted flux range as being inherently dark.

A study of very early UVOT observations of GRBs by Roming et al. (2006a) combined the optical data with X–ray and γ–ray data sets in an attempt to quantify the apparent lack of optical, and in some cases X–ray, flux at early times. The results from their (limited) sample favour foreground extinction, circumburst absorption, and high–redshift as the dominant factors in optical non–detections, with tentative evidence for suppression of reverse shock emission. Rapid temporal decay and low–density environments are found not to be significant factors. The mechanisms responsible for non–detections in this sample were distributed approximately as follows:

- 25% due to Galactic dust
- 25% due to circumburst absorption
- 30% due to high–redshift Lyα absorption

Yost et al. (2007) presented several cases of optical observations during GRBs with ROTSE instruments which resulted in prompt limits but no detection of optical emission. Their prompt optical limits fall within the range of optical fluxes and optical–to–γ–ray flux ratios derived from prompt optical detections. This is a wide range, since prompt optical behaviour observed in GRBs has been varied, with diverse relationships with the contemporaneous γ–rays . These results suggest that prompt optical non–detections are associated with events from the faint end of the range of GRB prompt optical emission, and do not require different intrinsic or environmental properties from events with prompt detections. Prompt non–detections may be partly explained by the limited sensitivity of many of the small telescopes engaged in prompt follow–up observations.

2.3.3 X–ray Afterglows

One of the major results of the *Swift* mission has been the discovery of previously unexpected features in GRB X–ray afterglows. Before *Swift* , most observations of X–ray afterglows took place several hours after the burst, when the flux typically exhibited a simple, smooth power–law decay $\sim t^{-1}$, while the early afterglow period from $\sim 10^2$ to $\sim 10^4$ s remained largely unexplored. Rapid follow–ups, typically ~ 100 s, with the XRT instrument on–board *Swift* allowed the early afterglow regime to be studied for the first time. A canonical X–ray afterglow behaviour has been identified (Nousek et al., 2006; Zhang et al., 2006), with five components (besides the prompt emission phase, denoted as 0 in Fig. 2.15), which may not all be present in a given burst, leading to some diversity in individual lightcurves. The five components are as follows (Zhang, 2007):

- **I – Steep decay phase:** Typically smoothly connected to the prompt emission, with a temporal decay slope ~ -3 or steeper, extending to $\sim 10^2 - 10^3$ s. The spectral slope is usually different from those of the later afterglow phases.
- **II – Shallow decay phase:** The temporal decay slope is typically ~ -0.5 or flatter, extending to $\sim 10^3 - 10^4$ s, when a temporal break is observed before the normal decay phase.
- **III – Normal decay phase:** Typical temporal decay slope of ~ -1.2, in agreement with predictions of the standard afterglow model (Mészáros and Rees, 1997).
- **IV – Post jet break phase:** Occasionally observed following the normal decay phase, typically with a temporal decay slope of ~ -2, in agreement with predictions of the jet model.
- **V – X–ray flares:** Observed in nearly half of GRB afterglows, occasionally with multiple flares in a single burst. Rise and decay slopes are typically very steep (e.g. Burrows et al., 2005b).

Apart from the normal decay and jet–break phases, all of the other afterglow features were generally unexpected pre–*Swift*. X–ray emission during the steep decay phase is thought to be produced by the same processes responsible for the γ–ray emission, i.e. internal shocks in an ultra–relativistic outflow, since the tail of the γ–ray light curve typically joins smoothly to the beginning of the X–ray afterglow (Panaitescu, 2006). The

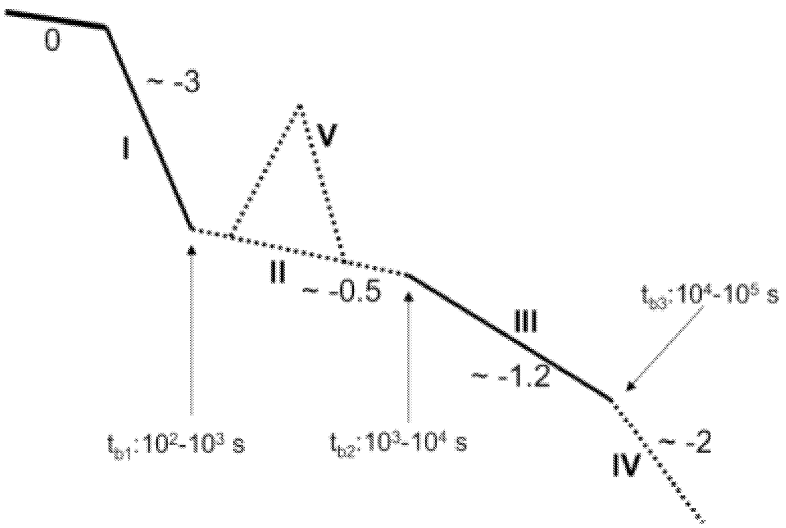

Figure 2.15: The canonical X–ray afterglow lightcurve revealed by *Swift* XRT observations. *From Zhang et al. (2006).*

rapid decay is attributed to the so–called curvature effect. In this scenario, emission from the internal shock region ceases abruptly, and since it is assumed that the ejecta has a conical geometry, the curvature of the radiation front causes a propagation delay for emission at high latitudes ($\theta > \Gamma^{-1}$) from the line of sight. Other interpretations have been discussed in the literature (see reviews in Zhang, 2007; Panaitescu, 2006), e.g. the internal shock afterglow scenario proposed by Fan and Wei (2005), which suggests that the internal shock emission does not cease abruptly but decays gradually with time. A study of spectral evolution in the steep decay phases of several GRB X–ray afterglows by Zhang et al. (2007) suggests that, while some steep decay phases are dominated by the curvature effect, a superposition of the curvature effect and an internal shock afterglow component may be required in others.

The shallow decay phase can follow the steep decay phase, or may immediately follow the prompt emission. Typically the optical light curve shows a similar shallow decay. Its origins may be in the forward shock energising the circumburst medium, though the mechanism responsible for the slow decay is unknown. A possible explanation is that the forward shock is continually refreshed by injections of energy (Zhang et al., 2006;

Nousek et al., 2006), due to late–time central engine activity, or a distribution of Lorentz factors among shells in the relativistic ejecta. Several other models have been proposed in the literature (see Zhang, 2007; Panaitescu, 2006), including delayed energy transfer to the forward shock, a structured outflow where the kinetic energy per solid angle increases with angle, and evolving microphysical parameters.

Swift has discovered that flares are common in X–ray afterglows, being observed in ∼50% of cases where early follow–up observations were carried out (see Burrows et al., 2007, and references therein). They vary in fluence from a few percent to ∼100% of the GRB fluence. Rise and fall times are typically very rapid, and considerably shorter than the time since the burst ($\delta t/t \ll 1$). Multiple flares have been observed in some GRBs, sometimes 4 or more, which generally soften as they progress, with later flares being more broadened and less energetic that earlier ones. In many light curves the flares are superimposed on a decaying afterglow component with the same decay slope before and after the flare. The observed properties of X–ray flares indicate that they are produced by internal shocks due to late–time activity of the central engine.

2.3.4 Short Burst Afterglows

The study of short GRBs has been inhibited by the lack of detected afterglows. It is challenging to produce accurate localisations from a smaller number of photons (compared to long bursts), and to carry out follow–up observations at sufficiently early times to detect the afterglow. In mid–2005, rapid and accurate localisations provided by *Swift* and *HETE–2* facilitated the first detections of short burst afterglows (Gehrels et al., 2005; Fox et al., 2005; Hjorth et al., 2005; Barthelmy et al., 2005b; Berger et al., 2005). Afterglows of short GRBs have now been detected at X–ray, UV/optical/IR and radio wavelengths. They are typically fainter on average than afterglows from long bursts, in some cases considerably fainter even when corrected for the lower γ–ray energy output. The first few identifications of host galaxies indicated that short GRBs are confined to moderate redshifts ($z < 1$, typically ∼0.2), though their inherent faintness may introduce a selection effect biased against observing short GRB afterglows at high redshift, and more recent observations hint at the existence of a high redshift population (see discussion in Levan, 2007).

The temporal and spectral properties of short burst afterglows at late times are similar to those of long bursts. The X–ray and optical light curves of all observed short bursts

exhibit a similar temporal power–law decay of $\alpha \sim 1 - 1.5$ after several hours, and power–law spectra with indices in the range $\beta \sim 0.5 - 1.5$. However the early X–ray emission is different from long GRBs. All early (~100 s) XRT observations of long GRBs have detected X–ray afterglows, whereas some short bursts exhibit no detectable X–ray emission at early times. The phases observed in the canonical X–ray afterglow light curve of long bursts (§**??**) are not observed in short GRBs. Several short bursts display a bright X–ray tail that follows the prompt γ–ray emission and lasts for ~100 s (e.g. Barthelmy et al., 2005b; Villasenor et al., 2005). This distinctive feature, absent in the X–ray afterglows of long bursts, appears to be common, though not ubiquitous, in short bursts. It is unclear if this phase is related to the prompt emission, the afterglow, or an unknown third process. Steep temporal decays are observed following bright X–ray tails (e.g. La Parola et al., 2006), which then lead into the normal afterglow decay. A shallow decay phase has not been observed in a short GRB so far.

The faintness of the optical afterglows of short bursts observed to date has inhibited observers in obtaining well sampled light curves, and few good quality spectral energy distributions have been produced. The best early optical light curve for a short GRB to date comes from GRB 060313, which was detected at very early times and monitored for several hours by UVOT (Roming et al., 2006b), the Danish 1.5m, and the VLT (Hjorth et al., 2006). Rapid, small amplitude variability was observed at late times, requiring energy input into the afterglow long after γ–ray emission has ceased, which presents significant problems for the standard compact binary merger models, since the final coalescence is expected to occur very rapidly.

2.3.5 Afterglow Temporal Breaks

Swift has allowed unprecedented coverage of the X–ray afterglow evolution from ~100 s up to several weeks after the GRB. A surprising finding has been the marked lack of achromatic temporal breaks consistent with jet breaks, as had previously been observed (§2.2.3). Many X–ray afterglows show single power–law decays extending to very late times, though Curran et al. (2008) suggest that there may be hidden breaks in some of these light curves. Temporal breaks have been identified in many X–ray afterglows, but in most cases the quality of the optical coverage has been inferior, preventing the firm identification of an achromatic break. Some afterglows have displayed achromatic breaks which are consistent with jet breaks (Panaitescu, 2007), but there have been problems in

intrepreting some of these within the jet model, and no robust idenfitication has been made (Covino et al., 2006b). In most other cases, the data seems not to support the presence of a jet break, and doubts have been cast on some of the previously identified jet breaks (Zhang, 2007).

The jet model is not the only possible interpretation for afterglow temporal breaks. Injection breaks can occur on the sudden cessation of energy injection (§2.1.2). Since this is a hydrodynamical process, such breaks should be achromatic, and the spectral indices should remain unchanged. Spectral breaks can be produced by the crossing of a characteristic synchrotron frequency through the observed band (§2.1.1), as observed in the optical light curve of GRB 050520a (Yost et al., 2006a). Similar breaks can be produced by the crossing of a photon spectral break, corresponding to a break in the energy spectrum of the accelerated electrons (Li and Chevalier, 2001), as observed in the X–ray light curve of GRB 060124 (Misra et al., 2007). These breaks are chromatic, progressing from high to low energy bands, and accompanied by predictable changes in spectral indices. At late times, a steepening temporal break is expected when the fireball's deceleration causes a transition from the highly relativistic phase to the non–relativistic phase (e.g. Wijers et al., 1997; Huang et al., 1998), although there is no robust evidence that such breaks appear in X–ray and optical light curves.

Chapter 3

GRB Counterpart Searches and Localisations

3.1 Counterpart Searches in the Pre–Afterglow Era

In many areas of astrophysics, multi–wavelength observations have been required in order to make significant advances in understanding the origins and emission processes of sources. An obvious example is soft γ–ray repeaters (SGRs), which were identified as being young, magnetised neutron stars in supernova remnants through combined observations at γ-ray, X–ray, optical, and radio wavelengths (Kouveliotou et al., 1994). In the absence of detected counterparts at longer wavelengths, GRBs remained largely mysterious until the late 1990's. The key question to be resolved was the distance scale, from which the energetics of the events could be inferred and constraints could be placed on the numerous models which had been proposed (see Nemiroff, 1994, for a list of more than 100 progenitor models published in refereed journals). The need for multi–wavelength observations was long recognised within the GRB research community, and significant efforts were devoted to counterpart searches long before the much–anticipated breakthrough in 1997 (see Schaefer, 1994; Fishman and Meegan, 1995; Hurley, 1998, for reviews of early counterpart searches). These searches were concentrated on optical wavelengths, though studies were also carried out at radio and X–ray energies.

3.1.1 Archival Plate Searches

The first hunts for GRB optical counterparts consisted of painstaking searches through archival plates at the locations of GRB error boxes. If the GRB had an optical counterpart which was recurrent (with a recurrence time within the limit of the total monitoring time afforded by the plate collection) it was expected that it could be detected in archival plates. Several groups conducted searches of various plate collections (see Hudec, 1992, 1993, for reviews), and a number of detections of possible new objects in and/or close to GRB error boxes were reported (e.g. Schaefer, 1981; Moskalenko et al., 1989). However a major problem associated with this technique was the very high number of false events detected. Candidate objects which could not be confirmed by a detection in a duplicate plate were of particular concern. Sources of false events included double exposures, plane flashes, asteroids, head–on meteors, and satellite glints, though the dominant sources of false positives were plate faults: emulsion defects in the photographic plate. Roughly 90% of plate faults could be recognised by their profile. In order to weed out the remaining 10%, Greiner et al. (1990) developed a technique called depth analysis, whereby the upper and lower layers of emulsion were examined using reflected light microscopy. This technique indicated that most of the archival candidates previously published were, in reality, plate faults (Greiner and Wenzel, 1991). In the absence of any convincing transient detections from archival searches, the question of whether or not GRBs were accompanied by optical counterparts remained open.

3.1.2 Wide–Field Monitoring

Searches for GRB optical counterparts were also carried out in the data from all–sky patrols by wide–field cameras which had serendipitously imaged the region of the GRB error box simultaneously with the detected burst (Greiner et al., 1994). In most cases, these instruments were engaged in unrelated projects, e.g. the Ondřejov meteor network, a photographic system of 12 fish–eye cameras at 10 stations, which simultaneously imaged the error boxes of 30 BATSE GRBs (Hudec and Soldán, 1994) while patrolling the sky as part of a European meteor tracking network (Oberst et al., 1998). One instrument which was dedicated to searching for optical flashes coincident with BATSE GRBs was the Explosive Transient Camera, or ETC (Krimm et al., 1996). The main drawback with these instruments was that their very large fields of view resulted in images with poor

spatial resolution and, crucially, limited sensitivity (Greiner et al., 1992). These studies did, however, provide solid evidence that GRBs were not typically accompanied by simultaneous optical flashes brighter than $\sim 5^{th}$ magnitude.

3.1.3 Follow–Up Observations

Another method employed in the search for counterparts to GRBs was to carry out follow–up observations some time after the burst using position information derived from orbiting γ–ray detectors, like BATSE and COMPTEL on-board the Compton Gamma-Ray Observatory (CGRO), the WATCH wide-field monitors aboard the GRANAT and EURECA satellites, and the satellites of the Interplanetary Gamma-Ray Burst Timing Network (IPN). The error boxes, typically a few degrees in size, could be imaged to deeper limiting magnitudes than was possible with wide–field sky patrols, at the expense of a time delay while the position was being determined. Typical delay times varied, from ~ 4 hours for BATSE (Kippen et al., 1994) to ~ 1 day for the IPN (Hurley et al., 1993b).

Given the size of the error boxes, large (1 m class) Schmidt telescopes, which are capable of imaging wide fields to deep limits, were ideally suited to these observations. Boër et al. (1994c) imaged 19 GRB error boxes, from 1 to 34 days after the trigger, to limiting magnitudes of ~ 18 as part of a target–of–opportunity program at ESO. Castro-Tirado et al. (1994) conducted a similar study using GRB positions determined by WATCH, with their earliest observation reaching a limiting magnitude of 16 at 0.5 days after the burst. Deep imaging down to $B \sim 19.5$ was carried out for three GRB fields several days after the bursts by Barthelmy et al. (1994) using the CTIO and KPNO Schmidt telescopes

The BATSE/COMPTEL/NMSU (BCN) rapid burst response campaign utilised preliminary localisations by BATSE, accelerated imaging by COMPTEL, and a world–wide network of observers to carry out early observations of COMPTEL error boxes (Kippen et al., 1994). Its first successful application occured with GRB 930131, "The Superbowl Burst", which was localised to an accuracy better than 2° within 6.5 hours of the burst (Kippen et al., 1994), allowing for observations by several optical and radio telescopes from ~ 7 hours after the burst. The BCN campaign resulted in optical observations of 10 GRB error boxes to limiting magnitudes of $12 - 20$ within a few days of the initial γ–ray detection, as well as radio observations at a variety of frequencies and sensitivities (McNamara et al., 1995a). Extensive radio follow–ups of individual bursts were also carried out by other groups (e.g. Frail et al., 1994; Koranyi et al., 1994). X–ray imaging of GRB error

boxes was performed using the *Einstein* and *ROSAT* satellites (e.g. Boër et al., 1994a,b). These observations were generally carried out at very late times, typically tens of days, due to the difficulty in scheduling target–of–opportunity observations with a satellite.

The failure to detect counterparts in any of these studies suggested that GRBs do not produce an optical counterpart brighter than 17th magnitude or a radio counterpart brighter than 10^{-17} ergs cm^{-2} s^{-1} from $\sim$ 1 to 99 days after the burst. The time versus flux regimes examined by the studies discused above are shown in Fig. 3.1. Based on these studies, and on the theoretical models which predicted the presence of GRB counterparts, McNamara et al. (1995b) concluded that optical follow–up work required deep imaging with response times of the order of minutes or less. Radio studies could be carried out days later, but would need to reach very low flux limits, while X–ray studies would depend on the next generation of X–ray satellites, e.g. BeppoSAX (§3.3.2) and *HETE-2* (§3.4.3).

3.2 BACODINE/GCN

In order to carry out such rapid follow–up observations of GRB fields, observers required precise GRB positions to be calculated and distributed on timescales of minutes or less. This era of truly rapid localisations began with the development of the BATSE COordinates DIstribution NEtwork (BACODINE), a hardware/software system developed at the Goddard Space Flight Centre (GSFC) that determined the positions of GRBs detected by BATSE and transmitted the positions to sites world–wide on timescales of seconds (Barthelmy et al., 1995).

The opportunity for developing BACODINE came about when the CGRO's on–board tape recorders failed and data had to be transmitted to ground in real–time. This was achieved by accumulating count rates for BATSE's 8 Large Area Detectors (LAD) in 4 energy bands for two 1.024 s intervals, then transmitting the data to one of two TDRSS[1] satellites over the next 2.048 s. During transmission, the count-rates for the next 2 1.024 s intervals were accumulated. The data was relayed by the nearest TDRSS satellite to the NASA White Sands Ground Station in New Mexico and retransmitted to DOMSAT before being sent to the GSFC Data Capture Facility for analysis. Light travel time from ground to geosynchronous orbit and buffering at the Ground Station resulted in another 1.0 s of

[1]The Tracking and Data Relay Satellite System (TDRSS) is a network of satellites in geosynchronous orbit used for relaying signals between low earth orbiting spacecraft and earth

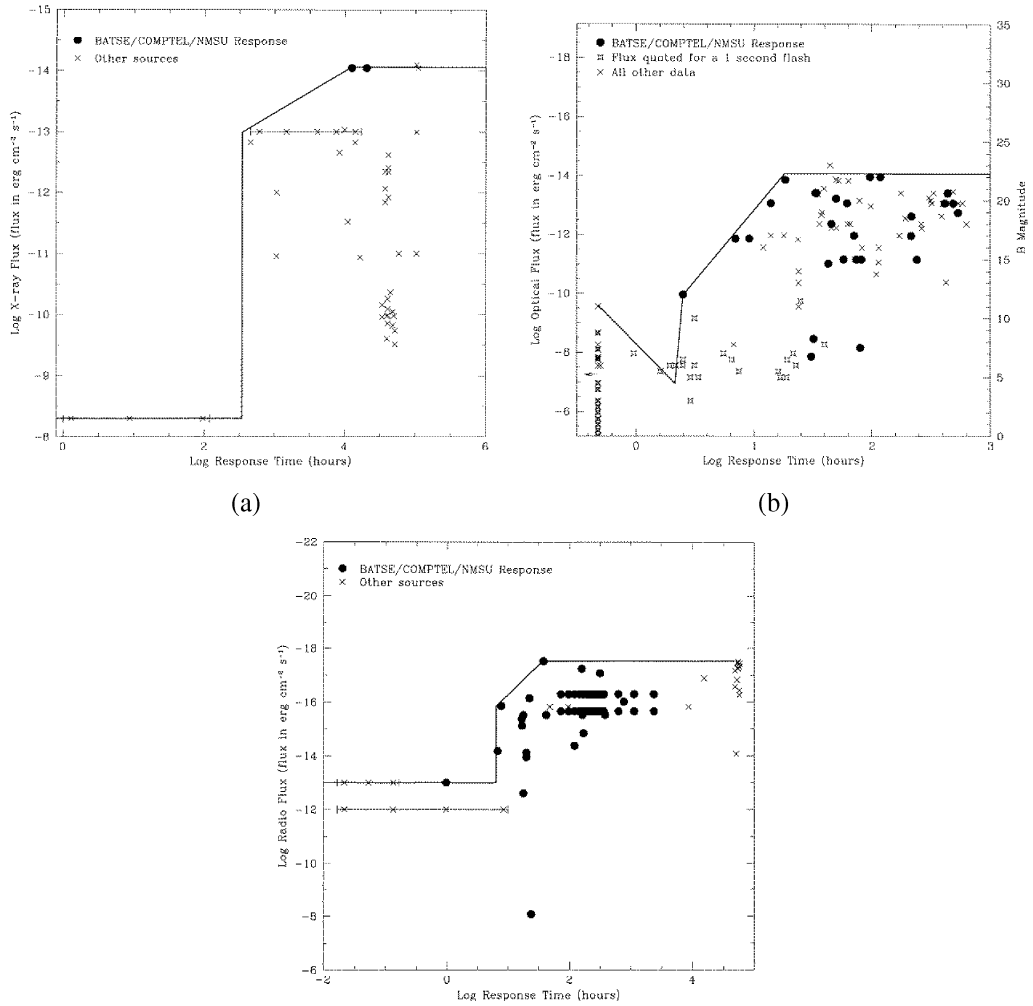

Figure 3.1: X–ray (a), optical (b), and radio (c) follow-up to GRBs, plotted as log of flux vs. the log of the time (in hours) from the burst trigger to the X–ray/optical/radio observation of the burst field. The optical flux limit is also plotted as an equivalent B magnitude on the right-hand y-axis in (b). The vertical series of points at the extreme left of the figure represent simultaneous observations. The flux domain which was sampled by various studies up to 1995 is below the solid lines. *From McNamara et al. (1995b).*

time delay.

Software running on several machines at GSFC monitored the telemetry stream, continuously extracting background rates and general housekeeping information. When the BATSE in–flight processor indicated that a burst was in progress, the software used the current count rates and the recently extracted background to calculate the source count rate and identify the 3 brightest detectors. After solving a set of simultaneous equations to calculate the burst location, the position was automatically transmitted to ground–based instruments capable of making follow–up observations. The data processing required to

determine the burst location took ∼0.1 s, and coordinates could be transmitted over a dedicated phone–line as fast as 0.3 s, resulting in a total (optimal) time lag, from γ–ray detection by BATSE to coordinates arriving at telescopes, of 3.5 – 5.5 s (Fig. 3.2). Since more than half of the bursts being detected by BATSE were longer than 5.5 seconds, it was now possible to observe GRBs at other wavelengths while they were still active in γ–rays.

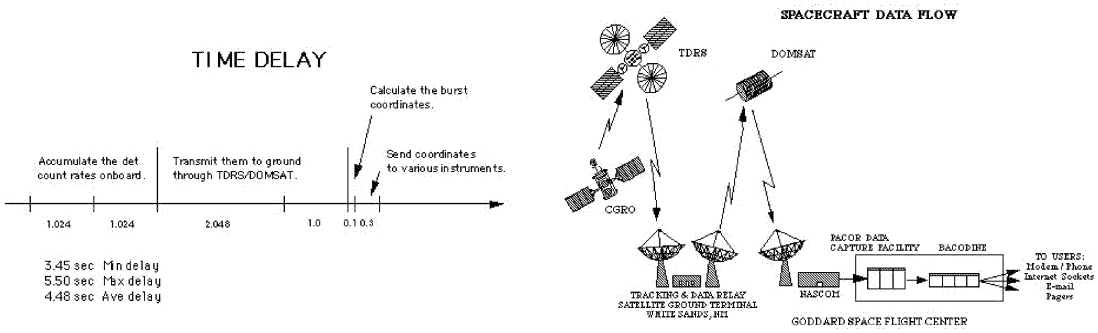

(a) (b)

Figure 3.2: The time delay (a) incurred in the data transmission (b) and processing steps from γ–ray detection by BATSE to GRB coordinates determination and distribution by BACODINE. *From the GCN website: http://gcn.gsfc.nasa.gov*

Over the next number of years, the BACODINE system was expanded to include and distribute coordinates of GRBs detected by other orbiting high-energy observatories and was re-named the Gamma-ray burst Coordinates Network (GCN) to reflect this expansion (Barthelmy et al., 1998). Every source of GRB location information that has come online in the intervening years has been added to the GCN (Fig. 3.3), so that it now provides a wide range of error box sizes over a range of delay times (Table 3.1). A variety of methods are available for receiving GRB coordinates (Table 3.2), and sites can apply many criteria to filter the types of notices they receive, e.g. based on error box size, time delay etc. Information on connection and filtering options for each site is stored in a line in the GCN's sites.cfg file, the current copy of which can be viewed on the GCN website[2].

A key feature of the modern GCN system is the distribution of GCN Circulars, short messages from researchers summarising observations that have been made, results, and plans for future observations, thereby allowing the follow–up community to make optimum use of the resources at their disposal. Another product which has recently been made available is the GCN Report. This is a short (1 – 2 page) final description of the

[2]http://gcn.gsfc.nasa.gov

observations and results of a group's follow–up efforts on a specific burst. The main purpose of these reports is to facilitate the publication of data which, by itself, would not be sufficient for a paper, and also to allow the *Swift* team to distribute their γ–ray, X–ray, and optical lightcurves in a more timely manner. All GCN Circulars and Reports are archived on a page on the GCN website, which is updated in real time. In addition, there is a burst information page for each satellite, which is also updated in real time.

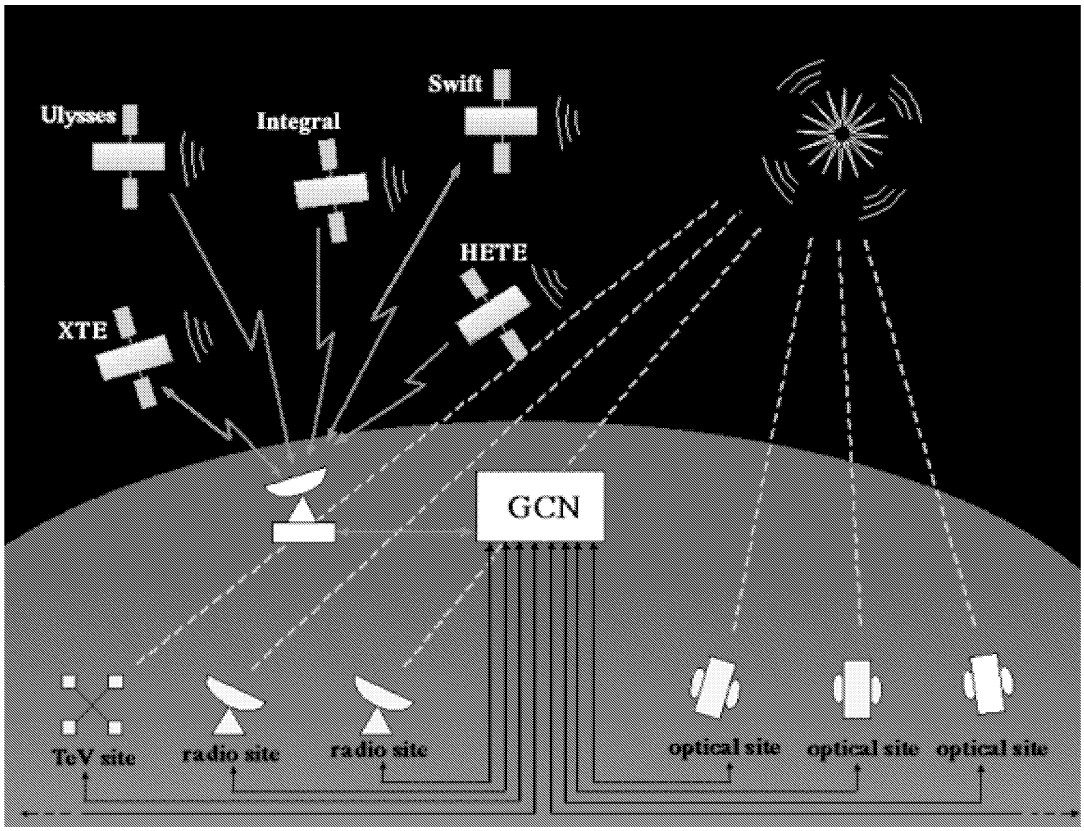

Figure 3.3: The Gamma-ray burst Coordinates Network (GCN). *From the GCN website: http://gcn.gsfc.nasa.gov*

3.3 Localisations: Previous Missions

3.3.1 CGRO

The Compton Gamma–Ray Observatory (CGRO) was launched in April 1991, and carried out observations of the high–energy sky until it re–entered the Earth's atmosphere in June 2000. Its 4 instruments, BATSE, COMPTEL, OSSE and EGRET, covered a wide range of the high energy spectrum, from 30 keV – 30 GeV. The Burst And Transient Source Ex-

SOURCE	TIME DELAY	ERROR BOX	RATE
Swift-BAT_POS	13–40 s	1–5′	2–5/week
Swift-XRT_POS	30–80 s	9″	2–5/week
Swift-UVOT_POS	1–9 hr	3″	1–3/week
HETE_SC_ALERT	10–20 s	n/a	8/month
HETE_SC_UPDATE	10–60 s	30″/14′	2/month
HETE_SC_LAST	20–60 s	30″/7′	1/month
HETE_GDNANA	1–3 hr	10″/2–5′	2/month
INTEGRAL_WAKEUP	~ 1 m	> 10′	1/month
INTEGRAL_REFINED	1–2 m	~ 5′	1/month
INTEGRAL_OFFLINE	1–3 hr	< 5′	1/month
IPN_POS	0.5–1.5 days	5–20′	3/month
RXTE-ASM	1–2 hr	4′ x 15–150′	~ 8/year
RXTE-PCA	3–5 hr	6–40′	~ 6/year

Table 3.1: Sources of GRB Locations. See §3.4 for further details. *Adapted from the GCN website: http://gcn.gsfc.nasa.gov*

TIME DELAY	METHOD	COMMENTS
0.1–2.0 s	Socket	Fast, suited for automated instruments
5–30 s	E-mail	To any network address
60–180 s	Pager	Message with RA, Dec, UT, Intensity
60–180 s	Short Pager	Message with RA, Dec
5–180 s	Subject only	Email with RA, Dec in the Subject line
5–180 s	Subj HHMM only	Email with RA, Dec, Time, Intensity the Subject line as RA=HH:MM:SS
0.3 s	Dedicated Phone	Continuous phone/modem connection (no longer implemented)
30 - 90 s	Dialed Phone	Slower, much cheaper than dedicated (no longer implemented)

Table 3.2: GRB Coordinate Distribution Methods. *From the GCN website: http://gcn.gsfc.nasa.gov*

periment (BATSE, Fishman et al. 1989b), which served as an all–sky monitor for CGRO, detected and localised more than 2700 GRBs during the mission's lifetime. It comprised 8 large area detectors (LAD) composed of Na(Tl) crystals (sodium iodide doped with thallium), with one located at each corner of the spacecraft. GRBs were triggered on–board by examining the count rates in each of the 8 LADs for statistically significant increases in the observed flux at three time resolutions (64 ms, 256 ms and 1024 ms). BATSE's sensitivity was divided into 4 energy channels: 30–50 keV; 50–100 keV; 100–300 keV; and 300 keV – 1 MeV. The statistical significance required to trigger on a burst was separately set for the 3 timescales and at least 2 LADs had to exceed the threshold for a trigger to

occur. BATSE detected GRBs at a rate of ~ 0.8/day, with error box sizes of 5°–20°.

The Imaging Compton Telescope (COMPTEL, Schönfelder et al. 1993), had a field of view of 1 sr and could image γ–ray sources with a localisation accuracy of $1^\circ - 2^\circ$. The uppermost of COMPTEL's two detector layers was filled with a liquid scintillator which Compton scattered incoming γ–ray photons. These photons were then absorbed by NaI(Tl) crystals in the lower layer. The instrument recorded the time, location, and energy of the events in each layer of detectors, which made it possible to determine the direction and energy of the original photon and reconstruct an image and energy spectrum of the source. Around 5 GRBs per year of sufficient brightness and hardness for COMPTEL to produce a localisation occurred in its field of view.

3.3.2 BeppoSAX

BeppoSAX (Boella et al., 1997) was an Italian–Dutch X–ray satellite in orbit from April 1996 to April 2002 which was capable of detecting GRBs simultaneously at soft and hard X–ray energies. Its science payload was made up of 3 types of instruments: an all–sky GRB monitor (GRBM), 2 wide field cameras (WFC) and 4 narrow field instruments (NFI). The GRBM, whose primary role was as an anti–coincidence shield to minimise background, was sensitive to γ–rays in the energy range $40 - 700$ keV (Feroci et al., 1997). The WFCs (Jager et al., 1997) were coded–mask instruments sensitive in the $2 - 28$ keV energy band with $40^\circ \times 40^\circ$ fields of view, pointing in opposite directions and oriented perpendicularly to the NFI ($0.1 - 10$ keV). The WFCs were usually operated simultaneously with NFI observations, each lasting up to several days. On a positive detection of a GRB in the WFC, the NFI were pointed in the direction of the burst. Through its use of coded–mask technology, the WFCs were capable of determining GRB positions accurate to $20'$ or better within $2 - 3$ hr of the initial detection, while subsequent follow–ups with the NFI could further refine positions to $\sim 100''$. The unprecedented accuracy of these localisations paved the way for the first detections of GRB counterparts. In its 6 year lifetime, BeppoSAX detected and localised 51 GRBs simultaneously with the GRBM and WFCs, and 36 of these were followed up with the NFI (de Pasquale et al., 2006).

3.4 Localisations: Current Missions

3.4.1 Swift

NASA's *Swift* mission (Gehrels et al., 2004) is a multiwavelength observatory dedicated to the study of GRBs (Figure 3.4). Launched into low-earth orbit in November 2004, it comprises a wide-field γ–ray detector (BAT, §3.4.1.1), an X–ray telescope (XRT, §3.4.1.2), and a UV/optical telescope (UVOT, §3.4.1.3). *Swift* is the first GRB mission to cover the UV/optical wavelength range. As well as determining burst locations with unprecedented accuracy and speed with the BAT instrument, *Swift* can also study the little known regime of very early X–ray and UV/optical emission due to its rapid, autonomous slewing capabilities. With each new burst detected and localised by BAT, a Figure Of Merit (FOM) algorithm residing in the BAT flight software decides, based on a series of criteria, if the current observations of the XRT and UVOT instruments should be interrupted. If observing constraints are met, the satellite rapidly slews to the burst location to facilitate early (~ 100 s) observations with the narrow-field X–ray and UV/optical instruments. Burst locations determined by all three instruments are transmitted to ground as soon as they are available via the nearest TDRSS satellite before being distributed to the community by the GCN (§3.2). Full data sets are downlinked in several daily passes over the Italian Space Agency's ground station at Malindi, Kenya.

3.4.1.1 BAT

Swift's Burst Alert Telescope (BAT, Barthelmy et al., 2005a) is a large FOV γ–ray detector which provides GRB triggers and initial positions accurate to $\sim 4'$. Its sensitivity spans the energy range from $15-500$ keV, with an energy resolution of ~ 7 keV. The detector array comprises 32,768 pieces of CdZnTe of dimensions 44×2 mm, forming a sensitive area of 1.2×0.6 m in the detector plane. Background radiation is minimised by a graded–Z shield located under the detector plane and surrounding the mask and detector plane. This shield comprises layers of Pb, Ta, Sn, and Cu, with increasing thickness nearest the detector plane.

Coded Aperture Technique Wide field imaging at γ–ray energies is not technologically possible using traditional focusing optics. Instead, instruments designed for high–energy imaging use the coded aperture technique. In coded aperture instruments, the

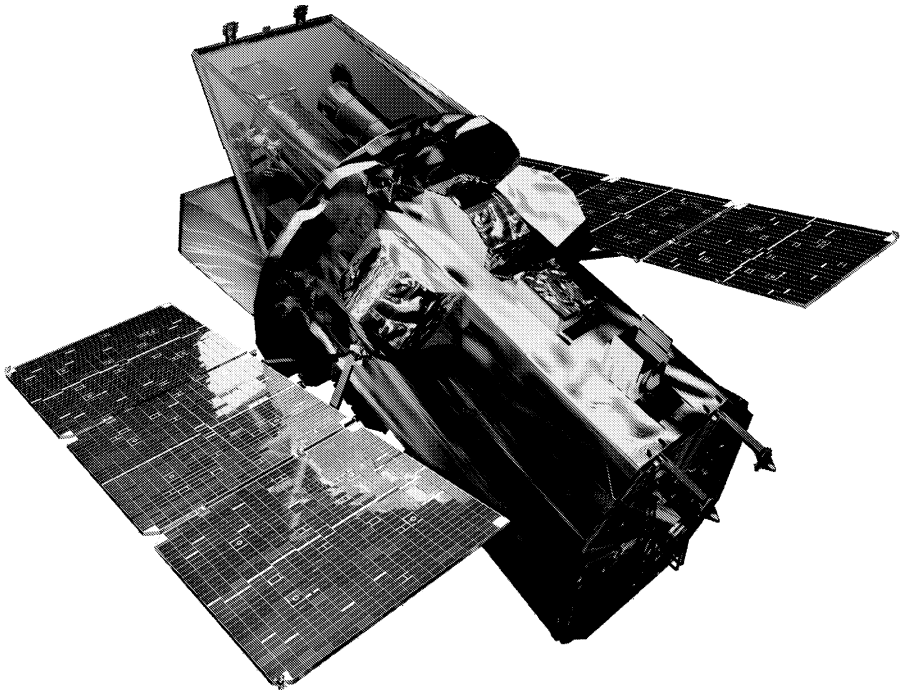

Figure 3.4: The *Swift* satellite. *Credit: NASA*

source radiation is spatially modulated by a mask of opaque and transparent elements before being recorded on a position sensitive detector, allowing simultaneous measurement of the source + background and background fluxes (see Figure 3.5). The total recorded image (shadowgram) is the sum of the shadows projected by all sources in the field of view plus a background term. Mask patterns are designed to allow each source to cast a unique shadowgram on the detector in order to avoid ambiguities in the reconstruction of the sky image. Sources in the central part of the field of view (the fully–coded region) illuminate the full detector plane, while sources closes to the edge of the field of view (the partially–coded region), illuminate only a fraction of the detector plane. Reconstruction is performed in a process called deconvolution, whereby the recorded image is correlated with a decoding array derived from the mask pattern. The field of view of the instrument is determined by the dimensions of the detector, plane and mask, and the detector-mask distance. The instrument's limiting angular resolution is determined by the dimensions of the mask cells and detector pixels, and by the detector–mask distance. The accuracy of individual source localisations depend on the signal to noise ratio of the source.

The coded aperture used by the BAT instrument is composed of $\sim$52,000 lead tiles in a random, 50% open – 50% closed pattern, located 1 m above the CZT detector plane.

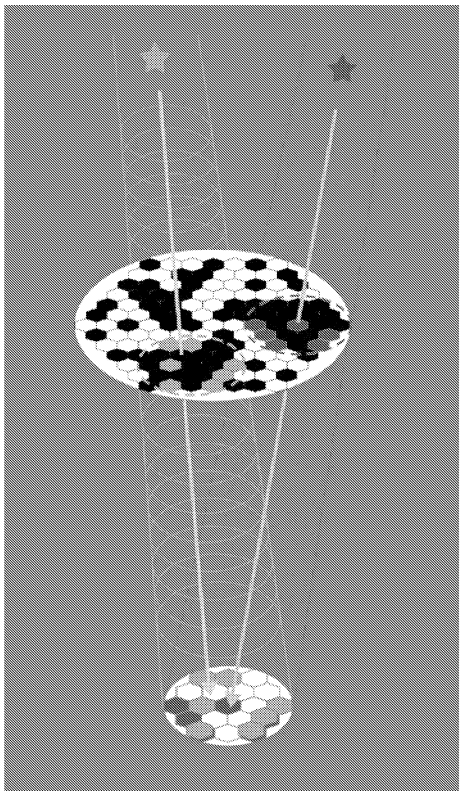

Figure 3.5: The basic concept of coded–mask imaging is illustrated above. Two point sources illuminate a position–sensitive detector through a mask. The detector thus records two projections of the mask pattern. The shift of each projection encodes the position of the corresponding point source in the sky; the "strength" of each projection encodes the intensity of the point source. (*Credit: ESA*).

The mask is 2.4×1.2 m, yielding a half–coded field of view of $100^\circ \times 60^\circ$, or 1.4 sr.

Burst Detection and Localisation GRBs are detected by a burst trigger algorithm which looks for excesses in the detector count rate above those expected from background and constant sources. Accurate triggering is complicated by variations in the detector background rate: in *Swift's* Low Earth Orbit, the background can vary by a factor of 2 or more during a 90 min orbit. The wide variety of durations (from milliseconds to minutes) and temporal profiles of GRBs presents further difficulties. These challenges are addressed by a triggering system which is capable of extrapolating the background and comparing it to the measured count rate over a variety of timescales and in several energy bands.

BAT's trigger algorithms are based on those developed for the HETE–2 GRB mission. A large variety of criteria are continuously applied, specifying the pre–burst background

intervals (typically 0 – 100 s), the order of the background extrapolation (constant, linear, and parabolic with time), the duration of the burst emission test interval (4 ms – 32 s), the region of the detector plane illuminated, and the energy range (typically 4 different bandpasses). A second triggering method is also employed which uses a FFT imaging algorithm to scan the detector array for point sources every 64 s. Detected sources are compared with an on–board catalog to determine if a new source is present in the field.

Once an excess count rate has been detected, source and background data are extracted according to the energy range and time intervals flagged by the trigger in order to determine if the trigger corresponds to a point source. An FFT–based algorithm correlates the pattern of detector count rates with the coded aperture mask pattern, a process which takes about 12 s to produce a 1024×512 pixel image showing the locations of transient sources to an accuracy limited by the pixel size of $14'$. Once an approximate source location has been determined, a back–projection algorithm produces an image of the region of interest with an arbitrarily small pixel size (typically $1'$), resulting in a peak with the intrinsic $17'$ FWHM PSF of the instrument. The source location is determined to the limiting instrumental accuracy by centroiding this peak. The accuracy of the final position is typically $1' - 4'$, depending on the intensity of the burst. The burst position is transmitted to ground via the TDRSS system, before being distributed to the community via the GCN. Burst positions are typically available on the ground within 20 s of the trigger, while light curves in 4 energy bands are transmitted after ~ 2 min.

While searching for GRBs, BAT also carries out an all-sky hard X–ray survey to a limiting sensitivity of ~ 2 mCrab, aswell as monitoring for hard X–ray transients.

3.4.1.2 XRT

The XRT (Burrows et al., 2005a) is a sensitive, broad–band (0.2 – 10 keV) X–ray imager designed to measure fluxes, spectra and light curves of GRBs and their afterglows, and in particular to provide rapid and accurate positional information. The instrument uses a focusing X–ray telescope and a single thermoelectrically cooled CCD detector, originally designed for the *XMM-NEWTON* mission, yielding a field of view of $23' \times 23'$. The CCD readout mode is automatically adjusted to one of three available modes (Imaging, Windowed Timing, and Photon Counting) in order to cover the wide dynamic range and rapid variability expected from GRB afterglows. Positions accurate to $5''$ are obtained within 10 s of target acquisition for a typical GRB and transmitted to ground via the TDRSS

system.

3.4.1.3 UVOT

UVOT (Roming et al., 2005) is a 30 cm modified Ritchey-Chrètien telescope designed for the photometric and spectroscopic study of GRB UV/optical counterparts in the 170 – 600 nm wavelength range. The instrument, based on the Optical Monitor on *XMM-NEWTON*, is equipped with filter wheels carrying 11 broadband colour filters, UV/optical grisms, and a clear filter. The detectors are micro–channel channel plate intensified (MIC) CCDs, capable of operating in both imaging and photon counting modes. The telescope's 17′ FOV is co-aligned with the XRT. Imaging sensitivity calculations for UVOT predicted a B–band limiting magnitude of 24 in a 1000 s "white" (or clear) filter exposure, comparable to the sensitivity of a 4 m ground-based telescope.

The telescope's main function is to perform broadband UV/optical photometry of GRB counterparts from early (~ 100 s) to late times, and provide finding charts accurate to 0.3″ within ~ 300 s for ground-based follow-up observations. Once the initial 100 s V–band finding chart exposure has been completed, one of two automated observing sequences is carried out, based on whether the burst is bright or dim. The two data collection modes, event (photon counting) and imaging, can be used simultaneously. Timing resolution in event mode is limited by the CCD frame rate of ~ 11 ms. Photometric redshifts can be measured for bursts in the range $1.5 < z < 4.5$ (the Lyman–α cutoff is shifted beyond UVOT's sensitivity range for $z \geq 5$). Low–resolution grism spectroscopy can be performed on bright bursts, which can also facilitate redshift determinations.

3.4.2 INTEGRAL

The INTEGRAL satellite is an ESA observatory–class mission primarily designed for high–resolution spectroscopy, imaging and accurate positioning of sources in the γ-ray domain (Winkler et al., 2003). Its main scientific objectives include studies of γ-ray line processes in stellar nucleosynthesis and large-scale structures, the high-energy physics of compact objects, and γ-ray bursts. It is capable of providing rapid and precise localisations to enable afterglow studies. The main instruments are the high-resolution spectrometer, SPI (20 keV – 8 MeV, Vedrenne et al. (2003)), and a high angular resolution imager called IBIS (15 keV – 10 MeV, Ubertini et al. (2003)). INTEGRAL is also capable of

multi-wavelength observations with its X–ray monitor (JEM-X, Lund et al. (2003)) and Optical Monitoring Camera (OMC, Mas-Hesse et al. (2003)). All three of INTEGRAL's high-energy instruments use coded aperture techniques to image, localise and resolve γ–ray sources (§3.4.1.1).

IBAS

Unlike other γ-ray missions, INTEGRAL has no on–board triggering system for transients. Instead, the search for GRBs is performed on the ground by the INTEGRAL Burst Alert System, IBAS (Mereghetti et al., 2001), a system of automated, near real-time analysis software running at the INTEGRAL Science Data Centre. Data from the telemetry stream is extracted and fed to IBAS, which monitors the incoming count rates in the IBIS instrument looking for significant excesses with respect to a running average, similar to the method employed in on–board triggering systems. In order to optimise the system's sensitivity to GRBs, the data stream is simultaneously searched at many different time scales and energy ranges. On detection of a candidate event, image analysis processes are run in order to verify the nature of the source, i.e. check that it is not due to a background variation or instrumental malfunction. Images are accumulated for different time intervals (derived from the GRB lightcurve in order to optimise the signal to noise ratio), deconvolved using a fast algorithm, and compared to pre–burst reference images. If the event is found to be genuine, positional coordinates for the source are derived from satellite attitude information and transmitted to the GCN for worldwide distribution. Positional accuracy is typically of the order of $\sim 2'$–$3'$, with an approximate detection rate of 1/month.

INTEGRAL can also detect GRBs with SPI's anti–coincidence shield (ACS). The ACS allows the rejection of a significant fraction of background events caused by high–energy secondary particles and cosmic rays, and provides a large effective area for the detection of transient sources (von Kienlin et al., 2003). In isolation it has coarse positional resolution, but when utilised as part of the IPN (§3.4.4) the accuracy of network localisations is improved (Hurley et al., 2004). The ACS detects about one confirmed burst every three days, as well as numerous other bursts which are below the thresholds of the other IPN instruments and are therefore unconfirmed, but which are almost certainly of cosmic origin.

3.4.3 HETE-2

The High Energy Transient Explorer (HETE-2) is a multi-wavelength mission dedicated to observations and localisations of γ–ray bursts (Ricker et al., 2003). It is equipped with a wide field γ–ray detector, FREGATE (1 – 500 keV, Atteia et al. (2003)), and two coded aperture X–ray detectors, the Wide-field X–ray Monitor (WXM, 2 – 25 keV, Kawai et al. (2003)), and the Soft X–ray Camera (SXC, 0.5 – 10 keV, Villasenor et al. (2003)), which can determine GRB positions accurate to $10'$ and $30''$ respectively. GRB locations are calculated by on–board software in real time, and transmitted to ground over a VHF link to an array of burst alert stations, which in turn transmit them to the MIT control center for immediate relay to the GCN, within seconds of the burst trigger. Automated analysis engines process raw data after it has been downlinked, and generate refined positions, typically 15 mins – 2 hours post–burst.

3.4.4 IPN

The Interplanetary Network provides localisations of GRBs detected by a group of earth orbiting satellites and space probes located throughout the solar system. Using relative differences in the arrival time of the γ-rays at the various spacecraft, the burst position may be determined by triangulation. Each pair of spacecraft gives an annulus of possible arrival directions whose centre is defined by the vector joining the two spacecraft, and whose radius θ depends on the difference in arrival times divided by the distance between the spacecraft. The precision of the interplanetary network in use is maximized when three or more detectors are situated at mutually great (1 to several AU) distances.

The IPN has been in existence in various forms since 1976, contributing to the studies of GRBs, SGRs, and bursting pulsars. Networks have generally been developed through modification of experiments designed for other purposes. The most recent incarnation, IPN3, began operations in 1990 with the launch of the ESA/NASA Ulysses mission, a solar X–ray/cosmic γ–ray burst experiment whose unique trajectory, taking it first to Jupiter then out of the ecliptic plane over the poles of the sun, made it the first mission with a γ–ray detector to travel beyond the orbit of Mars (Hurley et al., 1993a). Operating, at various periods, in conjunction with CGRO (from 1991), Pioneer Venus Orbiter, Mars Observer, and NEAR, the unprecented length of baselines achieved brought the resulting GRB localisations to within the arcminute range, enabling deep counterpart searches in

other wavebands for about 25 events/year, albeit at a time delay of 0.5 – 1 days post-burst. The main missions currently contributing to IPN3 are Ulysses, KONUS-WIND, INTEGRAL, HETE-2, 2001 Mars Odyssey, RHESSI, and Swift, with GLAST due to be added to the network after its launch. The IPN is expected to detect about 32% of events detected by GLAST's GBM instrument, and will reduce the sizes of their error boxes substantially (Hurley, 2007).

3.4.5 RXTE

The Rossi X–ray Timing Explorer (RXTE) was launched in December 1995 to study the variability of X–ray sources at high time resolution. GRB positions are provided by the All Sky Monitor (ASM, Levine et al. (1996), which is sensitive in the energy range 2–12 keV. A GRB of sufficient brightness in the 2–12 keV band to be observed by the ASM occurs in its field of view about 8 times per year. Analysis software monitoring the telemetry stream from the ASM responds to BATSE GRB alerts and attempts to localise the GRB if it is within the ASM's field of view. If a position can be obtained a mission scientist is then notified so that the position can be checked (and recalculated if necessary) before being sent to the GCN for distribution. Time delay from burst detection is usually 2–4 hours, with a typical error box of $4' \times 15$–$150'$.

3.4.6 AGILE

The AGILE Mission was launched by the Italian Space Agency in April 2007 (Tavani et al., 2006). Its main characteristic is its ability to simultaneously image sources at γ–ray and hard X–ray energies over a wide field of view with arcminute angular resolution. On–board triggering and localisation algorithms detect bursts and calculate positions, which are rapidly transmitted to ground. Its two primary instruments are the Gamma–Ray Imaging Detector (GRID) in the 30 MeV –50 GeV range, and the hard X–ray monitor Super–AGILE in the 10 – 40 keV range. GRID can image GRBs to an angular resolution of $15'$, while Super–AGILE can reach accuracies of $2-3'$. The broadband detection of GRBs and the study of implications for particle acceleration and high energy emission are the primary goals of the mission. AGILE is also engaged in studies of AGN, Galactic compact objects, supernova remnants, and unidentified γ–ray sources.

Chapter 4

Robotic Telescopes

4.1 Introduction

A number of terms are used in the discussion of instruments capable of carrying out observations with limited or no human intervention. The definitions given by Baruch (1995) (see also Williams and Mulherin (2001)), described below, have been widely adopted in the literature and are used in this work.

Automatic Automatic telescopes can be compared to the early robot arms used in industry. These were trained to repeat a particular series of operations ad nauseum, with the only external control provided by a sensor to detect the presence of the object to be painted/fitted/stamped/etc. In astronomy, the equivalent instrument involves the observer acquiring the various calibration frames, locating the object to be observed, and leaving the telescope to continuously monitor the object through the night. The automatic system may also feature sensors which can detect dawn or precipitation and carry out an automatic shutdown. Such systems can be useful for continuous monitoring, e.g of bright variable stars. They require extensive human involvement in the control loop.

Automated An automated telescope is capable of running a script to perform a pre–determined observation run, pointing to objects and collecting data for subsequent analysis. Such systems require significantly more advanced telescope control systems, drives, and encoders to facilitate the locating of targets: the quality of these elements is in fact key to successful automation. Many large professional telescopes operate in this manner, with the observing run coordinated and supervised from the control room by the

observing astronomer, whose main tasks are to confirm that the target has been correctly located, engage tracking on a guide star, and monitor weather conditions (or more commonly, respond to instructions from the observatory's duty astronomer regarding weather conditions). The system may be extended by automating more of the astronomer's duties, e.g. using a telescope pointing solution (Wallace, 1988) to allow the telescope to acquire targets without human intervention. This mode of operation is also common among satellites and radio telescopes, which receive their observing programmes at regular intervals, perform the observations, and return the raw (or, in some cases, on–board processed) data.

Remote The next level of sophistication is remote operation, particularly useful at sites which aren't easily accessed by humans (e.g. high-quality observing sites, by their very nature). Since the first steps at remote operation in the early 1980's (Robinson et al., 1982), remotely operated systems have been successfully developed at several major observatories, including the European Southern Observatory site in Chile, and the 4,000 m peak of Maunu Kea in Hawaii. Remote systems have also been developed by consortia of universities to provide their students with observing facilities (e.g. the Apache Point Telescope in New Mexico).

Robotic Robotic telescopes add full automated control of the observatory and instruments to the features of remote, automated systems. The key ability of the robotic system is that it can observe completely autonomously. The system processes observing request and generates its own schedule according to the priority assigned to each observation, altitude of the target, etc. Targets are located with pattern recognition used to confirm that the target has been successfully acquired, often providing feedback to the control system if corrections are required. Scheduling is flexible, responding to new requests or events, or to feedback from environmental monitoring sensors. The system can be accessed and controlled remotely if required, and provide remote users with access to data.

4.2 Robotic Telescope Astronomy

A very large proportion of the available funding for ground–based astronomical instrumentation has traditionally been directed toward high–profile, large–scale projects which aim to build bigger and bigger telescopes. However, at the other end of the scale, an

ever–growing number of science programmes are being carried out by smaller instruments operated in an automated or robotic manner. Scientists have found their research programmes hampered by the inflexibility and limited availability of observing time at large telescopes, and have devoted considerable effort to developing robotic systems better suited to their scientific requirements. Such instruments have become increasingly sophisticated due to a variety of technological advances, in particular the advent of CCD detectors and the widespread availability of powerful, affordable computers since the early 1990s. For overviews of the technological and scientific advances being made in the area of robotic telescope astronomy at various times since the mid 1990's see Henry and Eaton (1994); Bode (1995); Chen et al. (2001); Oswalt (2003).

The main advantage of robotic telescopes lies in their flexibility, which allows variability to be studied in ways that are not possible with traditional facilities (Eaton et al., 2003). The study of variable sources like active galactic nuclei (AGN) (van Breda, 1995) and variable stars (Szabados, 2003) greatly benefits from long–term monitoring programs that robotic facilities can carry out so effectively. Rapid, automated response capabilities make them ideally suited to observations of transient sources like supernovae and GRBs: where manually operated telescopes can respond on timescales of minutes at best, robotic telescopes can begin observing the target in seconds, opening up a previously unexplored regime in the time–domain study of GRBs (Andersen and Pedersen, 2004). Other areas in which robotic telescopes excel are surveys (cosmological studies of the large–scale structure of the universe have been based on catalogues made on small telescopes (Huchra, 2003), and calibration tasks like extinction monitoring.

4.3 GRBs and Robotic Telescopes

Robotic telescopes are particularly well suited to the study of GRBs. The unpredictable and transient nature of these events precludes the scheduling of observations and demands automated responses on the shortest possible timescales. Small ($<$ 1 m aperture) telescopes are sensitive enough to detect the optical emission in many cases, particularly since they can carry out observations at very early times when the counterpart is at its brightest (Andersen and Pedersen, 2004). A selection of experiments focused on GRB follow–up observations with robotic telescopes are described below.

4.3.1 First Generation Instruments

One of the first instruments designed to automatically respond to BACODINE alerts was the Gamma-Ray Optical Counterpart Search Experiment (GROCSE), developed at the Lawrence Livermore National Laboratory in California in 1993 (Lee et al., 1997). GROCSE comprised a wide field lens and an adapted camera array originally developed by the military as part of a missile defence program. Fibre optic bundles transported light from the lens focal plane to image intensifiers. The output of each intensifier was then fed to one of 23 CCDs, each of dimensions 384×576 pixels. The system regularly achieved response times of 30 s or less, and imaged several BATSE error boxes simultaneously with the γ–ray emission during its operational period from January 1994 to June 1996. No optical counterparts were detected to limiting magnitudes of $m_v \sim 8.5$, though this work did provide constraints on the ratio of (V–band) optical flux to γ–ray fluence for a number of bursts (Park et al., 1997a).

The next generation GRB follow–up instruments utilised an array of 4 telephoto lenses, each imaging to a wide format CCD detector, to achieve sensitivity improvements of 5 mag. or greater while still maintaining a large field of view to match the BATSE error boxes (typically $16^\circ \times 16^\circ$). Two systems were developed based on this design: LOTIS at Lawrence Livermore National Laboratory (Park et al., 1999), which began operation in late 1996; and ROTSE–I (Marshall et al., 1997) at Los Alamos National Laboratory, which operated from early 1998. The utility of this design was spectacularly demonstrated on January 23rd 1999, when ROTSE–I detected, for the first time, a bright optical flash contemporaneous with a γ–ray burst, the exceptionally bright GRB 990123 (Akerlof et al., 1999). However, this burst proved to be the exception rather than the rule, as no similar events were detected by either ROTSE–I (Akerlof et al., 2000) or LOTIS (Park et al., 1997b) in several years of operation. It became clear that to effectively observe GRB optical counterparts, rapid response systems capable of imaging to deeper limits would be required.

4.3.2 Current Instruments

In the years following these early experiments, an increasing number of groups have become involved in the development of robotic optical telescopes for GRB follow–up observations. Such instruments have become particularly relevant in the Swift era when

accurate GRB localisations are being made available with unprecedented speed and regularity. Different scientific goals and varying levels of funding have resulted in a wide range of approaches being taken in the design of robotic follow–up instruments. A variety of instruments are now in operation, fulfilling different and often complementary roles in the study of GRB optical emission. Some loosely defined categories of instrument are described below, together with examples of each class.

4.3.2.1 Small Aperture

The definition of a small aperture telescope continues to change as large instruments get larger. For the discussion at hand, small is taken to mean < 1 m in diameter. The key advantage of these instruments for GRB follow–up observations is their ability to respond rapidly to alerts, on timescales of tens of seconds or less. Their limited sensitivity is therefore offset by their ability to observe optical counterparts at very early times, when they are at their brightest. Instruments of this size can be constructed relatively cheaply, often using high–quality commercially available components designed for the increasingly sophisticated amateur mass market. Their low cost means that, with sufficient funding, multiple copies can be built, opening up possibilities for a worldwide network for continuous sky coverage, or simultaneous multi–colour photometry.

The version of the ROTSE system currently in operation is ROTSE–III (Akerlof et al., 2003). This is a worldwide network of 4 identical instruments at different longtitudes (Texas, Namibia, Turkey, and Australia), which can provide continuous coverage of the night sky. A key consideration in the design process was simplicity of optical design and ease of installation, so that multiple instruments could be set up with a minimum of expense and complication. Despite the accurate localisations provided by current missions removing the requirement for follow–up instruments to have wide fields of view, the ROTSE team continued with the wide field design based on their experience with ROTSE–1, since it allows searches for orphan optical transients to be conducted (Rykoff et al., 2005a). Another characteristic feature of the system is its very high slewing speed ($35^{\circ}s^{-1}$ in both axes), which allows it to begin imaging targets within seconds of receiving alerts.

Each ROTSE–III system is made up of a 45 cm telescope and a detector with a 2 k×2 k Marconi CCD chip, resulting in a total field of view of $\sim 2^{\circ}\times 2^{\circ}$(Fig. 4.1). A custom telescope optical and mechanical design was developed, based on the Cassegrain design. Fab-

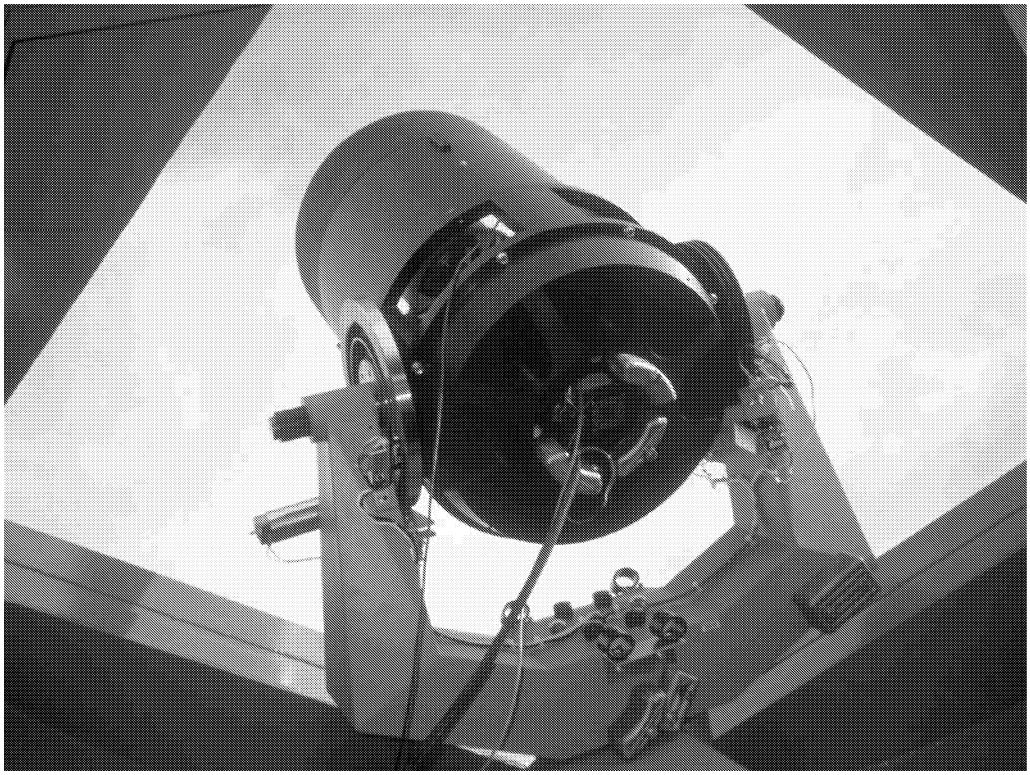

Figure 4.1: The ROTSE–IIIa telescope. *From http://www.rotse.net/equipment/*

rication of the telescope components, the mechanical housing and readout for the CCD, and the self–contained enclosure were outsourced to contractors. The mount was based on a commercially available model which was modified to provide high slewing speeds, more accurate tracking, and improved mechanical tolerances. The system's data acquisition system is based on the software designed for the ROTSE–I project. Separate daemons providing functions like device control, observation scheduling, and system monitoring communicate with a central control daemon via shared memory, while manual operation and real–time monitoring is achieved via a simple telnet compatible shell based on *rc*.

The 25 cm TAROT telescopes are also wide–field instruments (Fig. 4.2), with slewing speeds of up to $80^\circ\,s^{-1}$, resulting in extremely short target acquisition times of $1-1.5$ s (Boer et al., 2003). The project currently operates two instruments, one at the Calern Observatory in France and another, TAROT–S, at the ESO facility at La Silla. TAROT–S serves as a very rapid wide–field companion to the REM experiment (§4.3.2.2).

The PROMPT experiment is a robotic telescope system comprising six 0.40 m telescopes (Reichart et al., 2005). Five of the telescopes are designed for imaging (Fig. 4.3), with each one optimised for a different wavelength range from NIR through to UV, while

the sixth is equipped with a polarimeter. The system's capabilities for simultaneous multi–colour imaging enable it to construct spectral energy distributions across 8 filter bands and estimate photometric redshifts.

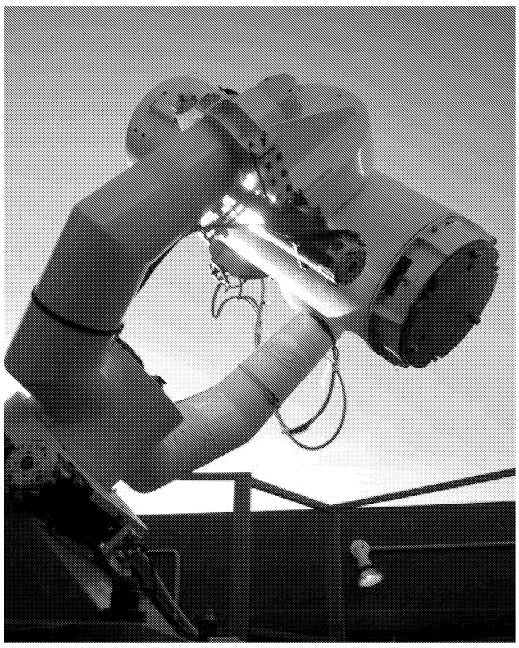

Figure 4.2: The TAROT telescope at the Calern observatory in France.
From http://tarot.obs-hp.fr

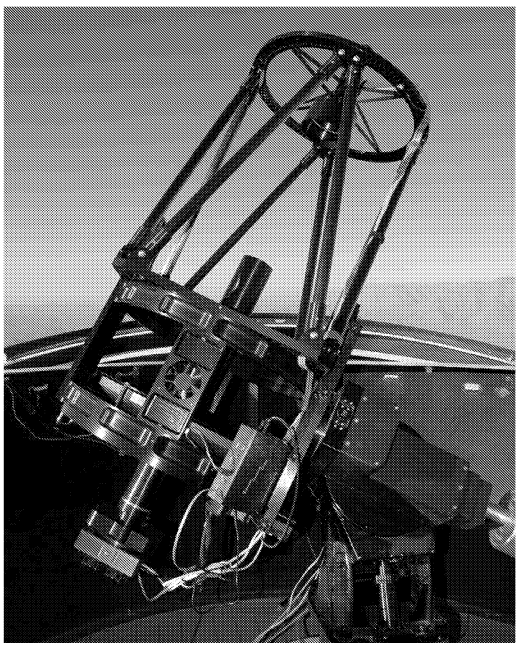

Figure 4.3: One of the PROMPT telescopes at Cerro Tololo, Chile.
From http://www.physics.unc.edu/skynet

The RAPTOR experiment (Vestrand et al., 2002) combines several approaches to optical transient searches. The system links together eight wide–field monitoring and three narrow–field response telescopes to act as an autonomous system capable of identifying optical transients and carrying out follow–up observations in real–time. The narrow–field instruments can perform simultaneous multi–colour imaging, low–resolution spectroscopy, and polarimetry. The salient feature of this system is its closed loop operation, whereby intelligent intercommunication and a real–time analysis pipeline enables it to generate and respond to its own alerts (Vestrand et al., 2004a).

4.3.2.2 Near–IR

In recent years, a number of robotic telescopes have been developed to study GRBs at near–infrared wavelengths (NIR, 0.9–2.5 μm). Around 50% of GRBs are not detected in the optical despite deep observations carried out within minutes/hours of the event (dark bursts, see §2.3.2). One possible explanation for optical non–detections is dust

extinction in the host galaxy, a significant amount of which can be expected if the burst occurs in a high–density, star–forming region. Since the infrared flux undergoes much less absorption than the optical, a NIR counterpart may be observed in these cases. The amount of absorption can be determined by combining simultaneous optical and NIR datasets, as was done for GRB 980703 (Castro-Tirado et al., 1999). A small fraction of GRBs will not be detected in the optical due to their very high redshift, since Lyα absorption affects optical wavelengths from $z > 6$. Colour–Colour techniques can be used to distinguish between high redshift and dust extincted events. If the event is found to be at high redshift, spectroscopic observations can then be planned at large instruments.

BOOTES–IR (Castro-Tirado et al., 2006), located at Observatorio de Sierra Nevada in Spain, and REM (Zerbi et al., 2001), at ESO's La Silla site in Chile, are two examples of NIR robotic telescopes currently dedicated to GRB follow–up observations. Both are 60 cm Ritchey–Chrètien telescopes equipped with high–throughput NIR cameras featuring HAWAII HgCdTe Infrared detector arrays (Hodapp et al., 1996). BOOTES–IR has a blue–band enhanced optical CCD at one of the telescope's Nasmyth foci along with the NIR camera, using a dichroic to split the incoming light into visible and infrared, thereby allowing simultaneous observations in two bands. REM has a similar configuration (Fig. 4.4), but with the optical light fed to a spectrograph (ROSS), which can acquire slitless spectroscopy of any object in the field. Both instruments operate as part of larger experiments which also involve optical imaging telescopes. BOOTES–IR is part of the BOOTES network (Castro-Tirado et al., 2004), a system of geographically separated wide–field imagers and narrow field response telescopes located in Southern Spain, while the TAROT telescope (§4.3.2.1) acts as a wide–field rapid response optical companion to REM at La Silla.

4.3.2.3 Large Aperture

A large aperture robotic telescope is taken here to refer to ∼1–2 m class instruments, since these are the largest instruments which have been fully robotised to date. Such instruments have deep imaging capabilities, at the expense of longer slewing times. Whereas small robotic telescopes excel at carrying out very early observations of GRB optical counterparts, large robotic telescopes can continue to monitor the afterglow long after it has decayed below the detection limits of smaller instruments, but before target–of–opportunity observations have been initiated manually at truly large instruments like the VLT. The sen-

Figure 4.4: The REM robotic telescope. *Credit: P. Aniol/ESO*.

sitivity of these instruments also opens the possibility for spectroscopy and polarimetry of bright GRB afterglows at early times.

The Liverpool Robotic Telescope (Gomboc et al., 2005) is a 2 m telescope owned and operated by Liverpool John Moores University and situated at La Palma (Fig. 4.5). A limiting magnitude of R=19 can be reached in a 10 s exposure, and a slew rate of $2^\circ\,s^{-1}$ allows observations to commence within 2–5 mins of GRB alerts. The telescope has five available ports for permanently mounted instruments, which can be selected within 30 s. The main imaging instrument is a 2k×2k optical CCD with a 4.6′ x 4.6′ field of view and 8 available filters. Imaging in the near infrared is achieved with a 256×256 pixel CCD with Z, J, H and K' filters and a 1.7′ x 1.7′ field of view. The telescope's instrumentation also includes a low–resolution spectrograph and a ring polarimeter (Steele et al., 2006). GRB 060418 was observed with the polarimeter 203 s from the trigger, and a robust upper limit on the percentage of polarisation was determined, ruling out the presence of a large–scale ordered magnetic field in the emitting region (Mundell et al., 2007). An automated image analysis pipeline can identify an unknown optical transient and choose an appropriate observation sequence (Guidorzi et al., 2006).

Figure 4.5: The Liverpool telescope. *Credit: Dr Robert Smith, Liverpool John Moores University*

4.4 Robotic Telescope Networks

The advantages of observing with robotic telescopes can be multiplied by combining individual instruments into networks. Robotic telescope networks can take various forms depending on the science goals. In its simplest form, a network can comprise several independent instruments operated by the same institution or collaboration. These systems can be distributed around the world with the aim of constantly monitoring the night sky (e.g. ROTSE–III), or can operate at the same site in order to perform simultaneous multi–colour photometry, spectroscopy, and/or polarimetry (e.g PROMPT).

The next level of sophistication is an intelligent network, capable of identifying interesting phenomena and communicating with other instruments to request observations (Vestrand et al., 2004b). The RAPTOR system operates in this manner, powered by TALON (White et al., 2004), a network server that allows intercommunication of alert triggers from internal and external sources and controls distribution of these triggers to each of the telescopes in the network. The eSTAR project (Allan et al., 2004) integrates on–line catalogues and databases into the network, using intelligent agent technologies to coordinate observations among the available resources. The system is deployed on RoboNet–1.0 (Mottram and Fraser, 2008), a network of three 2 m telescopes (the Liverpool Telescope and two Faulkes Telescopes), as well as on the UKIRT and JCMT at the Joint Astronomy Centre in Hawaii. The eSTAR and TALON projects, along with a handful of other institutions, formed the Heterogeneous Telescope Network (HTN) consortium in 2005. The goal of the HTN is to create a system of networks and instruments that communicate using common languages to negotiate and allocate a diverse range of astronomical resources world–wide (White and Allan, 2008).

Common communication protocols are essential to the operation of advanced networks. One format which has been widely adopted is VOEvent, an XML–based protocol designed to communicate information on transient events (White et al., 2006). The VOEventNet[1] project combines information on transient events from many organisations and observing programs and distributes alerts in the VOEvent format (Drake et al., 2006). Instruments on the network can then feed their results back into the system using the same messaging format. VOEvent alerts are openly available to the astronomical community, and currently provide information on supernovae, GRBs, and microlensing events. The

[1] http://voeventnet.org/

RTML format (Hessman, 2006), also based on XML, provides a generic description of astronomical observations and is used by the HTN to handle observation requests.

Chapter 5

System Description I: Hardware

The goal of the Watcher project was to develop a fully robotic optical telescope system capable of responding to GRB alerts generated by orbiting satellites, in particular the *Swift* mission. The main design drivers from the science point of view were that the system should be fast and sensitive enough to explore GRB optical emission in the early–time regime, tens of seconds or less after the initial trigger, ideally while the burst is still active in γ–rays. The technical challenges in carrying out such observations have meant that very early–time GRB optical emission has been very sparsely studied in the pre–*Swift* era, and as a result poorly understood. The unprecedented rate, speed and accuracy of GRB positions from *Swift* allows for extensive study of early GRB optical emission. While a number of robotic telescopes dedicated to GRB follow–ups were already in operation, a world–wide network of such instruments is required in order to maximise coverage of the night sky and gather as much early–time optical data as possible. A suitable instrument located at an appropriate site could contribute significantly to these studies.

An important design driver from the technical point of view was that system be constructed on a low budget, with just one research student working full–time on the project. In these circumstances, it would be necessary to reuse and adapt existing technologies wherever possible. Since the mid 1990's, the components being mass produced for the amateur astronomy market have become increasingly sophisticated and affordable (Mobberley, 2003). The major advances have been in the availability of high quality CCD detectors and motorised computer–controlled telescope mounts with GOTO capabilities, which allow the user to slew the telescope to the desired target by sending commands from a PC. A research quality instrument can now be constructed on a relatively low

budget using high–end amateur components. Watcher was developed on this basis, with commercially available components augmented by custom solutions wherever necessary.

The hardware components of the Watcher system are described in this chapter. As the project evolved, so did our design requirements, and components were added, adapted, or discarded accordingly. The technical specifications and salient features which satisfied (or failed to satisfy) the design requirements will be discussed.

5.1 Detector

The first component acquired for the Watcher system was its detector. This is an Apogee AP6e CCD camera, supplied by Apogee Instruments Inc.[1] The AP6e uses a scientific grade (< 100 bad pixels) front–illuminated Kodak KAF-1001e sensor with a 1024×1024 array of 24 μm pixels. A PC interface is provided by a PCI card, which also powers the camera. Digital resolution is 14–bit, and the gain is 8 e^-/ADU. Read noise is typically $\sim$ 13–15 e^- rms. The system's fast readout time of 1.5 s makes it ideal for time–critical applications like observing GRB optical counterparts, where dead time during CCD readout should be minimised. This feature was a key factor in the choice of detector. The CCD is thermoelectrically cooled and is normally operated at $-20.0 \pm 1°$, at which the dark current is $\sim$1.5 e^- pixel^{-1} s^{-1}. The KAF-1001e is part of a Kodak product range which have good quantum efficiency (QE) across the visible spectrum, maintaining QE > 50% from ~520 nm to 840 nm, encompassing the wavelength range of the R–band. The sensor specifications are summarised in Table 5.1, and the QE curve is shown in Fig. 5.1.

Array Size (pixels)	1024 x 1024
Pixel Size	24 x 24 μm
Chip Size	24.6 mm x 24.6 mm
Sat. Signal	200,000 e$^-$
Sensor Noise	13 e$^-$
Dynamic Range	> 83 dB
QE @ 400 nm	40%
Peak QE (550 nm)	72%

Table 5.1: Kodak KAF–1001E CCD specifications

[1] http://www.ccd.com

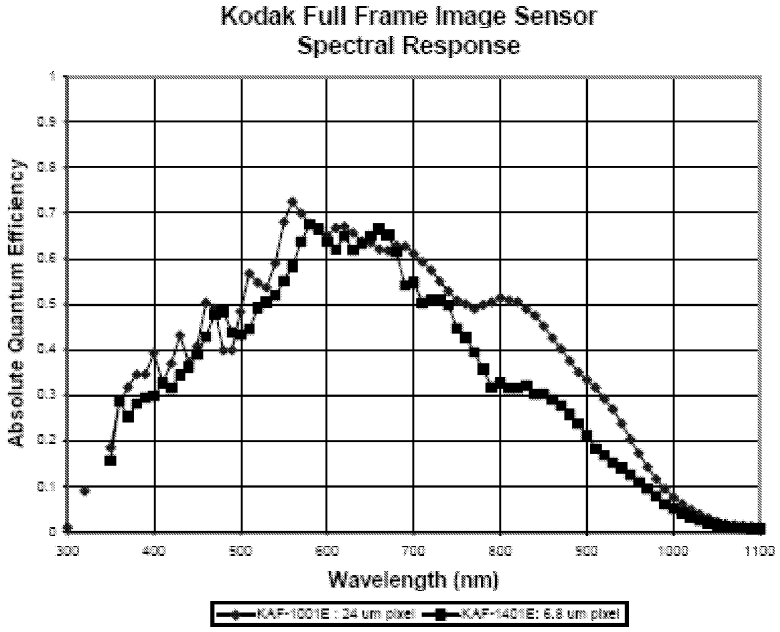

Figure 5.1: Kodak KAF–1001e quantum efficiency curve. *From www.ccd.com*

5.2 Optical Tube Assembly

Watcher's optical tube assembly (OTA) was provided by Optical Guidance Systems[2] (OGS). A key consideration in choosing a telescope is matching it to the detector with which it will be used. The telescope aperture and focal length and the CCD pixel and array size combine to determine the instrument's field of view and plate scale as follows (Howell, 2000):

$$FOV = \frac{3438' \times D}{F}$$

$$scale = \frac{206265'' \times P}{F}$$

where FOV is the field of view in arcminutes, D is the CCD chip diameter in mm, F is the telescope focal length in mm, *scale* is the plate scale in arcsec/pixel, and P is the pixel width in mm[3]. The plate scale is a measure of how much sky is imaged by each pixel.

A wide field of view was not required since the system was designed to respond to

[2]http://www.opticalguidancesystems.com

[3]Simply dividing D or P by F results in an answer in radians. Multiplying by 3438 or 206265 converts the answer to arcminutes or arcseconds, since 1 radian = 57.3°= 3438′ = 206265″

alerts from the *Swift* mission, which are accurate to ~3′ or better, and would not engage in wide–field surveys or monitoring for orphan afterglows. However it was necessary to have a plate scale which would ensure good sampling of stellar point spread functions (PSF). A sampling parameter, r, can be defined as follows (Howell et al., 1996):

$$r = \frac{FWHM}{P}$$

where $FWHM$ is the full width at half maximum of the stellar PSF, and $FWHM$ and P are expressed in the same units (e.g. arcseconds). For r less than about 1.5, digital data are considered to be undersampled, and standard software techniques for astrometry and photometry produce increasingly large errors due to uncertainty about the shape of the PSF. Oversampling the PSF results in increased spatial resolution, but reduces the system's sensitivity. The Nyquist sampling theorem provides a rule of thumb whereby optimal pixel sampling on a CCD is obtained when a source PSF is sampled over about two pixels, i.e. $FWHM \sim 2\times$pixel size. Atmospheric seeing at Watcher's site, the Boyden Observatory (§7.2) is typically $\sim 2''$, so an optimal plate scale would be $\lesssim 1''$/pixel.

To maximise the sensitivity of the instrument within our budget constraints, a 16″ OTA was chosen. The weight of an instrument of this size is near the upper limit of the load carrying capacity of commercially available mounts designed for the high end of the amateur mass market. Exceeding this limit results in a significant increase in the cost of the required mount. A telescope of this size can also be slewed rapidly, particularly if it is of a compact design. The OTA that was chosen is of the Classical Cassegrain design, which comprises a parabolic primary mirror and a hyperbolic secondary mirror which focuses light down through a hole in the primary. One of the foci of the secondary is located at the same position as that of the primary, while the detecor is placed at the second focus, behind the primary (Fig. 5.2). Folding the optics in this manner makes this a compact design. The tube is made from OGS's Tuned Carbon Fiber XZe material, which is lightweight and very thermally stable. The OTA's physical dimensions are summarised in Table 5.2.

This combination of OTA and CCD results in a field of view of 14.6′ × 14.6′ and a plate scale of 0.86″/pixel. The light curves of the only three GRBs to be detected at optical wavelengths on timescales of minutes in the pre–*Swift* era are shown in Fig. 5.3. The predicted signal–to–noise ratio at three different exposure times for Watcher's

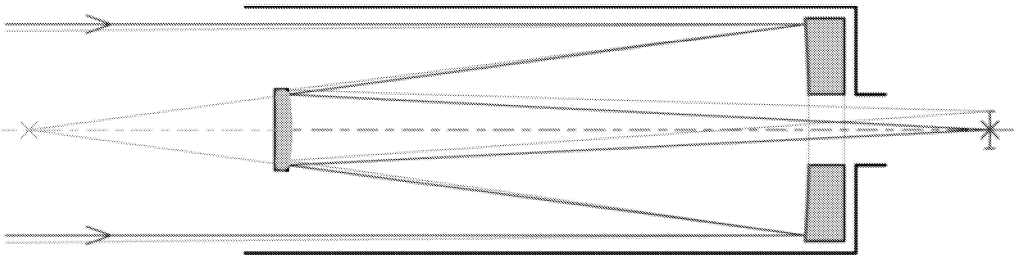

Figure 5.2: The Classical Cassegrain telescope design

Aperture	16″
f/ratio	f/14.25
Secondary Diameter	4.25″
Back Focus	10″
Tube Diameter	19.5″
Tube Length	54″
Focuser Tube Internal Diameter	2.5″
Weight	42 kgs

Table 5.2: OGS 16″ Classical Cassegrain specifications

optical set–up, calculated according to Nemiroff and Rafert (1999), is shown in Fig. 5.4. Assuming that the observations shown in Fig. 5.3 are typical of GRB optical counterparts, then Watcher should be sensitive enough to detect early optical emission from GRBs and monitor the afterglow for several hours.

5.3 Mount

The detector and optics are mounted on a motorised, computer–controlled telescope mount. The main requirements for this component of the system were that it would have a sufficient instrument load capacity for Watcher's OTA and detector, and that it should be capable of slewing at high speeds in order to minimise the response times to GRB alerts.

The mount that was initially chosen was the Paramount ME, a german equatorial mount developed by Software Bisque[4]. However, in early 2003 when components for the Watcher system were being acquired, Software Bisque had a waiting list of ∼1 year for the Paramount. It was decided that this would cause an unacceptable delay in development of the system, and an alternative should be sourced. Watcher's instrument load was at the upper limit of the capacities of high–end amateur mounts, and the selection of

[4]http://www.bisque.com

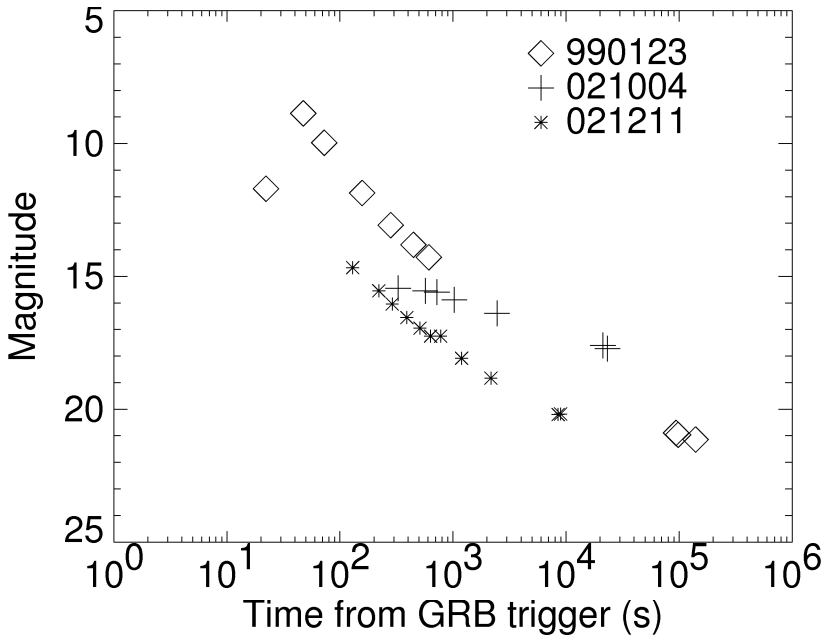

Figure 5.3: Early optical light curves of GRB 990123, GRB 021004, and GRB 021211. *Data from Akerlof et al. (1999); Fox (2003); Li et al. (2003).*

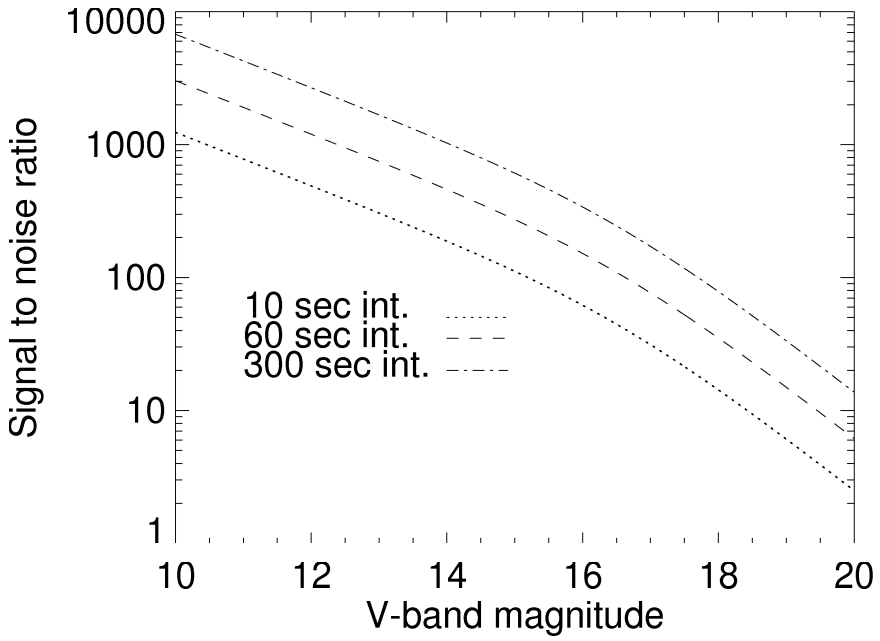

Figure 5.4: Predicted sensitivity of Watcher in terms of S/N ratio vs. visual magnitude (V–band) for three different exposure times.

alternatives was very limited. Around this time, a new mount came to the market from the German manufacturers of the Millennium Mount[5]. This new mount, the Millennium Mount II (MM–II, Fig. 5.6), was a heavy–duty version of the company's existing product. The MM–II seemed to satisfy our requirements, and so was initially selected to be the mount for Watcher.

5.3.1 Millennium Mount II

The MM-II has high–quality axles, bearings, and gears, driven by ESCAP stepper motors. Its instrument load capacity is ~70 kgs, with slewing speeds of up to 7°/s. The MM–II uses a dovetail plate to attach OTAs. This was found to be unwieldy for an OTA as heavy as Watcher's 16″ Cassegrain. A mounting plate was constructed which acted as an adapter between the MM–II's dovetail and the OTA's clamping rings. This adapter plate was permanently fixed to the mount via the dovetail plate, and the OTA was attached by inserting the clamping rings' 4 threaded rods through holes in the adapter plate. The mount was secured to the pier at Boyden using three threaded rods embedded in the pier and a levelling plate (Fig. 5.5). In order to balance Watcher's heavy instrument load, an extension to the mount's counterweight shaft and additional counterweights were made. The total counterweight load used to balance the system around the RA axis is 25 kg. In order to balance the telescope around the Dec axis, a small counterweight shaft and counterweight were added to the telescope mounting plate.

The MM–II is controlled by the Dynostar X3 telescope drive, manufactured by Boxdöerfer Elektronik[6] (Fig. 5.7). The Dynostar controls the mount's stepper motors and facilitates user adjustments to certain motor settings via an integrated LCD display and firmware menu system. Two cables connect the Dynostar to the RA and Dec motors on the MM–II. It is useful to mark the RA cable with electrical tape once it has been identified to assist in correctly reconnecting the cables in the future. The Dynostar and mount are powered by a variable DC supply set to 24 V and A, the optimal level for high slew speeds specified by the manufacturers. The mount can be moved manually using the RA and Dec direction buttons, which are also used for navigating the menus on the controller. Its GOTO capabilities allow for manual input of target coordinates or the selection of targets from the internal catalog. The controller's GOTO functions can also be accessed from popu-

[5]http://www.millenniummount.de
[6]http://www.boxdoerfer.de

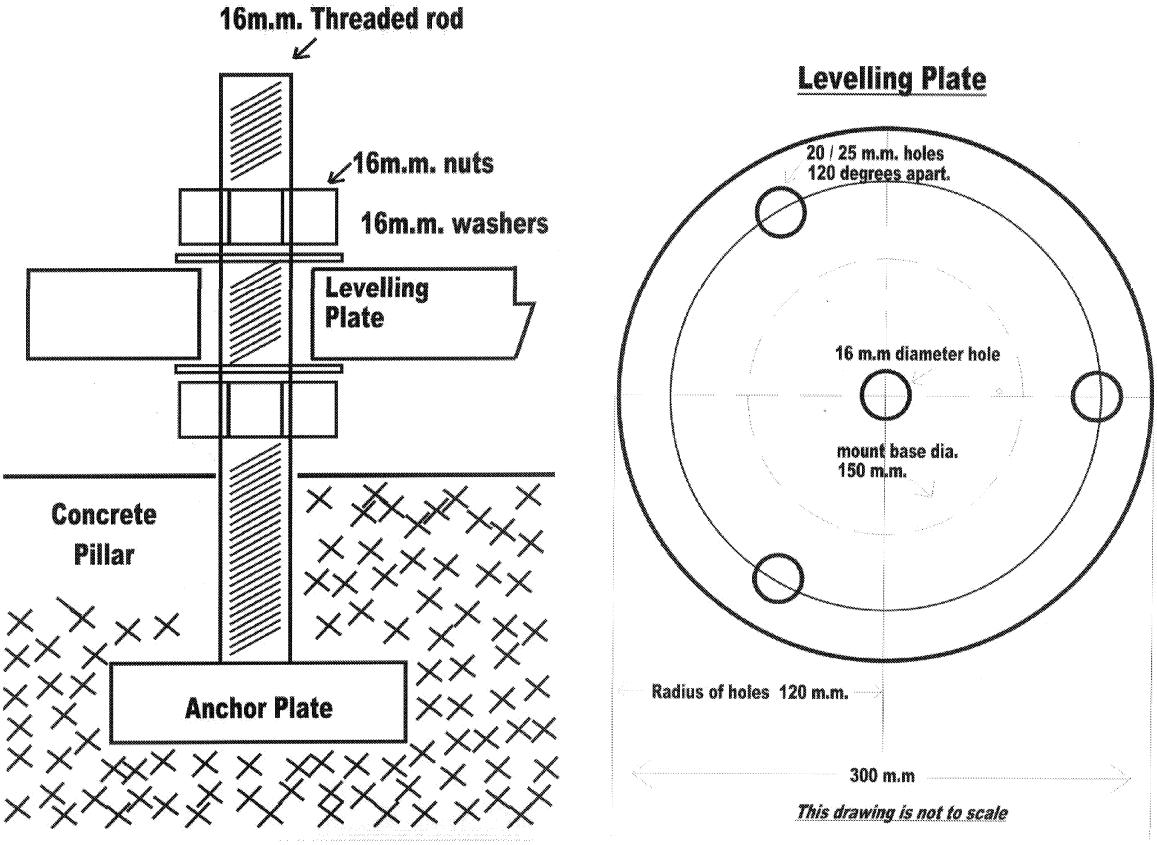

Figure 5.5: Hardware used to secure the Millennium Mount II to the pier

lar astronomy software packages like Software Bisque's The Sky. The Dynostar can be connected to a PC serial port via the supplied ribbon cable which connects to the 20–pin male connector on the underside of the controller. The Dynostar firmware can also be updated through a serial connection to a Windows PC. Full details on setup and control of the MM–II mount using the Dynostar X3 controller using Version 3.00d of the firmware can be found in the technical manual (Boxdörfer, 2003). An overview of the mount setup is given in §7.3.

As we gained more experience during the development process, it became clear that the MM–II was not the ideal choice. The mount suffered from several shortcomings, many of which were worked around using custom hardware and software solutions, including the lack of parking and safety functions (see §6.3.2.2). However, it became apparent that the MM–II lacked the sophistication needed for a remote, robotic observatory. In late 2005, between the first and second phase of installation of the Watcher system, the Paramount ME became available through a German distributor. The mount is equipped

Figure 5.6: Millennium Mount II

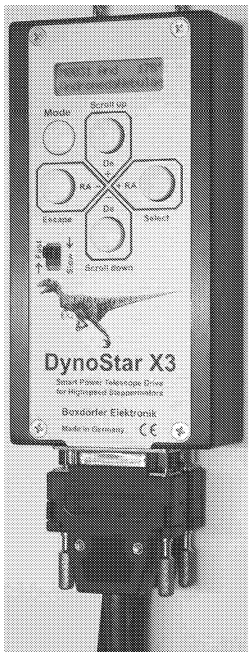

Figure 5.7: Dynostar X3 controller

with design features unique among mass market mounts, making it the only so–called amateur mount that is genuinely suited to remote robotic observing. Additional funding for equipment purchase also became available at this time, and so the Paramount ME was purchased to replace the Millennium Mount II.

5.3.2 Paramount ME

The Paramount ME (Fig. 5.8) is the most sophisticated telescope mounting available for the amateur market (Mobberley, 2003), and is used extensively in research systems (e.g. the PROMPT and BOOTES robotic telescopes, §4.3) and by the U.S. military. The system is very robust, with research–grade gears and substantial bearings, and is capable of carrying instrument loads of up to 70 kgs at slew speeds of up to 7°/s. The built–in MKS 4000 electronics system controls brushless DC servo motors, which have a long life expectancy.

The Paramount has two main features which make it particularly suited to robotic observing. Accurate homing sensors and a homing function allow the mount to be initialised to exactly the same physical position on start–up. This allows the mount to be restarted remotely, without any additional synchronisation, and still provide repeatable pointing and tracking performance night–to–night. Built–in software slewing limits (set to 5° past the

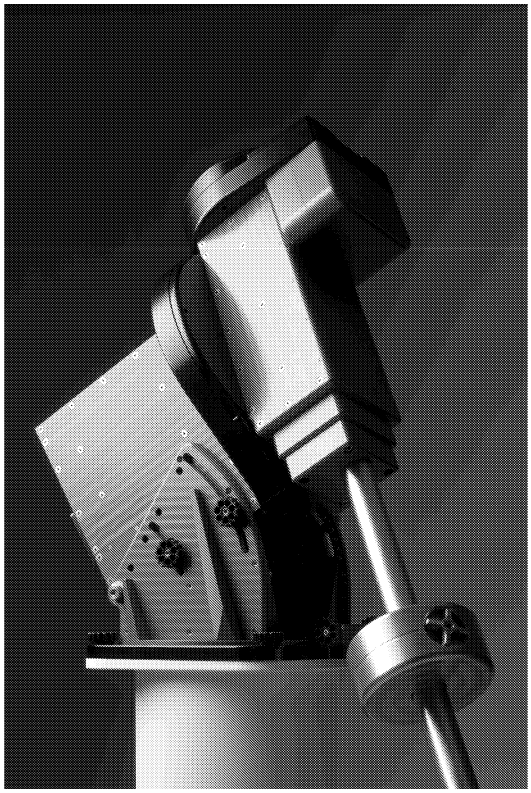

Figure 5.8: Paramount ME

meridian) prevent damage to the telescope and mount and cause the mount to be decelerated as the limit is approached. The system also features a hardware limit which prevents the mount from slewing more than 7° past the meridian. A number of instrument ports are provided which are wired directly from the adaptor panel at the rear of the mount to the instrument panel on the telescope mounting plate. The mount's design also allows for additional cabling to be passed through the mount, which eliminates problems with cables dragging or becoming entangled.

The Paramount connects to the PC via the serial port. Limited manual control is possible using a joystick which plugs into the instrument panel. If the mount needs to be rebooted manually it can be homed using the joystick. The mount settings and GOTO functions are accessed from the PC. An overview of the mount setup is given in §7.3. Full details can be found in the user's guide.[7] The telescope's clamping rings are fixed to the mount via Bisque's Versa plate.[8] The mount was fixed to the pier with a custom base plate made by the University of the Free State mechanical technicians based on Bisque's

[7] http://www.bisque.com/SC/Download?File=Bulk/PDFs/ParamountMEManual.pdf
[8] http://www.bisque.com/SC/Download/FloatingRoot/Bulk/pdfs/METopPlateSpecs.pdf

pier adapter template[9] and the existing pier specifications. It was unnecessary to provide levelling capabilities in the base plate since the Paramount has built–in levelling features.

5.4 Filter Wheel

The IFW filter wheel provided by Optec[10] (Fig. 5.9) is a computer controlled system for astronomical observing with various photometric filters. The wheel itself hold 5 filters, each of 50 mm diameter: Bessell B, V, R, and I photometric filters (Bessell, 1995), and a clear filter. The passbands for the filters are shown in Fig. 5.10.

The IFW is installed on the telescope via an adapter to the OTA's Astrophysics 2″ rack–and–pinion focuser at the primary focus. The CCD is attached to the other side of the IFW via a supplied mounting ring, which threads onto the IFW, and an adapter which threads onto the front of the CCD. For added security, an additional CCD mounting bracket fits on to the drawtube of the telescope's primary focuser and is secured to the base of the CCD.

An O–ring affixed to the circumference of the wheel makes friction contact with a small stepper motor causing the wheel to rotate. Approximately 2000 steps are required for a full revolution of the wheel, which takes about 16 seconds. A single filter change takes approximately 3.2 seconds. Wheel position is determined by small magnets in the wheel opposite each filter. As the wheel is rotated, Hall effect sensors in the housing send pulses to the control electronics when a magnet passes by. Position number 1 and the wheel itself are identified by a single magnet placed in one of another set of 5 holes.

The IFW is controlled and powered by a microcontroller based handset, which provides basic manual control functions and an LED display (for feedback of current filter position), as well as a PC interface for computer controlled operation. The controller is connected to the IFW by a control cable with an 8–pin modular (RJ45) connector at the controller end and a 9–pin sub-D connector (female) at the IFW end. PC connectivity is via an RJ12 serial reverse cable which connects to the PC serial port using the supplied serial port converter.

[9] http://www.bisque.com/SC/Download/FloatingRoot/Bulk/PDFs/MEBaseAndPier.pdf
[10] http://www.optecinc.com

Figure 5.9: IFW filter wheel system

5.5 Focuser

The Robofocus focus driver provides PC control over the telescope's focus. A microprocessor controls a stepper motor which drives the telescope's existing focus mechanism, allowing for PC control and feedback of the current focus position. The device was initially installed on the primary focuser supplied with the telescope by removing one of the focus knobs and securing the Robofocus to the exposed focus shaft with the supplied shaft coupling. The Robofocus was then secured to the focuser's drawtube using a custom–made mounting. The Robofocus stepper motor turns the primary focus shaft which in turn moves the telescope drawtube, to which the imaging system (CCD and filter wheel) are attached. The focus lock was removed from the primary focuser. The Robofocus can securely hold focus position without the focus lock, and can be damaged if operated with the lock secured.

While the motor is capable of moving this load, it was felt that the life of the motor could be prolonged and more accurate focus control achieved by installing the Robofocus onto the telescope's secondary focus. The OTA came with a JMI motorised focuser fitted

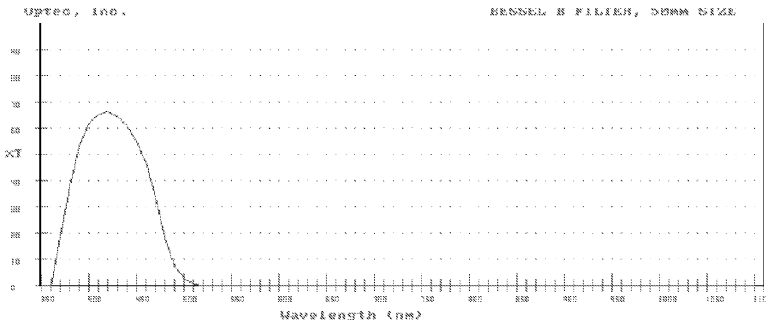

(a) B-band

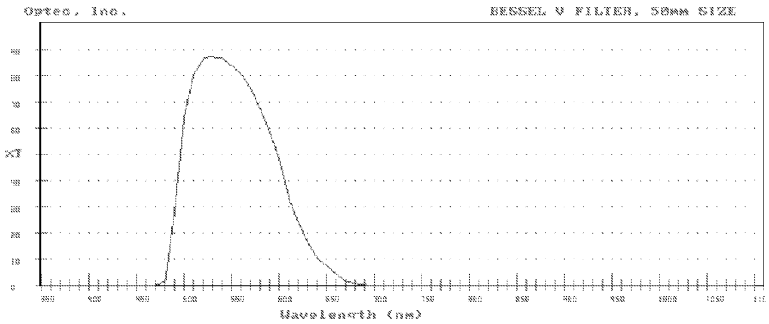

(b) V-band

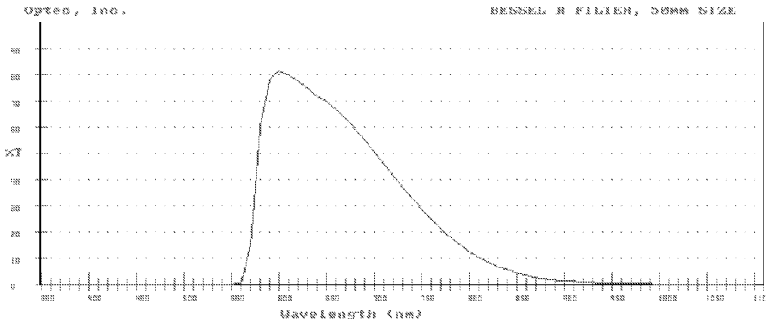

(c) R-band

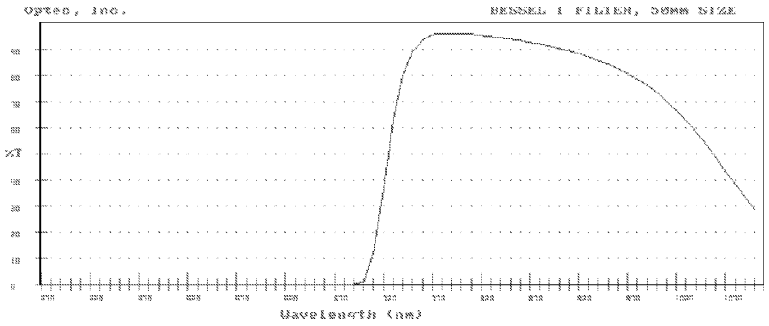

(d) I-band

Figure 5.10: Transmission curves for the Bessell BVRI filters

to the secondary focus. The device was operated using a hand controller and could not be computer controlled. The JMI stepper motor was removed, and replaced by the Robofocus, which was then mounted securely behind the secondary mirror. The Robofocus serial cable was routed along one of the three spider vanes supporting the secondary mirror. The section of the light–grey coloured serial cable which travelled along the spider to the Robofocus was covered in black insulating tape in order to minimise scattering of light.

A particularly useful feature of the Robofocus is its support for an optional Remote Power Module accessory. This device connects to the Robofocus via a six conductor telephone type cable (supplied), and plugs into the mains for its power supply. It supplies four switchable power outlets, each with its own pilot light, which are controllable via the software interface to remotely power on and off devices in the observatory. At the Watcher installation, the Remote Power Module supplies AC power to the Paramount ME (to facilitate remote rebooting of the mount in case of minor failure), and also to a light in the telescope room, to assist in debugging problems via the webcam during the hours of darkness.

5.6 Enclosure

Watcher is housed in an existing small telescope building at Boyden Observatory (§7.2), one of several such structures at the site which had lain disused for a number of years. It has a separate control room and telescope room, the roof of which could be manually rolled back via a winch. Front and rear views of the building are shown in Fig. 5.11. In preparation for Watcher's arrival at Boyden, the building was extensively refurbished. As part of this work a new concrete pier was installed, the roof mechanism was overhauled, and the support structure of the roof was adapted. The original design of the roof required the observer to ensure the safety of the telescope while the roof was being opened and closed, since the telescope protruded into the roof space during its operation and could be struck by horizontal beams in the roof support structure. This would be a dangerous situation for an unattended system if an error caused the roof to close before the telescope had been moved to safety. The support structure was adapted to remove these horizontal beams and provide enough free space for the roof to be moved safely regardless of the position of the telescope.

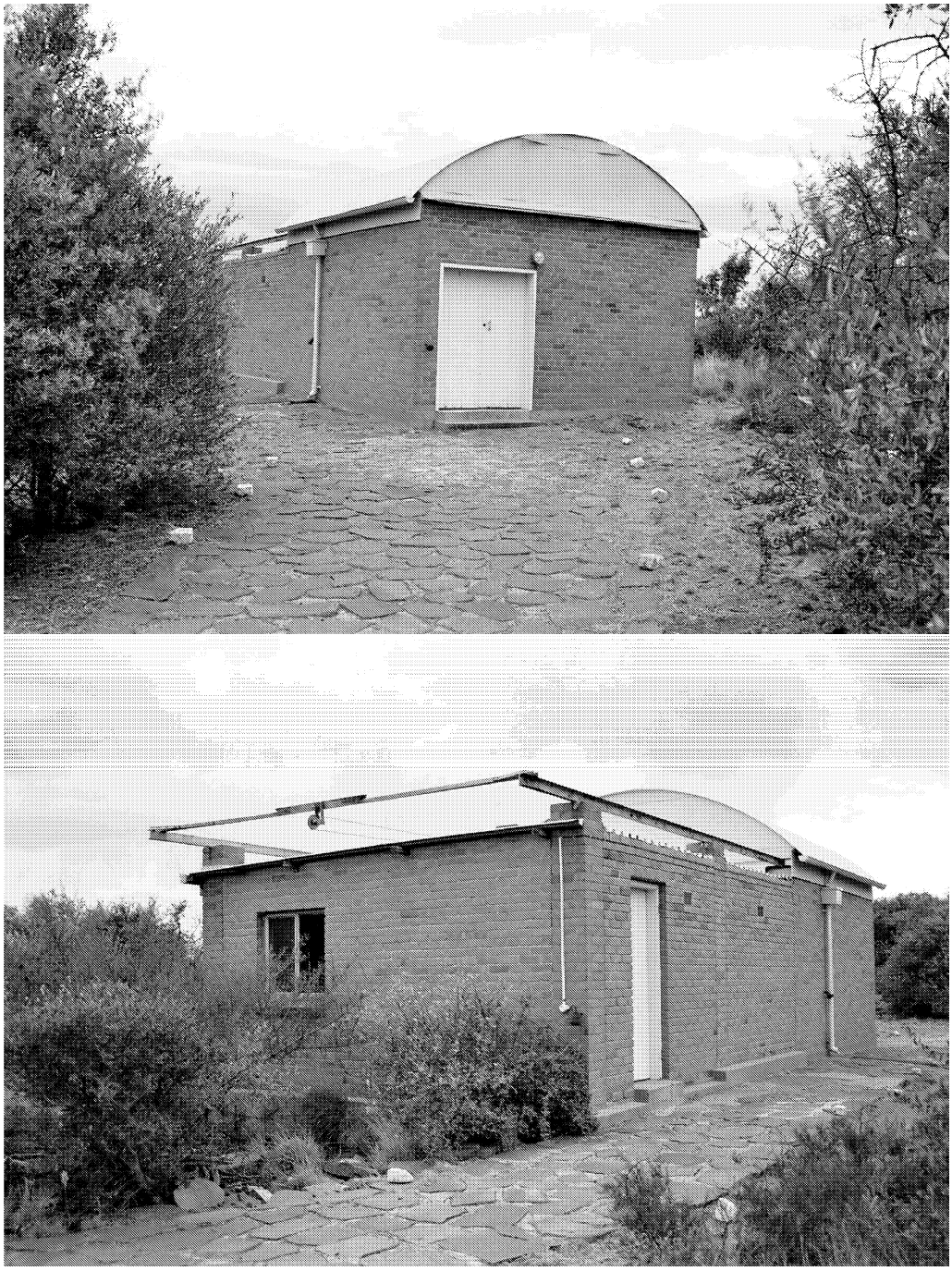

Figure 5.11: Front and rear views of the Watcher building. The front room, with the roll–off roof, houses the telescope, while the control room housing the computers and other equipment is at the rear.

The telescope room's dimensions are 4.9 m×4.6 m, with 2.82 m high walls. When determining the required pier height, a trade–off had to be made between being able to observe objects at low altitudes and ensuring the telescope fit within the maximum space allowable by the existing roof. A 2 m pier permits the telescope to view down to $\sim 8°$,

except for small regions in the north and south where visibility is reduced to $\sim 17^\circ$ and $\sim 25^\circ$ respectively. These obstructions are caused by the rolled–back roof to the north and a part of the building added on the southern side to fill the space created when the roof structure was adapted (Fig. 5.12).

Figure 5.12: Watcher with the roof opened. Note that the roof can be retracted ~ 1 m further than is shown here.

The existing winch mechanism was motorised and interfaced to a PC for software automation. The handle was replaced with a three–phase motor powered by a Hitachi SJ100 Series Inverter and controlled by custom electronics built in the UCD workshops. The motor can be operated using a hand controller located in the telescope room or from a PC interface box in the control room. Both controllers are wired in parallel into the roof control circuit. When one of the controllers closes the relevant (open or close) switch, a relay is energised which activates the motor and moves the roof in the required direction. The motor remains activated until the roof reaches the end of its travel and opens a microswitch which denergises the relay and stops the motor. The motor can only be activated again by closing the opposite directional switch. Additional circuitry signals to the PC interface when the roof motion has started and stopped. This signal is monitored in software and an error is flagged if the timeout is exceeded.

5.7 Weather Station

Environmental conditions are monitored by a Vantage Pro wireless weather station provided by Davis Instruments.[11] The Vantage Pro's integrated sensor suite (ISS) has an anemometer and rain collector as well as temperature and humidity sensors. The unit is solar–powered and communicates wirelessly with a console mounted to the wall in the telescope room. The console, which also features a barometer and temperature and humidity sensors, collects data and sends it to a PC over a serial port connection. The ISS array is augmented by a Leaf Wetness/Temperature station, which is also solar–powered and communicates wirelessly with the console. This unit has two sensors: a precipitation event detector and a cloud detector, both supplied by ROBOSky.[12] The weather station is mounted on the roof of a structure which forms part of the auditorium at Boyden (§7.2).

The cloud detector is composed of two aluminium plates covered in white gloss epoxy enamel paint having high transparency at 10 microns. Each plate has a temperature probe embedded in it, coupled with a heat sink compound. The plates are separated by an insulated rigid polyethylene mounting plate. The detector measures the radiation from the sky and from the ground on the top and bottom plates respectively. At night the sky appears cooler than the ground when there is no cloud cover. When clouds pass overhead radiation is reflected back to the ground and the temperature of the upper plate increases. The differential temperature between the top and bottom plates gives an indication of the cloud cover. The detector is mounted on the same structure as the rest of the station, at the edge of the roof where it has an unobstructed view of the ground and the sky. This structure is unheated and so will not distort the detector readings. The concrete surface beneath the detector has high emissivity. In the future this sensor will be replaced by a thermoelectric sensor manufactured in the Czech republic which will provide increased accuracy in cloud monitoring.

5.8 Computers

The system is controlled by two PCs (watcher1 and watcher2), each with Pentium 4 2.4 GHz processors and 512 MB of RAM, running the Suse 9.2 distribution of the Linux

[11] http://www.davisnet.com/weather
[12] http://www.robosky.com

operating system.[13] One of these machines also has Windows XP installed on another partition and is dual–bootable, allowing the user to choose at boot time which operating system to boot into, with Linux as the default. This provides the capability for on–site observers to control the mount and CCD using Windows programs, as was done for a period during the initial setup of the system. Extra control ports have been added to the machines via PCI cards. A NetMos PCI card was installed on watcher1 providing it with two extra serial ports. A Decision PCI8255 card provides an I/O interface used to communicate with the roof control system. A PCI card also provides a control port for the AP6e CCD. The devices connected to each machine, and the ports to which they are connected, are shown in Table 5.3. Both machines have internal DVD writers which can be used for limited data backups. Each machine was initially equipped with a 40 GB system disk and a 200 GB data disk, with disks being shared between the machines over NFS. One of these data disks is the main archive, while the second serves as a backup. Recently, two 750 GB external disks have been added, to facilitate backing up large volumes of data and transporting it back to Ireland.

Both machines are connected to a switch which in turn is connected to the Boyden network. A microwave link operating at 512 kb/s allows the Boyden network to connect to the outside world via the main University of the Free State (UFS) network. The network settings for the Watcher machines are shown in Table 5.4. Boyden is behind the main University firewall, which strictly regulates incoming and outgoing traffic. The Watcher machines can only be accessed over a secure shell (`ssh`[14]) from a handful of specific IP addresses. The UFS network security policy does not allow any other ports to be opened to the outside world from machines on the campus network. An exception was made to allow the GCN server to open a socket connection to watcher1 so that Watcher could receive GCN notices. In order to send and receive data using http (e.g. to view weather data via the Meteo PHP web browser interface), http can be tunnelled over ssh by port forwarding.

[13] http://en.opensuse.org
[14] http://www.openssh.org/

watcher1	port	watcher2	port
roof	PCI card	CCD	PCI card
focuser	/dev/ttyS4	mount	/dev/ttyS1
filter wheel	/dev/ttyS1	weather station	/dev/ttyS0
UPS	USB	webcam	USB

Table 5.3: Device connections

Hostname	watcher1.uovs.ac.za	watcher2.uovs.ac.za
IP Address	196.21.180.41	196.21.180.40
MAC Address	00:07:E9:4E:45:AB	00:07:E9:6B:26:95
DNS Server	146.182.9.12	
Gateway	196.21.180.2	
Subnet	255.255.255.0	
Proxy	http://wpad.uovs.ac.za	

Table 5.4: Network settings

5.9 UPS

Backup power is provided by an MGE Systems Pulsar Evolution 2200 Uninterruptible Power Supply[15] with a power rating of 1.54 kW / 2200 VA. Critical devices like the PCs, mount, roof motor and roof control interface are powered from the UPS so that the system can shut down safely in case of a power cut.[16] The UPS provides surge protection to these devices and also shields the system from voltage spikes on the network lines through its data–line protection function. An MGE system was chosen since the company already supply and provide support for UPS systems at Boyden. The UPS's power rating provides substantial headroom for expansion of the system. With both PCs running, the telescope being parked, and the roof being closed simultaneously, the load on the system is ~20% of its full capacity. Shutting down the system consumes ~1–2% of the total battery power. The critical battery level at which the observatory is shut down is set to a conservative value of 30%. This provides over an hour of battery–powered operation. When the mains power returns, the PCs reboot automatically due to settings in the BIOS. All observatory control software starts automatically at boot time, so the system is ready to recommence operations.

[15] http://www.mgeups.com/

[16] These are an increasingly common occurrence due to South Africa's ongoing energy supply crisis (see http://news.bbc.co.uk/2/hi/africa/7208628.stm).

Chapter 6

System Description II: Software

6.1 Automation Solutions

Many packages have been developed for the amateur market to provide various levels of automation for astronomical observing. At the most basic level is the sequencer, a program which can carry out a simple pre–determined observing plan. Software Bisque's Orchestrate[1] package is an example of a sequencer. Observing commands and parameters are entered in a spreadsheet–style interface and executed via device control programs like The Sky and CCDSoft. More advanced automation can be achieved using scripting languages. The ASCOM[2] initiative promotes and facilitates scripted automation capabilities and aims to establish a set of interface standards for drivers that provide plug–and–play control of astronomical instruments and related devices. It is based on the Windows COM interface standard, which can be controlled by Window's built–in scripting languages like VBScript and Jscript. A further level of sophistication is achieved by programs like ACP[3], which is a combined scripted sequencer capable of total observatory control via 3rd party programs and the ASCOM platform. A review of automation techniques for astronomy can be found in Denny (2003).

Most commercially available software is written for the world's dominant operating system, Windows. Similarly, all astronomy components are provided with Windows drivers. However, we found the available automation techniques mentioned above to be unsuitable for controlling an autonomous robotic system which would be capable of re-

[1] http://www.bisque.com/Products/Orchestrate/orchestrate.asp
[2] http://ascom-standards.org
[3] http://acp3.dc3.com

sponding to transient alerts. Packages are generally proprietary and so cannot be customised or adapted since the source code cannot be accessed. The Windows operating system is not the ideal platform for a remote robotic observatory from the point of view of reliability and connectivity.

Research groups who have set up robotic telescope systems (§4.3.2) have all developed custom control code on the Linux platform. Most take the same basic approach: a central control program (or daemon) manages the various devices, each controlled by its own dedicated daemon, communicating via a common protocol. Separate programs schedule and carry out observations via the central daemon, while another program listens for transient alerts from the internet and interrupts the current observations to carry out a pre–determined observation sequence when an alert arrives. Since sharing code with the community is not common practice, there has been much duplication of effort.

We did not have the resources to develop custom control code from scratch. A possible solution to our software problem was presented at a GRB conference in Santa Fe in September 2003 by the Czech group who had set up the BART robotic telescope (Jelínek et al., 2004). They described RTS2, the custom software package they had developed for robotic telescope control which was being made available to the community.

6.2 RTS2

RTS2[4] is an integrated suite of programs designed for complete management of a robotic observatory, with a particular emphasis on GRB follow–up observations. It runs on the Linux operating system, and is entirely open source. In its current incarnation RTS2 is coded in C++ and uses the PostgreSQL database system. The structure of RTS2 is similar to the control code used by other robotic observatories: it comprises several device daemons, observational clients, and a central server which communicate over a custom communication library based on TCP/IP. The system currently controls 6 telescopes on four continents.

[4]The RTS2 home page is located at http://lascaux.asu.cas.cz/rts2. The most recent version of the source code can be found in an SVN repository hosted by SourceForge (see http://rts-2.wiki.sourceforge.net).

6.2.1 Structure

The RTS2 system consists of a suite of executable programs. All executables share the same codebase for processing command line arguments and calling other system–level functions. Executables can be divided into groups, as follows:

central server The main executable is `rts2-centrald`. This is the central server which oversees management of the whole observatory. Every device daemon registers with the central server in order to be accessible to client programs and executing daemons. Client programs contact the central server which then passes their requests for information or actions on to devices. It maintains information on all currently connected devices, keeps track of the observatory status (whether it is *on, off*, or in *standby*), and manages transitions from the various states (*day–evening–dusk–night–dawn–morning–day*).

device daemons Each device is managed by its own dedicated device daemon. These programs share common code for registering with the central server and processing TCP/IP commands issued by clients through the central server. Device daemons also implement a layer for interacting with devices at the hardware level, using either their own code or an external library. The hardware currently supported by RTS2 device daemons is shown in Table 6.1. The following device daemons are running on the Watcher system:

- `rts2-teld-paramount`: controls the Paramount ME telescope mount
- `rts2-camd-apogee`: controls the Apogee AP6e CCD
- `rts2-filterd-ifw`: controls the Optec IFW Filter Wheel
- `rts2-focusd-robofocus`: controls the Robofocus focuser
- `rts2-dome-dublin`: controls the roof via a custom interface box

executing daemons These daemons carry out various observing–related tasks. `rts2-selector` selects the next target to be observed, `rts2-executor` carries out the observation, and `rts2-imgproc` manages the processing of the subsequent images. Another program, `rts2-grbd`, creates a socket connection to the GCN, waits for incoming alerts, and processes them by creating a new target in the database based on the information contained

Devices	Manufacturer	Notes
Mounts	Software Bisque	Paramount ME with proprietary serial port driver
	Gemini	Losmandy mounts, Mountain Instrument mounts and custom mounts
	Meade	all LX200 protocol models
	Astelco	*BOOTES–IR* mount, OpenTPL interface
	Millennium Mount II	uses LX200 protocol and the Dynostar X3 controller
CCDs	Apogee	all models, including Alta series (with patched drivers)
	FLI	all models
	SBIG	all models, including new USB models
	Starlight Xpress	all models
Photometers	Optec	ISA I/O card based photometer, with own kernel driver
Filter wheels	FLI	all models
	Optec	Intelligent Filter Wheel (IFW)
	SBIG	filter head integrated to SBIG cameras
Focusers	Robofocuser	all models
	FLI focuser	all models
	Astelco	OpenTPL controlled focuser
	Optec	TCF–S and TCF–S3
Mirrors	Astelco	OpenTPL controlled mirror
	custom design	serial controlled mirrors
Weather stations	Davis	all models supported by modified Meteo (http://meteo.othello.ch) package
	own design	stations communicating through TI I/O cards
Roof and cupola	custom controllers	custom design serial I/O board (FRAM, BART, Watcher), TI I/O card controlled roofs
	cupola	Profibus–based serial interface

Table 6.1: Hardware supported by RTS2

in the alert. This target will automatically have the highest priority, and so will be immediately selected by the scheduler. All of these daemons interact extensively with the database by reading information on targets and writing information on observations and images.

monitoring programs `rts2-mon` is the main monitoring interface. It is based on ncurses, a programming library used to write text–based user interfaces which resemble graphical user interfaces (GUIs) but can be run in a terminal, with much less latency than a conventional GUI when run remotely. `rts2-mon` displays and updates, in real time, information on the status of the central server, all connected devices, and all running execting daemons. The central server can be switched to *off* or *on* via `rts2-mon`, and simple commands can be sent to devices. A recently added feature allows some device settings to be altered di-

rectly, e.g. the cooling temperature of the CCD or the currently selected filter in the filter wheel. A screenshot of `rts2-mon` is shown in Fig. 6.1. Image grabbers, which run on the console (`rts2-focusc`) or through X–Windows (`rts2-xfocusc`) allow direct control over the CCD in order to manually acquire images for focusing or calibration. Work is currently in progress on `rts2-soap`, a program to facilitate access to the RTS2 system through a web browser using the Simple Object Access Protocol (SOAP).

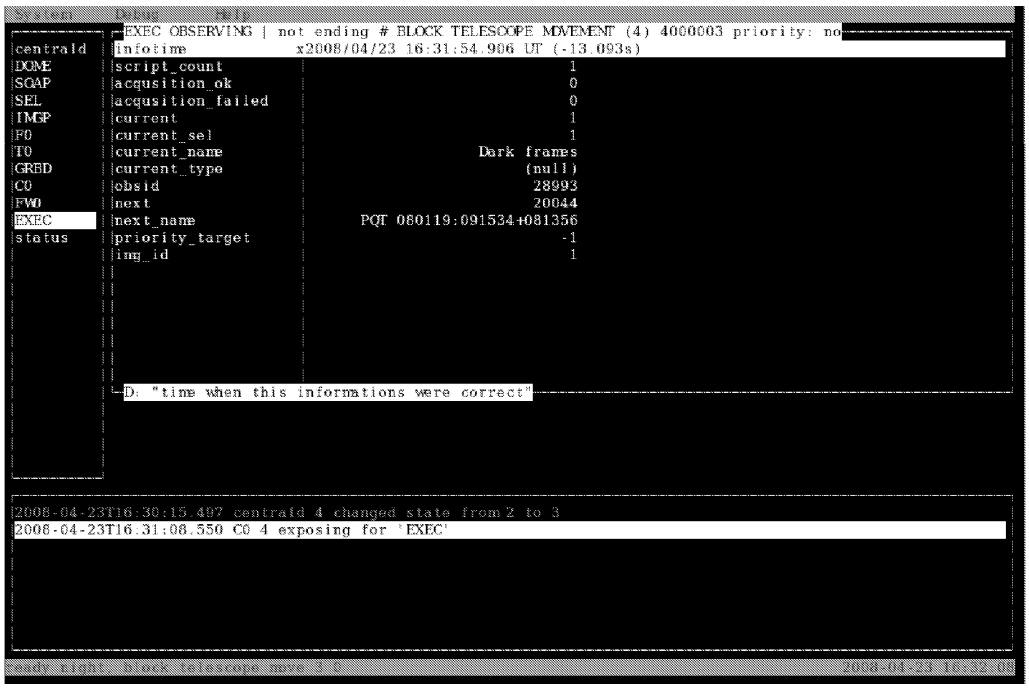

Figure 6.1: Screenshot of the main RTS2 monitoring program, `rts2-mon`, showing the status of the observation executing daemon `rts2-executor`, which is registered with the central server under the label `EXEC`. Log information, displayed in the lines below the main window, shows that the central server has recently changed state from 2 to 3 (*evening* to *dusk*). It can be seen in the main window that the system is currently taking dark frames, and the next observations which will be carried out will be of PQT 080119:091534+081356, an optical transient detected by the Palomar–Quest survey (Donalek et al., 2008).

database tools A variety of command line tools exist for accessing and updating information stored in the database. `rts2-target` manages individual target entries, allowing for the enabling and disabling of targets, changing of target priority, editing of target–specific observation scripts, and other management tasks. `rts2-newtarget` allows new targets to be added to the database. `rts2-user` is used to manage user entries. An observing plan can be loaded using `rts2-plan`. `rts2-targetlist` and `rts2-targetinfo`

provide target information, while `rts2-nightreport` provides observation reports on a night–by–night basis.

additional tools There are a variety of task–specific tools, the most useful of which are `rts2-tpm`, which is used to extract data from FITS headers to be used in the generation of pointing models, and `rts2-telmodeltest`, which tests the subsequent model.

6.2.2 Database

RTS2 uses a PostgreSQL[5] database, with three main tables. The TARGETS table contains information on possible targets, including their coordinates and type (GRB, object, calibration etc.). Several fields can be used to define how the target is to be observed. The IMAGES table contains information on all acquired images which have had their astrometry computed by the real–time image processing script. The OBSERVATIONS table links TARGETS and IMAGES, forming a log of all observations carried out. A variety of other tables are used for specific types of information. The RTS2 source code contains SQL code to create an empty database. The database may be edited and queried manually with SQL commands using `psql`, a terminal–based front end to PostgreSQL.

6.2.3 Configuration

Configuration information is stored in `/etc/rts2`. Parameters relating to the Apogee CCD are stored in `apogee.ini`. Site–specific parameters like observatory coordinates and port number to use for connecting to the GCN are specified in the main configuration file, `rts2.ini`. A variety of user–configurable options can be set here, including the default observing script and the exposure times required for dark frames. The RTS2 startup script, `/etc/init.d/rts2`, uses three configuration files, `centrald`, `devices`, and `services`, to determine which device daemons and services should be started on a particular PC and on which machine the central server is to be found. Command line options for each device daemon can be specified in `devices`. The entire suite of RTS2 programs can be started, stopped, or restarted using the startup script, which is run automatically when the PC boots. The configuration files currently in use on Watcher are shown in Appendix B.

[5] http://www.postgresql.org

6.2.4 Scheduling

The scheduling of observations is a crucial consideration in the design of robotic telescope software. A variety of approaches can be taken, each with their own advantages and disadvantages (see Granzer, 2004, and references therein for a discussion of types of scheduling). RTS2 supports two modes of operation: dispatch scheduling and queue scheduling. Dispatch scheduling uses an algorithm to select targets in real time according to the current observational conditions. The algorithm calculates a merit for each target, and then schedules observations of the target with the highest merit. Each target in the RTS2 database has a priority, which is one of the main criteria used when determining the target's merit. Other criteria in use include altitude, lunar distance, time since last observation, and total number of observations. New GRB targets always have the highest priority, so that any observations in progress are always overridden in favour of observing the GRB.

This mode is ideally suited to autonomous operation. However, it is difficult to predict what will be observed on a given night. Queue scheduling is a far simpler approach. The user specifies a sequence of observations (listing the target and start time for the observation), and the system simply carries out the observations in the pre–determiend sequence. This approach is very limited, but can be useful when observations of a specific target at a specific time are required. Queue scheduling is implemented within the dispatch scheduling algorithm in RTS2. The user–defined observation sequence is stored in the database under a plan target. If a viable observing plan is loaded by the user, the priority of the plan target increases, and it is selected by the scheduler.

6.2.5 Scripting

RTS2 supports customisable scripting of observations. Individual scripts can be specified for each target, with a default script (specified in `rts2.ini` used in the absence of a target–specific script. In the case of GRBs, different scripts can be specified depending on the time which has elapsed since the burst. Simple scripts take the form F *filter no.* E *exposure time*, e.g. on Watcher the script

```
F 2 E 60 E 60 F 0 E 120 E 120
```

represents two 60 s exposures using the R–band filter and two 120 s exposures using the B–band filter. More sophisticated scripting is supported, since some RTS2 setups

use multiple imaging devices and guide cameras which require signalling commands to synchronise the devices being referenced by the script (see Kubánek et al., 2006, for examples).

6.2.6 Server States

The observatory's current status depends on the state of the central server. The server determines when to change to *dusk, night, dawn* and *day* based on the position of the sun, calculated using the current system time and the *libnova* library. The *evening* and *morning* states are offset from *dusk* and *dawn* by a fixed time in order to allow the CCD to cool or return to ambient temperature. In addition to these states, the central server also has three higher level states: *off, on* and *standby*. The system can be switched to *off* manually as a precaution if bad weather is forecast or if some maintenance task is being carried out on the system. No operations will be performed in this state. The system switches to *standby* automatically when it determines that the weather is bad. In this state, the telescope is parked and the roof is closed, but the CCD is kept cooled so that observations can recommence quickly if the weather improves. The weather is determined to be bad when a non–zero value is read from the rain sensor or if the windspeed exceeds a pre–defined threshold. If for some reason no weather data is received the system assumes that the weather is bad as a precaution. When the weather is known to be good, the system is *on* and operations are controlled by the lower level state changes as described below.

During *day* the roof is closed, the telescope is parked, and the CCD is at the ambient temperature. When the state changes to *evening*, the CCD daemon begins to cool the camera. At *dusk*, `rts2-executor` assumes control and begins to take calibration (dark and flat field) frames. Twilight flats are acquired by observing one of a number of targets in the database whose coordinates are centered on reasonably blank regions of the sky. Observations are carried during the *night* state, until *dawn*, when calibration frames are again acquired. The CCD is ramped to the ambient temperature at *morning*.

6.3 Watcher and RTS2

RTS2 presented several key advantages to the Watcher project. It provided an existing solution for complicated software tasks like central observatory control, scheduling, and

inter–program communications, and took a similar overall approach to robotic observatory management to that which has been employed successfully by a number of other groups. RTS2 also included support for a PostgreSQL database and has client programs for querying the database. The package was originally designed with GRB follow–up observations in mind, and is therefore optimised for this task, while still supporting other types of observations. Its target operating system, Linux, is more suitable for running a robotic observatory from the point of view of reliability and remote management. Crucially, RTS2 was open source, and therefore could be customised and expanded according to our requirements.

There were also a number of drawbacks to be considered. The system was still in the early stages of its development, and had not yet been installed and used by anyone other than the original developers. It supported a very limited range of devices, which did not include any of Watcher's components, most of which were not supplied with Linux drivers. Also, virtually no documentation existed, and the source code was poorly commented (sometimes in Czech[6]). However it was decided that these drawbacks were outweighed by the potential advantages, and could be overcome. Since the package was open–source and documentation existed for the communication protocols used by our devices, drivers and other additional code could be developed and integrated into RTS2. Some support would also be available from Petr Kubánek, who was by then the sole developer of the RTS2 package.

6.3.1 Installation

Since RTS2 was not neatly packaged like commercial software, and had only ever been used by the original developers, installation of the system required considerable effort, and represented a steep learning curve in the nuts and bolts of the Linux operating system. Many dependencies (3rd party programs required by RTS2) were encountered which had to be resolved. A PostgreSQL database system was installed, the RTS2 database was built and configured, and the database server was set to start automatically at boot time. The main external libraries required by RTS2 are CFITSIO, *libnova*, and WCSTools. The CFITSIO[7] package is a library of C subroutines used for reading and writing files

[6]This resulted in the author learning some Czech along with various programming and scripting languages. Having encountered the word "chyba" numerous times in source code comments, he was dismayed to find that it translates as "mistake, error, lapse, slip, slip-up, erratum, fault, failing, defect, inadequacy".

[7]http://heasarc.nasa.gov/docs/software/fitsio/fitsio.html

in the Flexible Image Transport System (FITS) format. *libnova*[8] is a library for calculating celestial mechanics and astrodynamics. WCSTools[9] is a package of programs and a library of utility subroutines for setting and using the world coordinate systems (WCS) in the headers of astronomical images. These libraries should all be installed in `/usr/local/lib`. An array of lower level libraries are also required which may or may not already be present depending on the individual Linux installation. When using the Suse 9.2 Linux distribution, it was found that the additional libraries which had to be installed were ncurses–devel, libefence, libjpeg–devel, and XFree86–devel. Depending on the individual Linux installation, numerous issues can arise with the locations and versions of installed libraries, and these must be resolved on a case by case basis.

6.3.2 Driver Development

Each device daemon is compiled from at least two primary source code files. The higher–level daemon code manages communications with the central server and calls functions from the lower–level driver code, which manages hardware–level communications with the device. New device daemons were developed by studying the daemon code to find what functions it called and what feedback it required from the driver, and then writing device–specific drivers to implement these functions. Drivers were tested using command line test programs which simulated the high–level daemon code. Test programs accepted user input, called driver functions, and returned status information similar to the way in which the daemons interact with the central server. Source code for test programs can be found on the lab computer network in `/home/jfrench/testdir`. At the time that the drivers were being developed, RTS2 was coded in C, and so all drivers (and test programs) were written in C. All code has since been ported to object–oriented C++.

6.3.2.1 CCD

Linux drivers for Apogee CCDs are produced by Random Factory[10]. Different versions of the driver package are available, the simplest providing just the drivers and a GUI for controlling the CCD main functions. The drivers are provided as kernel modules and are pre–compiled for a number of versions of popular Linux distributions. Kernel modules

[8] http://libnova.sourceforge.net/
[9] http://tdc-www.harvard.edu/software/wcstools/
[10] http://www.randomfactory.com/apogee-lfa.html

are pieces of code that can be loaded and unloaded into the Linux kernel (the core of the operating system) on demand. They extend the functionality of the kernel, and are often used as device drivers, allowing applications to access hardware via the kernel. No module was provided for the version of Suse Linux (8.1) in use at that time, so a different version of the package was used. This version provided all the source code and tools used to build the drivers. The appropriate kernel module was built, and the system was configured so that the module would load automatically at boot time[11]. The CCD could then be controlled using the GUI.

The source code for the CCD driver, written in C++, is complex, reflecting the sophistication of the CCD control electronics. Developing a C version of the code to integrate into RTS2 would have been a very time consuming task in light of the steep learning curve involved. An alternative approach was offered by the scripting interface included in the driver package. This interface provides driver and image buffer management functionality in the Tcl[12] scripting language. The interface was tested manually using the *wish* shell, a command line interface to Tk which is an extension to Tcl allowing it to interface easily with the Linux display environment, X Windows. The *wish* shell is included in the driver source distribution, as are a number of sample scripts for carrying out basic CCD functions.

An RTS2 driver was developed by embedding Tcl code in C. C programs can make use of Tcl commands by integrating a Tcl interpreter into the C application (Welch et al., 1999). C functions can use the interpreter to execute Tcl commands and read or set variables in the Tcl code. A simple C program which uses a Tcl interpreter to evaluate an arithmetic expression was used as a template (Pather, 1996). A single Tcl file was written containing all the required code to interface with the CCD driver. This file also called out to an initialisation script which initialised the CCD at the driver level. The first test program in C created a Tcl interpreter, used it to load the main Tcl code, and started a *wish* shell from which the Tcl commands could subsequently be called manually from the command line. The next level test programs read CCD variables from Tcl like the camera and cooler status flags and the temperature, and also set variables like the cooling temperature. Temperature values were based on rolling averages of 20 temperature readings which were read every 0.5 s, in order to reduce the random fluctuations produced by read

[11] Kernel modules can be loaded using the command `/sbin/insmod` [path to module], with root permissions. This can be done automatically at boot time by adding the command to the file /etc/init.d/boot.local

[12] http://www.tcl.tk/

noise. A test program was then developed which took exposures of a specified duration and saved the output to FITS files on the hard disk.

In RTS2, the CCD device daemon reads out the image buffer and saves the data to a shared memory segment, a method of interprocess communication (IPC) whereby 2 or more processes communicate by sharing a single chunk of memory. The address of the shared memory segment is returned to the central server, which passes it on to the client program. This program then takes responsibility for reading the data from memory and writing it to the disk in the FITS format. The driver source code included examples of Tcl functions to manipulate image buffers, including one function which copied the image data to shared memory. Tcl code was developed to create a shared memory segment, and then copy image data to memory using the example function. This code, embedded in C, returned the address of the shared memory segment. Test code was developed which used Tcl to read image data from the CCD to shared memory and then use functions from the CFITSIO library to write the data to disk in FITS format. Example C code for accessing shared memory was found in Marshall (1999). The readout code was then integrated into an RTS2 device daemon, which passed the memory address of the data back to the client program. Safely managing and accessing the shared memory was an important task, since memory management errors could cause the program to crash and potentially make the operating system unstable.

6.3.2.2 Millennium Mount II

The MM–II, controlled by the Dynostar X3 interface, can be operated from the PC using ASCII commands sent over an RS232 serial port connection operating at 9600 Baud, 8 data bits, no parity, 1 stop bit, and no flow control[13]. The interface uses the same protocol as the popular Meade LX200 telescopes, and supports a small subset of the protocol's command set. The commands supported by version 3.00d of the Dynostar firmware are summarised in Table 6.2.

During testing of the mount in UCD we became familiar with its features and gained a fuller understanding of our requirements. It became clear that the mount lacked some capabilities which were necessary for operation as part of an unattended, remote system. One drawback was the lack of a park function which would move the telescope to some

[13]The serial port is configured when the connection is opened. Serial port configuration and control is managed on Linux using the system–level commands provided by the POSIX terminal interface (Sweet, 2005).

Command	Function	Command	Function
:GR#	read mount RA	:Qw#	stop slew west
:GD#	read mount Dec	:Q#	stop all slews
:Mn#	slew north	:Sr#	set target RA
:Ms#	slew south	:Sd#	set target Dec
:Me#	slew east	:Gr#	read target RA
:Mw#	slew west	:Gd#	read target Dec
:Qn#	stop slew north	:MS#	move to target
:Qs#	stop slew south	:CM#	sync to target
:Qe#	stop slew east	:U#	toggle data format

Table 6.2: LX200 ASCII commands supported by the Dynostar X3

pre-determined position and disable tracking in order to securely store the telescope while not in operation. The lack of a pre–determined park position was easily worked around in software by calculating the equatorial coordinates of the required park position. The Right Ascension (RA) coordinate of the park position is defined by adding 6 hours to the local sidereal time, while the Declination (Dec) coordinate is set to $-87°$. This results in a position slightly offset from the celestial pole in order to ensure that the telescope is always parked in the same physical position (pointing south with the counterweight shaft almost perpendicular to the ground).

Once moved to the park position, the mount continued to track at the sidereal rate, as if it was observing a target. Tracking could be disabled manually by holding down the MODE key on the Dynostar, but no facility was provided for disabling tracking via a command from the PC. On corresponding with the manufacturers of the Dynostar X3, it was established that the MODE key can also be accessed via the 20–pin connector at the back of the controller. Pulling the relevant pin high (to TTL logic level 1) has the same effect as manually pressing the MODE key. The serial interface to the PC which shared this connector utilised only the most basic three–wire implementation of the RS-232 serial communications protocol[14], leaving the remaining handshaking and control lines on the PC's 9–pin serial port unused. Of these remaining lines, two (the DTR and RTS lines) are outputs which can be controlled by the PC. The pin diagrams for the Dynostar 20–pin connector and the PC 9–pin serial port can be found in Appendix A.

These lines are sometimes put to unorthodox uses, e.g. powering small serial port devices (Engdahl, 2000). By wiring one of these lines (RTS) to the MODE pin on the Dynostar connector and implementing code to toggle the level of the line in the MM–

[14]The three wires are denoted G (ground), RxD (receive data), and TxD (transmit data)

II drive, the MODE key can be controlled from the driver using the Linux system calls provided by the POSIX terminal interface (Sweet, 2005). A new PC–Dynostar cable was made which had a built–in circuit with an RS232 – TTL level converter on the RTS line to convert the PC serial port outputs of ±12 V to the TTL logic levels of 0–5 V used by the Dynostar. This new functionality was also applied at startup, since the motors were off by default when powered on and would not respond to any GOTO commands until they had been switched on by pressing the MODE key. This could now be done from the PC when the driver was initialising the connection to the telescope.

The MM-II was also without safety features which would prevent the mount from crashing the telescope into the pier either during slews or when tracking an object for a long period during which it crosses the meridian. Since the mount is a German Equatorial design, the telescope should be positioned on the opposite side of the mount from the target being observed. If the telescope crosses the meridian without first undergoing a meridian flip, it will soon crash the telescope into the pier. A meridian flip involves moving the telescope to the other side of the mount by slewing over the pole. When the mount was commanded to slew to a new target, it simply chose the shortest route to the target, regardless of whether this route involved an unsafe crossing of the meridian or not.

An `idle` function in the driver monitors the hour angle (HA) of the mount while it is tracking in order to determine when it has tracked the target past the meridian. The HA of the meridian is 0°, so a change in the sign of the mount's HA indicates that the meridian has been crossed. When this occurs, the mount is homed and then slewed back to the target. Before the mount slews to a new target, the driver calculates the shortest route to the new position from the current position (since this is the route that the mount will try to take). If this path results in an unsafe crossing of the meridian, the mount is homed and then slewed to the new target.

6.3.2.3 IFW Filter Wheel

The IFW filter wheel communicates with the PC via an RS232 serial port connection operating at 19.2 K baud with 8 data bits, one stop bit and no parity. Basic ASCII commands can be sent to the controller to select and identify filters. The manufacturers provide a VisualBasic program for Windows to control the IFW, and the communications protocol is documented in the user's manual. The commands implemented in the driver are described in Table 6.3.

Before sending commands to the IFW, serial communications must be initiated with the WSMODE command. Once this command has been received and accepted, the IFW responds with the character "!", and full serial communications are then possible. If during the execution of any commands an error condition is encountered, the IFW responds with an error number which can be used to identify the problem. The error numbers and their meanings are described in Table 6.4.

Command	Return	Function
WSMODE	!	Initialise PC serial connection
WHOME	y (=A,B,C,D,or E)	Go to position 1/identify wheel
WFILTR	x(=1,2,3,4,or 5)	Return current filter position
WGOTOx	*	Go to position x (x=1,2,3,4 or 5)
WEXITS	END	Closes serial connection

Table 6.3: IFW ASCII commands implemented in RTS2 Driver

Error No.	Meaning
1	HOME position has not been reached after the expected number of steps
2	invalid filter requested (SBIG mode)
3	invalid wheel ID read from IFW
4	wheel is stuck or moving too slowly
5	invalid filter requested
6	position change has taken too many steps

Table 6.4: Explanation of IFW error codes

6.3.2.4 Focuser

The Robofocus is supplied with a Windows based graphical control program, which includes an ASCOM compliant scripting interface and example VBScript functions to access the interface. The software interface is fully documented in the user's manual. The Robofocus communicates with the PC via an RS232 serial interface operating at 9600 baud, 8 bit, with no parity. The Robofocus can be controlled using ASCII commands of the form `FX?NNNNNZ`, where

- `F` signifies a focuser command
- `X` specifies the command
- `?` is an arbitrary placeholder

- NNNNNN are six decimal digits with leading zeros as necessary
- Z is a checksum character of value 0 – 255, computed by adding all the previous characters together and setting Z equal to the least significant byte.

No end of command character is used, and it is important to ensure that no subsequent characters or commands are sent to the device until execution of the current command has completed, as this will be interpreted as a stop command. On receipt of a command, the Robofocus confirms its validity by scanning for illegal characters and computing and comparing the checksum. Invalid commands will be ignored. If the received command is valid and a request for movement, the device will respond with a series of "ticks" comprising a string of the character I or O (depending on the direction of movement) for each step of the motor, at a rate of about 10 – 50 per second, until the operation is complete. On successful completion, the device sends a packet confirming execution of the command and the new focus position in the form FXNNNNNNZ, where X depends on the command that was just executed. The commands implemented in the RTS2 driver and the responds expected from the Robofocus are as follows:

- FG?XXXXXZ – This command serves a dual function. If ?XXXXX are all zeros, then the command interrogates the Robofocus for its current focus position, which is returned in the form FD?XXXXXZ. If ?XXXXX contains non-zero digits, then this number is taken to be the new target position and the Robofocus will move to this position, responding with ticks as described above, until the position is reached and the device sends confirmation in the form FD?XXXXXZ, where ?XXXXX is the new position.
- FI?XXXXXZ – Commands Robofocus to move in by ?XXXXXZ steps. The device responds with movement ticks until execution of the command is complete, when it returns the current position.
- FO?XXXXXZ – Commands Robofocus to move out by ?XXXXXZ steps. The device responds with movement ticks until execution of the command is complete, when it returns the current position.
- FP??XXXXZ – Controls or queries Remote Power Module settings. The power sockets are numbered 1 – 4 from left to right. Setting an X = 1 turns the relevant

socket off, while `X` = 2 turns it on. The present status of the module can be queried by setting `??XXXX` = 0, causing the Robofocus to return the current settings in the form `FP??XXXXZ`. (Values other than 0 – 2 are taken to be 0 by the Robofocus).

- `FTXXXXXXZ` – Interrogates the focuser for its current temperature reading, which is returned in the form `FTXXNNNNZ`, where `NNNN` is the temperature reading in raw counts (0 – 1024) from the 10–bit analog–digital converter. The counts correspond to twice the temperature in Kelvin to an expected accuracy of 1%.

6.3.2.5 Roof Interface

The roof interface communicates with the PC through a PCI interface card based on the 8255 Programmable Peripheral Interface (PPI) I/O chip.[15] The 8255 has 3 8–bit TTL–compatible I/O ports, which can be configured in a variety of different modes which define whether each port operates as an input, output, or is bi–directional. The chip can be accessed directly from software by reading/writing to/from its hardware address using the low–level port access functions `inb` and `outb`. The base address of the chip can be found using the Linux `lspci` command. The required configuration is set by writing the relevant control word to the control port, which is located at address `BASE+3`, where `BASE` is the card's base address[16]. The three ports, denoted PA1, PB1, and PC1, are located at addressed `BASE+0`, `BASE+1`, and `BASE+2` respectively. The PCI card in use on Watcher, a Decision 8255 PCI bus adapter, features 2 8255 chips, and so has another 3 ports, PA2, PB2, and PC2, at addresses `BASE+4`, `BASE+5`, and `BASE+6`. These additional ports are unused.

Watcher uses ports PA1 and PC1, configured to be an output and input respectively, to communicate with the enclosure interface. Roof opening and closing operations are performed by writing values to PA1. The status of the operation is monitored on the PC1 input. The binary operation `value & 2`, where `value` is read from the PC1 input, evaluates to true when the motor is running and false when the roof has reached one of the limit switches and the motor is stopped. If the motor is still running after a hard–coded timeout period has elapsed, then the roof is deemed to be stuck and the alarm is raised by sending emails, and sms messages if such a facility exists. The values written to PA1 and

[15] Information on programming the 8255 was found at http://www.decisioncards.com/io/tutorials/8255_tut.html

[16] Watcher's 8255 card is located at base address `0xde00` on `watcher1`

the functions they carry out are shown in Table 6.5.

Value	Address	Function
137	BASE+3	Configure I/O ports
2	BASE	Open roof
4	BASE	Close roof

Table 6.5: Values written to the I/O port controlling the roof interface

6.4 Additional Software

6.4.1 Weather Station

The weather station is managed by the Meteo package,[17] an open source suite of programs for retrieving, storing, and visualising data from Davis weather stations. Data is stored in a MySQL[18] database once every minute and can be visualised using a set of dynamically created graphs and a PHP–based browser interface. The meteo programs use separate processes to retrieve the data from the weather station, to compute averages over intervals of 5 min, 30 min, 2 hr and a day, and to draw graphs suitable for a web page. A full installation will have three processes permanently running:

- `meteopoll` collects data from the station and writes a record to a message queue used to decouple database operations from weather station communication.
- `meteodequeue` pulls update messages from the message queue and inserts them into the database. By handling database updates outside the process that communicates with the weather station, long database queries which block the main station data table will not cause weather data being read from the station to be lost.
- `meteoavg` computes averages over time intervals longer than one minute. As these averaging operations can be quite time consuming, they are also moved outside the meteopoll program to improve reliability.

Graphs are produced by the `meteodraw` program, which is usually run automatically and regularly from a cron job. It is also run by the PHP browser interface script, `meteobrowser.php`, to dynamically create graphs. The browser interface allows data to be visualised on an

[17] http://meteo.othello.ch
[18] http://www.mysql.com

hourly, daily, weekly, monthly or yearly basis. Examples of the graphs that can be produced are shown in Fig. 6.2.

The database also contains structural information about the station's sensors which is used by the applications which write to the database. A station can be composed of a number of separate sensor arrays, and each array can only have one sensor of a given type. Each sensor array and sensor type has its own unique id in the database, as does the station, since a single database is capable of supporting several stations. The source distribution contains the SQL script `meteo.sql` to create an initially empty database with the necessary tables and fields. Structural information can be added on the command line using the `mysql` program to send SQL statements directly to the database. The database structural information specific to Watcher is shown below.

```
table: station
+--------+-----+----------+--------+-----------+----------+----------+
| name   | id  | timezone | offset | longitude | latitude | altitude |
+--------+-----+----------+--------+-----------+----------+----------+
| Boyden | 127 | UTC      |      0 |       -29 |       20 |     1400 |
+--------+-----+----------+--------+-----------+----------+----------+

table: sensor
+---------+----+-----------+
| name    | id | stationid |
+---------+----+-----------+
| console | 10 |       127 |
| iss     | 11 |       127 |
| leaf1   | 13 |       127 |
| leaf2   | 14 |       127 |
+---------+----+-----------+
```

The station is designated `Boyden`. The `console` sensor array is the Weather Envoy console, and `iss` is the Integrated Sensor Suite (§5.7). The `leaf1`[19] array comprises the wetness sensor and the top plate of the cloud detector, while the `leaf2` array has only one

[19] Additional sensor arrays are normally used as leaf and soil moisture/temperature stations, so `leaf` and `soil` are the main additional array names which are available in Meteo.

sensor, the bottom plate of the cloud detector. Since the Meteo database only supports one sensor type per array, this additional array was created in order to separate the two temperature sensors in the cloud detector into different arrays.

All the configuration information used by the meteo weather station tools to communicate with the station and with the database is stored in an XML file, `meteo.xml`, in `/usr/local/etc` on `watcher1`. This file also specifies which graphs should be created from the data by `meteodraw` and configures the settings for each graph. Full details on configuration options can be found in the `meteo.xml` man page.

Weather data must be passed to the RTS2 system so that it can make decisions about closing and opening the roof. Initial tests were carried out using Perl scripts to read data directly from the station via the serial port. Problems were encountered in correctly parsing the complex binary data which was read from the station. This approach also did not function well alongside the Meteo programs, since both were attempting to read the same data, creating problems relating to serial port access and data loss. The existing Meteo data acquisition and archival system was utilised by developing C code to access the MySQL database. After opening a connection to the database, SQL queries could be generated and passed to it and the results could be read back. Weather reading functions were integrated into the roof control code using a separate weather monitoring thread. The weather was determined to be bad if any of the following conditions were met: the wetness sensor returned a non–zero value; the timestamp on the last entry from the rain meter was within the last 30 minutes; or the wind speed exceeded the user–defined safe threshold. The central server was then switched to the standby state, causing the roof to close and the telescope to park, but the CCD was kept cooled in case conditions improved and observations could resume. The weather monitor thread then slept for 30 minutes before rechecking the conditions.

While this custom code functioned satisfactorily in laboratory tests, it has since been replaced by new features in RTS2 which perform weather checking functions in a more efficient and reusable manner. Another RTS2 installation at the site of the Pierre–Auger Observatory in Argentina required that an additonal feature be added to the package. A weather station at that site communicates with various programs by sending UDP packets over the network. RTS2 was adapted to be capable of receiving weather data in this manner. In order to expand RTS2's weather station support, a modified version of `meteopoll` was written. This new program, `meteopolludp`, adds the ability to send weather data in

UDP packets immediately on being read from the weather station. The RTS2 roof control daemon receives weather data every second, and the system load is reduced in the absence of frequent querying of the database.

6.4.2 UPS

Watcher's Uninterruptible Power Supply (UPS) is managed by the Network UPS Tools[20] (NUT) package. NUT is an open source suite of programs which provide a common interface for monitoring and administering UPS hardware over a network. It supports a variety of UPS models via hardware–specific drivers which provide device level communication functions. The driver passes UPS status information to the central server `upsd`, which manages communications with various client programs on the network. The main client program is `upsmon` which monitors the status of the UPS and manages the safe shut down of the PC when critical battery level is reached. User scripts can also be run at shutdown using `upsmon`.

The central server in the Watcher NUT installation is running on `watcher1` and communicating with the UPS hardware (connected to the same machine) using the `newhidups` driver. A `upsmon` client is running on both `watcher1` and `watcher2`, in master and slave mode respectively.[21] A simple C program, `rts2-upsshutdown` was written which uses the RTS2 communication libraries to connect to the RTS2 central server and switch it to the *off* state. When the server is switched to this state, the observatory is shut down (the roof is closed, the telescope is parked and CCD cooling is set to ramp to the ambient temperature). This program is run by `upsmon` when the UPS has reached critical battery level and before the PCs are shut down. User–definable parameters in the UPS hardware (such as the critical battery level) can be set using the `upsrw` command line tool. The current status of the UPS (e.g. battery charge, load etc.) can be viewed using the `upsc` client.

6.4.3 Miscellaneous

System time is used in a variety of ways by RTS2, e.g. calculating celestial mechanics and writing time stamps in FITS headers. Therefore it is crucial that the system time is

[20] http://www.networkupstools.org

[21] Master mode is used on a machine when the UPS is directly connected to it. In slave mode, the monitor waits for shutdown instructions from the master machine.

accurate. This is achieved through use of the Network Time Protocol[22] (NTP) which is designed to synchronise PC clocks over a network. Accurate time is kept on both Watcher PCs using `ntpd`, the Network Time Protocol daemon,[23] which communicates with an NTP server at the University of the Free State.[24]

The webcam is controlled by SPCATools[25] using the `gspca` loadable kernel module driver. A live video feed can be viewed using the `spcaview` program, which can also be used to take a single image.

[22]http://www.ntp.org
[23]http://www.cis.udel.edu/ mills/ntp/html/ntpd.html
[24]The address of the UFS NTP server is ntp.uovs.ac.za
[25]http://mxhaard.free.fr/sview.html

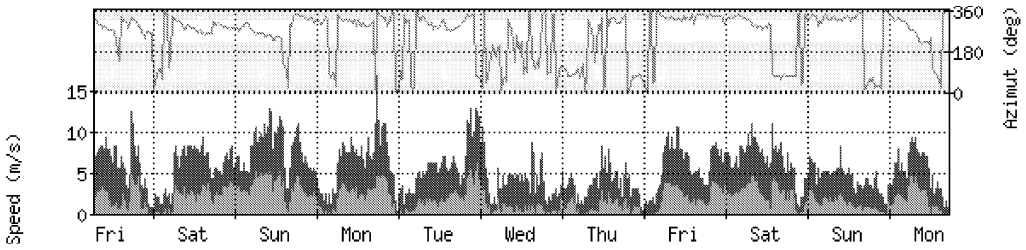

The lower part of the graph shows the average wind speed during the sampling interval in light green and the maximum speed in dark green (scale on the left). The upper part shows the wind direction (azimuth) in blue (scale on the right).

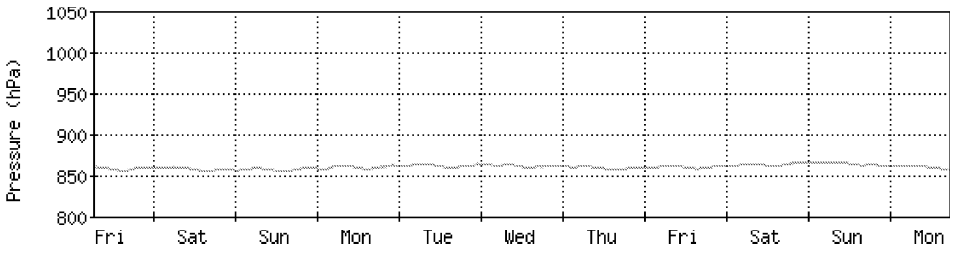

Average barometric pressure

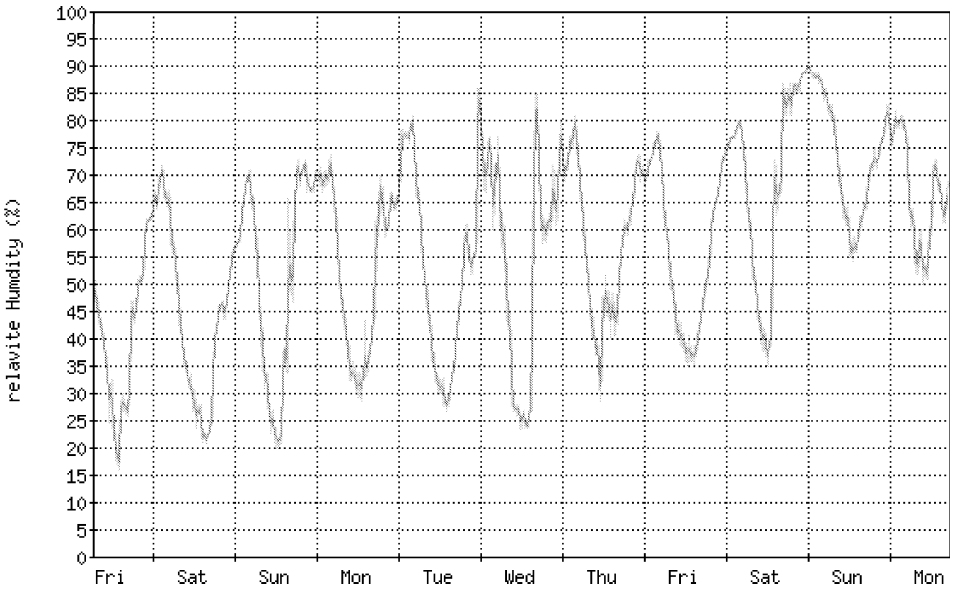

Relative humidity

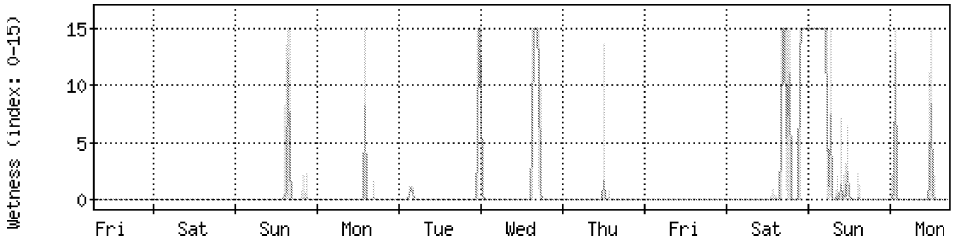

Wetness index (0–15)

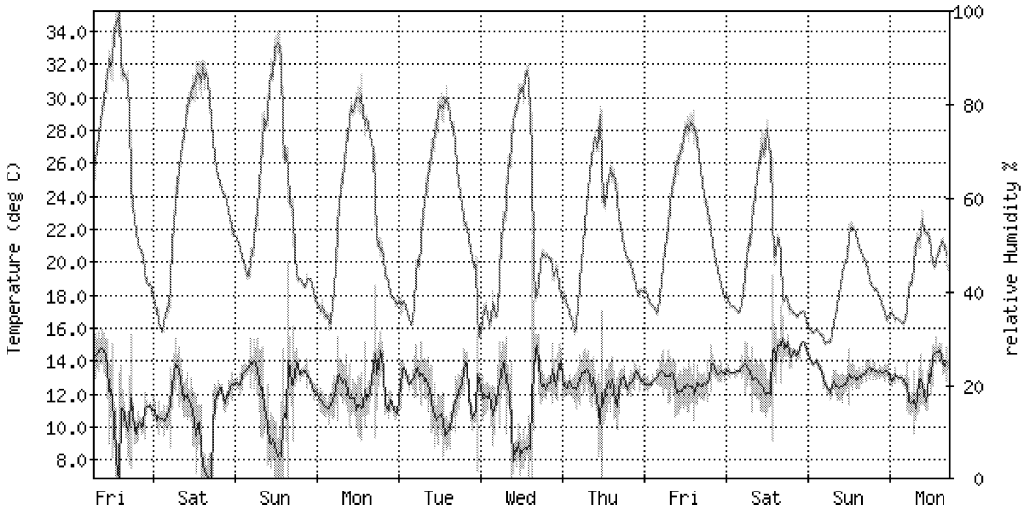

The red curve shows the temperature and the light red area shows the range between maximum and minimum temperature during the sampling interval. The blue curve shows the dew point, the temperature at which dew begins to form.

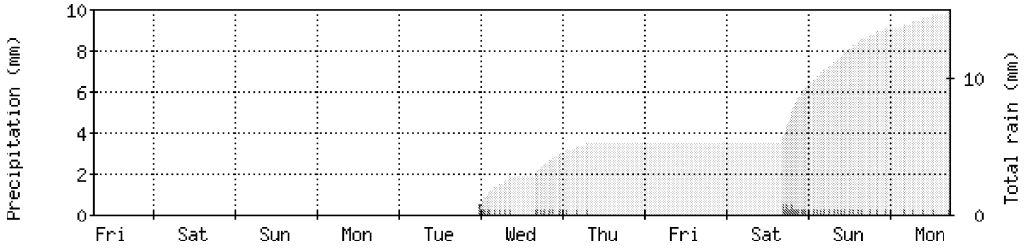

The total rain (or moisture content of the precipitation) in mm during the sampling interval is shown in blue (scale on the left). The total cumulative rain is shown in turquoise (scale on the right).

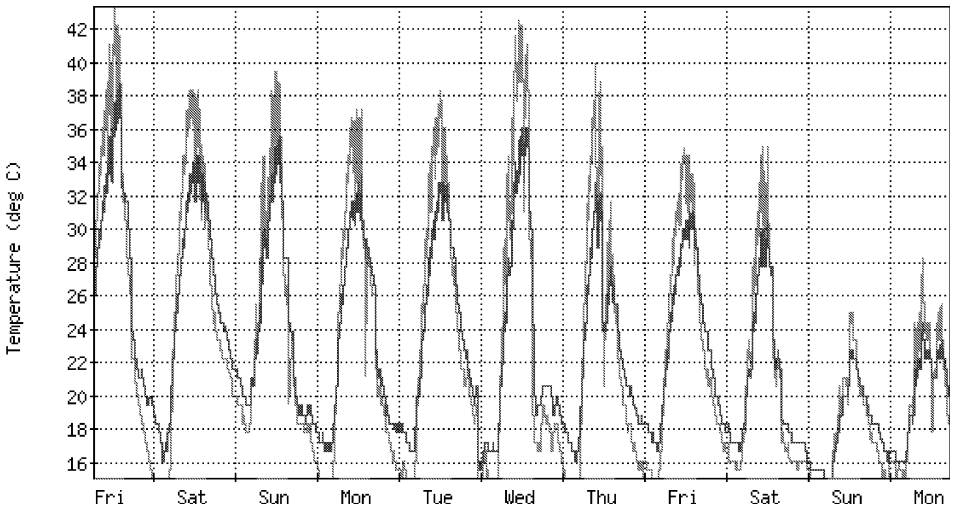

The temperatures of the top and bottom plates of the cloud detector are shown in blue and red respectively

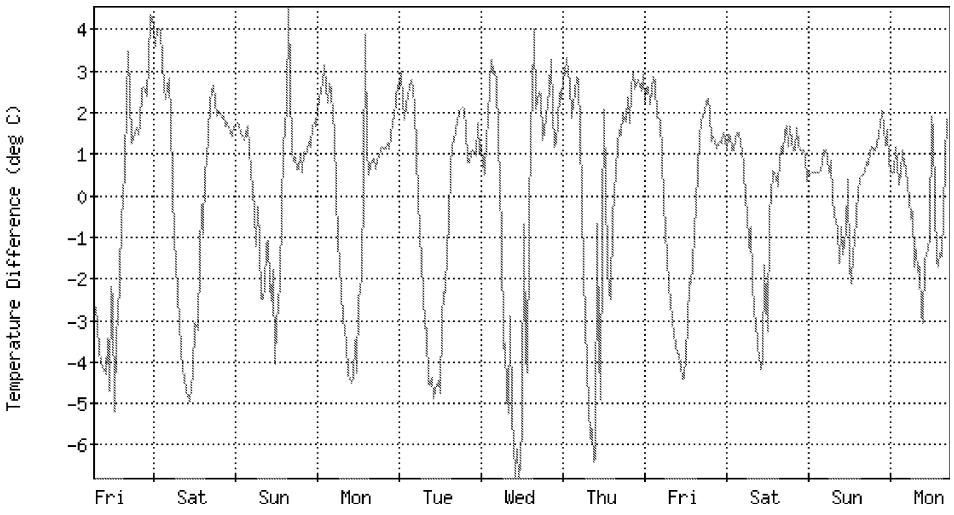

The temperature difference between the two plates of the cloud sensor. A nighttime difference of $\lesssim 3°$suggests that there may be some cloud cover

Figure 6.2: Examples of Meteo weather graphs for the week 03/02/2008 to 09/02/2008 at Boyden Observatory.

Chapter 7

Testing, Installation, and Operations

7.1 Initial System Testing

Testing of the main system components was performed in UCD prior to shipment to South Africa. A temporary enclosure was erected on the roof of the School of Physics building. This comprised a garden shed with wheels fitted to the base allowing it to be rolled back along a track. A small iron pier was bolted to existing rods in the roof structure. The MM–II mount, supporting the OTA and CCD, was secured to the pier. This setup allowed the basic functionalities of the instrument to be tested.

Initial testing of computer control of devices was carried out using the Windows platform, since all devices had readily available control software on this platform. For the focuser, filter wheel and weather station, these programs were supplied by the manufacturer. Software Bisque's[1] CCDSoft and The Sky packages were used to control the CCD and mount respectively. On the Linux platform, the CCD was controlled using the Random Factory driver and GUI (see §6.3.2.1), while the XEPhem [2] astronomy package was used to communicate with the mount. No Linux control programs existed for the focuser or filter wheel. More detailed testing of computer control of the serial port devices (mount, focuser and filter wheel) was carried out using the Kermit[3] terminal emulation program, which allows the user to communicate directly with the device at the hardware level using each device's specific ASCII communication protocol. A full understanding of hardware–level communications was required in order to develop device drivers for RTS2.

[1] http:www.bisque.com
[2] http://www.clearskyinstitute.com/xephem
[3] http://www.columbia.edu/kermit

This drivers were tested using custom C programs which simulated communications with higher–level RTS2 programs (§6.3.2).

Having developed drivers and integrated them into RTS2 device daemons, tests were carried out on full RTS2 control of the system in the UCD Space Science laboratory. While this dummy system could not carry out real observations of the night sky, it could be seen if RTS2 was attempting to carry out the appropriate tasks and identify any problems being encountered. The system could be safely run over long periods in order to discover intermittent or unpredictable problems. A number of test targets were added to the database so that observations would be scheduled and the system would attempt to carry out observations. We also registered with the GCN at this time and received a unique port number used by `rts2-grbd` to listen for GCN notices. Initially, test notices were received in addition to burst alerts. These artificially generated notices, identical in format and content to the normal mission notices, are distributed every 3.5 – 6 hrs. A dummy roof motor was connected to the roof interface box to simulate the roof motor.

7.2 Observing Site

A high–quality site is vital in order to do science with any kind of ground–based telescope. The site selected for Watcher is the Boyden Observatory,[4] situated at an altitude of 1387 m in South Africa's Highveld region, 26 km from the city of Bloemfontein (29°02′20″ South, 26°24′20″ East, Fig. 7.1). Boyden was initially established as Harvard University's southern observatory in Peru in 1889, and was relocated to South Africa in 1927. After a number of years of being operated solely by Harvard, the observatory was subsequently run by an international consortium, including Ireland's Dunsink Observatory, until 1976, when it was presented to the University of the Free State (UFS). Following some years of decline, Boyden has been revitalised in recent years thanks to the efforts of the University's Physics Department and the Friends of Boyden organisation. The original 1.5 m telescope has been refurbished and is actively engaged in research programs. Construction of the Boyden Science Centre Auditorium was completed not long before Watcher was installed, providing space for talks as well as a night sky viewing platform on its roof. The Observatory has a very active educational and public outreach program, frequently holding open evenings and school visits which make use of the refurbished 13″ refractor,

[4] http://www.assabfn.co.za/friendsofboyden/boyden.htm

the solar telescope, and Watcher. The observatory layout is shown is Fig. 7.2.

Several factors contributed to this choice of site. In order to maximise opportunities for observing GRB optical counterparts from the ground, a globally distributed network of instruments which can provide round the clock coverage of the entire night sky is required. Since sky coverage with dedicated robotic telescopes at southern latitudes is relatively sparse, and only one other system is in operation in Africa (ROTSE-IIIc at the HESS site in Namibia), Boyden was a rational choice from this perspective. Atmospheric conditions at the site are generally very stable, particularly in the winter as the region's dominant high–pressure systems act as a barrier to moisture streams. However during the summer high surface temperatures and streams of warm moisture–laden air from the Indian Ocean can result in cloud formation and occasional violent thunderstorms (Jarrett, 1987). Though the site is at a relatively high altitude and is sufficiently remote to avoid major light pollution problems, it is still very accessible, which facilitates installation and particularly maintenance. Technical staff at UFS provide support, and a member of the department who lives in the on–site residence is available to perform maintenance tasks. A number of disused small telescope buildings with roll–off roofs are located on the site. One of these was refurbished and adapted to accommodate Watcher, which saved on the expense and work involved in constructing a new enclosure. Network connectivity to the main UFS network is provided by a microwave link, which was installed as part of the preparations for Watcher's arrival.

7.3 Installation

Watcher was installed over the course of three on–site visits: two in 2005 (July 19 – July 31 and September 09 – October 21) and one in early 2006 (March 13 – April 04). The first visit was largely spent setting up the PCs and instruments. Some of the main setup tasks are described below. The telescope had been balanced, polar aligned and focused and testing of the pointing capabilities had begun, when the visit had to be cut short due to unforeseen personal circumstances. The second visit was focused mainly on resolving pointing problems with the MM–II which had started to become apparent at the end of the first trip. The installation and configuration of a new version of RTS2 was another key task carried out during this visit. The pointing problems were not resolved, and as the South African summer was approaching the weather was hampering our efforts with

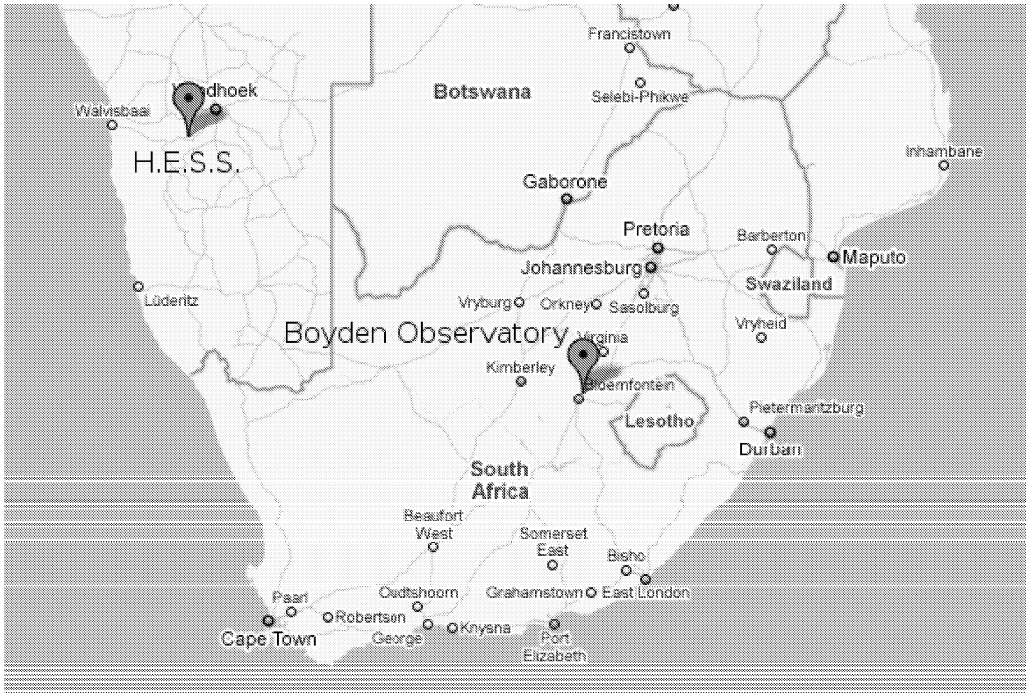

Figure 7.1: Map of southern Africa showing the location of the Boyden Observatory and the site of the H.E.S.S. high–energy γ–ray project in Namibia, where the ROTSE–IIIc robotic telescope is located. *From Google maps.*

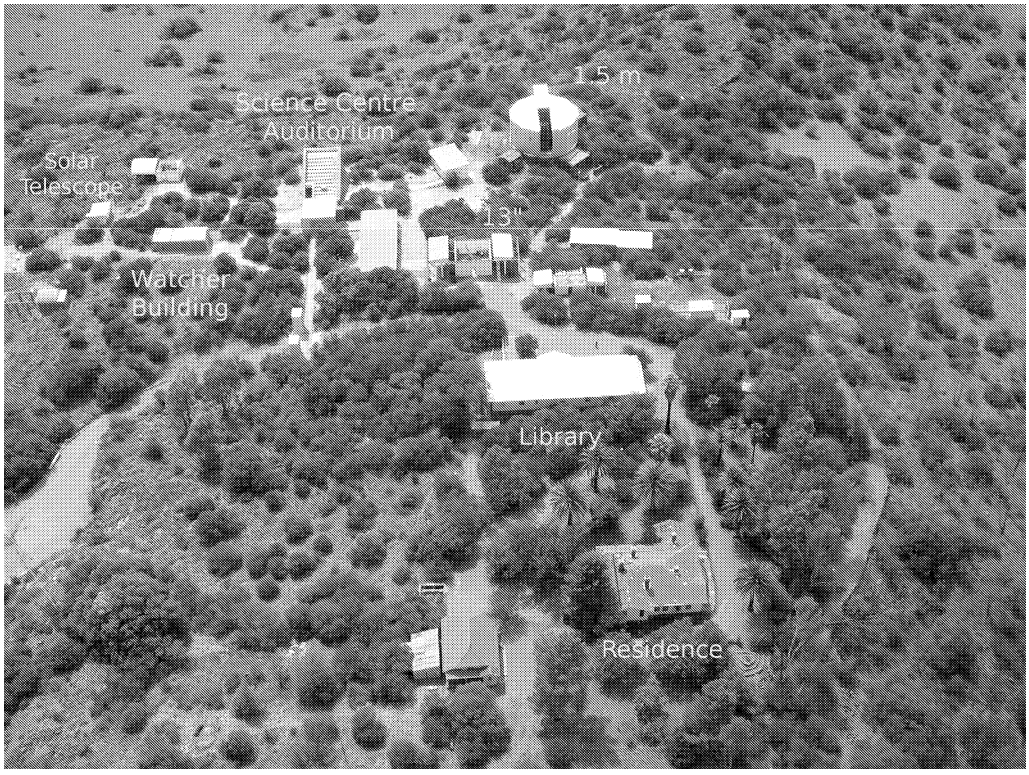

Figure 7.2: Layout of Boyden Observatory. *Credit: Juan Olivier.*

increasing regularity. It was decided not to extend the trip, but to return in the new year when the weather would be more reliable. In light of the problems experienced with the MM–II, in late 2005 it was decided to change mounts, since a Paramount ME had become available, as had additional funds. This mount was installed on the third trip, and the system began operations (under close supervision) during the last week of March 2006.

Figure 7.3: Watcher, soon after being mounted on the MM–II, during the first installation trip.

7.3.1 Telescope and Mount Setup

7.3.1.1 Motors

The MM–II's Dynostar controller is designed to be used with a variety of mounts and stores settings specific to each one. By selecting the MM–II from the controller's menu, parameters like the motor current, frequency and microstep settings are set to values specific to the motors of the MM–II. Tests were then carried out to check the rotation direction of the motors. The direction of the Right Ascension (RA) motor can be adjusted by changing the sign of the SetGearing parameter on the Dynostar, and the direction of the Declination (Dec) motor can be changed via the SwitchDec parameter. Full details

of motor settings can be found in the Dynostar manual (Boxdörfer, 2003). Some motor settings are not automatically accessible on the controller, and can only be edited after the Service Code (1589) has been entered.

The Paramount settings are stored in on–board flash memory. The mount is most commonly used with the Windows program TheSky, which provides full access to all of the mount's settings. Settings can also be accessed using a Windows command line program (Fig. 7.4), provided by Bisque, which is usually used for reprogramming the motor index angles when the control electronics have been replaced. This program can be used in conjunction with the `wine`[5] Windows emulation software to access the Paramount settings on the Linux platform, e.g. by running the following command with superuser permissions on `watcher2`:

```
wine /home/jfrench/mkser4.exe com2
```

where `com2` refers to the second serial port (`ttyS1`) in Windows nomenclature. Full details on the Paramount's configurable settings can be found in the user's guide.[6]

7.3.1.2 Synchronisation

In order for the MM–II to slew to targets automatically in GOTO mode, the mount must first be synchronised to a position on the sky. Two kinds of alignment are possible, one–star and two–star alignment, selected using the Align1 and Align2 functions on the Dynostar. One–star alignment assumes that the mount has been polar aligned, so that the RA and Dec axes are aligned with the celestial sphere (§7.3.1.4). By centering a star in the instrument's field of view and synchronising the mount on it, the mount should be able to find any position on the sky, with accuracy limited only by the polar alignment and the inherent abilities of the mount. When setting up the mount in the northern hemisphere, it is tempting to use Polaris as the reference star, since it is easily identifiable and has already been used as a reference point when polar aligning the mount. However, since lines of RA converge at the pole, minor errors incurred when centering and synchronising on Polaris can translate to large pointing errors in RA. When the Dynostar is powered off, the last position is stored and the RA is incremented at the sidereal rate so that when it is powered back on it can be resynchronised to the current position.

[5] http://www.winehq.org
[6] http://www.bisque.com/SC/Download?File=Bulk/PDFs/ParamountMEManual.pdf

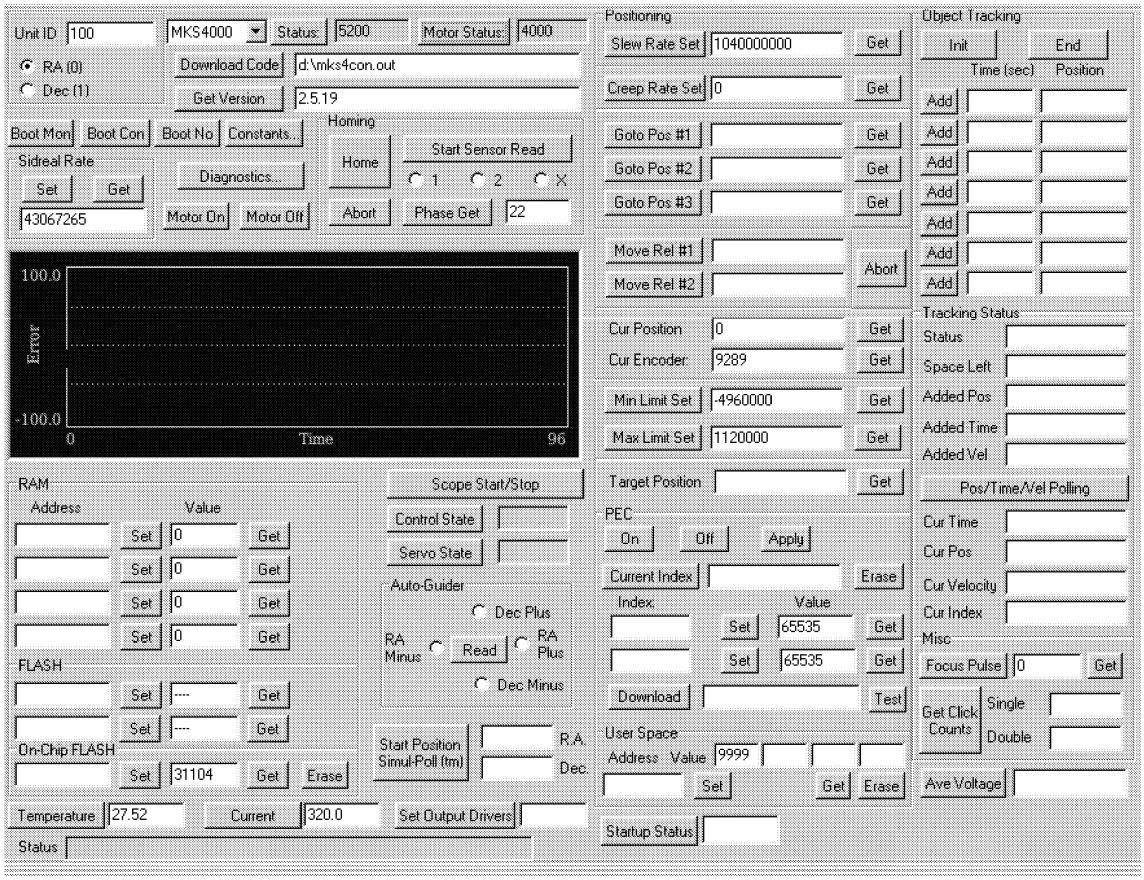

Figure 7.4: Screenshot of the `mkser4` command line tool for accessing the Paramount ME settings.

The Paramount ME's homing sensors allow the mount to be reset to an exact physical position. Having initially homed the mount, using TheSky to synchronise the mount on a star then allows the hour angle and declination of the home position to be calculated from the angles between the home position and the current position. These angles are measured from the motor axis indices, which are 0 at the home position. The coordinates of the home position are then stored in the Paramount's flash memory, so that no further resynchronisation is necessary, even if the mount if powered off. The Sky can then compute the coordinates of the telescope at any time using the coordinates of the home position and the current readings of the motor axis indices. In RTS2, the coordinates of the home position are hard–coded to an approximate value. The Paramount driver library then computes telescope coordinates which are subsequently corrected by the TPoint model for any offset errors in the coordinates of the home position (§7.3.1.5).

7.3.1.3 Balancing

The telescope should be properly balanced around the polar (RA) and Dec axes to facilitate smooth slewing and to avoid putting excess strain on the motors. Proper balance is crucial for accurate tracking, and it is also possible to model the telescope's pointing performance more accurately if it is well balanced, since the model is not well–equipped to compensate for the pointing errors that may occur if the telescope is particularly poorly balanced when pointing at certain areas of the sky. In practice, perfect balance in all positions is extremely difficult to achieve, but a reasonably well-balanced system should perform satisfactorily.

In order to test the balance on each axis, the clutch on the axis must be released, or in the case of the clutch–less Paramount, the worm gear is disengaged. Only one axis should be released at a time to facilitate safe handling of the instrument. The telescope must first be balanced around the Dec axis in order to position the centre of gravity along the axis of the counterweight shaft (Fig. 7.5). Before this was carried out, the telescope was focused, since any subsequent movement of the CCD and filter wheel would affect the balance about the Dec axis. The mount was positioned so that the tube and counterweight shaft were parallel to the ground and the tube was pointing south. A custom–made counterweight on a small counterweight shaft mounted to the telescope mounting plate was used to balance the telescope. While keeping the telescope in the same position the Dec axis was secured and the RA axis released. Balance around this axis was achieved by moving the main counterweights along the counterweight shaft. The balance was then tested in various positions for both axes and fine adjustments were made. The final positions of the counterweights were marked with tape for future reference.

7.3.1.4 Polar Alignment

In order for the telescope to accurately track targets as they move across the sky, its RA axis must be aligned so that it points as closely as possible to the celestial pole. Significant polar misalignment leads to trailing in CCD images, as stars appear to drift across the image during the exposure, which limits the duration of useful exposures. Misalignment can also degrade the telescope's pointing performance.

Various methods by which accurate polar alignment may be achieved are described below. Each subsequent technique can achieve greater accuracy than the previous one,

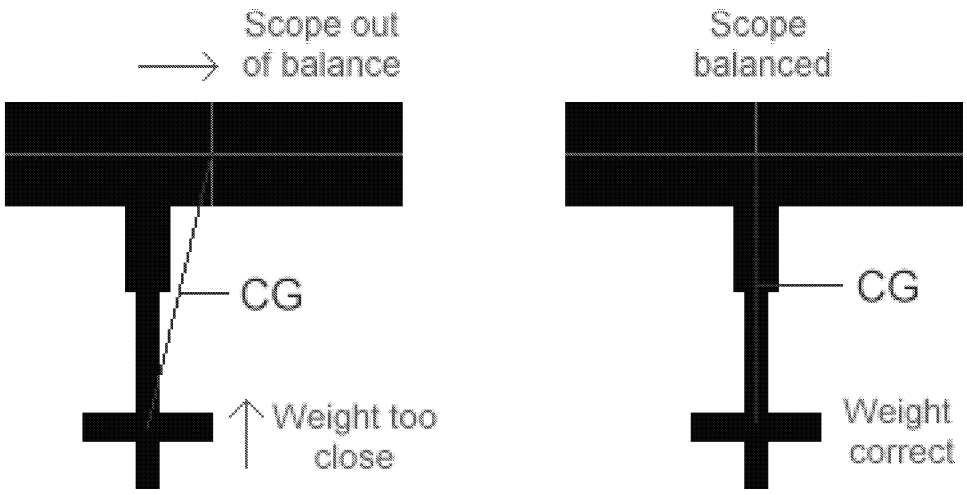

Figure 7.5: Balancing the telescope about the Dec axis positions the centre of gravity along the counterweight shaft. *From http://starizona.com/acb/ccd/settingupbal.aspx*

and if followed in the suggested order the time taken to complete each step is minimised.

Polar Finderscope The MM–II is supplied with a Losmandy Polar Finderscope to assist in preliminary polar alignment. The Dec axis may be positioned so that holes in the mount allow the user to look straight through the RA axis. The finderscope is placed in the underside of the RA axis and illuminated with the supplied LED. The constellation shown at the edge of the reticle provides an indication of its correct orientation (note that these constellations are not visible in the field of view). The device is designed for use in both hemispheress, with corresponding reference markings for each. Northern hemisphere alignment will be discussed first. Having oriented the mount to point roughly north, the mount is physically moved in elevation and azimuth using its adjustment knobs until Polaris is positioned at the appropriate point in the finderscope. The reference stars are then positioned between the markings by a combination of elevation and azimuth adjustments and rotation of the reticle. For southern hemisphere, the procedure is similar, employing the appropriate set of reticle markings (Fig. 7.6).

Drift Method Accurate polar alignment may be achieved using the method of declination drift, in conjunction with a CCD camera. Once the CCD has been focused, a relatively bright star is chosen close to the eastern horizon (from $\sim 10^\circ$ to $\sim 20^\circ$ above the horizon to minimise the effects of atmospheric turbulence) and close to the celestial equator (Dec

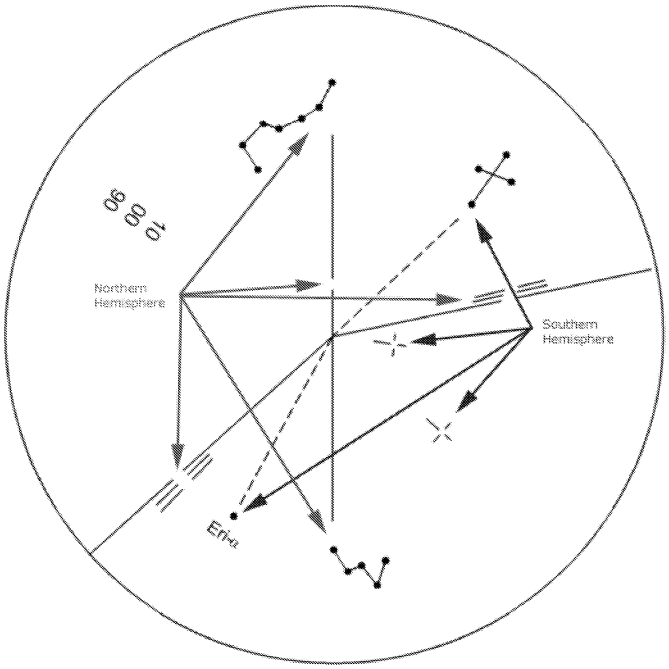

Figure 7.6: Losmandy polar finder reticle

$\sim 0°$), and centered roughly on the CCD. Next, movements of the telescope on the sky are correlated with the movements of the reference star in the image, in order to determine the direction of north/south in the image. The pixel coordinates of the star are noted, and with the mount tracking at the sidereal rate, the telescope is moved a little to the north using the mount hand controller. (The extent of the movement should be enough to allow for a clear change in the star's pixel coordinates, without causing the star to leave the CCD's field of view. For Watcher's optical setup, $1' - 2'$ was appropriate). The directional change in the X coordinates corresponding to north is noted (e.g. north: +X), and the mount movement is reversed for verification, and to return the reference star to a position near to the centre of the CCD. It is only necessary to determine the direction of the north–south axis, since only drift in declination is relevant.

The pixel coordinates of the reference star are noted, then the telescope is allowed to track the star for a period of time, while taking a sequence of CCD exposures. The coordinates of the star will change with each exposure. The direction of drift along the north–south axis will allow the direction of polar alignment in elevation to be determined, i.e. if the star drifts north, then the mount should be moved to the south, and vice versa. To determine the misalignment in azimuth, the procedure is repeated using a reference star near the meridian (also at Dec $\sim 0°$). Declination drift to the north indicates a mis-

alignment to the west, i.e. the mount should be rotated to the east, and vice versa. There is likely to also be some small change in the RA coordinates, which should be ignored for the purposes of polar alignment. This drift is not caused by polar misalignment, but by the periodic error in the mount's worm gears.

In order to speed up the process, it is best to use a relatively short exposure time (e.g. 20 s, hence the choice of a relatively bright star), and to take a sequence of exposures, rather than taking a single long exposure. This approach allows the user to check each image as it is read from the CCD and to quickly determine the direction of drift for the first couple of iterations of the method, when the mount is likely to be in very poor alignment and the declination drift becomes apparent very quickly. As adjustments are made to the polar alignment and the procedure is repeated, it will take longer and longer for declination drift to become apparent, due to the improved alignment. The procedure is repeated until the drift in declination over a few minutes is negligible. Given the qualitative rather than quantitative nature of the method, there is a practical limit to the accuracy that can be obtained. A drift of ~ 2 pixels over a period of ~ 8 minutes was the practical limit to the accuracy that we could achieve with this method.

Polar Alignment with TPoint Polar alignment can be further refined quantitatively by analysing pointing data using the TPoint software package (§7.3.1.5). Once a pointing model has been fitted to pointing data from twenty or more stars, TPoint can give reliable information on the extent of polar misalignment. The terms ME and MA in the standard equatorial mount model correspond to polar axis misalignment in elevation and azimuth respectively, expressed in arcseconds. A positive ME value indicates that the mount is aligned below the celestial pole. A positive MA value indicates that the mount is aligned east of the celestial pole. The elevation and azimuth adjustment knobs on the Paramount ME are calibrated, so that each knob "tic" (raised edges on the circumference) correspond to $2'$ of adjustment.

Note that, due to refraction, the celestial pole appears slightly higher in the sky than it would in the absence of an atmosphere. Aligning the mount to this refracted pole minimises the effects of field rotation in the polar region and restores the standard $15''$ per sidereal second tracking rate at the zenith region. At Boyden's latitude and elevation ($-30°$, 1390 m), the celestial pole is raised by $\sim 85''$. Therefore, an ideal value for the ME term would the $+85''$ (in the northern hemisphere, the appropriate value would be

negative).

7.3.1.5 Pointing Model

The factors which contribute to the difficulty of accurately pointing a telescope are best summarised by Patrick Wallace, author of the TPoint pointing analysis software package (Wallace, 1988): "we live on a spinning and wobbling planet, in orbit around a star, looking up through an atmosphere and using imperfect machinery". Analysing the system's pointing imperfections and applying corrections can have several benefits. Most importantly for a robotic system, it facilitates "blind pointing", whereby the telescope can point to the correct location on the sky first–time, without any human intervention. Tracking is also improved, since it is another form of pointing (in this case, differential). A pointing analysis can also provide useful diagnostic information on the physical system, in particular on polar misalignments, and may help to reveal mechanical defects present in the system. Since all telescopes exhibit a small number of defects which can be effectively analysed, these effects can be accounted for in a pointing model and the telescope can be instructed to slew to the corrected position. The six purely geometrical pointing model terms that can be applied to all equatorial mounts are shown in Table 7.1

Term	Description
IH	Index error in HA
ID	index error in Dec
NP	Nonperpendicularity of HA and Dex axes
CH	Nonperpendicularity of Dec and Pointing axes
ME	Polar axis misalignment in elevation
MA	Polar axis misalignment in azimuth

Table 7.1: Standard geometric terms in a pointing model for an equatorial mount

The IH and ID terms serve as zero–point corrections to the mount's encoder readouts in RA and Dec. CH corrects for any error in collimation of the telescope optics within the tube. Any non–perpendicularity between the RA and Dec axes is corrected by the NP term. Polar misalignment in elevation and and azimuth is dealt with by the ME and MA terms respectively. In addition to these standard terms, other terms may be applied as required. The most common supplementary term for equatorial mounts is TF, which corrects for flexure in the optical tube which is most pronounced when pointing to low altitudes. Harmonic terms may also be useful to deal with miscentering and eccentricity in the mount's drives.

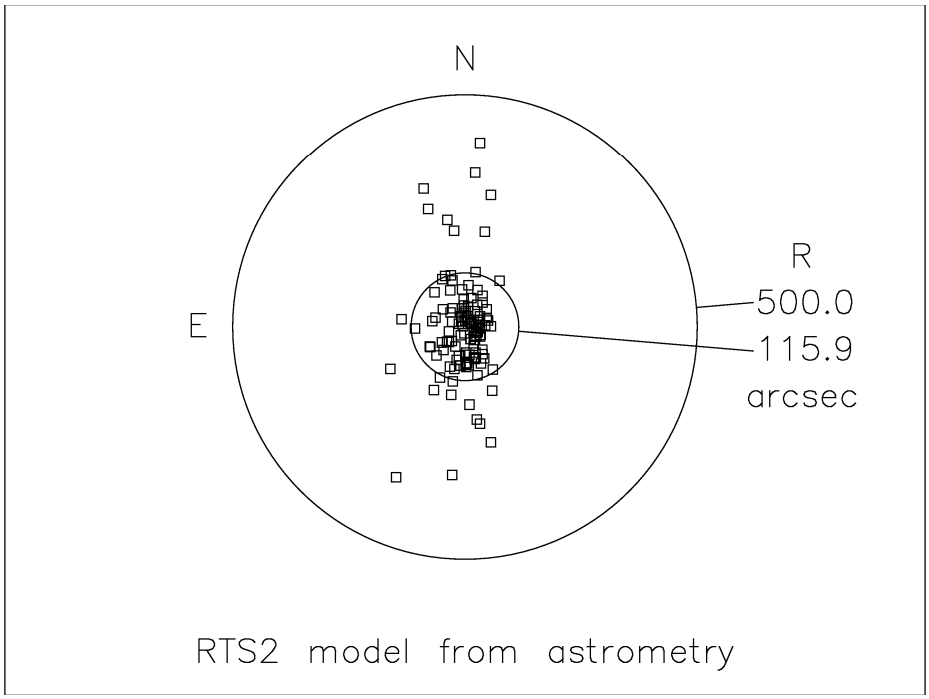

Figure 7.7: Scatter diagram of pointing errors from a TPoint modelling run on Watcher, with the RMS pointing error indicated by the inner circle.

Pointing data is collected by enabling the "target" with ID 4 in the rts2 database. This "target" generates a series of observations randomly distributed around the celestial sphere. Astrometry is automatically performed on the resultant images, and the pointing error (the difference between the telescope's raw position and its actual position on the sky) is recorded in the FITS header. The FITS headers may then be scanned by an rts2 utility to produce an input data file in a suitable format for TPoint, e.g.:

```
rts2-tpm  <path to images>/*.fits > pointing.dat
```

will scan the headers of the referenced modelling images, extract pointing data, parse it into a format suitable for TPoint, and save the result into the file `pointing.dat`.

7.3.2 Additional Setup

7.3.2.1 Robofocus

The direction of the Robofocus stepper motor's movement was first verified using the IN and OUT buttons on the hand controller. The Robofocus can be operated regardless of the direction of the motor, however it is worthwhile to ensure that the directions are correct to avoid confusion, particularly in the software interface which makes use of directional

commands. In order for the Robofocus to provide meaningful absolute focus position information, it must be calibrated to the length of travel available to the focusing system (any positional information stored before this procedure is carried out is a remnant from factory testing). The Robofocus is first driven to the limit of travel in the OUT direction of motion before the device is put into "training" mode which allows it to determine the number of positional increments required to reach the innermost limit. For Watcher's optical setup this figure was ~20,000. Further details of calibration procedures can be found in the Robofocus manual.

Since the Robofocus was originally installed on a rack and pinion focus mechanism which required it to support the weight of the imaging system, the settings of the clutch, which maintains the focus position, were checked. The telescope was oriented perpendicular to the ground so that the imaging system was exerting the maximum force on the stepper motor. The focus position was then changed with the IN button on the hand controller (moving the imaging system away from the floor), while watching for any slippage. The clutch screws should be tightened if slippage does occur when the Robofocus is operated in this manner.

7.3.2.2 Filter Wheel

The IFW has three modes of operation: manual, PC (RS-232), and SBIG (the latter is compatible with the protocol used by camera/filter controllers manufactured by Santa Barbara Instrument Group, and will not be discussed here). When the IFW is powered on, it will automatically rotate the wheel to the HOME position (filter 1), and stop. The NEXT and BACK buttons may be used to manually select filters by cycling through the positions one at a time. The IFW will not accept any input while the wheel is moving. At the beginning and end of a filter change, the controller will beep and the display will flash. To operate the IFW in PC (RS-232) mode, the mode switch must be set to PC. The device may be operated manually until serial communication is initiated by the PC, after which no manual input will be accepted until the PC relinquishes control or the device is powered off.

The most likely cause of errors in the IFW system is the O–ring which provides friction between the wheel and the stepper motor. If it is not providing proper friction, the wheel can slip or become stuck. In addition, if an O–ring is fitted incorrectly or develops a flat spot the wheel may stick. Cleaning the O–ring or manually manipulating the O–ring

to work out any bumps or flat spots can resolve these issues. This part is subject to the most wear and tear, and occasionally needs to be replaced.

7.3.2.3 Remote Power Module

The Robofocus Remote Power Module accessory provides remotely switchable power outlets which can be controlled through the robofocus device daemon. The mount is powered from one of the module's outlets, allowing it to be rebooted remotely. A halogen light was installed in the telescope room and connected to another of the module's outlets. If a problem is encountered at night, the telescope room can be viewed with the webcam by switching on the light. The power module itself is connected to the UPS. The power outlets can be controlled from the `rts2-mon` monitoring program by using the arrow keys to select the focuser and entering `switch <number> <state>` where the outlets are numbered 0 – 3 and 0/1 corresponds to off/on, e.g. `switch 0 1` turns on outlet 0. The light is connected to outlet 0 and the mount is connected to outlet 1.

7.3.2.4 Cabling

A small hole in the wall between the telescope room and the control room allows cables to be passed through from the PCs to the instrument. These cables run along the floor to the pier and are protected by cable raceways. The adaptor panel at the rear of the Paramount ME has a number of ports which are wired through to the instrument panel at the back of the telescope mounting plate (Fig. 7.8). The filter wheel and focuser are connected to these ports. In addition, the Paramount has an internal cable conduit allowing cabling to be passed through the mount (Fig. 7.9). The CCD cable is routed in this manner. These features eliminate the risk of dangling cables becoming entangled.

7.4 Operations

7.4.1 Commissioning

Watcher began operating at the end of March 2006. An image of the currently operating system is shown in Fig. 7.10, and the first light image is shown in Fig. 7.11. The system was closely supervised in the early stages, particularly since the roof did not close reliably. For the first week, the system was supervised closely by the UCD team who had installed

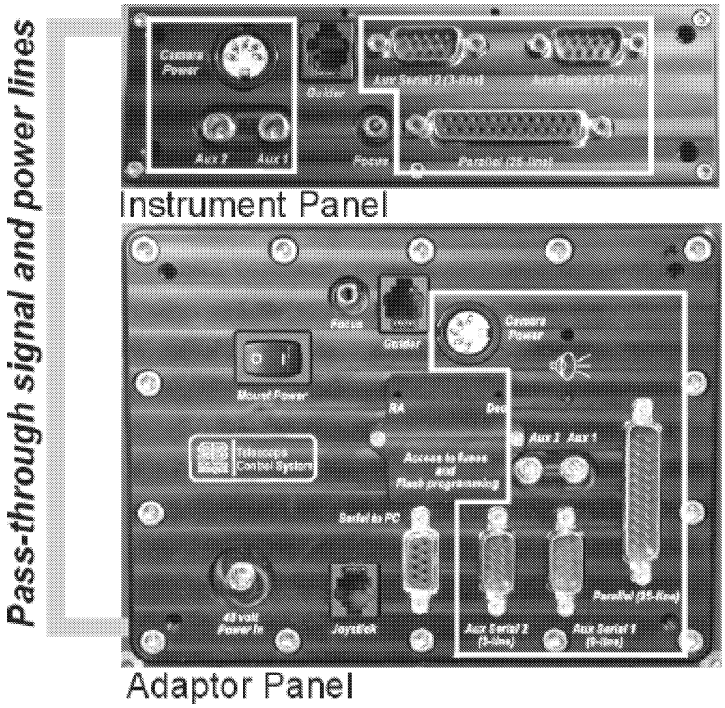

Figure 7.8: The outlined areas on the Paramount ME's adaptor and instrument panels show the connectors which are wired through the mount. *From the Paramount ME User's Guide*.

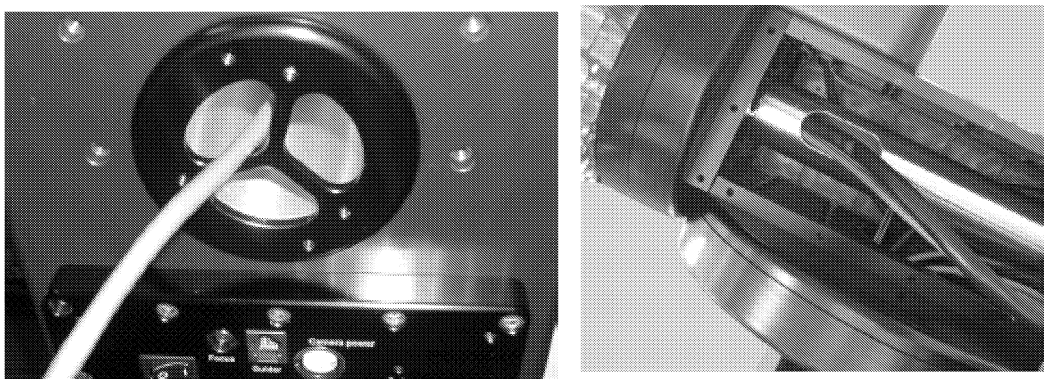

Figure 7.9: Paramount ME through the mount cabling. Cables enter the RA shaft at the rear of the mount, exit the RA shaft in the declination box, and are passed up through the Dec axis and out through a cable channel on the telescope mounting plate. *From the Paramount ME User's Guide*.

the system. After the team had returned home, the system was supervised jointly by the UCD team and collaborators at UFS. Weather conditions in the general area were monitored closely using forecasts and composite radar and satellite maps from the South African Weather Service[7] (Fig. 7.12). The system was only turned on if the weather was very likely to be good all night, and our on–site collaborators visited the telescope in the morning to check if the roof had closed and to close it manually if it had not. The roof problem was resolved when it was found that the motor had been wired incorrectly for the South African power supply. The system was then able to operate fully robotically from May 19, 2006.

7.4.2 Equipment Failures

Three major equipment failures have occurred thus far. On April 6, 2006, a failure in the PCI card used to communicate with the roof interface resulted in the roof not being closed. Tests were carried out on–site by UFS electronics technicians, communicating in real time with UCD using the Linux command line `talk` program. The main 8255 chip on the PCI card (§6.3.2.5) had failed, possibly due to a floating ground connection in the roof interface box. The chip was quickly replaced, the floating ground was fixed, and the system resumed operations within two days of the failure.

Lightning strikes appear to have been responsible for the other two failures. Lightning protection measures currently employed consist of a lightning conductor located on top of the Boyden Science Centre Auditorium (see Fig. 7.2), using plug boards with built–in surge protectors, and the surge protection provided by the UPS. These measures can only provide a limited degree of protection in the event of a very nearby or direct lightning strike. However, in the two cases where damage has been caused by lightning, it has been limited. After a lightning storm on October 10, 2006, it was found that serial communications could not be established with the telescope mount. On–site tests and communications with the mount's manufacturers established that the MKS 4000 card, the heart of the Paramount's control system electronics, had failed. The card was removed and a replacement card was provided[8] which resolved the problem, allowing operations to resume on March 13, 2007. The long delay was due to problems with the manufacturer shipping an incorrect card in the first instance and subsequently shipping the correct

[7] http://www.weathersa.co.za

[8] This new card was reprogrammed with axis indices specific to the mount (see §7.3.1.1).

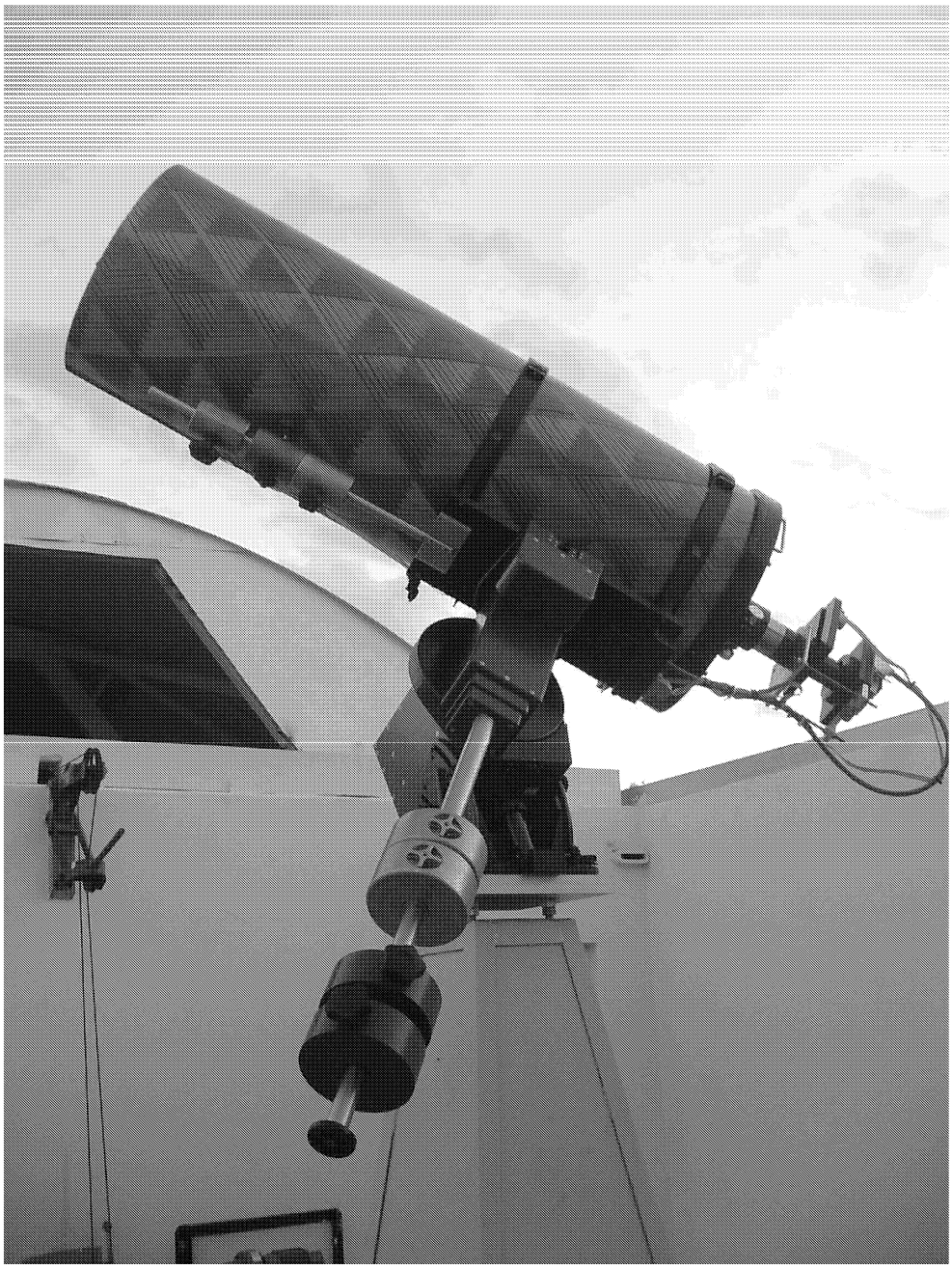

Figure 7.10: Watcher at sunrise, having just completed one of its first observing nights, near the end of the final installation trip.

Figure 7.11: Watcher first light image of Eta Carinae.

card to incorrect addresses. On April 8, 2007, a lightning strike also damaged a network switch which connected the Watcher building to the rest of the Boyden network. This was replaced by UFS Computer Services staff on April 16, and subsequently reconfigured on April 25, allowing Watcher operations to resume.

7.4.3 Duty Cycle

From April 1, 2006 to April 30, 2008, Watcher successfully carried out observations on 385 nights (partial or full).[9] The number of nights in each month during which observations were possible is shown in Fig. 7.13. The main factors limiting the instrument's

[9]This was determined by finding the number of nights of each month for which there is image metadata in the database. For image metadata to be added to the database, the automatic image processing script must have been able to calculate an astrometric solution for the image.

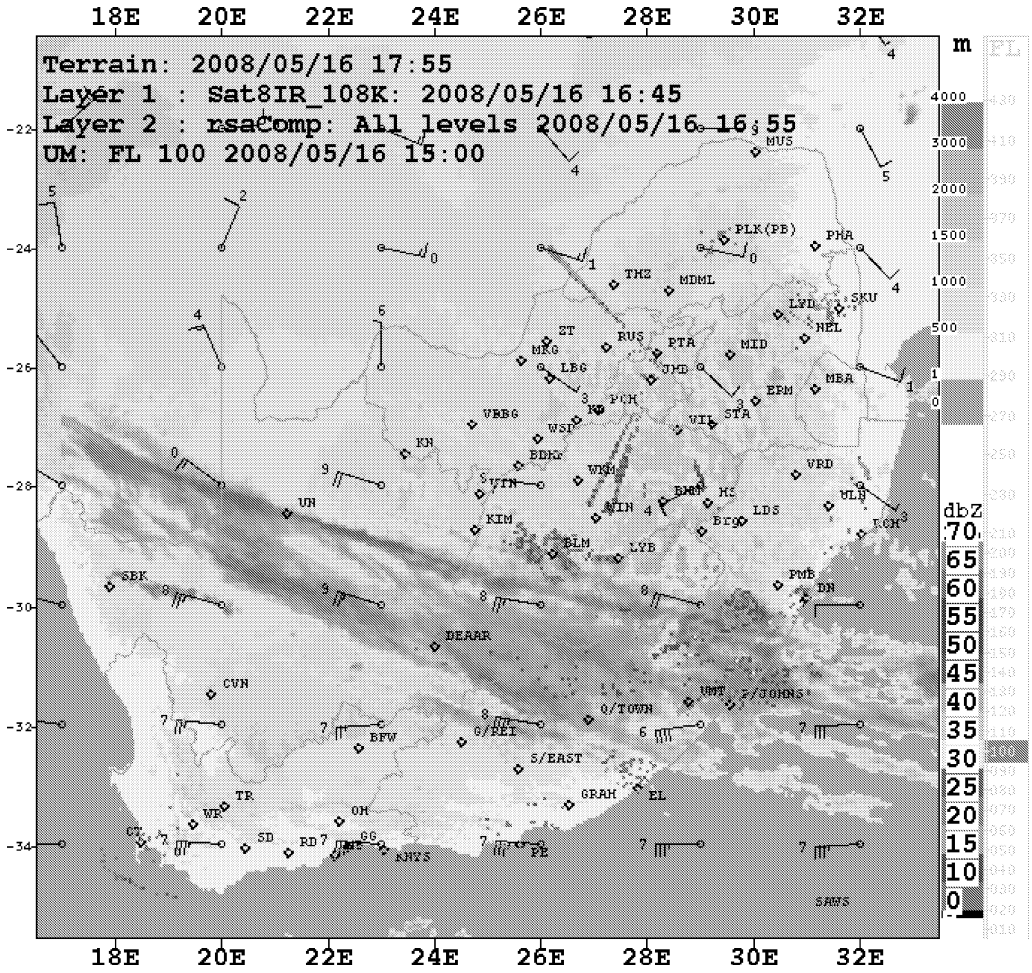

Figure 7.12: Example of a composite radar and satellite map for South Africa. These were used during the commissioning of Watcher to establish when it was safe to open the roof. The reflectivity of cloud cover is measured in dBZ, which can be used to estimate rainfall as shown in Table 7.2. *From the South African Weather Service website: http://www.weathersa.co.za*

dBZ	Rain rate ($mm\,h^{-1}$)	Comments
10	~ 0.2	Significant but mostly non-precipitating clouds
20	~ 1	Drizzle, very light rain
30	~ 3	Light rain
40	~ 10	Moderate rain, showers
50	~ 50	Heavy rain, thundershowers, some hail possible
60	~ 200	Extremely heavy rain, severe thunderstorm, hail likely

Table 7.2: Guidelines for estimating rainfall from dBZ factors in radar images

duty cycle were instrument down time and poor weather conditions. The main causes of instrument down time were the failure of the Paramount control board and a number of network outages. Power failues were generally infrequent, except during the period from mid–October 2007 to March 2008 when South Africa experienced a nationwide energy crisis and the system was shut down 13 times by the UPS. Considering instrument down time alone, Watcher's duty cycle for the two year period is ~ 72%. Considering weather alone, the duty cycle is ~ 70%. The total duty cycle for the period is ~ 50%.

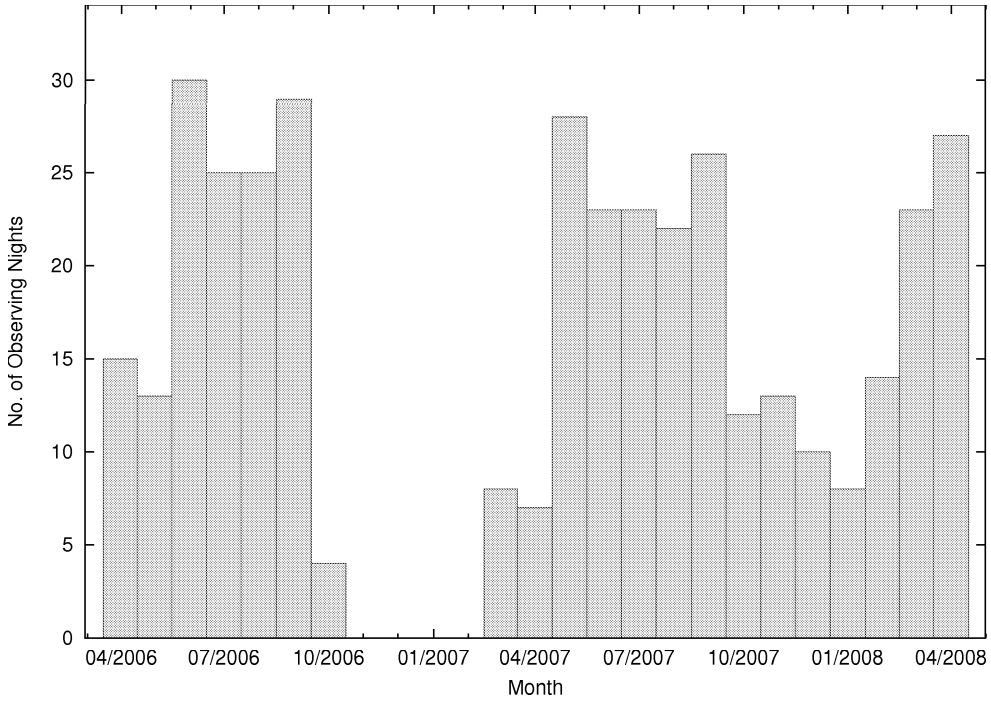

Figure 7.13: Number of observing nights for each month of Watcher operations, from April 1, 2006, to April 30, 2008.

Chapter 8

Observations, Analysis & Results

8.1 Data Reduction

Standard CCD data reduction requires three different types of calibration frames which are used to correct for basic instrumental effects in the raw data frames. The three calibration frames required are as follows:

Bias A bias frame consists of a zero second exposure, i.e. the CCD is simply read out, and the shutter remains closed. The resultant frame contains the random read noise, the DC offset level (the amplifier zero–point offset), and the variations in this offset across the array caused by the on–chip electronics. The rms value of the bias level corresponds to the CCD's read noise, i.e. the underlying noise level in every CCD frame. In order to obtain a good statistical sample of the noise variations, it is recommended to average at least ten bias frames to create a master bias.

Dark A dark frame consists of an exposure taken with the shutter closed of a duration corresponding to the duration of the data frame being reduced, and at a similar CCD temperature to the data frame. The resultant frame contains the dark current or thermal noise present in the CCD at the given temperature. Dark frames can also provide information on hot pixels and the rate of cosmic ray strikes at the site. In general, the dark current increases approximately exponentially with temperature and linearly with exposure time. Expensive CCD systems which utilise liquid nitrogen cooling systems can achieve operating temperatures where the dark current is essentially negligible, thus precluding the need for the dark frames in the reduction process. However, for less expensive, ther-

moelectrically cooled CCDs (such as Watcher's Apogee AP6e), where typical operating temperatures of -20° C are more realistic, significant dark current can still remain and need to be accounted for. In this case, bias frames are no longer needed, since the dark frame also contains the bias level. Where data frames of different exposure lengths are being reduced, it is tempting to use a single exposure length dark frame and scale the dark current to the required exposure length, based on the assumption that the dark current increases linearly with time. However, this is inadvisable since temperature instabilities in thermoelectrically cooled systems can cause the dark current to vary with time. A master dark frame, comprising at least 10 frames of the same exposure length at similar temperatures, should be used in order to accurately sample the dark current.

Flat Field A flat field is taken by uniformly illuminating the CCD with a sufficiently bright light source for the duration necessary to achieve a high signal to noise. Typical sources of illumination are the twilight or night sky, or a dome screen (or the inside of the dome) illuminated by a lamp. The most convenient method for a remote observatory is to take twilight exposures of a relatively empty part of the sky in the morning and evening. Flat fields correct for pixel–to–pixel variations in the CCD response as well as any non–uniform illumination of the detector itself. Since the detector response varies with wavelength, separate flat fields are required for each filter band used in target observations. Several flats should be median combined to generate a master flat for each filter, having subtracted an appropriate dark frame from each prior to combining.

Watcher acquires calibration frames automatically every evening and morning. The database contains a large number of targets corresponding to relatively empty areas of the sky which are suitable for generating flat field frames. Data is reduced offline using the tools provided by IRAF, the Image Reduction and Analysis Facility[1] (Tody, 1993). Darks with a mean count of > 500 and flats with a mean count of < 1000 are not used in the reduction process.[2]

[1]IRAF is distributed by the National Optical Astronomy Observatories, which are operated by the Association of Universities for Research in Astronomy, Inc., under cooperative agreement with the National Science Foundation.

[2]The author found Charles Pullen's "Zen Of IRAF: A Spiritual User's Guide to the 'Image Reduction and Analysis Facility' for the Linux Novice" to be a highly useful and enjoyable introduction to data reduction, photometry, and achieving enlightenment through use of IRAF: http://www.aavso.org/observing/programs/ccd/zen_of_iraf.pdf

8.2 Image Analysis

An astrometric solution is automatically calculated for each image using the `past` program, part of the `JIBARO` package (de Ugarte Postigo et al., 2005). `past` employs a sigma–clipped third–degree polynomial surface fit and comparison with the USNO B1.0 catalog (Monet et al., 1998), using all sources detected at more than 10σ significance in the image. Source detection is performed using the `SExtractor` package (Bertin and Arnouts, 1996). Instrumental magnitudes are measured using the IRAF aperture photometry routine `phot`.[3] A circular aperture of radius r is centered on the source in question, and a concentric sky annulus is used to sample the sky background to be subtracted from the source counts. For optimal signal–to–noise, a radius of $r = 1.4 \times FWHM$ is used (Howell, 2000), where $FWHM$ is the average full width at half maximum for the sources in the image and is stored in the header of the FITS file during the initial astrometric processing. Images were visualised and compared with catalogs using the DS9 FITS viewer (Joye and Mandel, 2003). Instrumental magnitudes were transformed to a standard photometric system using a magnitude zero point determined from the median offset of a number of reference stars to their USNO B1.0 magnitudes. Since the unfiltered CCD has a peak response similar to an R-band filter, unfiltered magnitudes are calibrated relative to R–band magnitudes to calculate C_R magnitudes (as is done for unfiltered observations with other robotic telescopes, e.g. ROTSE–III (Rykoff et al., 2006a)). Quick–look analysis was carried out using `GAIA`, part of the Starlink Software Collection.[4] `GAIA` is a general purpose image viewer which also acts as a front–end to other Starlink applications, e.g. for source detection and photometry.

8.3 GRB follow–up observations

8.3.1 Observing Strategy

Initially it was anticipated that Watcher would generate multi–colour lightcurves of GRB optical counterparts. The earliest employed GRB observing strategy consisted of a se-

[3] Bill Romanishin's "An Introduction to Astronomical Photometry Using CCDs" was a valuable guide: http://observatory.ou.edu/book2513.html

[4] The Starlink Project was an initiative of the UK astronomical community dedicated to the development of general–purpose data reduction software. Since the project terminated in 2005, the Starlink Software Collection has been supported by the Joint Astronomy Centre: http://starlink.jach.hawaii.edu

quence of 5 and 10 s exposures for the first 5 minutes after the trigger, 30 s exposures up to 10 minutes, 60 s exposures up to 1 hour, and 120 s exposures thereafter, with all 5 filters (B, V, R, I and clear) being used in each time regime. However it was found that for all but the very brightest events this was not a realistic goal. For typical GRB optical transients, this observing strategy resulted in poorly sampled light curves, since images from different filters could not be combined. It was decided to abandon multi–colour photometry and carry out GRB observations exclusively unfiltered. This allows Watcher to collect as many photons as possible and optimises chances of detecting an optical counterpart by combining subsequent images to achieve deeper limits. The present observing strategy comprises 10 s exposures up to 10 minutes after the GRB trigger, 30 exposures up to 1 hour, 60 s exposures up to 2 hours, and 120 with all observations carried out using the clear filter.

8.3.2 GRBs Observed

Of the 224 GRBs detected by various missions between April 1 2006 and April 30 2008[5], Watcher carried out follow–up observations of 141. 106 of these bursts were observed within 1 day of the trigger, 27 within 1 hour and 10 within 1 minute. A histogram of times from the GRB trigger to the first Watcher observation for all bursts observed within 1 day of the trigger is shown in Fig. 8.1. Where an optical transient was detected or a useful upper limit could be determined, a notice was distributed to the GRB community through the GCN (see §8.3.3). In many cases, the observations yielded no useful information due to adverse observing conditions, or due to the field being obscured by part of the enclosure.

Response times to GCN alerts are typically ~ 30 s, the fastest response being 12.5 s in the case of GRB 070707. In recent months, Watcher has spent a significant portion of each night pointing at the centre of *Swift's* current field–of–view. A target in the RTS2 database is dynamically updated with the coordinates of the current *Swift* pointing, and its priority is set so that it will be selected by the scheduler if it is observable. The aim of this strategy is to have Watcher pointing in approximately the right direction in order to minimise response times to *Swift* GRBs. In the future, proximity to the current *Swift* pointing will be implemented as a merit function in RTS2's scheduler.

[5] 198 of these were detected by *Swift*, 14 by INTEGRAL, 8 by the IPN and 4 by AGILE. Statistics were obtained from Jochen Greiner's GRB page: http://www.mpe.mpg.de/ jcg/grbgen.html

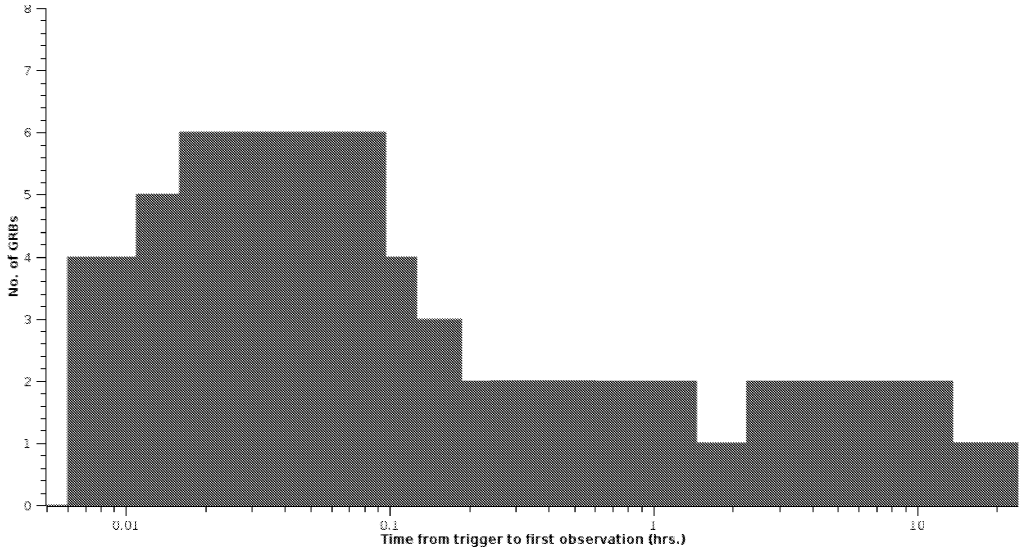

Figure 8.1: Histogram of times from GRB trigger to first Watcher observation for all GRBs observed by Watcher within 1 day of the trigger. The bin size is 0.005 hrs, (18 s). Follow–ups to non–GRB GCN alerts are not included.

8.3.3 GCN Notices

Up to the end of April 2008, GCN notices reporting Watcher observations have been published on 17 GRBs. Detection of an optical transient was reported for 4 of these bursts, in 2 cases while the burst was still active in γ–rays. For the remaining bursts, an upper limit was reported on any optical emission associated with the burst. For GRBs observed within 5 minutes of the trigger, an upper limit was determined for the first individual 10 s exposure (typically ~ 16 mag) and for a subsequent set of ~ 10 combined images (typically ~ 18 mag). Limiting magnitudes were worse in cases where the GRB was observed under adverse conditions, e.g. during twilight or at high airmass. Watcher GRB observations resulting in GCN notices are summarised in Table 8.1.

8.4 GRB 060526

8.4.1 Observations

At 16:28:30 UT on May 26, 2006, the BAT instrument on–board *Swift* detected and localised GRB 060526 at RA 15 h 31 m 23 s, Dec +00 d 14′ 39″ (J2000) (Campana et al., 2006b). The burst was composed of two well separated episodes of emission. The first

GRB	Target ID	ΔGRB	ΔGCN	GCN No.	Comments	T_{90} (s)	F_γ ($\times 10^{-7}$erg cm^{-2})	RA (J2000)	Dec. (J2000)	z	OA
080414[a]	50364	2m50s	33s	7619	upper limit	~10	3	18:08:32.21	-18:49:44.76	-	N
080218b	50333	59s	19s	7316	upper limit	6.2	5.1	11:51:49.77	-53:05:49.6	-	N
070628	50239	36m26s	35m57s	6586	upper limit	39.1	35	07:41:06.2	-20:16:47.1	-	Y
070621	50234	40s	24s	6562	upper limit	33.3	43	21:35:10.14	-24:49:03.1	-	Y
070615[a]	50230	1m22s	45s	6538	upper limit	~30	-	02:57:15.37	-04:24:26.6	-	N
070611	50225	1m18s	41s	6528	OT: 18.5 mag.	12.2	3.91	00:08:01.0	-29:45:21.6	2.04	Y
070610	50224	54s	24s	6500	upper limit	4.6	2.4	19:55:09.6	26:14:06.7	-	Y
070330	50200	6m9s	5m54s	6233	upper limit	9	1.83	17:58:09.8	-63:47:36.1	-	Y
060926	50131	1m1s	47s	5615	upper limit	8	2.19	17:35:43.93	13:02:18.4	3.208	Y
060912b[a]	50121	1m	50s	5566	upper limit	~200	-	18:04:52	-19:52:48	-	N
060904b	50116	1m	48s	5510	OT: 17.1 mag	171.5	16.2	03:52:50.26	-00:43:32.5	0.703	Y
060901[a]	50114	82m	1m17s	5492	upper limit	~20	7	19:08:37.98	-06:38:07.84	-	N
060614	50072	4h19m26s	4h19m8s	5257	OT: 19.0 mag	108.7	204	21:23:32.00	-53:01:39.4	0.125	Y
060607b	50069	3h1m	3h0m46s	5247	upper limit	102.2	25.5	21:58:50.1	-22:29:49.9	3.082	Y
060602b	50064	14m35s	15s	5199	upper limit	9	1.8	17:49:31.6	-28:08:03.2	-	N
060526	50056	36s	20s	5165	OT: 16 mag	298.2	12.6	15:31:18.41	00:17:05.7	3.21	Y
060413	50026	4h12m56s	4h5m45s	4960	upper limit	147.7	35.6	19:25:07.7	13:45:27.3	-	N

Table 8.1: GRBs observed by Watcher. Target ID refers to a unique identifier in the RTS2 database on Watcher. ΔGRB and ΔGCN are the times to the first Watcher observation from the time of the GRB trigger and receipt of the GCN notice respectively. Fluence (F_γ) is given in the energy range 15–150 keV for *Swift* bursts and 20–200 keV for INTEGRAL bursts. Unless otherwise indicated, all GRBs were detected by *Swift*. OA indicates if an optical afterglow was detected by any other instrument. Data are taken from the GRBlog database (Quimby et al., 2004) and the *Swift* GRB table[b].

[a] GRB detected by INTEGRAL

[b] http://swift.gsfc.nasa.gov/docs/swift/archive/grb_table.html

episode consisted of two FRED–like peaks starting at $T_0 - 3$ s and $T_0 + 6$ s respectively, with the second peak ending at $T_0 + 13$ s. The second episode, from $T_0 + 230$ s and $T_0 + 270$ s, was a symmetric pulse peaking at $T_0 + 270$ s. The BAT light curve is shown in Fig. 8.2.

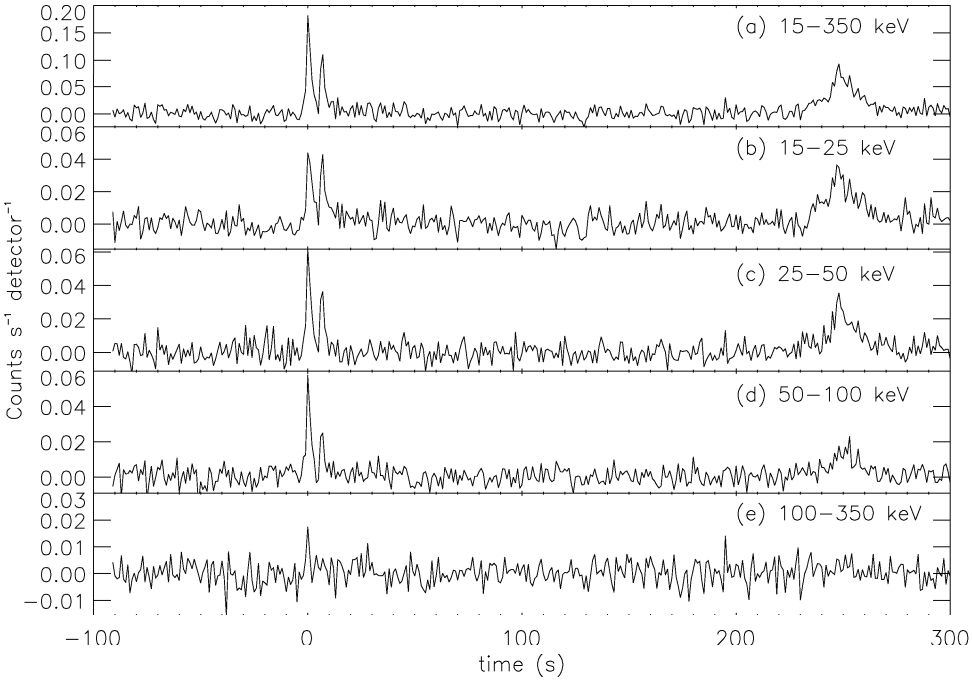

Figure 8.2: Background–subtracted BAT light curve of GRB 060526 in units of counts s^{-1} (fully illuminated detector)$^{-1}$ at 1 s resolution for 5 different energy bands from the top to the bottom: 15–350 keV, 15–25 keV, 25–50 keV, 50–100 keV and 100–350 keV.

Swift's XRT instrument began observing the BAT error box at $T_0 + 73$ s, and an X–ray counterpart was detected at RA 15 h 31 m 18.4 s, DEC +00d 17′ 11.0″ (J2000) (Campana et al., 2006b). The X–ray light curve decayed slowly up to $\sim T_0 + 200$ s, when two major flaring episodes occurred, lasting until $\sim T_0 + 400$ s (Campana et al., 2006d). The first of these flares was coincident with the second peak of the BAT emission. Both of these flares decayed very steeply, with power–law indices of -7.7 ± 0.7 and -8.6 ± 0.2 respectively (Campana et al., 2006d). The X–ray light curve displayed a break to a much flatter decay of -0.7 ± 0.5 at around 600 s, and another break to a much steeper slope of -2.8 ± 0.1 at $1.1 \pm 0.3 \times 10^5$ s (Moretti et al., 2006). The XRT light curve is shown in Fig. 8.3.

On receipt of the GCN notice, Watcher automatically slewed to the location of the BAT error circle, and began imaging the field 36.2 seconds after the Swift trigger (19.6 seconds after receipt of the GCN notice). The field at this time was 13° above the horizon,

at an airmass of 4.4. Watcher was the first ground–based telescope to observe the field of GRB 060526, and the only one to carry out very early observations (the next earliest observations were carried out by ROTSE–IIIc in Namibia, 45 minutes later (Rykoff et al., 2006b)). The first 5 minutes of observations consisted of 5 s and 10 s exposures in BVRI and clear filters. From 5 minutes to 30 minutes, exposures were of 30 s and 60 s duration, switching to 120 s exposures from 30 minutes onwards. No optical counterpart was detected in any of the 5 s exposures down to limiting magnitudes of ~ 14. An uncatalogued source at the position of the XRT error box was marginally detected in a 10 s R–band image beginning at T_0 + 45 s and clearly detected in a 10 s unfiltered exposure beginning at T_0 + 88 s. Quick–look analysis determined a magnitude of ~ 16, calibrated relative to the USNO–B1 catalogue (French and Jelinek, 2006). The source was subsequently detected in later UV, optical and IR observations with a number of instruments, including UVOT (Campana et al., 2006c), and confirmed to be an optical counterpart to GRB 060526 (Rykoff et al., 2006b; Lin et al., 2006; Rumyantsev et al., 2006; Covino et al., 2006a; Cobb, 2006; Terra et al., 2006; Baliyan et al., 2006; Khamitov et al., 2006; Cobb, 2006; Morgan and Dai, 2006; Kann and Hoegner, 2006; Thoene et al., 2006). Spectroscopic observations of the optical afterglow determined a redshift of 3.21 (Berger and Gladders, 2006). Watcher continued to observe the field for the rest of the night and for the next three nights. The afterglow was detected on two subsequent nights by combining a large number of 120 s unfiltered exposures. Watcher images showing the detection of the optical transient are shown in Fig. 8.4. Prompt Watcher data is shown in Fig. 8.5, and the full Watcher light curve is shown in Fig. 8.6.

8.4.2 Modelling

The optical light curve obtained by Watcher displays a number of features: a broad early bump followed by a sharp decay at ~ 400 s; a plateau phase until $\sim 10^4$ s; and a typical afterglow decay. In addition a number of bumps are superimposed on these broad features. Our initial approach in modelling the optical light curve of GRB 060526 was to split it into two components and fit these separately with broken power–law functions. The first component was the early bump and subsequent steep decay ($T < 500$ s), while the second component comprised the plateau phase and the break ($500 < T < 5.4 \times 10^4$ s), while excluding the flare at $T_0 \sim 5.4 \times 10^4$ s. In addition to Watcher data, later data was also included from observations with the MDM 1.3 m and 2.4 m (Dai et al., 2007). The broken

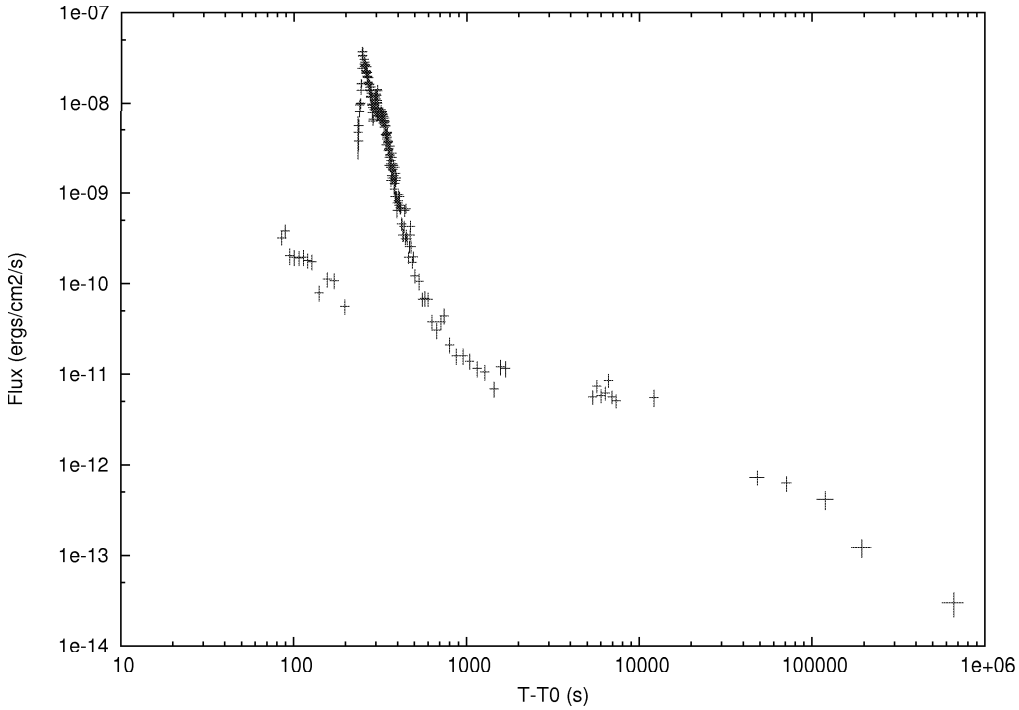

Figure 8.3: XRT light curve of GRB 060526 (0.3 keV – 10 keV)

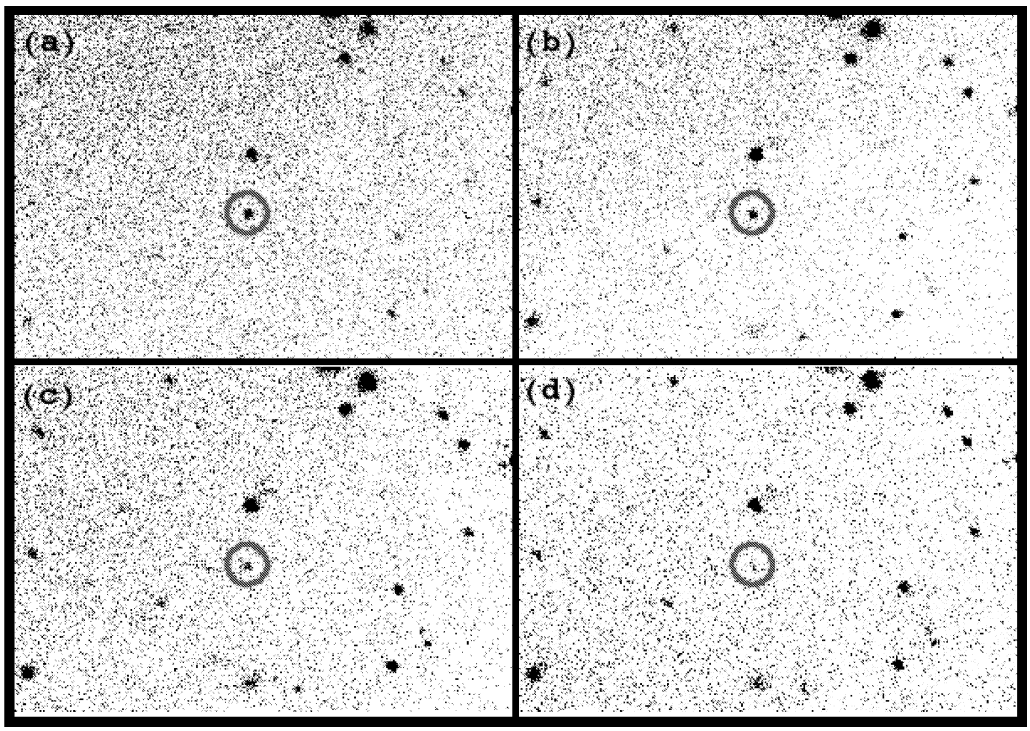

Figure 8.4: Examples of single exposures taken by Watcher showing the decay of the optical afterglow of GRB 060526. (a) is a 60 s exposure starting at T_0 + 6.1 min, while (b), (c) and (d) are 120 s exposures starting at T_0 + 0.6 hrs., T_0 + 3.2 hrs., and T_0 + 5.5 hrs respectively.

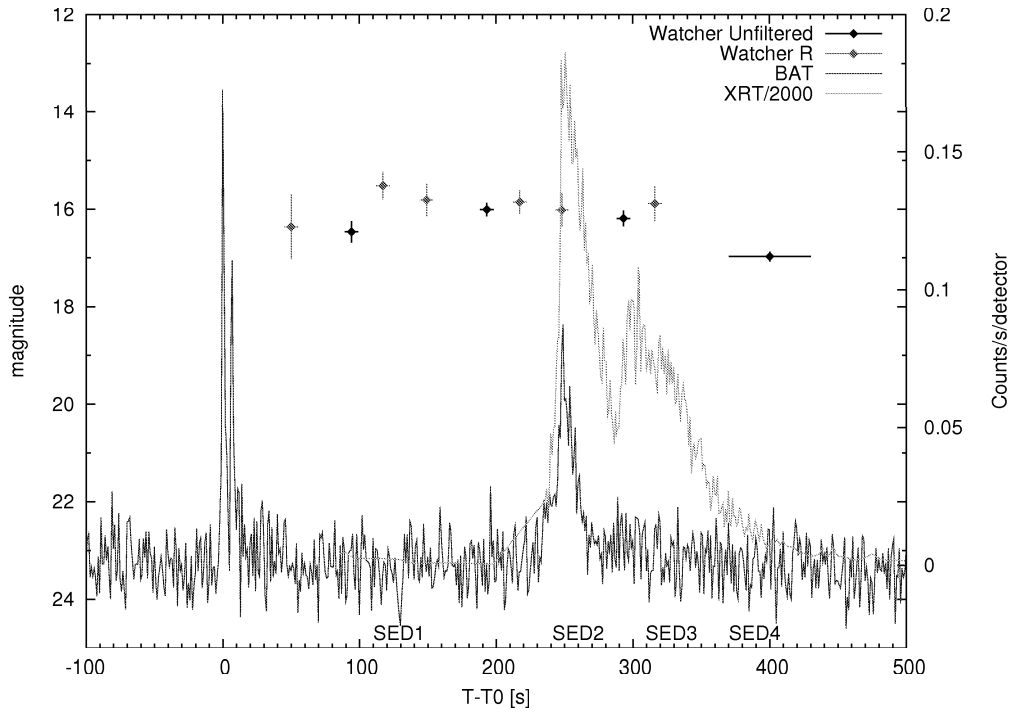

Figure 8.5: Prompt Watcher observations of GRB 060526 (scale on the left), with the BAT and XRT light curves included for comparison (scale on the right). The XRT light curve has been scaled down by a factor of 2000.

power–law functions employed are of the form given by Beuermann et al. (1999):

$$F(t) \propto [(t/t_b)^{\alpha_1 n} + (t/t_b)^{\alpha_2 n}]^{-1/n},$$

where n is a smoothness parameter and α_1 and α_2 are the temporal slopes before and after the break, which occurs at time t_b. The best fit for the early component of the light curve resulted in temporal slopes of $\alpha_1 = 0.47 \pm 0.48$ and $\alpha_2 = -7.8 \pm 4.92$, with the break occuring at $t_b = 398 \pm 60$ s. The reduced χ^2 for the fit was 1.29, with 6 d.o.f. The best fit to the second component of the light curve resulted in decay slopes of -0.28 ± 0.04 before and -1.36 ± 0.03 after the break at 11887 ± 867 s. The reduced χ^2 for the fit was 1.90, with 64 d.o.f. The light curve and the fitted broken power–law functions are shown in Fig. 8.6. The smoothness parameter n was fixed to 0.5 for the first component and 4.8 for the second. A much lower value was used for the first component because the fit was improved by making the break in the power–law function very smooth.

The complex and highly variable light curve of GRB 060526 is similar to that of a number of other GRBs, in particular GRB 021004. A slow decay up to $\sim T_0 + 0.1$ days and numerous bumps are common features to both light curves. GRB 021004 was suc-

cessfully modelled by adding multiple energy injection episodes (de Ugarte Postigo et al., 2005) using the model proposed by Björnsson et al. (2004). This model extends the standard fireball model by assuming that the central engine ejects several discrete shells with different Lorentz factors simultaneously. The fastest moving shell drives the evolution of the afterglow, but as it decelerates, the slower moving shells catch up with the shock front, producing an energy injection. Full details of the model can be found in Jóhannesson et al. (2006).

This model was applied to Watcher data combined with X–ray data and multi–colour photometric data obtained at later times by a number of instruments (Thöene et al., in preparation). The best fit (χ^2/d.o.f. = 2.8) was achieved using a model with a total of six energy injections. The times and energies of the energy injections, in units of E_0, the initial energy injected into the outflow (= 10^{50} erg), are shown in Table 8.2, and the fit to the data is shown in Fig. 8.7. The total energy release in the afterglow is found to be 2.67×10^{51} erg. Further results of the modelling show a high density circumburst medium of $n_0 = 200\,\mathrm{cm}^{-3}$, comparable to the high–z GRB 050904 (Frail et al., 2006), a relatively narrow opening angle of $\theta_0 = 1.2°$, and an electron index of $p = 2.11$. Furthermore, the microphysical parameters representing the fraction of the energy in electrons and the magnetic field respectively are found to be $\epsilon_e = 8 \times 10^{-3}$ and $\epsilon_B = 7 \times 10^{-5}$ (Sari et al., 1998; Jóhannesson et al., 2006). The early bump in the Watcher data is found to be due to the characteristic synchrotron frequency ν_m passing through the optical band at very early times. The cooling break ν_c is found to be between the optical and the X–ray bands up to 6 days after the burst, i.e. the entire data span.

This model reproduces the optical/NIR light curves well, with the high χ^2/d.o.f. = 2.8 resulting from the inability to fit the microvariability of the afterglow. The X–ray light curve is also fitted well until after the last energy injection, when the model predicts a steeper decay than that seen in the data. On the other hand, the last data points in the optical show a steeper decay than the model. The powerful X–ray flare has not been included in the fit, as it is produced by internal shocks and is therefore part of the prompt emission of the GRB.

8.4.3 Discussion

GRB 060526 is one of the few bursts to have been observed at optical wavelengths during the prompt γ–ray emission. A broad early bump is observed in the optical light curve

Time (days)	Energy (in units of E_0)
0.008	0.45
0.015	1.3
0.04	3.6
0.09	3.1
0.40	6.8
0.62	9.4

Table 8.2: Results of energy injection modelling of GRB 060526

which precedes the second episode of BAT emission and the X–ray flares. The timing of this rise with respect to the high energy emission, which is produced by internal shocks resulting from continued central engine activity, suggests that another process is responsible for the optical bump. Applying the energy injection model to the data finds that this bump is due to the characteristic frequency ν_m of the afterglow synchrotron spectrum crossing the optical band. This mechanism was also used by Molinari et al. (2007) to explain the early optical rises seen in GRB 060418 and GRB 060607a, and has also been invoked in interpreting the light curves of GRB 050801 (Rykoff et al., 2006a), GRB 060206 and GRB 060210 (Stanek et al., 2007).

The broken power–law fit to the early component of the light–curve also supports this hypothesis. The best fit was found to have a very smooth break, consistent with the interpretation from the energy injection model. The pre–break slope of $\alpha_1 = 0.47 \pm 0.48$, though not well constrained, is much shallower than was observed in the well–sampled light curves of GRB 060418 and GRB 060607a. This may indicate that the density profile of the ambient medium is consistent with the wind environment proposed by Chevalier and Li (2000), as opposed to the homogneous (ISM) case. For $\nu < \nu_c$ the flux is expected to rise as t^3 for the ISM case, while a wind model predicts a slower rise of $\lesssim 1/3$. The post–break decay of $\alpha_2 = -7.48 \pm 4.92$ is much steeper than the typical decay of ~ -1 expected after the peak of the afterglow. It is consistent, however, with the slope of the X–ray emission at this time, which was displaying a steep decay of -8.6 ± 0.2 from the second X–ray flare. The subsequent slow decay of -0.28 ± 0.04 until $\sim T_0 + 10^4$ s is also inconsistent with a typical afterglow, which is not seen until after the break at $\sim 10^4$ s when the light curve decays with $\alpha = -1.36 \pm 0.03$. The X–ray light curve, though sparsely sampled at this time, also shows a similar decay.

We propose that the normal afterglow phase which would be expected after ν_m has crossed the optical band is masked initially by a contribution from an optical counterpart

to the γ–ray and X–ray flares from $230-400$ s. An excess of emission can be seen over that predicted by the crossing of ν_m through the optical by the energy injection model, which suggests the presence of a contribution from the internal shocks, as does the similarity of the optical and X–ray decay slopes at the end of the X–ray flares. The typical afterglow decay is subsequently masked by a series of energy injections, the first of which occurs at ~ 700 s. In the gap between the energy injection at 0.09 days and 0.4 days, we see the light curve begin a typical afterglow decay, which is further disturbed by two more energy injections.

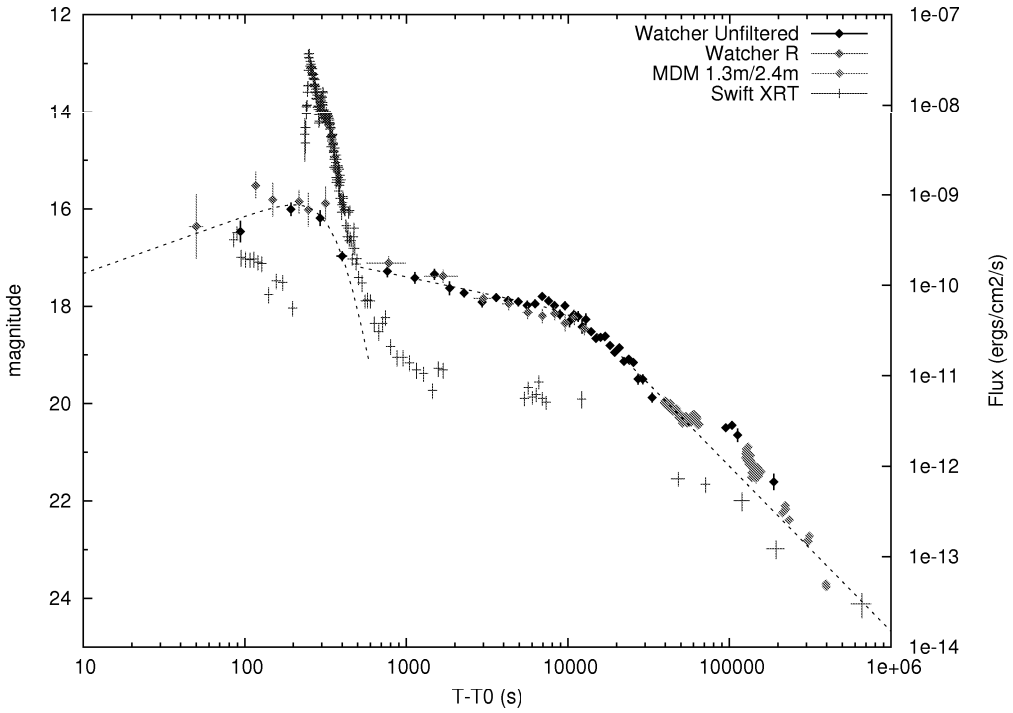

Figure 8.6: The optical light curve of GRB 060526 observed by Watcher (scale on the left). Later data from the MDM 1.3 m and 2.4 m telescopes is also included (Dai et al., 2007). The XRT light curve is also shown (scale on the right). The results of broken power–law fits to the early ($T < T_0 + 500\,\mathrm{s}$) and later ($T_0 + 500\,\mathrm{s} < T < T_0 + 5.4 \times 10^4\,\mathrm{s}$) components are shown by the dashed lines.

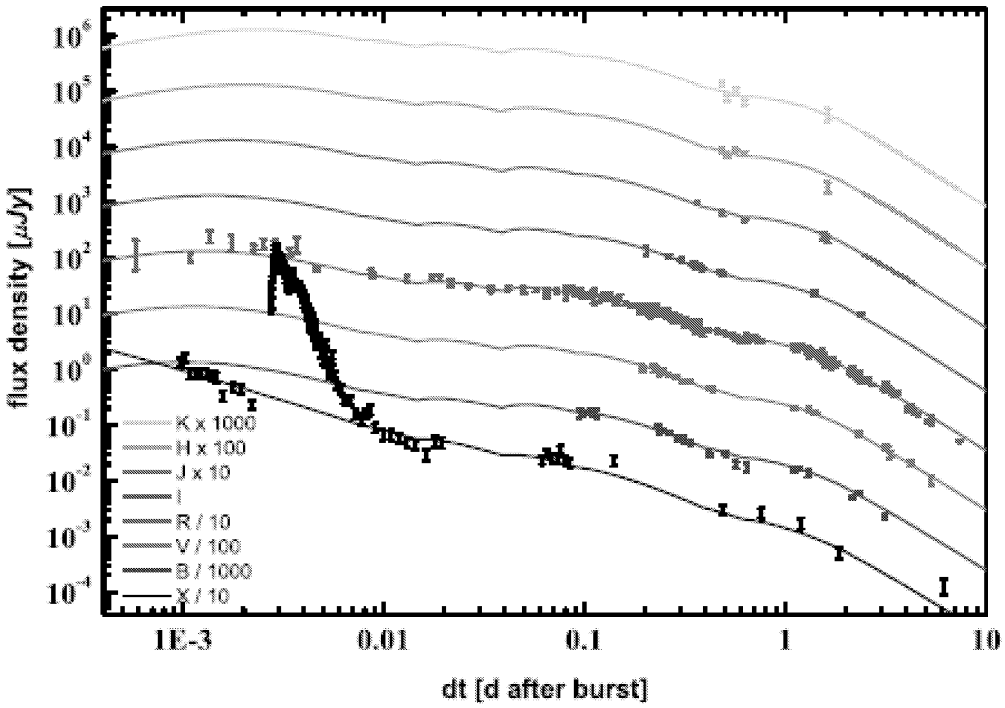

Figure 8.7: The X–ray and optical/NIR (*BVRIJHK2*) light curves of GRB 060526 modelled with energy injections. The X–ray flares have been excluded from the modelling.

T – T0 (hrs)	Filter	Mag.	Error
0.0125141	R	16.36	0.66
0.0247363	clear	16.46	0.22
0.0311251	R	15.52	0.28
0.040014	R	15.81	0.35
0.0522362	clear	16.01	0.14
0.058903	R	15.85	0.24
0.0675139	R	16.02	0.35
0.0800141	clear	16.19	0.16
0.0864029	R	15.89	0.35
0.102792	clear	16.97	0.10
0.156681	R	17.12	0.14
0.203903	clear	17.28	0.12
0.305014	clear	17.42	0.12
0.358903	R	17.39	0.13
0.405847	clear	17.34	0.11
0.506958	clear	17.63	0.14
0.616403	clear	17.73	0.09
0.72057	R	17.84	0.12
0.800847	clear	17.91	0.11
0.985292	clear	17.82	0.09
1.08918	R	17.96	0.14
1.16946	clear	17.88	0.09
1.3539	clear	17.91	0.09
1.45779	R	18.13	0.14
1.53835	clear	17.98	0.10
1.72279	clear	17.95	0.09
1.82668	R	18.20	0.15
1.90696	clear	17.80	0.08
2.09196	clear	17.89	0.09
2.19613	R	18.15	0.14
2.27668	clear	17.99	0.09
2.46085	clear	18.17	0.10
2.56501	R	18.35	0.18
2.64529	clear	17.99	0.09
2.82974	clear	18.31	0.12
2.9339	R	18.24	0.15
3.01418	clear	18.17	0.10
3.19918	clear	18.21	0.11
3.30307	R	18.46	0.14
3.38362	clear	18.42	0.14
3.56807	clear	18.27	0.12
3.73362	clear	18.52	0.04
4.00529	clear	18.66	0.05
4.27696	clear	18.64	0.05
4.58251	clear	18.62	0.05
4.88807	clear	18.81	0.06
5.22751	clear	18.95	0.06
5.60085	clear	18.85	0.04
5.97446	clear	19.13	0.05
6.38168	clear	19.09	0.05
6.82307	clear	19.15	0.06
7.29835	clear	19.50	0.11
7.80751	clear	19.50	0.10
8.92751	clear	19.88	0.10
25.2072	clear	20.50	0.07
27.5839	clear	20.44	0.08
29.9981	clear	20.65	0.14
49.2514	clear	21.61	0.17

Table 8.3: Watcher photometric data of the optical counterpart of GRB 060526.

Chapter 9

Conclusions & Future Work

9.1 Conclusions

We have developed a robotic optical telescope system capable of carrying out rapid follow–up observations of GRBs. The system, called Watcher, was developed on a small budget with limited manpower, and made use of existing commercially available and open–source technology wherever possible. The development of Watcher may provide a useful template for other groups who wish to develop a low–budget robotic telescope capable of high–quality science.

The system has been operating fully robotically since May 2006, and routinely carries out early observations of GRB error boxes on timescales of tens of seconds to minutes. The system has detected 4 optical transients, two of which were observed while the GRB was still active in γ–rays, and has determined early upper limits to optical emission for a number of other GRBs. The highlight of Watcher's observations has been the detection of prompt optical emission from GRB 060526. The light curve of this burst is complex and displays a number of features, including possible signatures of energy injections and optical emission from internal shocks.

Watcher utilises the open–source robotic observatory management software RTS2. The Watcher development process involved writing new code and integrating it into RTS2, thereby expanding the range of hardware supported by the package. An increasing number of groups are now making use of this powerful open–source solution.

9.2 Future Work

9.2.1 Watcher

Automated Data Pipeline The obvious next step in the progression of the Watcher system is the development of an automated data reduction and analysis pipeline. This is currently the main area of human involvement in the system's routine operations and is well suited to automation. Part of this process is already automated: object frames are sent to a processing queue as soon as they are taken, and an astrometric fit is performed on them using the `past` program, part of the `JIBARO` package (de Ugarte Postigo et al., 2005), which utilises `SExtractor` (Bertin and Arnouts, 1996). Astrometric data is then stored in the database as image metadata, and positional corrections, if necessary, are fed back to the mount control program. An automated pipeline for Watcher is already in the advanced stages of development. The reduction aspects are largely completed, and current work is focused on automated analysis capable of accurate photometry and the detection of candidate optical transients, or determining upper limits in the event of non–detections. The reduction scripts assemble the appropriate calibration frames, check their quality, and create master calibration frames. Object frames are then reduced using these calibration frames and passed to an automated analysis pipeline.

Non-GRB Science Watcher has already carried out observations as part of science programs unrelated to GRBs. One of the areas in which Watcher has been active is in blazar monitoring. Combining optical data with radio and high energy observations can contribute to the understanding of the continuum emission of blazars. This emission, which is observed to be extremely intense and to vary rapidly, is thought to originate in a relativistic plasma jet which is accelerated by a billion solar mass black hole. Watcher has also been involved in the monitoring of cataclysmic variables (CVs), in conjunction with Simon Jeffery of Armagh Observatory. CVs are close binaries in which a low–mass companion (a star of late spectral type) transfers material onto a compact object, which may be a white dwarf, neutron star, or black hole. Violent outbursts are often observed in these systems. Multi–wavelength observations can contribute to the understanding of the underlying processes. It is intended to expand Watcher's involvement in such monitoring campaigns in the future. Another way in which Watcher's productivity could be maximised is by becoming part of a network of robotic telescopes. The VOEventNet project

(§4.4) in particular could allow Watcher to carry out rapid follow–up observations of other transient sources such as supernovae and microlensing events.

Education and Outreach A small robotic telescope can provide a valuable practical element to undergraduate astronomy studies (Percy, 2003). The UCD School of Physics has recently established an undergraduate degree programme in Physics with Astronomy and Space Science. The course has a substantial emphasis on hands–on experience in astronomical techniques, which will include planning observations with Watcher and analysing the resulting data. It is also intended that Watcher will contribute to the very active and expanding outreach program at Boyden Observatory.

9.2.2 Further Development of RTS2

Development of RTS2 is ongoing, with additional features and support for new devices being added regularly. One key improvement which is plannned is the addition of a merit function in the scheduler which will favour targets that are in the vicinity of the current *Swift* pointing, thereby improving follow–up times to GRB alerts generated by *Swift*. Much of the present development work is focused on the development of a web–based GUI for managing observations in order to improve the system's user–friendliness. An increasing number of groups (6 at present) are planning to develop robotic telescope systems based on RTS2, and plans are being made to host a workshop in UCD in order to enhance cooperation within this community and to streamline future development efforts.

9.2.3 Future GRB Missions

9.2.3.1 GLAST

The next generation space-based gamma-ray astrophysics mission is the Gamma-ray Large Area Space Telescope (*GLAST*, de Angelis, 2001, Fig. 9.1), due for launch into low earth orbit in June 2008 for a planned operational lifetime of 5 – 10 years. *GLAST* will consist of two instruments, the Large Area Space Telescope (LAT) and Glast Burst Monitor (GBM). LAT will detect γ–rays in the $\sim 20\,\mathrm{MeV} - 30\,\mathrm{GeV}$ range by tracking e^+ e^- pairs using silicon strip detectors. LAT is expected to make improvements over EGRET and Agile due to its larger effective area and lower dead time. Since the peak energy of GRBs is lognormally distributed about a value of 250 keV (Preece et al., 2000), which is well

below the energy range of LAT, the second GRB instrument (GBM) has been included in the payload. The goal of GBM is to extend the energy range of *GLAST* down to $\sim 10\,\mathrm{keV}$. The GBM consists of 12 NaI detectors oriented such that any burst within 120° of the viewing access will illuminate at least 3 detectors. This is similar to the BATSE LAD principle and it will enable computation of on–board locations for GRBs that are out of the field of view of LAT allowing repointing of LAT to observe any delayed high–energy emission. Prompt high–energy emission may also be detected in the case of a short slew to a long duration burst.

GBM is expected to detect ~ 200 bursts per year, more than 60 of which should be within the field of view of the LAT detector. Positions will be determined and sent to the GCN for distribution within $\sim 10\,\mathrm{s}$. Initial GBM error boxes will be $< 15°$and subsequently refined to $< 5°$after ground analysis. The size of LAT error boxes will typically be $\gtrsim 10'$.

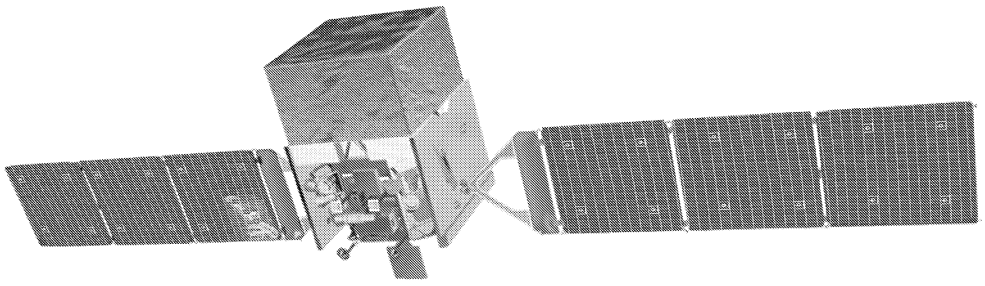

Figure 9.1: The Gamma–ray Large Area Space Telescope (*GLAST*). *Credit: NASA/-Sonoma State University/Aurore Simonnet.*

Bibliography

Akerlof, C., Balsano, R., Barthelmy, S., Bloch, J., Butterworth, P., Casperson, D., Cline, T., Fletcher, S., Frontera, F., Gisler, G., Heise, J., Hills, J., Hurley, K., Kehoe, R., Lee, B., Marshall, S., McKay, T., Pawl, A., Piro, L., Szymanski, J., and Wren, J.: 2000, *Astrophys. J., Lett.* **532**, L25

Akerlof, C., Balsano, R., Barthelmy, S., Bloch, J., Butterworth, P., Casperson, D., Cline, T., Fletcher, S., Frontera, F., Gisler, G., Heise, J., Hills, J., Kehoe, R., Lee, B., Marshall, S., McKay, T., Miller, R., Piro, L., Priedhorsky, W., Szymanski, J., and Wren, J.: 1999, *Nature* **398**, 400

Akerlof, C. W., Kehoe, R. L., McKay, T. A., Rykoff, E. S., Smith, D. A., Casperson, D. E., McGowan, K. E., Vestrand, W. T., Wozniak, P. R., Wren, J. A., Ashley, M. C. B., Phillips, M. A., Marshall, S. L., Epps, H. W., and Schier, J. A.: 2003, *Publ. Astron. Soc. Pac.* **115**, 132

Allan, A., Naylor, T., Steele, I. A., Jenness, T., Cavanagh, B., Economou, F., Saunders, E., Adamson, A., Etherton, J., and Mottram, C.: 2004, in H. Lewis and G. Raffi (eds.), *Advanced Software, Control, and Communication Systems for Astronomy*, Vol. 5496 of *Presented at the Society of Photo-Optical Instrumentation Engineers (SPIE) Conference*, pp 313–322

Aloy, M. A., Müller, E., Ibáñez, J. M., Martí, J. M., and MacFadyen, A.: 2000, *Astrophys. J., Lett.* **531**, L119

Amati, L.: 2006, *ArXiv: astro-ph/0611189*

Amati, L., Frontera, F., Tavani, M., in't Zand, J. J. M., Antonelli, A., Costa, E., Feroci, M., Guidorzi, C., Heise, J., Masetti, N., Montanari, E., Nicastro, L., Palazzi, E., Pian, E., Piro, L., and Soffitta, P.: 2002, *Astron. Astrophys.* **390**, 81

Amati, L., Frontera, F., Vietri, M., in't Zand, J. J. M., Soffitta, P., Costa, E., Del Sordo, S., Pian, E., Piro, L., Antonelli, L. A., Fiume, D. D., Feroci, M., Gandolfi, G., Guidorzi, C., Heise, J., Kuulkers, E., Masetti, N., Montanari, E., Nicastro, L., Orlandini, M., and Palazzi, E.: 2000, *Science* **290**, 953

Andersen, M. I. and Pedersen, H.: 2004, *Astronomische Nachrichten* **325**, 490

Atkins, R., Benbow, W., Berley, D., Chen, M. L., Coyne, D. G., Dingus, B. L., Dorfan, D. E., Ellsworth, R. W., Evans, D., Falcone, A., Fleysher, L., Fleysher, R., Gisler, G., Goodman, J. A., Haines, T. J., Hoffman, C. M., Hugenberger, S., Kelley, L. A., Leonor, I., McConnell, M., McCullough, J. F., McEnery, J. E., Miller, R. S., Mincer, A. I., Morales, M. F., Nemethy, P., Ryan, J. M., Shen, B., Shoup, A., Sinnis, C., Smith, A. J., Sullivan, G. W., Tumer, T., Wang, K., Wascko, M. O., Westerhoff, S., Williams, D. A., Yang, T., and Yodh, G. B.: 2000, *Astrophys. J., Lett.* **533**, L119

Atteia, J.-L., Boer, M., Cotin, F., Couteret, J., Dezalay, J.-P., Ehanno, M., Evrard, J., Lagrange, D., Niel, M., Olive, J.-F., Rouaix, G., Souleille, P., Vedrenne, G., Hurley, K., Ricker, G., Vanderspek, R., Crew, G., Doty, J., and Butler, N.: 2003, in G. R. Ricker and R. K. Vanderspek (eds.), *Gamma-Ray Burst and Afterglow Astronomy 2001: A Workshop Celebrating the First Year of the HETE Mission*, Vol. 662 of *American Institute of Physics Conference Series*, pp 17–24

Böttcher, M.: 2000, *Astrophys. J.* **539**, 102

Bailyn, C., van Dokkum, P., Buxton, M., Cobb, B., and Bloom, J. S.: 2003, *GRB Coordinates Network* 2486

Baliyan, K. S., Ganesh, S., Vats, H. O., and Jain, J. K.: 2006, *GRB Coordinates Network* 5185

Band, D., Matteson, J., Ford, L., Schaefer, B., Palmer, D., Teegarden, B., Cline, T., Briggs, M., Paciesas, W., Pendleton, G., Fishman, G., Kouveliotou, C., Meegan, C., Wilson, R., and Lestrade, P.: 1993, *Astrophys. J.* **413**, 281

Barbier, L., Barthelmy, S., Cummings, J., Fenimore, E., Gehrels, N., Hullinger, D., Krimm, H., Markwardt, C., Norris, J., Nousek, J., Palmer, D., Parsons, A., Sakamoto, T., Sato, G., Suzuki, M., and Tueller, J.: 2005, *GRB Coordinates Network* 3162

Barraud, C., Olive, J.-F., Lestrade, J. P., Atteia, J.-L., Hurley, K., Ricker, G., Lamb, D. Q., Kawai, N., Boer, M., Dezalay, J.-P., Pizzichini, G., Vanderspek, R., Crew, G., Doty, J., Monnelly, G., Villasenor, J., Butler, N., Levine, A., Yoshida, A., Shirasaki, Y., Sakamoto, T., Tamagawa, T., Torii, K., Matsuoka, M., Fenimore, E. E., Galassi, M., Tavenner, T., Donaghy, T. Q., Graziani, C., and Jernigan, J. G.: 2003, *Astron. Astrophys.* **400**, 1021

Barthelmy, S., Barbier, L., Cummings, J., Fenimore, E., Gehrels, N., Hullinger, D., Krimm, H., Koss, M., Markwardt, C., Palmer, D., Parsons, A., Sakamoto, T., Sato, G., Stamatikos, M., and Tueller, J.: 2006, *GRB Coordinates Network* 5256

Barthelmy, S., Burrows, D., Cummings, J., Fenimore, E., Gehrels, N., Goad, M., Hullinger, D., Krimm, H., Markwardt, C., Marshall, F., McLean, K., Nousek, J., Osborne, J., Palmer, D., Parsons, A., Sato, G., Suzuki, M., Tagliaferri, G., and Tueller, J.: 2004, *GRB Coordinates Network* 2874

Barthelmy, S. D., Barbier, L. M., Cummings, J. R., Fenimore, E. E., Gehrels, N., Hullinger, D., Krimm, H. A., Markwardt, C. B., Palmer, D. M., Parsons, A., Sato, G., Suzuki, M., Takahashi, T., Tashiro, M., and Tueller, J.: 2005a, *Space Science Reviews* **120**, 143

Barthelmy, S. D., Butterworth, P., Cline, T. L., and Gehrels, N.: 1998, in *Bulletin of the American Astronomical Society*, Vol. 30 of *Bulletin of the American Astronomical Society*, pp 875–+

Barthelmy, S. D., Butterworth, P., Cline, T. L., Gehrels, N., Fishman, G. J., Kouveliotou, C., and Meegan, C. A.: 1995, *Astrophys. Space. Sci.* **231**, 235

Barthelmy, S. D., Chincarini, G., Burrows, D. N., Gehrels, N., Covino, S., Moretti, A., Romano, P., O'Brien, P. T., Sarazin, C. L., Kouveliotou, C., Goad, M., Vaughan, S., Tagliaferri, G., Zhang, B., Antonelli, L. A., Campana, S., Cummings, J. R., D'Avanzo, P., Davies, M. B., Giommi, P., Grupe, D., Kaneko, Y., Kennea, J. A., King, A., Kobayashi, S., Melandri, A., Mészáros, P., Nousek, J. A., Patel, S., Sakamoto, T., and Wijers, R. A. M. J.: 2005b, *Nature* **438**, 994

Barthelmy, S. D., Palmer, D. M., and Schaefer, B. E.: 1994, in G. J. Fishman (ed.), *Gamma-Ray Bursts*, Vol. 307 of *American Institute of Physics Conference Series*, pp 392–+

Baruch, J. E. F.: 1995, in M. F. Bode (ed.), *Robotic Observatories*, Wiley - Praxis Series in Astronomy and Astrophysics, pp 3–9, John Wiley & Sons, ISBN 0-471-95690-2

Belczynski, K., Bulik, T., and Kalogera, V.: 2002, *Astrophys. J., Lett.* **571**, L147

Beloborodov, A. M.: 2000, *Astrophys. J., Lett.* **539**, L25

Berger, E. and Gladders, M.: 2006, *GRB Coordinates Network* 5170

Berger, E., Kulkarni, S. R., and Frail, D. A.: 2002, *GRB Coordinates Network* 1612

Berger, E., Price, P. A., Cenko, S. B., Gal-Yam, A., Soderberg, A. M., Kasliwal, M., Leonard, D. C., Cameron, P. B., Frail, D. A., Kulkarni, S. R., Murphy, D. C., Krzeminski, W., Piran, T., Lee, B. L., Roth, K. C., Moon, D.-S., Fox, D. B., Harrison, F. A., Persson, S. E., Schmidt, B. P., Penprase, B. E., Rich, J., Peterson, B. A., and Cowie, L. L.: 2005, *Nature* **438**, 988

Bertin, E. and Arnouts, S.: 1996, *Astron. Astrophys. Suppl. Ser.* **117**, 393

Bessell, M. S.: 1995, *CCD Astronomy* **2**, 20

Bethe, H. A. and Brown, G. E.: 1998, *Astrophys. J.* **506**, 780

Beuermann, K., Hessman, F. V., Reinsch, K., Nicklas, H., Vreeswijk, P. M., Galama, T. J., Rol, E., van Paradijs, J., Kouveliotou, C., Frontera, F., Masetti, N., Palazzi, E., and Pian, E.: 1999, *Astron. Astrophys.* **352**, L26

Björnsson, G., Gudmundsson, E. H., and Jóhannesson, G.: 2004, *Astrophys. J., Lett.* **615**, L77

Blain, A. W. and Natarajan, P.: 2000, *Mon. Not. R. Astron. Soc.* **312**, L35

Blake, C. H., Bloom, J. S., Starr, D. L., Falco, E. E., Skrutskie, M., Fenimore, E. E., Duchêne, G., Szentgyorgyi, A., Hornstein, S., Prochaska, J. X., McCabe, C., Ghez, A., Konopacky, Q., Stapelfeldt, K., Hurley, K., Campbell, R., Kassis, M., Chaffee, F., Gehrels, N., Barthelmy, S., Cummings, J. R., Hullinger, D., Krimm, H. A., Markwardt, C. B., Palmer, D., Parsons, A., McLean, K., and Tueller, J.: 2005, *Nature* **435**, 181

Blandford, R. D. and McKee, C. F.: 1976, *Physics of Fluids* **19**, 1130

Blandford, R. D. and Znajek, R. L.: 1977, *Mon. Not. R. Astron. Soc.* **179**, 433

Blinnikov, S. I., Novikov, I. D., Perevodchikova, T. V., and Polnarev, A. G.: 1984, *Soviet Astronomy Letters* **10**, 177

Bloom, J. S., Djorgovski, S. G., Kulkarni, S. R., and Frail, D. A.: 1998, *Astrophys. J., Lett.* **507**, L25

Bloom, J. S., Frail, D. A., and Kulkarni, S. R.: 2003, *Astrophys. J.* **594**, 674

Bloom, J. S. and Kulkarni, S. R.: 1998, *GRB Coordinates Network* 161

Bloom, J. S., Kulkarni, S. R., and Djorgovski, S. G.: 2002, *aj* **123**, 1111

Bloom, J. S., Sigurdsson, S., and Pols, O. R.: 1999, *Mon. Not. R. Astron. Soc.* **305**, 763

Bode, M. F. (ed.): 1995, *Robotic Observatories*, Wiley - Praxis Series in Astronomy and Astrophysics, John Wiley & Sons, ISBN 0-471-95690-2

Boella, G., Butler, R. C., Perola, G. C., Piro, L., Scarsi, L., and Bleeker, J. A. M.: 1997, *Astron. Astrophys. Suppl. Ser.* **122**, 299

Boër, M., Atteia, J. L., Damerdji, Y., Gendre, B., Klotz, A., and Stratta, G.: 2006, *Astrophys. J., Lett.* **638**, L71

Boër, M., Greiner, J., Kahabka, P., Motch, C., and Voges, W.: 1994a, in G. J. Fishman (ed.), *Gamma-Ray Bursts*, Vol. 307 of *American Institute of Physics Conference Series*, pp 453–+

Boër, M., Greiner, J., Kahabka, P., Motch, C., Voges, W., Sommer, M., Hurley, K., Niel, M., Laros, J., Klebesadel, R., Kouveliotou, C., Fishman, G., and Cline, T.: 1994b, in G. J. Fishman (ed.), *Gamma-Ray Bursts*, Vol. 307 of *American Institute of Physics Conference Series*, pp 458–+

Boer, M., Klotz, A., Atteia, J.-L., Buchholtz, G., Daigne, F., Eysseric, J., Goldoni, P., Jean, P., Lecavelier Des Etangs, A., Lopez, M., Malina, R., Marcowith, A., Marquette, J. B., Mayet, A., Mirabel, F., Mochkovitch, R., Pacheco, J., Pares, L., Paul, J., Pedersen, H., Pinna, H., and Sivan, J.-P.: 2003, *The Messenger* **113**, 45

Boër, M., Pederson, H., Smette, A., Fishman, J., Kouveliotou, C., and Hurley, K.: 1994c, in G. J. Fishman (ed.), *Gamma-Ray Bursts*, Vol. 307 of *American Institute of Physics Conference Series*, pp 396–+

Bond, H. E.: 1997, *IAU Circ.* **6654**, 2

Boxdörfer, S.: 2003, *Dynostar X3 Version 3.00d*, Boxdöerfer Elektronik, http://www.boxdoerfer.de/man310be.pdf

Brandt, N. and Podsiadlowski, P.: 1995, *Mon. Not. R. Astron. Soc.* **274**, 461

Briggs, M. S., Band, D. L., Kippen, R. M., Preece, R. D., Kouveliotou, C., van Paradijs, J., Share, G. H., Murphy, R. J., Matz, S. M., Connors, A., Winkler, C., McConnell, M. L., Ryan, J. M., Williams, O. R., Young, C. A., Dingus, B., Catelli, J. R., and Wijers, R. A. M. J.: 1999, *Astrophys. J.* **524**, 82

Bromm, V. and Loeb, A.: 2006, in S. S. Holt, N. Gehrels, and J. A. Nousek (eds.), *Gamma-Ray Bursts in the Swift Era*, Vol. 836 of *American Institute of Physics Conference Series*, pp 503–512

Bromm, V. and Loeb, A.: 2007, *ArXiv:astro-ph/0706.2445*

Burrows, D. N., Falcone, A., Chincarini, G., Morris, D., Romano, P., Hill, J. E., Godet, O., Moretti, A., Krimm, H., Osborne, J. P., Racusin, J., Mangano, V., Page, K., Perri, M., and Stroh, M.: 2007, *ArXiv:astro-ph/0701046*

Burrows, D. N., Hill, J. E., Nousek, J. A., Kennea, J. A., Wells, A., Osborne, J. P., Abbey, A. F., Beardmore, A., Mukerjee, K., Short, A. D. T., Chincarini, G., Campana, S., Citterio, O., Moretti, A., Pagani, C., Tagliaferri, G., Giommi, P., Capalbi, M., Tamburelli, F., Angelini, L., Cusumano, G., Bräuninger, H. W., Burkert, W., and Hartner, G. D.: 2005a, *Space Science Reviews* **120**, 165

Burrows, D. N., Romano, P., Falcone, A., Kobayashi, S., Zhang, B., Moretti, A., O'Brien, P. T., Goad, M. R., Campana, S., Page, K. L., Angelini, L., Barthelmy, S., Beardmore, A. P., Capalbi, M., Chincarini, G., Cummings, J., Cusumano, G., Fox, D., Giommi, P., Hill, J. E., Kennea, J. A., Krimm, H., Mangano, V., Marshall, F., Mészáros, P., Morris, D. C., Nousek, J. A., Osborne, J. P., Pagani, C., Perri, M., Tagliaferri, G., Wells, A. A., Woosley, S., and Gehrels, N.: 2005b, *Science* **309**, 1833

Campana, S., Barthelmy, S., Gehrels, N., Gronwall, C., Krimm, H., Markwardt, C., Page, K., Palmer, D., and Perri, M.: 2006a, *GRB Coordinates Network* 4533

Campana, S., Barthelmy, S. D., Boyd, P. T., Brown, P. J., Burrows, D. N., Cummings, J. R., Guidorzi, C. G., Holland, S. T., Kennea, J. A., Markwardt, C. B., Marshall, F. E., Moretti, A., Page, K. L., Stamatikos, M., Tagliaferri, G., and vanden Berk, D. E.: 2006b, *GRB Coordinates Network* 5162

Campana, S., Barthelmy, S. D., Burrows, D. N., Gehrels, N., Guidorzi, C., Kennea, J. A., Marshall, F. E., McLean, K. M., Moretti, A., Stamatikos, M., Tagliaferri, G., and Berk, D. E. V.: 2006c, *GRB Coordinates Network* 5163

Campana, S., Moretti, A., Guidorzi, C., Chincarini, G., and Burrows, D. N.: 2006d, *GRB Coordinates Network* 5168

Castro-Tirado, A. J., Brandt, S., Lund, N., and Guziy, S. S.: 1994, in G. J. Fishman (ed.), *Gamma-Ray Bursts*, Vol. 307 of *American Institute of Physics Conference Series*, pp 404–+

Castro-Tirado, A. J., Cunniffe, R., de Ugarte Postigo, A., Jelínek, M., Vitek, S., Kubánek, P., Gorosabel, J., Castillo Carrión, S., Mateo Sanguino, T. J., Riva, A., Conconi, P., di Caprio, V., Zerbi, F., Amado, P., Cárdenas, C., Claret, A., Guziy, S., Martín-Ruiz, S., Sánchez, M. A., García Teodoro, P., Castro Cerón, J. M., Díaz Verdejo, J., Hudec, R., López Soler, J. M., Berná Galiano, J. Á., Casares, J., Fabregat, J., Páta, P., Sánchez Fernández, C., Sabau-Graziati, M. D., Trigo-Rodríguez, J. M., and Vitali, F.: 2006, in L. M. Stepp (ed.), *Ground-based and Airborne Telescopes, pp. 62670I*, Vol. 6267 of *Presented at the Society of Photo-Optical Instrumentation Engineers (SPIE) Conference*

Castro-Tirado, A. J., Jelínek, M., Mateo Sanguino, T. J., de Ugarte Postigo, A., and the BOOTES team: 2004, *Astronomische Nachrichten* **325**, 679

Castro-Tirado, A. J., Zapatero-Osorio, M. R., Gorosabel, J., Greiner, J., Heidt, J., Herranz, D., Kemp, S. N., Martínez-González, E., Oscoz, A., Ortega, V., Röser, H.-J., Wolf, C., Pedersen, H., Jaunsen, A. O., Korhonen, H., Ilyin, I., Duemmler, R., Andersen, M. I., Hjorth, J., Henden, A. A., Vrba, F. J., Fried, J. W., Frontera, F., and Nicastro, L.: 1999, *Astrophys. J., Lett.* **511**, L85

Chen, W. P., Lemme, C., and Paczynski, B. (eds.): 2001, *Small Telescope Astronomy on Global Scales*, Vol. 246 of *Astronomical Society of the Pacific Conference Series*

Chevalier, R. A. and Li, Z.-Y.: 1999, *Astrophys. J., Lett.* **520**, L29

Chevalier, R. A. and Li, Z.-Y.: 2000, *Astrophys. J.* **536**, 195

Ciardi, B. and Loeb, A.: 2000, *Astrophys. J.* **540**, 687

Clark, J. P. A., van den Heuvel, E. P. J., and Sutantyo, W.: 1979, *Astron. Astrophys.* **72**, 120

Cobb, B. E.: 2006, *GRB Coordinates Network* 5180

Colgate, S. A.: 1968, *Canadian Journal of Physics. Proceedings of the 10th International Conference on Cosmic Rays* **46**, 476

Conselice, C. J., Vreeswijk, P. M., Fruchter, A. S., Levan, A., Kouveliotou, C., Fynbo, J. P. U., Gorosabel, J., Tanvir, N. R., and Thorsett, S. E.: 2005, *Astrophys. J.* **633**, 29

Costa, E., Frontera, F., Heise, J., Feroci, M., in 't Zand, J., Fiore, F., Cinti, M. N., dal Fiume, D., Nicastro, L., Orlandini, M., Palazzi, E., Rapisarda, M., Zavattini, G., Jager, R., Parmar, A., Owens, A., Molendi, S., Cusumano, G., Maccarone, M. C., Giarrusso, S., Coletta, A., Antonelli, L. A., Giommi, P., Muller, J. M., Piro, L., and Butler, R. C.: 1997, *Nature* **387**, 783

Covino, S., Israel, G. L., Ghinassi, F., and Pinilla, N.: 2006a, *GRB Coordinates Network* 5167

Covino, S., Malesani, D., Tagliaferri, G., Vergani, S. D., Chincarini, G., Kann, D. A., Moretti, A., and Stella, L.: 2006b, *ArXiv:astro-ph/0612643*

Crew, G., Villasenor, J., Vanderspek, R., Doty, J., Monnelly, G., Butler, N., Cline, T., Jernigan, J. G., Levine, A., Martel, F., Morgan, E., Prigozhin, G., Azzibrouck, G., Braga, J., Manchanda, R., Pizzichini, G., Ricker, G., Atteia, J., Kawai, N., Lamb, D., Woosley, S., Shirasaki, Y., Graziani, C., Matsuoka, M., Tamagawa, T., Torii, K., Sakamoto, T., Yoshida, A., Fenimore, E., Galassi, M., Tavenner, T., Donaghy, T., Nakagawa, Y., Takahashi, D., Suzuki, M., Satoh, R., Urata, Y., Boer, M., Olive, J., Dezalay, J., Barraud, C., and Hurley, K.: 2002, *GRB Coordinates Network* 1734

Cummings, J., Barbier, L., Barthelmy, S., Hullinger, D., Fenimore, E., Gehrels, N., Krimm, H., Markwardt, C., Palmer, D., Parsons, A., Sakamoto, T., Sato, G., and Tueller, J.: 2005, *GRB Coordinates Network* 3858

Curran, P. A., van der Horst, A. J., and Wijers, R. A. M. J.: 2008, *Mon. Not. R. Astron. Soc.* pp 315–+

Dai, X., Halpern, J. P., Morgan, N. D., Armstrong, E., Mirabal, N., Haislip, J. B., Reichart, D. E., and Stanek, K. Z.: 2007, *Astrophys. J.* **658**, 509

Dai, Z. G. and Cheng, K. S.: 2001, *Astrophys. J., Lett.* **558**, L109

Dar, A. and de Rújula, A.: 2004, *Phys. Rep.* **405**, 203

de Angelis, A.: 2001, in A. M. Mourao, M. Pimenta, P. M. Sa, and J. M. Velhinho (eds.), *New worlds in astroparticle physics*, p. 140

de Pasquale, M., Piro, L., Gendre, B., Amati, L., Antonelli, L. A., Costa, E., Feroci, M., Frontera, F., Nicastro, L., Soffitta, P., and in't Zand, J.: 2006, *Astron. Astrophys.* **455**, 813

de Ugarte Postigo et al.: 2005, in A. J. Castro-Tirado, B. de la Morena, and J. Torresi (eds.), *Astrofísica Robótica en España*, pp 35–50, Ed. Sirius, Madrid

de Ugarte Postigo, A., Castro-Tirado, A. J., Gorosabel, J., Jóhannesson, G., Björnsson, G., Gudmundsson, E. H., Bremer, M., Pak, S., Tanvir, N., Castro Cerón, J. M., Guzyi, S., Jelínek, M., Klose, S., Pérez-Ramírez, D., Aceituno, J., Campo Bagatín, A., Covino, S., Cardiel, N., Fathkullin, T., Henden, A. A., Huferath, S., Kurata, Y., Malesani, D., Mannucci, F., Ruiz-Lapuente, P., Sokolov, V., Thiele, U., Wisotzki, L., Antonelli, L. A., Bartolini, C., Boattini, A., Guarnieri, A., Piccioni, A., Pizzichini, G., del Principe, M., di Paola, A., Fugazza, D., Ghisellini, G., Hunt, L., Konstantinova, T., Masetti, N., Palazzi, E., Pian, E., Stefanon, M., Testa, V., and Tristram, P. J.: 2005, *Astron. Astrophys.* **443**, 841

Della Valle, M.: 2005, *Nuovo Cimento C Geophysics Space Physics C* **28**, 563

Della Valle, M., Chincarini, G., Panagia, N., Tagliaferri, G., Malesani, D., Testa, V., Fugazza, D., Campana, S., Covino, S., Mangano, V., Antonelli, L. A., D'Avanzo, P.,

Hurley, K., Mirabel, I. F., Pellizza, L. J., Piranomonte, S., and Stella, L.: 2006a, *Nature* **444**, 1050

Della Valle, M., Malesani, D., Benetti, S., Testa, V., Hamuy, M., Antonelli, L. A., Chincarini, G., Cocozza, G., Covino, S., D'Avanzo, P., Fugazza, D., Ghisellini, G., Gilmozzi, R., Lazzati, D., Mason, E., Mazzali, P., and Stella, L.: 2003, *Astron. Astrophys.* **406**, L33

Della Valle, M., Malesani, D., Bloom, J. S., Benetti, S., Chincarini, G., D'Avanzo, P., Foley, R. J., Covino, S., Melandri, A., Piranomonte, S., Tagliaferri, G., Stella, L., Gilmozzi, R., Antonelli, L. A., Campana, S., Chen, H.-W., Filliatre, P., Fiore, F., Fugazza, D., Gehrels, N., Hurley, K., Mirabel, I. F., Pellizza, L. J., Piro, L., and Prochaska, J. X.: 2006b, *Astrophys. J., Lett.* **642**, L103

Denny, R. B.: 2003, in S. W. Teare and D. A. Kenyon (eds.), *Proceedings of the 22nd IAPPP Western Wing Conference: Symposium on Telescope Science*, pp 17–27, IAPPP Western Wing Inc., http://www.socastrosci.org/Files/Proceedings2003.pdf

Dermer, C. D. and Mitman, K. E.: 1999, *Astrophys. J., Lett.* **513**, L5

Dingus, B. L.: 2001, in *American Institute of Physics Conference Series*, p. 383

Djorgovski, S. G., Kulkarni, S. R., Bloom, J. S., and Frail, D. A.: 1999, *GRB Coordinates Network* 289

Djorgovski, S. G., Metzger, M. R., Kulkarni, S. R., Odewahn, S. C., Gal, R. R., Pahre, M. A., Frail, D. A., Feroci, M., Costa, E., and Palazzi, E.: 1997, *Nature* **387**, 876

Donaghy, T. Q., Lamb, D. Q., Sakamoto, T., Norris, J. P., Nakagawa, Y., Villasenor, J., Atteia, J. ., Vanderspek, R., Graziani, C., Kawai, N., Ricker, G. R., Crew, G. B., Doty, J., Prigozhin, G., Jernigan, J. G., Shirasaki, Y., Suzuki, M., Butler, N., Hurley, K., Tamagawa, T., Yoshida, A., Matsuoka, M., Fenimore, E. E., Galassi, M., Boer, M., Dezalay, J. ., Olive, J. ., Levine, A., Martel, F., Morgan, E., Sato, R., Woosley, S. E., Braga, J., Manchanda, R., Pizzichini, G., Takagishi, K., and Yamauchi, M.: 2006, *ArXiv:astro-ph/0605570*

Donalek, C., Mahabal, A., Drake, A. J., Djorgovski, S. G., Glikman, E., Williams, R.,

Graham, M. J., Herczeg, G., Baltay, C., Rabinowitz, D., and The PQ Team: 2008, *The Astronomer's Telegram* **1362**, 1

Drake, A. J., Djorgovski, G., Graham, M., Williams, R., Mahabal, A., Donalek, C., Glikman, E., Bloom, J., Vastrand, T., White, R., Rabinowitz, D., and Baltay, C.: 2006, in *Bulletin of the American Astronomical Society*, Vol. 38 of *Bulletin of the American Astronomical Society*, pp 1002–+

Duncan, R. C. and Thompson, C.: 1992, *Astrophys. J., Lett.* **392**, L9

Eaton, J. A., Henry, W., and Fekel, F. C.: 2003, in T. D. Oswalt (ed.), *The Future of Small Telescopes in the New Millennium*, Vol. II, pp 189–207, Kluwer Academic Publishers

Eichler, D., Livio, M., Piran, T., and Schramm, D. N.: 1989, *Nature* **340**, 126

Engdahl, T.: 2000, *Get power out of PC RS-232 port*, http://www.tkk.fi/Misc/Electronics/circuits/rspower.html

Fan, Y. Z. and Wei, D. M.: 2005, *Mon. Not. R. Astron. Soc.* **364**, L42

Fan, Y. Z., Zhang, B., and Wei, D. M.: 2005, *Astrophys. J., Lett.* **628**, L25

Fenimore, E. E. and Ramirez-Ruiz, E.: 2000, *ArXiv: astro-ph/0004176*

Feroci, M., Frontera, F., Costa, E., dal Fiume, D., Amati, L., Bruca, L., Cinti, M. N., Coletta, A., Collina, P., Guidorzi, C., Nicastro, L., Orlandini, M., Palazzi, E., Rapisarda, M., Zavattini, G., and Butler, R. C.: 1997, in O. H. Siegmund and M. A. Gummin (eds.), *EUV, X-Ray, and Gamma-Ray Instrumentation for Astronomy VIII*, Vol. 3114 of *Presented at the Society of Photo-Optical Instrumentation Engineers (SPIE) Conference*, pp 186–197

Fishman, G. F., Meegan, C., Wilson, R. B., Paciesas, W. S., Parnell, T. A., Austin, R. W., Rehage, J. R., Matteson, J. L., Teegarden, B. J., Cline, T. L., Schaefer, B. E., Pendelton, G. N., Berry, F. A. J., M., H. J., Storey, S. D., Brock, M. N., and Lestrade, J. P.: 1989a, in W. N. Johnson (ed.), *GRO Science Workshop 1989, GSFC*, p. 2

Fishman, G. F., Meegan, C., Wilson, R. B., Paciesas, W. S., Parnell, T. A., Austin, R. W., Rehage, J. R., Matteson, J. L., Teegarden, B. J., Cline, T. L., Schaefer, B. E., Pendelton,

G. N., Berry, F. A. J., M., H. J., Storey, S. D., Brock, M. N., and Lestrade, J. P.: 1989b, in W. N. Johnson (ed.), *GRO Science Workshop 1989, GSFC*, p. 2

Fishman, G. J. and Meegan, C. A.: 1995, *Ann. Rev. Astron. Astrophys.* **33**, 415

Foley, S., McGlynn, S., Hanlon, L., McBreen, S., and McBreen, B.: 2008, *Astron. Astrophys.* **484**, 143

Ford, L. A., Band, D. L., Matteson, J. L., Briggs, M. S., Pendleton, G. N., Preece, R. D., Paciesas, W. S., Teegarden, B. J., Palmer, D. M., Schaefer, B. E., Cline, T. L., Fishman, G. J., Kouveliotou, C., Meegan, C. A., Wilson, R. B., and Lestrade, J. P.: 1995, *Astrophys. J.* **439**, 307

Fox, D. B., Frail, D. A., Price, P. A., Kulkarni, S. R., Berger, E., Piran, T., Soderberg, A. M., Cenko, S. B., Cameron, P. B., Gal-Yam, A., Kasliwal, M. M., Moon, D.-S., Harrison, F. A., Nakar, E., Schmidt, B. P., Penprase, B., Chevalier, R. A., Kumar, P., Roth, K., Watson, D., Lee, B. L., Shectman, S., Phillips, M. M., Roth, M., McCarthy, P. J., Rauch, M., Cowie, L., Peterson, B. A., Rich, J., Kawai, N., Aoki, K., Kosugi, G., Totani, T., Park, H.-S., MacFadyen, A., and Hurley, K. C.: 2005, *Nature* **437**, 845

Fox, D. W.: 2003, *Nature* **422**, 284

Frail, D. A., Cameron, P. B., Kasliwal, M., Nakar, E., Price, P. A., Berger, E., Gal-Yam, A., Kulkarni, S. R., Fox, D. B., Soderberg, A. M., Schmidt, B. P., Ofek, E., and Cenko, S. B.: 2006, *Astrophys. J., Lett.* **646**, L99

Frail, D. A., Kulkarni, S. R., Hurley, K. C., Fishman, G. J., Kouveliotou, C., Meegan, C. A., Sommer, M., Boer, M., Niel, M., and Cline, T.: 1994, *Astrophys. J., Lett.* **437**, L43

Frail, D. A., Kulkarni, S. R., Nicastro, L., Feroci, M., and Taylor, G. B.: 1997, *Nature* **389**, 261

Frail, D. A., Kulkarni, S. R., Sari, R., Djorgovski, S. G., Bloom, J. S., Galama, T. J., Reichart, D. E., Berger, E., Harrison, F. A., Price, P. A., Yost, S. A., Diercks, A., Goodrich, R. W., and Chaffee, F.: 2001, *Astrophys. J., Lett.* **562**, L55

Frail, D. A., Kulkarni, S. R., Sari, R., and et al: 2001, *Astrophys. J., Lett.* **562**, L55

French, J. and Jelinek, M.: 2006, *GRB Coordinates Network* 5165

Fruchter, A. S., Levan, A. J., Strolger, L., Vreeswijk, P. M., Thorsett, S. E., Bersier, D., Burud, I., Castro Cerón, J. M., Castro-Tirado, A. J., Conselice, C., Dahlen, T., Ferguson, H. C., Fynbo, J. P. U., Garnavich, P. M., Gibbons, R. A., Gorosabel, J., Gull, T. R., Hjorth, J., Holland, S. T., Kouveliotou, C., Levay, Z., Livio, M., Metzger, M. R., Nugent, P. E., Petro, L., Pian, E., Rhoads, J. E., Riess, A. G., Sahu, K. C., Smette, A., Tanvir, N. R., Wijers, R. A. M. J., and Woosley, S. E.: 2006, *Nature* **441**, 463

Fruchter, A. S., Pian, E., Thorsett, S. E., Bergeron, L. E., González, R. A., Metzger, M., Goudfrooij, P., Sahu, K. C., Ferguson, H., Livio, M., Mutchler, M., Petro, L., Frontera, F., Galama, T., Groot, P., Hook, R., Kouveliotou, C., Macchetto, D., van Paradijs, J., Palazzi, E., Pedersen, H., Sparks, W., and Tavani, M.: 1999, *Astrophys. J.* **516**, 683

Fryer, C. L., Woosley, S. E., and Hartmann, D. H.: 1999, *Astrophys. J.* **526**, 152

Fynbo, J. P. U., Starling, R. L. C., Ledoux, C., Wiersema, K., Thöne, C. C., Sollerman, J., Jakobsson, P., Hjorth, J., Watson, D., Vreeswijk, P. M., Møller, P., Rol, E., Gorosabel, J., Näränen, J., Wijers, R. A. M. J., Björnsson, G., Castro Cerón, J. M., Curran, P., Hartmann, D. H., Holland, S. T., Jensen, B. L., Levan, A. J., Limousin, M., Kouveliotou, C., Nelemans, G., Pedersen, K., Priddey, R. S., and Tanvir, N. R.: 2006a, *Astron. Astrophys.* **451**, L47

Fynbo, J. P. U., Watson, D., Thöne, C. C., Sollerman, J., Bloom, J. S., Davis, T. M., Hjorth, J., Jakobsson, P., Jørgensen, U. G., Graham, J. F., Fruchter, A. S., Bersier, D., Kewley, L., Cassan, A., Castro Cerón, J. M., Foley, S., Gorosabel, J., Hinse, T. C., Horne, K. D., Jensen, B. L., Klose, S., Kocevski, D., Marquette, J.-B., Perley, D., Ramirez-Ruiz, E., Stritzinger, M. D., Vreeswijk, P. M., Wijers, R. A. M., Woller, K. G., Xu, D., and Zub, M.: 2006b, *Nature* **444**, 1047

Fynbo, J. U., Jensen, B. L., Gorosabel, J., Hjorth, J., Pedersen, H., Møller, P., Abbott, T., Castro-Tirado, A. J., Delgado, D., Greiner, J., Henden, A., Magazzù, A., Masetti, N., Merlino, S., Masegosa, J., Østensen, R., Palazzi, E., Pian, E., Schwarz, H. E., Cline, T., Guidorzi, C., Goldsten, J., Hurley, K., Mazets, E., McClanahan, T., Montanari, E., Starr, R., and Trombka, J.: 2001, *Astron. Astrophys.* **369**, 373

Gal-Yam, A., Fox, D. B., Price, P. A., Ofek, E. O., Davis, M. R., Leonard, D. C., Soderberg, A. M., Schmidt, B. P., Lewis, K. M., Peterson, B. A., Kulkarni, S. R., Berger, E., Cenko, S. B., Sari, R., Sharon, K., Frail, D., Moon, D.-S., Brown, P. J., Cucchiara, A., Harrison, F., Piran, T., Persson, S. E., McCarthy, P. J., Penprase, B. E., Chevalier, R. A., and MacFadyen, A. I.: 2006, *Nature* **444**, 1053

Galama, T. J., Briggs, M. S., Wijers, R. A. M. J., Vreeswijk, P. M., Rol, E., Band, D., Paradijs, J. V., Kouveliotou, C., Preece, R. D., Bremer, M., Smith, I. A., Tilanus, R. P. J., Bruyn, A. G. D., Strom, R. G., Pooley, G., Castro-Tirado, A. J., Tanvir, N., Robinson, C., Hurley, K., Heise, J., Telting, J., Rutten, R. G. M., Packham, C., Swaters, R., Davies, J. K., Fassia, A., Green, S. F., Foster, M. J., Sagar, R., Pandey, A. K., Nilakshi, Yadav, R. K. S., Ofek, E. O., Leibowitz, E., Ibbetson, P., Rhoads, J., Falco, E., Petry, C., Impey, C., Geballe, T. R., and Bhattacharya, D.: 1999, *Nature* **398**, 394

Galama, T. J., Reichart, D., Brown, T. M., Kimble, R. A., Price, P. A., Berger, E., Frail, D. A., Kulkarni, S. R., Yost, S. A., Gal-Yam, A., Bloom, J. S., Harrison, F. A., Sari, R., Fox, D., and Djorgovski, S. G.: 2003, *Astrophys. J.* **587**, 135

Galama, T. J., Vreeswijk, P. M., van Paradijs, J., Kouveliotou, C., Augusteijn, T., Böhnhardt, H., Brewer, J. P., Doublier, V., Gonzalez, J.-F., Leibundgut, B., Lidman, C., Hainaut, O. R., Patat, F., Heise, J., in't Zand, J., Hurley, K., Groot, P. J., Strom, R. G., Mazzali, P. A., Iwamoto, K., Nomoto, K., Umeda, H., Nakamura, T., Young, T. R., Suzuki, T., Shigeyama, T., Koshut, T., Kippen, M., Robinson, C., de Wildt, P., Wijers, R. A. M. J., Tanvir, N., Greiner, J., Pian, E., Palazzi, E., Frontera, F., Masetti, N., Nicastro, L., Feroci, M., Costa, E., Piro, L., Peterson, B. A., Tinney, C., Boyle, B., Cannon, R., Stathakis, R., Sadler, E., Begam, M. C., and Ianna, P.: 1998a, *Nature* **395**, 670

Galama, T. J., Wijers, R. A. M. J., Bremer, M., Groot, P. J., Strom, R. G., Kouveliotou, C., and van Paradijs, J.: 1998b, *Astrophys. J., Lett.* **500**, L97+

Gehrels, N., Cannizzo, J. K., and Norris, J. P.: 2007, *New Journal of Physics* **9**, 37

Gehrels, N., Chincarini, G., Giommi, P., Mason, K. O., Nousek, J. A., Wells, A. A., White, N. E., Barthelmy, S. D., Burrows, D. N., Cominsky, L. R., Hurley, K. C., Marshall, F. E., Mészáros, P., Roming, P. W. A., Angelini, L., Barbier, L. M., Belloni, T.,

Campana, S., Caraveo, P. A., Chester, M. M., Citterio, O., Cline, T. L., Cropper, M. S., Cummings, J. R., Dean, A. J., Feigelson, E. D., Fenimore, E. E., Frail, D. A., Fruchter, A. S., Garmire, G. P., Gendreau, K., Ghisellini, G., Greiner, J., Hill, J. E., Hunsberger, S. D., Krimm, H. A., Kulkarni, S. R., Kumar, P., Lebrun, F., Lloyd-Ronning, N. M., Markwardt, C. B., Mattson, B. J., Mushotzky, R. F., Norris, J. P., Osborne, J., Paczynski, B., Palmer, D. M., Park, H.-S., Parsons, A. M., Paul, J., Rees, M. J., Reynolds, C. S., Rhoads, J. E., Sasseen, T. P., Schaefer, B. E., Short, A. T., Smale, A. P., Smith, I. A., Stella, L., Tagliaferri, G., Takahashi, T., Tashiro, M., Townsley, L. K., Tueller, J., Turner, M. J. L., Vietri, M., Voges, W., Ward, M. J., Willingale, R., Zerbi, F. M., and Zhang, W. W.: 2004, *Astrophys. J.* **611**, 1005

Gehrels, N., Norris, J. P., Barthelmy, S. D., Granot, J., Kaneko, Y., Kouveliotou, C., Markwardt, C. B., Mészáros, P., Nakar, E., Nousek, J. A., O'Brien, P. T., Page, M., Palmer, D. M., Parsons, A. M., Roming, P. W. A., Sakamoto, T., Sarazin, C. L., Schady, P., Stamatikos, M., and Woosley, S. E.: 2006, *Nature* **444**, 1044

Gehrels, N., Sarazin, C. L., O'Brien, P. T., Zhang, B., Barbier, L., Barthelmy, S. D., Blustin, A., Burrows, D. N., Cannizzo, J., Cummings, J. R., Goad, M., Holland, S. T., Hurkett, C. P., Kennea, J. A., Levan, A., Markwardt, C. B., Mason, K. O., Mészáros, P., Page, M., Palmer, D. M., Rol, E., Sakamoto, T., Willingale, R., Angelini, L., Beardmore, A., Boyd, P. T., Breeveld, A., Campana, S., Chester, M. M., Chincarini, G., Cominsky, L. R., Cusumano, G., de Pasquale, M., Fenimore, E. E., Giommi, P., Gronwall, C., Grupe, D., Hill, J. E., Hinshaw, D., Hjorth, J., Hullinger, D., Hurley, K. C., Klose, S., Kobayashi, S., Kouveliotou, C., Krimm, H. A., Mangano, V., Marshall, F. E., McGowan, K., Moretti, A., Mushotzky, R. F., Nakazawa, K., Norris, J. P., Nousek, J. A., Osborne, J. P., Page, K., Parsons, A. M., Patel, S., Perri, M., Poole, T., Romano, P., Roming, P. W. A., Rosen, S., Sato, G., Schady, P., Smale, A. P., Sollerman, J., Starling, R., Still, M., Suzuki, M., Tagliaferri, G., Takahashi, T., Tashiro, M., Tueller, J., Wells, A. A., White, N. E., and Wijers, R. A. M. J.: 2005, *Nature* **437**, 851

Golenetskii, S. V., Mazets, E. P., Aptekar, R. L., and Ilinskii, V. N.: 1983, *Nature* **306**, 451

Gomboc, A., Bode, M. F., Carter, D., Guidorzi, C., Monfardini, A., Mundell, C. G., Newsam, A. M., Smith, R. J., Steele, I. A., and Meaburn, J.: 2005, in L. Burderi, L. A.

Antonelli, F. D'Antona, T. di Salvo, G. L. Israel, L. Piersanti, A. Tornambè, and O. Straniero (eds.), *Interacting Binaries: Accretion, Evolution, and Outcomes*, Vol. 797 of *American Institute of Physics Conference Series*, pp 181–186

González, M. M., Dingus, B. L., Kaneko, Y., Preece, R. D., Dermer, C. D., and Briggs, M. S.: 2003, *Nature* **424**, 749

Goodman, J.: 1986, *Astrophys. J., Lett.* **308**, L47

Gotz, D., Mereghetti, S., Shaw, S., Beck, M., and Borkowski, J.: 2004, *GRB Coordinates Network* 2866

Granzer, T.: 2004, *Astronomische Nachrichten* **325**, 513

Greiner, J., Klose, S., Salvato, M., Zeh, A., Schwarz, R., Hartmann, D. H., Masetti, N., Stecklum, B., Lamer, G., Lodieu, N., Scholz, R. D., Sterken, C., Gorosabel, J., Burud, I., Rhoads, J., Mitrofanov, I., Litvak, M., Sanin, A., Grinkov, V., Andersen, M. I., Castro Cerón, J. M., Castro-Tirado, A. J., Fruchter, A., Fynbo, J. U., Hjorth, J., Kaper, L., Kouveliotou, C., Palazzi, E., Pian, E., Rol, E., Tanvir, N. R., Vreeswijk, P. M., Wijers, R. A. M. J., and van den Heuvel, E.: 2003a, *Astrophys. J.* **599**, 1223

Greiner, J., Peimbert, M., Estaban, C., Kaufer, A., Jaunsen, A., Smoke, J., Klose, S., and Reimer, O.: 2003b, *GRB Coordinates Network* 2020

Greiner, J. and Wenzel, W.: 1991, *Advances in Space Research* **11**, 149

Greiner, J., Wenzel, W., and Degel, W.: 1990, *Astron. Astrophys.* **234**, 251

Greiner, J., Wenzel, W., Hudec, R., Moskalenko, E. I., Fishman, G. J., Kouveliotou, C., Meegan, C. A., Paciesas, W. S., and Wilson, R. B.: 1992, in W. S. Paciesas and G. J. Fishman (eds.), *American Institute of Physics Conference Series*, Vol. 265 of *American Institute of Physics Conference Series*, pp 327–331

Greiner, J., Wenzel, W., Hudec, R., Moskalenko, E. I., Metlov, V., Chernych, N. S., Getman, V. S., Ziener, R., Birkle, K., Bade, N., Tritton, S. B., Fishman, G. J., Kouveliotou, C., Meegan, C. A., Paciesas, W. S., and Wilson, R. B.: 1994, in G. J. Fishman (ed.), *Gamma-Ray Bursts*, Vol. 307 of *American Institute of Physics Conference Series*, pp 408–+

Groot, P. J., Galama, T. J., Vreeswijk, P. M., Wijers, R. A. M. J., Pian, E., Palazzi, E., van Paradijs, J., Kouveliotou, C., in 't Zand, J. J. M., Heise, J., Robinson, C., Tanvir, N., Lidman, C., Tinney, C., Keane, M., Briggs, M., Hurley, K., Gonzalez, J.-F., Hall, P., Smith, M. G., Covarrubias, R., Jonker, P., Casares, J., Frontera, F., Feroci, M., Piro, L., Costa, E., Smith, R., Jones, B., Windridge, D., Bland-Hawthorn, J., Veilleux, S., Garcia, M., Brown, W. R., Stanek, K. Z., Castro-Tirado, A. J., Gorosabel, J., Greiner, J., Jaeger, K., Bohm, A. B., and Fricke, K. J.: 1998, *Astrophys. J., Lett.* **502**, L123+

Guidorzi, C., Monfardini, A., Gomboc, A., Mottram, C. J., Mundell, C. G., Steele, I. A., Carter, D., Bode, M. F., Smith, R. J., Fraser, S. N., Burgdorf, M. J., and Newsam, A. M.: 2006, *Publ. Astron. Soc. Pac.* **118**, 288

Guidorzi, C., Vergani, S. D., Sazonov, S., Covino, S., Malesani, D., Molkov, S., Palazzi, E., Romano, P., Campana, S., Chincarini, G., Fugazza, D., Moretti, A., Tagliaferri, G., Llorente, A., Gorosabel, J., Antonelli, L. A., Capalbi, M., Cusumano, G., D'Avanzo, P., Mangano, V., Masetti, N., Meurs, E., Mineo, T., Molinari, E., Morris, D. C., Nicastro, L., Page, K. L., Perri, M., Sbarufatti, B., Stratta, G., Sunyaev, R., Troja, E., and Zerbi, F. M.: 2007, *Astron. Astrophys.* **474**, 793

Hansen, B. M. S. and Phinney, E. S.: 1997, *Mon. Not. R. Astron. Soc.* **291**, 569

Harding, A. K.: 1991, *Phys. Rep.* **206**, 327

Harris, M. J. and Share, G. H.: 1998, *Astrophys. J.* **494**, 724

Harrison, F. A., Bloom, J. S., Frail, D. A., Sari, R., Kulkarni, S. R., Djorgovski, S. G., Axelrod, T., Mould, J., Schmidt, B. P., Wieringa, M. H., Wark, R. M., Subrahmanyan, R., McConnell, D., McCarthy, P. J., Schaefer, B. E., McMahon, R. G., Markze, R. O., Firth, E., Soffitta, P., and Amati, L.: 1999, *Astrophys. J., Lett.* **523**, L121

Heise, J., in't Zand, J., Kippen, R. M., and Woods, P. M.: 2001, in *Gamma-ray Bursts in the Afterglow Era*, pp 16–+

Henry, G. W. and Eaton, J. A. (eds.): 1994, *Robotic Telescopes: Current Capabilities, Present Developments, and Future Prospects for Automated Astronomy*, Vol. 79 of *Astronomical Society of the Pacific Conference Series*

Hessman, F. V.: 2006, *Astronomische Nachrichten* **327**, 751

Hjorth, J., Levan, A., Tanvir, N., Starling, R., Klose, S., Kouveliotou, C., Féron, C., Ferrero, P., Fruchter, A., Fynbo, J., Gorosabel, J., Jakobsson, P., Kann, D. A., Pedersen, K., Ramirez-Ruiz, E., Sollerman, J., Thöne, C., Watson, D., Wiersema, K., and Xu, D.: 2006, *The Messenger* **126**, 16

Hjorth, J., Møller, P., Gorosabel, J., Fynbo, J. P. U., Toft, S., Jaunsen, A. O., Kaas, A. A., Pursimo, T., Torii, K., Kato, T., Yamaoka, H., Yoshida, A., Thomsen, B., Andersen, M. I., Burud, I., Castro Cerón, J. M., Castro-Tirado, A. J., Fruchter, A. S., Kaper, L., Kouveliotou, C., Masetti, N., Palazzi, E., Pedersen, H., Pian, E., Rhoads, J., Rol, E., Tanvir, N. R., Vreeswijk, P. M., Wijers, R. A. M. J., and van den Heuvel, E. P. J.: 2003a, *Astrophys. J.* **597**, 699

Hjorth, J., Sollerman, J., Møller, P., Fynbo, J. P. U., Woosley, S. E., Kouveliotou, C., Tanvir, N. R., Greiner, J., Andersen, M. I., Castro-Tirado, A. J., Castro Cerón, J. M., Fruchter, A. S., Gorosabel, J., Jakobsson, P., Kaper, L., Klose, S., Masetti, N., Pedersen, H., Pedersen, K., Pian, E., Palazzi, E., Rhoads, J. E., Rol, E., van den Heuvel, E. P. J., Vreeswijk, P. M., Watson, D., and Wijers, R. A. M. J.: 2003b, *Nature* **423**, 847

Hjorth, J., Sollerman, J., Møller, P., Fynbo, J. P. U., Woosley, S. E., Kouveliotou, C., Tanvir, N. R., Greiner, J., Andersen, M. I., Castro-Tirado, A. J., Castro Cerón, J. M., Fruchter, A. S., Gorosabel, J., Jakobsson, P., Kaper, L., Klose, S., Masetti, N., Pedersen, H., Pedersen, K., Pian, E., Palazzi, E., Rhoads, J. E., Rol, E., van den Heuvel, E. P. J., Vreeswijk, P. M., Watson, D., and Wijers, R. A. M. J.: 2003c, *Nature* **423**, 847

Hjorth, J., Watson, D., Fynbo, J. P. U., Price, P. A., Jensen, B. L., Jørgensen, U. G., Kubas, D., Gorosabel, J., Jakobsson, P., Sollerman, J., Pedersen, K., and Kouveliotou, C.: 2005, *Nature* **437**, 859

Hodapp, K.-W., Hora, J. L., Hall, D. N. B., Cowie, L. L., Metzger, M., Irwin, E., Vural, K., Kozlowski, L. J., Cabelli, S. A., Chen, C. Y., Cooper, D. E., Bostrup, G. L., Bailey, R. B., and Kleinhans, W. E.: 1996, *New Astronomy* **1**, 177

Holland, S. and Hjorth, J.: 1999, *Astron. Astrophys.* **344**, L67

Horváth, I., Balázs, L. G., Bagoly, Z., Ryde, F., and Mészáros, A.: 2006, *Astron. Astrophys.* **447**, 23

Howell, S. B.: 2000, *Handbook of CCD Photometry*, pp 53–58, Cambridge University Press

Howell, S. B., Koehn, B., Bowell, E., and Hoffman, M.: 1996, *Astronomical Journal* **112**, 1302

Huang, Y. F., Dai, Z. G., and Lu, T.: 1998, *Astron. Astrophys.* **336**, L69

Huchra, J.: 2003, in T. D. Oswalt (ed.), *The Future of Small Telescopes in the New Millennium*, Vol. III, pp 343–354, Kluwer Academic Publishers

Hudec, R.: 1992, *Gamma-ray burst sources at optical wavelengths*, pp 113–118, Gamma-Ray Bursts - Observations, Analyses and Theories

Hudec, R.: 1993, *Astrophysical Letters Communications* **28**, 359

Hudec, R. and Soldán, J.: 1994, in G. J. Fishman (ed.), *Gamma-Ray Bursts*, Vol. 307 of *American Institute of Physics Conference Series*, pp 413–+

Hullinger, D., Barbier, L., Barthelmy, S., Cummings, J., Fenimore, E., Gehrels, N., Krimm, H., Koss, M., Markwardt, C., Palmer, D., Parsons, A., Sakamoto, T., Sato, G., Stamatikos, M., and Tueller, J.: 2006, *GRB Coordinates Network* 5142

Hurley, K.: 2007, in S. Ritz, P. Michelson, and C. A. Meegan (eds.), *American Institute of Physics Conference Series*, Vol. 921 of *American Institute of Physics Conference Series*, pp 284–288

Hurley, K., Rau, A., von Kienlin, A., and Lichti, G.: 2004, in V. Schoenfelder, G. Lichti, and C. Winkler (eds.), *5th INTEGRAL Workshop on the INTEGRAL Universe*, Vol. 552 of *ESA Special Publication*, pp 645–+

Hurley, K., Sari, R., and Djorgovski, S. G.: 2002, *Cosmic Gamma-Ray Bursts, Their Afterglows, and Their Host Galaxies*, [astro-ph/0211620 Review article for the book *Compact Stellar X-Ray Sources*, Editors W. Lewin and M. van der Klis, to be published by Cambridge University Press]

Hurley, K., Sommer, M., Boer, M., Niel, M., Laros, J., Fenimore, E., Klebesadel, R., Fishman, G., Kouveliotou, C., Meegan, C., Paciesas, W., Wilson, R., and Cline, T.: 1993a, *aas* **97**, 39

Hurley, K., Sommer, M., Cline, T., Boer, M., Niel, M., Fenimore, E., Klebesadel, R., Laros, J., Fishman, G., Kouveliotou, C., Meegan, C., and Wilson, R.: 1993b, in M. Friedlander, N. Gehrels, and D. J. Macomb (eds.), *American Institute of Physics Conference Series*, Vol. 280 of *American Institute of Physics Conference Series*, pp 769–773

Hurley, K. C.: 1998, in C. A. Meegan, R. D. Preece, and T. M. Koshut (eds.), *American Institute of Physics Conference Series*, Vol. 428 of *American Institute of Physics Conference Series*, pp 387–+

Jager, R., Mels, W. A., Brinkman, A. C., Galama, M. Y., Goulooze, H., Heise, J., Lowes, P., Muller, J. M., Naber, A., Rook, A., Schuurhof, R., Schuurmans, J. J., and Wiersma, G.: 1997, *Astron. Astrophys. Suppl. Ser.* **125**, 557

Jakobsson, P., Hjorth, J., Fynbo, J. P. U., Watson, D., Pedersen, K., Björnsson, G., and Gorosabel, J.: 2004, *Astrophys. J., Lett.* **617**, L21

Jakobsson, P., Levan, A., Fynbo, J. P. U., Priddey, R., Hjorth, J., Tanvir, N., Watson, D., Jensen, B. L., Sollerman, J., Natarajan, P., Gorosabel, J., Castro Cerón, J. M., Pedersen, K., Pursimo, T., Árnadóttir, A. S., Castro-Tirado, A. J., Davis, C. J., Deeg, H. J., Fiuza, D. A., Mykolaitis, S., and Sousa, S. G.: 2006, *Astron. Astrophys.* **447**, 897

Janka, H.-T., Eberl, T., Ruffert, M., and Fryer, C. L.: 1999, *Astrophys. J., Lett.* **527**, L39

Jarrett, A. H.: 1987, *Monthly Notes of the Astronomical Society of South Africa* **46**, 11

Jaunsen, A. O., Hjorth, J., Björnsson, G., Andersen, M. I., Pedersen, H., Kjernsmo, K., Korhonen, H., Sørensen, P. M., and Palazzi, E.: 2001, *Astrophys. J.* **546**, 127

Jelinek, M., Castro-Tirado, A. J., Postigo, A. d. U., Kubanek, P., Vitek, S., Gorosabel, J., Guziy, S., Hudec, R., Ceron, J. M. C., Pata, P., and Bernas, M.: 2005, *GRB Coordinates Network* 3929

Jelínek, M., Kubánek, P., Nekola, M., and Hudec, R.: 2004, *Astronomische Nachrichten* **325**, 678

Jelinek, M., Kubanek, P., Prouza, M., Nekola, M., and Hudec, R.: 2006, *GRB Coordinates Network* 4536

Jelínek, M., Prouza, M., Kubánek, P., Hudec, R., Nekola, M., Řídký, J., Grygar, J., Boháčová, M., Castro-Tirado, A. J., Gorosabel, J., Hrabovský, M., Mandát, D., Nosek, D., Nožka, L., Palatka, M., Pandey, S. B., Pech, M., Schovánek, P., Šmída, R., Trávníček, P., de Ugarte Postigo, A., and Vítek, S.: 2006, *Astron. Astrophys.* **454**, L119

Jóhannesson, G., Björnsson, G., and Gudmundsson, E. H.: 2006, *Astrophys. J.* **647**, 1238

Joye, W. A. and Mandel, E.: 2003, in H. E. Payne, R. I. Jedrzejewski, and R. N. Hook (eds.), *Astronomical Data Analysis Software and Systems XII*, Vol. 295 of *Astronomical Society of the Pacific Conference Series*, pp 489–+

Königl, A. and Granot, J.: 2002, *Astrophys. J.* **574**, 134

Kallman, T. R., Mészáros, P., and Rees, M. J.: 2003, *Astrophys. J.* **593**, 946

Kaneko, Y., Preece, R. D., Briggs, M. S., Paciesas, W. S., Meegan, C. A., and Band, D. L.: 2006, **166**, 298

Kann, D. A. and Hoegner, C.: 2006, *GRB Coordinates Network* 5182

Kann, D. A., Klose, S., and Zeh, A.: 2006, *Astrophys. J.* **641**, 993

Kann, D. A., Klose, S., Zhang, B., Malesani, D., Nakar, E., Wilson, A. C., Butler, N. R., Antonelli, L. A., Chincarini, G., Cobb, B. E., Covino, S., D'Avanzo, P., D'Elia, V., Della Valle, M., Ferrero, P., Fugazza, D., Gorosabel, J., Israel, G. L., Mannucci, F., Piranomonte, S., Schulze, S., Stella, L., Tagliaferri, G., and Wiersema, K.: 2007, *ArXiv: astro-ph/0712.2186*

Kawai, N., Yamada, T., Kosugi, G., Hattori, T., and Aoki, K.: 2005, *GRB Coordinates Network* 3937

Kawai, N., Yoshida, A., Matsuoka, M., Shirasaki, Y., Tamagawa, T., Torii, K., Sakamoto, T., Takahashi, D., Fenimore, E., Galassi, M., Tavenner, T., Lamb, D. Q., Graziani, C., Donaghy, T., Vanderspek, R., Yamauchi, M., Takagishi, K., and Hatsukade, I.: 2003, in G. R. Ricker and R. K. Vanderspek (eds.), *Gamma-Ray Burst and Afterglow Astronomy 2001: A Workshop Celebrating the First Year of the HETE Mission*, Vol. 662 of *American Institute of Physics Conference Series*, pp 25–32

Kelson, D. D., Illingworth, G. D., Franx, M., Magee, D., and Dokkum, P. G. v.: 1999, *IAU Circ.* **7096**, 3

Kennel, C. F. and Coroniti, F. V.: 1984, *Astrophys. J.* **283**, 694

Khamitov, I., Bikmaev, I., Sakhibullin, N., Aslan, Z., Kiziloglu, U., Gogus, E., Burenin, R., Pavlinsky, M., and Sunyaev, R.: 2006, *GRB Coordinates Network* 5173

Kippen, R. M.: 1999, *GRB Coordinates Network* 224

Kippen, R. M., Connors, A., Macri, J., McConnell, M., Ryan, J., Collmar, W., Greiner, J., Schönfelder, V., Varendorff, M., Fishman, G. J., Meegan, C., Kouveliotou, C., McNamara, B., Harrison, T., Hermsen, W., Kuiper, L., Bennett, K., Hanlon, L., and Winkler, C.: 1994, in G. J. Fishman (ed.), *Gamma-Ray Bursts*, Vol. 307 of *American Institute of Physics Conference Series*, pp 418–+

Kippen, R. M., Woods, P. M., Heise, J., in't Zand, J. J. M., Briggs, M. S., and Preece, R. D.: 2002, *Spectral Characteristics of X-ray Flashes compared to Gamma-Ray Bursts* , [astro-ph/0203114] To appear in the proceedings of the Woods Hole GRB Workshop (Nov. 2001) Journal-ref: AIP Conf.Proc. 662 (2003) 244-247

Klebesadel, R. W., Strong, I. B., and Olson, R. A.: 1973, *Astrophys. J., Lett.* **182**, L85+

Klotz, A., Boer, M., and Atteia, J. L.: 2006a, *GRB Coordinates Network* 4495

Klotz, A., Gendre, B., Stratta, G., Atteia, J. L., Boër, M., Malacrino, F., Damerdji, Y., and Behrend, R.: 2006b, *Astron. Astrophys.* **451**, L39

Kobayashi, S.: 2000, *Astrophys. J.* **545**, 807

Kobayashi, S., Piran, T., and Sari, R.: 1997, *Astrophys. J.* **490**, 92

Kobayashi, S. and Sari, R.: 2001, *Astrophys. J.* **551**, 934

Kobayashi, S. and Zhang, B.: 2003, *Astrophys. J., Lett.* **582**, L75

Koranyi, D. M., Green, D. A., Warner, P. J., Waldram, E. M., and Palmer, D. M.: 1994, *Mon. Not. R. Astron. Soc.* **271**, 51

Kouveliotou, C., Fishman, G. J., Meegan, C. A., Paciesas, W. S., van Paradijs, J., Norris, J. P., Preece, R. D., Briggs, M. S., Horack, J. M., Pendleton, G. H., and Green, D. A.: 1994, *Nature* **368**, 125

Kouveliotou, C., Meegan, C. A. Fishman, G. J., Bhat, N. P., Briggs, M. S., Koshut, T. M., Paciesas, W. S., and Pendleton, G. N.: 1993, *Astrophys. J.* **413**, L101

Krimm, H. A., Vanderspek, R. K., and Ricker, G. R.: 1996, *Astron. Astrophys. Suppl. Ser.* **120**, C251+

Kubanek, P., Jelinek, M., Prouza, M., Nekola, M., and Hudec, R.: 2006, *GRB Coordinates Network* 4535

Kubánek, P., Jelínek, M., Vítek, S., de Ugarte Postigo, A., Nekola, M., and French, J.: 2006, in H. Lewis and A. Bridger (eds.), *Advanced Software and Control for Astronomy*, Vol. 6274 of *Presented at the Society of Photo-Optical Instrumentation Engineers (SPIE) Conference*

Kulkarni, S. R., Frail, D. A., Sari, R., Moriarty-Schieven, G. H., Shepherd, D. S., Udomprasert, P., Readhead, A. C. S., Bloom, J. S., Feroci, M., and Costa, E.: 1999, *Astrophys. J., Lett.* **522**, L97

Kumar, P. and McMahon, E.: 2008, *Mon. Not. R. Astron. Soc.* **384**, 33

Kumar, P. and Piran, T.: 2000, *Astrophys. J.* **535**, 152

La Parola, V., Mangano, V., Fox, D., Zhang, B., Krimm, H. A., Cusumano, G., Mineo, T., Burrows, D. N., Barthelmy, S., Campana, S., Capalbi, M., Chincarini, G., Gehrels, N., Giommi, P., Marshall, F. E., Mészáros, P., Moretti, A., O'Brien, P. T., Palmer, D. M., Perri, M., Romano, P., and Tagliaferri, G.: 2006, *Astron. Astrophys.* **454**, 753

Lamb, D. Q. and Reichart, D. E.: 2000, *Astrophys. J.* **536**, 1

Lattimer, J. M. and Schramm, D. N.: 1976, *Astrophys. J.* **210**, 549

Lazzati, D.: 2006, *New Journal of Physics* **8**, 131

Lazzati, D., Ghisellini, G., and Celotti, A.: 1999, *Mon. Not. R. Astron. Soc.* **309**, L13

Le Floc'h, E., Duc, P.-A., Mirabel, I. F., Sanders, D. B., Bosch, G., Diaz, R. J., Donzelli, C. J., Rodrigues, I., Courvoisier, T. J.-L., Greiner, J., Mereghetti, S., Melnick, J., Maza, J., and Minniti, D.: 2003, *Astron. Astrophys.* **400**, 499

Lee, B., Akerlof, C., Band, D., Barthelmy, S., Butterworth, P., Cline, T., Ferguson, D., Gehrels, N., and Hurley, K.: 1997, *Astrophys. J., Lett.* **482**, L125+

Levan, A.: 2007, in A. Wells, R. A. M. Wijers, and M. J. Rees (eds.), *Gamma-ray bursts*, Vol. 365 of *Proc. R. Soc. London, Ser. A*, pp 1315–1321

Levine, A. M., Bradt, H., Cui, W., Jernigan, J. G., Morgan, E. H., Remillard, R., Shirey, R. E., and Smith, D. A.: 1996, *Astrophys. J., Lett.* **469**, L33+

Levinson, A. and Eichler, D.: 2003, *Astrophys. J., Lett.* **594**, L19

Li, L.-X.: 2007, *ArXiv: astro-ph/0710.3587*

Li, W., Filippenko, A. V., Chornock, R., and Jha, S.: 2003, *Astrophys. J.* **586**, L9

Li, Z. and Chevalier, R. A.: 2001, *Astrophys. J.* **551**, 940

Liang, E. and Kargatis, V.: 1996, *Nature* **381**, 49

Liang, E. and Zhang, B.: 2006, *Astrophys. J., Lett.* **638**, L67

Lidman, C., Doublier, V., Gonzalez, J.-F., Augusteijn, T., Hainaut, O. R., Boehnhardt, H., Patat, F., and Leibundgut, B.: 1998, *IAU Circ.* **6895**, 1

Lin, C. S., Huang, K. Y., and Ip, W. H.: 2006, *GRB Coordinates Network* 5169

Lipkin, Y. M., Ofek, E. O., Gal-Yam, A., Leibowitz, E. M., Poznanski, D., Kaspi, S., Polishook, D., Kulkarni, S. R., Fox, D. W., Berger, E., Mirabal, N., Halpern, J., Bureau, M., Fathi, K., Price, P. A., Peterson, B. A., Frebel, A., Schmidt, B., Orosz, J. A., Fitzgerald, J. B., Bloom, J. S., van Dokkum, P. G., Bailyn, C. D., Buxton, M. M., and Barsony, M.: 2004, *Astrophys. J.* **606**, 381

Lithwick, Y. and Sari, R.: 2001, *Astrophys. J.* **555**, 540

Lloyd, N. M. and Petrosian, V.: 2000, *Astrophys. J.* **543**, 722

Lund, N., Budtz-Jørgensen, C., Westergaard, N. J., Brandt, S., Rasmussen, I. L., Hornstrup, A., Oxborrow, C. A., Chenevez, J., Jensen, P. A., Laursen, S., Andersen, K. H., Mogensen, P. B., Rasmussen, I., Omø, K., Pedersen, S. M., Polny, J., Andersson, H., Andersson, T., Kämäräinen, V., Vilhu, O., Huovelin, J., Maisala, S., Morawski, M., Juchnikowski, G., Costa, E., Feroci, M., Rubini, A., Rapisarda, M., Morelli, E., Carassiti, V., Frontera, F., Pelliciari, C., Loffredo, G., Martínez Núñez, S., Reglero, V., Velasco, T., Larsson, S., Svensson, R., Zdziarski, A. A., Castro-Tirado, A., Attina, P., Goria, M., Giulianelli, G., Cordero, F., Rezazad, M., Schmidt, M., Carli, R., Gomez, C., Jensen, P. L., Sarri, G., Tiemon, A., Orr, A., Much, R., Kretschmar, P., and Schnopper, H. W.: 2003, *Astron. Astrophys.* **411**, L231

Mészáros, P.: 2006, *Reports of Progress in Physics* **69**, 2259

Mészáros, P. and Rees, M. J.: 1992, *Mon. Not. R. Astron. Soc.* **257**, 29P

Mészáros, P. and Rees, M. J.: 1993, *Astrophys. J.* **405**, 278

Mészáros, P. and Rees, M. J.: 1994, *Mon. Not. R. Astron. Soc.* **269**, L41+

Mészáros, P. and Rees, M. J.: 1997, *Astrophys. J.* **476**, 232

Mészáros, P., Rees, M. J., and Wijers, R. A. M. J.: 1998, *Astrophys. J.* **499**, 301

MacFadyen, A. I. and Woosley, S. E.: 1999, *Astrophys. J.* **524**, 262

Malesani, D., Tagliaferri, G., Chincarini, G., Covino, S., Della Valle, M., Fugazza, D., Mazzali, P. A., Zerbi, F. M., D'Avanzo, P., Kalogerakos, S., Simoncelli, A., Antonelli, L. A., Burderi, L., Campana, S., Cucchiara, A., Fiore, F., Ghirlanda, G., Goldoni, P., Götz, D., Mereghetti, S., Mirabel, I. F., Romano, P., Stella, L., Minezaki, T., Yoshii, Y., and Nomoto, K.: 2004, *Astrophys. J., Lett.* **609**, L5

Marshall, A. D.: 1999, *Programming in C: UNIX System Calls and Subroutines using C (lecture notes)*, http://www.cs.cf.ac.uk/Dave/C/

Marshall, S., Akerlof, C., Kehoe, R., Lee, B., McKay, T., Bloch, J., Casperson, D., Fletcher, S., Gisler, G., Partridge, G., Priedhorsky, W., Roussel-Dupre, D., and Szymanski, J.: 1997, in *Bulletin of the American Astronomical Society*, Vol. 29 of *Bulletin of the American Astronomical Society*, pp 1290–+

Mas-Hesse, J. M., Giménez, A., Culhane, J. L., Jamar, C., McBreen, B., Torra, J., Hudec, R., Fabregat, J., Meurs, E., Swings, J. P., Alcacera, M. A., Balado, A., Beiztegui, R., Belenguer, T., Bradley, L., Caballero, M. D., Cabo, P., Defise, J. M., Díaz, E., Domingo, A., Figueras, F., Figueroa, I., Hanlon, L., Hroch, F., Hudcova, V., García, T., Jordan, B., Jordi, C., Kretschmar, P., Laviada, C., March, M., Martín, E., Mazy, E., Menéndez, M., Mi, J. M., de Miguel, E., Muñoz, T., Nolan, K., Olmedo, R., Plesseria, J. Y., Polcar, J., Reina, M., Renotte, E., Rochus, P., Sánchez, A., San Martín, J. C., Smith, A., Soldan, J., Thomas, P., Timón, V., and Walton, D.: 2003, *Astron. Astrophys.* **411**, L261

McBreen, S., Hanlon, L., McGlynn, S., McBreen, B., Foley, S., Preece, R., von Kienlin, A., and Williams, O. R.: 2006, *Astron. Astrophys.* **455**, 433

McBreen, S., Quilligan, F., McBreen, B., Hanlon, L., and Watson, D.: 2001, *Astron. Astrophys.* **380**, L31

McNamara, B. J., Harrison, T. E., Ryan, J., Kippen, R. M., Bennett, K., Hanlon, L. O., Greiner, J., Fishman, G. J., Kouveliotou, C., and Meegan, C. A.: 1995a, *Astrophys. Space. Sci.* **231**, 251

McNamara, B. J., Harrison, T. E., and Williams, C. L.: 1995b, *Astrophys. J., Lett.* **452**, L25+

Medvedev, M. V.: 2006, *Astrophys. J.* **637**, 869

Meegan, C. A., Fishman, G. J., Wilson, R. B., Horack, J. M., Brock, M. N., Paciesas, W. S., Pendleton, G. N., and Kouveliotou, C.: 1992, *nat* **355**, 143

Mereghetti, S., Cremonesi, D. I., and Borkowski, J.: 2001, in A. Gimenez, V. Reglero, and C. Winkler (eds.), *Exploring the Gamma-Ray Universe*, Vol. 459 of *ESA Special Publication*, pp 513–516

Metzger, M. R., Cohen, J. G., Chaffee, F. H., and Blandford, R. D.: 1997a, *IAU Circ.* **6676**, 3

Metzger, M. R., Djorgovski, S. G., Kulkarni, S. R., Steidel, C. C., Adelberger, K. L., Frail, D. A., Costa, E., and Frontera, F.: 1997b, *Nature* **387**, 878

Mirabal, N., Halpern, J. P., Chornock, R., Filippenko, A. V., Terndrup, D. M., Armstrong, E., Kemp, J., Thorstensen, J. R., Tavarez, M., and Espaillat, C.: 2003, *Astrophys. J.* **595**, 935

Misra, K., Bhattacharya, D., Sahu, D. K., Sagar, R., Anupama, G. C., Castro-Tirado, A. J., Guziy, S. S., and Bhatt, B. C.: 2007, *Astron. Astrophys.* **464**, 903

Mobberley, M.: 2003, *The New Amateur Astronomer*, Springer-Verlag London Ltd

Molinari, E., Vergani, S. D., Malesani, D., Covino, S., D'Avanzo, P., Chincarini, G., Zerbi, F. M., Antonelli, L. A., Conconi, P., Testa, V., Tosti, G., Vitali, F., D'Alessio, F., Malaspina, G., Nicastro, L., Palazzi, E., Guetta, D., Campana, S., Goldoni, P., Masetti, N., Meurs, E. J. A., Monfardini, A., Norci, L., Pian, E., Piranomonte, S., Rizzuto, D., Stefanon, M., Stella, L., Tagliaferri, G., Ward, P. A., Ihle, G., Gonzalez, L., Pizarro, A., Sinclaire, P., and Valenzuela, J.: 2007, *Astron. Astrophys.* **469**, L13

Monet, D. B. A., Canzian, B., and Dahn, C.: 1998, *VizieR Online Data Catalog*, 1252

Moretti, A., Burrows, D. N., Campana, S., Chincarini, G., and Tagliaferri, G.: 2006, *GRB Coordinates Network* 5194

Morgan, N. D. and Dai, X.: 2006, *GRB Coordinates Network* 5175

Moskalenko, E. I., Popravko, G. V., Kramer, E. N., Shestaka, I. S., Karnashov, A. N., Nazarenko, V. V., Skoblikova, L. J., Lemeshchenko, V. F., Nazarenko, S. V., and Gorbanev, J. M.: 1989, *Astron. Astrophys.* **223**, 141

Mottram, C. J. and Fraser, S. N.: 2008, *Astronomische Nachrichten* **329**, 317

Mundell, C. G., Melandri, A., Guidorzi, C., Kobayashi, S., Steele, I. A., Malesani, D., Amati, L., D'Avanzo, P., Bersier, D. F., Gomboc, A., Rol, E., Bode, M. F., Carter, D., Mottram, C. J., Monfardini, A., Smith, R. J., Malhotra, S., Wang, J., Bannister, N., O'Brien, P. T., and Tanvir, N. R.: 2007, *Astrophys. J.* **660**, 489

Nakar, E. and Piran, T.: 2004, *Mon. Not. R. Astron. Soc.* **353**, 647

Narayan, R., Paczynski, B., and Piran, T.: 1992, *Astrophys. J., Lett.* **395**, L83

Narayan, R., Piran, T., and Shemi, A.: 1991, *Astrophys. J., Lett.* **379**, L17

Nardini, M., Ghisellini, G., and Ghirlanda, G.: 2007, *ArXiv e-prints* 710

Nemiroff, R. J.: 1994, in G. J. Fishman (ed.), *Gamma-Ray Bursts*, Vol. 307 of *American Institute of Physics Conference Series*, pp 730–+

Nemiroff, R. J. and Rafert, J. B.: 1999, *Publ. Astron. Soc. Pac.* **111**, 886

Norris, J. P.: 2002, *Astrophys. J.* **579**, 386

Norris, J. P. and Bonnell, J. T.: 2006, *Astrophys. J.* **643**, 266

Norris, J. P., Marani, G. F., and Bonnell, J. T.: 2000, *Astrophys. J.* **534**, 248

Norris, J. P., Nemiroff, R. J., Bonnell, J. T., and et al: 1996, *Astrophys. J.* **459**, 393

Nousek, J. A., Kouveliotou, C., Grupe, D., Page, K. L., Granot, J., Ramirez-Ruiz, E., Patel, S. K., Burrows, D. N., Mangano, V., Barthelmy, S., Beardmore, A. P., Campana, S., Capalbi, M., Chincarini, G., Cusumano, G., Falcone, A. D., Gehrels, N., Giommi, P., Goad, M. R., Godet, O., Hurkett, C. P., Kennea, J. A., Moretti, A., O'Brien, P. T., Osborne, J. P., Romano, P., Tagliaferri, G., and Wells, A. A.: 2006, *Astrophys. J.* **642**, 389

Nysewander, M., LaCluyze, A., Reichart, D., Crain, J. A., Foster, A., and Ivarson, K.: 2006, *GRB Coordinates Network* 4548

Nysewander, M., Reichart, D. E., Crain, J. A., Foster, A., Haislip, J., Ivarsen, K., Lacluyze, A., and Trotter, A.: 2007, *ArXiv: astro-ph/0708.3444*

Oberst, J., Molau, S., Heinlein, D., Gritzner, C., Schindler, M., Spurny, P., Ceplecha, Z., Rendtel, J., and Betlem, H.: 1998, *Meteoritics and Planetary Science* **33**, 49

Ofek, E. O., Cenko, S. B., Gal-Yam, A., Fox, D. B., Nakar, E., Rau, A., Frail, D. A., Kulkarni, S. R., Price, P. A., Schmidt, B. P., Soderberg, A. M., Peterson, B., Berger, E., Sharon, K., Shemmer, O., Penprase, B. E., Chevalier, R. A., Brown, P. J., Burrows, D. N., Gehrels, N., Harrison, F., Holland, S. T., Mangano, V., McCarthy, P. J., Moon, D.-S., Nousek, J. A., Persson, S. E., Piran, T., and Sari, R.: 2007, *Astrophys. J.* **662**, 1129

Oswalt, T. D. (ed.): 2003, *The Future of Small Telescopes in the New Millennium*, Kluwer Academic Publishers, ISBN 1-4020-0948-8

Paciesas, W. S., Meegan, C. A., Pendleton, G. N., Briggs, M. S., Kouveliotou, C., Koshut, T. M., Lestrade, J. P., McCollough, M. L., Brainerd, J. J., Hakkila, J., Henze, W., Preece, R. D., Connaughton, V., Kippen, R. M., Mallozzi, R. S., Fishman, G. J., Richardson, G. A., and Sahi, M.: 1999, *apjss* **122**, 465

Paczynski, B.: 1986, *Astrophys. J., Lett.* **308**, L43

Paczynski, B.: 1991, *Acta Astron.* **41**, 257

Paczynski, B.: 1998, *Astrophys. J., Lett.* **494**, L45+

Paczynski, B. and Xu, G.: 1994, *Astrophys. J.* **427**, 708

Page, M., Burrows, D., Beardmore, A., Palmer, D., J, ., Kennea, ., Gehrels, N., Markwardt, C., Page, K., Sakamoto, T., Chester, M., and Boyd, P.: 2005, *GRB Coordinates Network* 3830

Pal'shin, V. and Frederiks, D.: 2005, *GRB Coordinates Network* 3852

Panaitescu, A.: 2006, *ArXiv: astro-ph/0607396*

Panaitescu, A.: 2007, *Mon. Not. R. Astron. Soc.* **379**, 331

Panaitescu, A. and Kumar, P.: 2001, *Astrophys. J., Lett.* **560**, L49

Panaitescu, A., Mészáros, P., and Rees, M. J.: 1998, *Astrophys. J.* **503**, 314

Panaitescu, A. and Mészáros, P.: 2000, *Astrophys. J., Lett.* **544**, L17

Park, H. S., Ables, E., Band, D. L., Barthelmy, S. D., Bionta, R. M., Butterworth, P. S., Cline, T. L., Ferguson, D. H., Fishman, G. J., Gehrels, N., Hurley, K., Kouveliotou, C., Lee, B. C., Meegan, C. A., Ott, L. L., and Parker, E. L.: 1997a, *Astrophys. J.* **490**, 99

Park, H. S., Porrata, R. A., Williams, G. G., Ables, E., Band, D. L., Barthelmy, S. D., Bionta, R. M., Cline, T. L., Fishman, G. J., Gehrels, N., Hartmann, D., Hurley, K., Kouveliotou, C., and Meegan, C. A.: 1999, *Astron. Astrophys. Suppl. Ser.* **138**, 577

Park, H. S., Williams, G. G., Ables, E., Band, D. L., Barthelmy, S. D., Bionta, R., Butterworth, P. S., Cline, T. L., Ferguson, D. H., Fishman, G. J., Gehrels, N., Hartmann, D., Hurley, K., Kouveliotou, C., Meegan, C. A., Ott, L., Parker, E., and Wurtz, R.: 1997b, *Astrophys. J., Lett.* **490**, L21+

Patat, F. and Piemonte, A.: 1998, *IAU Circ.* **6918**, 1

Pather, S.: 1996, *Integrating a Tcl Interpreter into a C Application*, http://www.ittc.ku.edu/ niehaus/classes/f96-448/tcleval.ps

Percy, J. R.: 2003, in T. D. Oswalt (ed.), *The Future of Small Telescopes in the New Millennium*, Vol. I, pp 113–123, Kluwer Academic Publishers

Perri, M., Barthelmy, S., Boyd, P., Burrows, D., Cummings, J., Gehrels, N., Gronwall, C., Kennea, J., Krimm, H., Markwardt, C., Marshall, F., Palmer, D., and Sakamoto, T.: 2006, *GRB Coordinates Network* 4487

Phinney, E. S.: 1991, *Astrophys. J., Lett.* **380**, L17

Piran, T.: 2005, *Reviews of Modern Physics* **76**, 1143

Piran, T. and Sari, R.: 1998, in C. A. Meegan, R. D. Preece, and T. M. Koshut (eds.), *American Institute of Physics Conference Series*, Vol. 428 of *American Institute of Physics Conference Series*, pp 662–+

Piro, L., Frail, D. A., Gorosabel, J., Garmire, G., Soffitta, P., Amati, L., Andersen, M. I., Antonelli, L. A., Berger, E., Frontera, F., Fynbo, J., Gandolfi, G., Garcia, M. R., Hjorth, J., Zand, J. i., Jensen, B. L., Masetti, N., Møller, P., Pedersen, H., Pian, E., and Wieringa, M. H.: 2002, *Astrophys. J.* **577**, 680

Piro, L., Garmire, G., Garcia, M., Stratta, G., Costa, E., Feroci, M., Mészáros, P., Vietri, M., Bradt, H., Frail, D., Frontera, F., Halpern, J., Heise, J., Hurley, K., Kawai, N., Kippen, R. M., Marshall, F., Murakami, T., Sokolov, V. V., Takeshima, T., and Yoshida, A.: 2000, *Science* **290**, 955

Popham, R., Woosley, S. E., and Fryer, C.: 1999, *Astrophys. J.* **518**, 356

Preece, R. D., Briggs, M. S., Mallozzi, R. S., Pendleton, G. N., Paciesas, W. S., and Band, D. L.: 2000, *Astrophys. J., Suppl. Ser.* **126**, 19

Qin, Y.-P., Xie, G.-Z., Xue, S.-J., Liang, E.-W., Zheng, X.-T., and Mei, D.-C.: 2000, *Publ. Astron. Soc. Jpn.* **52**, 759

Quimby, R., McMahon, E., and Murphy, J.: 2004, in E. Fenimore and M. Galassi (eds.), *Gamma-Ray Bursts: 30 Years of Discovery*, Vol. 727 of *American Institute of Physics Conference Series*, pp 529–532

Rees, M. J.: 1999, *Astron. Astrophys. Suppl. Ser.* **138**, L491

Rees, M. J. and Mészáros, P.: 1992, *Mon. Not. R. Astron. Soc.* **258**, 41P

Rees, M. J. and Mészáros, P.: 1994a, *Astrophys. J., Lett.* **430**, L93

Rees, M. J. and Mészáros, P.: 1994b, *Astrophys. J., Lett.* **430**, L93

Rees, M. J. and Mészáros, P.: 1998, *Astrophys. J., Lett.* **496**, L1+

Reeves, J. N., Watson, D., Osborne, J. P., Pounds, K. A., O'Brien, P. T., Short, A. D. T., Turner, M. J. L., Watson, M. G., Mason, K. O., Ehle, M., and Schartel, N.: 2002, *Nature* **416**, 512

Reichart, D., Nysewander, M., Moran, J., Bartelme, J., Bayliss, M., Foster, A., Clemens, J. C., Price, P., Evans, C., Salmonson, J., Trammell, S., Carney, B., Keohane, J., and Gotwals, R.: 2005, *Nuovo Cimento C Geophysics Space Physics C* **28**, 767

Reichart, D. E.: 1999, *Astrophys. J., Lett.* **521**, L111

Reichart, D. E., Lamb, D. Q., Fenimore, E. E., Ramirez-Ruiz, E., Cline, T. L., and Hurley, K.: 2001, *Astrophys. J.* **552**, 57

Rhoads, J. E.: 1999, *Astrophys. J.* **525**, 737

Ricker, G. R., Atteia, J.-L., Crew, G. B., Doty, J. P., Fenimore, E. E., Galassi, M., Graziani, C., Hurley, K., Jernigan, J. G., Kawai, N., Lamb, D. Q., Matsuoka, M., Pizzichini, G., Shirasaki, Y., Tamagawa, T., Vanderspek, R., Vedrenne, G., Villasenor, J., Woosley, S. E., and Yoshida, A.: 2003, in G. R. Ricker and R. K. Vanderspek (eds.), *Gamma-Ray Burst and Afterglow Astronomy 2001: A Workshop Celebrating the First Year of the HETE Mission*, Vol. 662 of *American Institute of Physics Conference Series*, pp 3–16

Robinson, W. G., Schechter, P. L., and Janes, C. C.: 1982, in G. Burbidge and L. D. Barr (eds.), *International Conference on Advanced Technology Optical Telescopes*, Vol.

332 of *Presented at the Society of Photo-Optical Instrumentation Engineers (SPIE) Conference*, pp 238–242

Rol, E., Wijers, R. A. M. J., Kouveliotou, C., Kaper, L., and Kaneko, Y.: 2005, *Astrophys. J.* **624**, 868

Roming, P. W. A., Kennedy, T. E., Mason, K. O., Nousek, J. A., Ahr, L., Bingham, R. E., Broos, P. S., Carter, M. J., Hancock, B. K., Huckle, H. E., Hunsberger, S. D., Kawakami, H., Killough, R., Koch, T. S., McLelland, M. K., Smith, K., Smith, P. J., Soto, J. C., Boyd, P. T., Breeveld, A. A., Holland, S. T., Ivanushkina, M., Pryzby, M. S., Still, M. D., and Stock, J.: 2005, *Space Science Reviews* **120**, 95

Roming, P. W. A., Schady, P., Fox, D. B., Zhang, B., Liang, E., Mason, K. O., Rol, E., Burrows, D. N., Blustin, A. J., Boyd, P. T., Brown, P., Holland, S. T., McGowan, K., Landsman, W. B., Page, K. L., Rhoads, J. E., Rosen, S. R., Vanden Berk, D., Barthelmy, S. D., Breeveld, A. A., Cucchiara, A., De Pasquale, M., Fenimore, E. E., Gehrels, N., Gronwall, C., Grupe, D., Goad, M. R., Ivanushkina, M., James, C., Kennea, J. A., Kobayashi, S., Mangano, V., Mészáros, P., Morgan, A. N., Nousek, J. A., Osborne, J. P., Palmer, D. M., Poole, T., Still, M. D., Tagliaferri, G., and Zane, S.: 2006a, *Astrophys. J.* **652**, 1416

Roming, P. W. A., Vanden Berk, D., Pal'shin, V., Pagani, C., Norris, J., Kumar, P., Krimm, H., Holland, S. T., Gronwall, C., Blustin, A. J., Zhang, B., Schady, P., Sakamoto, T., Osborne, J. P., Nousek, J. A., Marshall, F. E., Mészáros, P., Golenetskii, S. V., Gehrels, N., Frederiks, D. D., Campana, S., Burrows, D. N., Boyd, P. T., Barthelmy, S., and Aptekar, R. L.: 2006b, *Astrophys. J.* **651**, 985

Rosswog, S. and Davies, M. B.: 2002, *Mon. Not. R. Astron. Soc.* **334**, 481

Rosswog, S., Ramirez-Ruiz, E., and Davies, M. B.: 2003, *Mon. Not. R. Astron. Soc.* **345**, 1077

Ruffert, M. and Janka, H.-T.: 1999, *Astron. Astrophys.* **344**, 573

Ruffert, M. and Janka, H.-T.: 2003, in *AIP Conf. Proc. 662: Gamma-Ray Burst and Afterglow Astronomy 2001: A Workshop Celebrating the First Year of the HETE Mission*, p. 193

Rumyantsev, V., Pozanenko, A., Ibrahimov, M., and Asfandyarov, I.: 2006, *GRB Coordinates Network* 5306

Rykoff, E. S., Aharonian, F., Akerlof, C. W., Alatalo, K., Ashley, M. C. B., Güver, T., Horns, D., Kehoe, R. L., Kiziloğlu, Ü., McKay, T. A., Özel, M., Phillips, A., Quimby, R. M., Schaefer, B. E., Smith, D. A., Swan, H. F., Vestrand, W. T., Wheeler, J. C., Wren, J., and Yost, S. A.: 2005a, *Astrophys. J.* **631**, 1032

Rykoff, E. S., Mangano, V., Yost, S. A., Sari, R., Aharonian, F., Akerlof, C. W., Ashley, M. C. B., Barthelmy, S. D., Burrows, D. N., Gehrels, N., Göğüş, E., Güver, T., Horns, D., Kızıloğlu, Ü., Krimm, H. A., McKay, T. A., Özel, M., Phillips, A., Quimby, R. M., Rowell, G., Rujopakarn, W., Schaefer, B. E., Smith, D. A., Swan, H. F., Vestrand, W. T., Wheeler, J. C., Wren, J., and Yuan, F.: 2006a, *Astrophys. J., Lett.* **638**, L5

Rykoff, E. S., Yost, S. A., Krimm, H. A., Aharonian, F., Akerlof, C. W., Alatalo, K., Ashley, M. C. B., Barthelmy, S. D., Gehrels, N., Göğüş, E., Güver, T., Horns, D., Kızıloğlu, Ü., McKay, T. A., Özel, M., Phillips, A., Quimby, R. M., Rujopakarn, W., Schaefer, B. E., Smith, D. A., Swan, H. F., Vestrand, W. T., Wheeler, J. C., and Wren, J.: 2005b, *Astrophys. J., Lett.* **631**, L121

Rykoff, E. S., Yost, S. A., Swan, H., and Rujopakarn, W.: 2006b, *GRB Coordinates Network* 5166

Sahu, K. C., Livio, M., Petro, L., Macchetto, F. D., van Paradijs, J., Kouveliotou, C., Fishman, G. J., Meegan, C. A., Groot, P. J., and Galama, T.: 1997, *Nature* **387**, 476

Salvaterra, R. and Chincarini, G.: 2007, *Astrophys. J., Lett.* **656**, L49

Sari, R. and Piran, T.: 1995, *Astrophys. J., Lett.* **455**, L143+

Sari, R. and Piran, T.: 1997, *Astrophys. J.* **485**, 270

Sari, R. and Piran, T.: 1999a, *Astrophys. J., Lett.* **517**, L109

Sari, R. and Piran, T.: 1999b, *Astrophys. J.* **520**, 641

Sari, R., Piran, T., and Halpern, J. P.: 1999, *Astrophys. J., Lett.* **519**, L17

Sari, R., Piran, T., and Narayan, R.: 1998, *Astrophys. J., Lett.* **497**, L17

Savaglio, S. and Fall, S. M.: 2004, *Astrophys. J.* **614**, 293

Schaefer, B. E.: 1981, *Nature* **294**, 722

Schaefer, B. E.: 1994, in G. J. Fishman (ed.), *Gamma-Ray Bursts*, Vol. 307 of *American Institute of Physics Conference Series*, pp 382–+

Schaefer, B. E.: 2007, *Astrophys. J.* **660**, 16

Schmidt, B., Wieringa, M., Frail, D. A., and Soderberg, A.: 2006, *GRB Coordinates Network* 4547

Schönfelder, V., Aarts, H., Bennett, K., de Boer, H., Clear, J., Collmar, W., Connors, A., Deerenberg, A., Diehl, R., von Dordrecht, A., den Herder, J. W., Hermsen, W., Kippen, M., Kuiper, L., Lichti, G., Lockwood, J., Macri, J., McConnell, M., Morris, D., Much, R., Ryan, J., Simpson, G., Snelling, M., Stacy, G., Steinle, H., Strong, A., Swanenburg, B. N., Taylor, B., de Vries, C., and Winkler, C.: 1993, *Astrophys. J., Suppl. Ser.* **86**, 657

Shao, L. and Dai, Z. G.: 2005, *Astrophys. J.* **633**, 1027

Shirasaki, Y., Graziani, C., Matsuoka, M., Tamagawa, T., Torii, K., Sakamoto, T., Yoshida, A., Fenimore, E., Galassi, M., Tavenner, T., Donaghy, T., Ricker, G., Atteia, J., Kawai, N., Lamb, D., Woosley, S., Villasenor, J., Vanderspek, R., Doty, J., Crew, G., Monnelly, G., Butler, N., Cline, T., Jernigan, J. G., Levine, A., Martel, F., Morgan, E., Prigozhin, G., Azzibrouck, G., Braga, J., Manchanda, R., Pizzichini, G., Boer, M., Olive, J., Dezalay, J., and Hurley, K.: 2002, *GRB Coordinates Network* 1565

Soderberg, A. M., Berger, E., Kasliwal, M., Frail, D. A., Price, P. A., Schmidt, B. P., Kulkarni, S. R., Fox, D. B., Cenko, S. B., Gal-Yam, A., Nakar, E., and Roth, K. C.: 2006, *Astrophys. J.* **650**, 261

Soderberg, A. M., Kulkarni, S. R., Berger, E., Fox, D. W., Sako, M., Frail, D. A., Gal-Yam, A., Moon, D. S., Cenko, S. B., Yost, S. A., Phillips, M. M., Persson, S. E., Freedman, W. L., Wyatt, P., Jayawardhana, R., and Paulson, D.: 2004, *Nature* **430**, 648

Spruit, H. C., Daigne, F., and Drenkhahn, G.: 2001, *Astron. Astrophys.* **369**, 694

Stanek, K. Z., Dai, X., Prieto, J. L., An, D., Garnavich, P. M., Calkins, M. L., Serven, J., Worthey, G., Hao, H., Dobrzycki, A., Howk, C., and Matheson, T.: 2007, *Astrophys. J., Lett.* **654**, L21

Stanek, K. Z., Matheson, T., Garnavich, P. M., Martini, P., Berlind, P., Caldwell, N., Challis, P., Brown, W. R., Schild, R., Krisciunas, K., Calkins, M. L., Lee, J. C., Hathi, N., Jansen, R. A., Windhorst, R., Echevarria, L., Eisenstein, D. J., Pindor, B., Olszewski, E. W., Harding, P., Holland, S. T., and Bersier, D.: 2003, *Astrophys. J., Lett.* **591**, L170

Steele, I. A., Bates, S. D., Carter, D., Clarke, D., Gomboc, A., Guidorzi, C., Melandri, A., Monfardini, A., Mottram, C. J., Mundell, C. G., Scott, A. B., Smith, R. J., and Swindlehurst, J.: 2006, in I. S. McLean and M. Iye (eds.), *Ground-based and Airborne Instrumentation for Astronomy, pp. 62695M*, Vol. 6269 of *Presented at the Society of Photo-Optical Instrumentation Engineers (SPIE) Conference*

Stern, B. E. and Poutanen, J.: 2004, *Mon. Not. R. Astron. Soc.* **352**, L35

Sweet, M. R.: 2005, *Serial Programming Guide for POSIX Operating Systems, 5th edition*, http://www.easysw.com/ mike/serial/serial.html

Szabados, L.: 2003, in T. D. Oswalt (ed.), *The Future of Small Telescopes in the New Millennium*, Vol. III, pp 207–223, Kluwer Academic Publishers

Tavani, M.: 1996, *Astrophys. J.* **466**, 768

Tavani, M., Barbiellini, G., Argan, A., Basset, M., Boffelli, F., Bulgarelli, A., Caraveo, P., Chen, A., Costa, E., De Paris, G., Del Monte, E., Di Cocco, G., Donnarumma, I., Feroci, M., Fiorini, M., Foggetta, L., Froysland, T., Frutti, M., Fuschino, F., Galli, M., Gianotti, F., Giuliani, A., Labanti, C., Lapshov, I., Lazzarotto, F., Liello, F., Lipari, P., Longo, F., Marisaldi, M., Mastropietro, M., Mattaini, E., Mauri, F., Mereghetti, S., Morelli, E., Morselli, A., Pacciani, L., Pellizzoni, A., Perotti, F., Picozza, P., Pittori, C., Pontoni, C., Porrovecchio, G., Prest, M., Pucella, G., Rapisarda, M., Rossi, E., Rubini, A., Soffitta, P., Traci, A., Trifoglio, M., Trois, A., Vallazza, E., Vercellone, S., Zambra, A., and Zanello, D.: 2006, in *Space Telescopes and Instrumentation II: Ultraviolet to Gamma Ray. Edited by Turner, Martin J. L.; Hasinger, Günther.*, Vol. 6266 of *Presented at the Society of Photo-Optical Instrumentation Engineers (SPIE) Conference*

Taylor, J. H. and Weisberg, J. M.: 1982, *Astrophys. J.* **253**, 908

Terra, F., Greco, G., Bartolini, C., Guarnieri, A., Piccioni, A., Nanni, D., Bruni, I., Galleti, S., and Pizzichini, G.: 2006, *GRB Coordinates Network* 5192

Thoene, C. C., Fynbo, J. P. U., and Joergensen, U. G.: 2006, *GRB Coordinates Network* 5179

Thompson, C.: 1994, *Mon. Not. R. Astron. Soc.* **270**, 480

Thompson, C. and Duncan, R. C.: 1993, *Astrophys. J.* **408**, 194

Tody, D.: 1993, in R. J. Hanisch, R. J. V. Brissenden, and J. Barnes (eds.), *Astronomical Data Analysis Software and Systems II*, Vol. 52 of *Astronomical Society of the Pacific Conference Series*, pp 173–+

Ubertini, P., Lebrun, F., Di Cocco, G., Bazzano, A., Bird, A. J., Broenstad, K., Goldwurm, A., La Rosa, G., Labanti, C., Laurent, P., Mirabel, I. F., Quadrini, E. M., Ramsey, B., Reglero, V., Sabau, L., Sacco, B., Staubert, R., Vigroux, L., Weisskopf, M. C., and Zdziarski, A. A.: 2003, *Astron. Astrophys.* **411**, L131

Usov, V. V.: 1992, *Nature* **357**, 472

Usov, V. V.: 1994, *Mon. Not. R. Astron. Soc.* **267**, 1035

van Breda, I. G.: 1995, in M. F. Bode (ed.), *Robotic Observatories*, Wiley - Praxis Series in Astronomy and Astrophysics, pp 101–105, John Wiley & Sons

van Paradijs, J., Groot, P. J., Galama, T., Kouveliotou, C., Strom, R. G., Telting, J., Rutten, R. G. M., Fishman, G. J., Meegan, C. A., Pettini, M., Tanvir, N., Bloom, J., Pedersen, H., Nordgaard-Nielsen, H. U., Linden-Vornle, M., Melnick, J., van der Steene, G., Bremer, M., Naber, R., Heise, J., In't Zand, J., Costa, E., Feroci, M., Piro, L., Frontera, F., Zavattini, G., Nicastro, L., Palazzi, E., Bennet, K., Hanlon, L., and Parmar, A.: 1997, *Nature* **386**, 686

Vedrenne, G., Roques, J.-P., Schönfelder, V., Mandrou, P., Lichti, G. G., von Kienlin, A., Cordier, B., Schanne, S., Knödlseder, J., Skinner, G., Jean, P., Sanchez, F., Caraveo, P., Teegarden, B., von Ballmoos, P., Bouchet, L., Paul, P., Matteson, J., Boggs, S., Wunderer, C., Leleux, P., Weidenspointner, G., Durouchoux, P., Diehl, R., Strong, A., Cassé, M., Clair, M. A., and André, Y.: 2003, *Astron. Astrophys.* **411**, L63

Vestrand, W. T., Borozdin, K. N., Brumby, S. P., Casperson, D. E., Fenimore, E. E., Galassi, M. C., McGowan, K., Perkins, S. J., Priedhorsky, W. C., Starr, D., White, R., Wozniak, P., and Wren, J. A.: 2002, in R. I. Kibrick (ed.), *Advanced Global Communications Technologies for Astronomy II*, Vol. 4845 of *Presented at the Society of Photo-Optical Instrumentation Engineers (SPIE) Conference*, pp 126–136

Vestrand, W. T., Theiler, J., and Woznia, P. R.: 2004a, *Astronomische Nachrichten* **325**, 477

Vestrand, W. T., Theiler, J., and Woznia, P. R.: 2004b, *Astronomische Nachrichten* **325**, 477

Vestrand, W. T., Wozniak, P. R., Wren, J. A., Fenimore, E. E., Sakamoto, T., White, R. R., Casperson, D., Davis, H., Evans, S., Galassi, M., McGowan, K. E., Schier, J. A., Asa, J. W., Barthelmy, S. D., Cummings, J. R., Gehrels, N., Hullinger, D., Krimm, H. A., Markwardt, C. B., McLean, K., Palmer, D., Parsons, A., and Tueller, J.: 2005, *Nature* **435**, 178

Vestrand, W. T., Wren, J. A., Wozniak, P. R., Aptekar, R., Golentskii, S., Pal'Shin, V., Sakamoto, T., White, R. R., Evans, S., Casperson, D., and Fenimore, E.: 2006, *Nature* **442**, 172

Vietri, M., Ghisellini, G., Lazzati, D., Fiore, F., and Stella, L.: 2001, *Astrophys. J., Lett.* **550**, L43

Vietri, M. and Stella, L.: 1998, *Astrophys. J., Lett.* **507**, L45

Vietri, M. and Stella, L.: 1999, *Astrophys. J., Lett.* **527**, L43

Villasenor, J. N., Dill, R., Doty, J. P., Monnelly, G., Vanderspek, R., Kissel, S., Prigozhin, G., Crew, G. B., and Ricker, G. R.: 2003, in G. R. Ricker and R. K. Vanderspek (eds.), *Gamma-Ray Burst and Afterglow Astronomy 2001: A Workshop Celebrating the First Year of the HETE Mission*, Vol. 662 of *American Institute of Physics Conference Series*, pp 33–37

Villasenor, J. S., Lamb, D. Q., Ricker, G. R., Atteia, J.-L., Kawai, N., Butler, N., Nakagawa, Y., Jernigan, J. G., Boer, M., Crew, G. B., Donaghy, T. Q., Doty, J., Fenimore, E. E., Galassi, M., Graziani, C., Hurley, K., Levine, A., Martel, F., Matsuoka, M.,

Olive, J.-F., Prigozhin, G., Sakamoto, T., Shirasaki, Y., Suzuki, M., Tamagawa, T., Vanderspek, R., Woosley, S. E., Yoshida, A., Braga, J., Manchanda, R., Pizzichini, G., Takagishi, K., and Yamauchi, M.: 2005, *Nature* **437**, 855

Vlahakis, N. and Königl, A.: 2003, *Astrophys. J.* **596**, 1080

von Kienlin, A., Beckmann, V., Rau, A., Arend, N., Bennett, K., McBreen, B., Connell, P., Deluit, S., Hanlon, L., Hurley, K., Kippen, M., Lichti, G. G., Moran, L., Preece, R., Roques, J.-P., Schönfelder, V., Skinner, G., Strong, A., and Williams, R.: 2003, *Astron. Astrophys.* **411**, L299

Vreeswijk, P. M., Ellison, S. L., Ledoux, C., Wijers, R. A. M. J., Fynbo, J. P. U., Møller, P., Henden, A., Hjorth, J., Masi, G., Rol, E., Jensen, B. L., Tanvir, N., Levan, A., Castro Cerón, J. M., Gorosabel, J., Castro-Tirado, A. J., Fruchter, A. S., Kouveliotou, C., Burud, I., Rhoads, J., Masetti, N., Palazzi, E., Pian, E., Pedersen, H., Kaper, L., Gilmore, A., Kilmartin, P., Buckle, J. V., Seigar, M. S., Hartmann, D. H., Lindsay, K., and van den Heuvel, E. P. J.: 2004, *Astron. Astrophys.* **419**, 927

Vreeswijk, P. M., Fruchter, A., Kaper, L., Rol, E., Galama, T. J., van Paradijs, J., Kouveliotou, C., Wijers, R. A. M. J., Pian, E., Palazzi, E., Masetti, N., Frontera, F., Savaglio, S., Reinsch, K., Hessman, F. V., Beuermann, K., Nicklas, H., and van den Heuvel, E. P. J.: 2001, *Astrophys. J.* **546**, 672

Wallace, P.: 1988, in L. B. Robinson (ed.), *Instrumentation for Ground-Based Optical Astronomy, Present and Future. The Ninth Santa Cruz Summer Workshop in Astronomy and Astrophysics, July 13- 24, 1987, Lick Observatory*, pp 691–+, Springer-Verlag, New York, NY, ISBN # 0-387-96730-3

Wang, X. and Loeb, A.: 2000, *Astrophys. J.* **535**, 788

Watson, D., Reeves, J. N., Hjorth, J., Jakobsson, P., and Pedersen, K.: 2003, *Astrophys. J., Lett.* **595**, L29

Wei, D. M. and Lu, T.: 2002, *Mon. Not. R. Astron. Soc.* **332**, 994

Wei, D. M., Yan, T., and Fan, Y. Z.: 2006, *Astrophys. J., Lett.* **636**, L69

Welch, B., Jones, K., and Hobbs, J.: 1999, *Practical Programming in Tcl and Tk*, Chapt. 44, pp 603–638, Prentice Hall, 3rd edition, http://www.beedub.com/book/3rd/Cprogint.pdf

White, R. R. and Allan, A.: 2008, *Astronomische Nachrichten* **329**, 232

White, R. R., Allan, A., Barthelmy, S., Bloom, J., Graham, M., Hessman, F. V., Marka, S., Rots, A., Scholberg, K., Seaman, R., Stoughton, C., Vestrand, W. T., Williams, R., and Wozniak, P. R.: 2006, *Astronomische Nachrichten* **327**, 775

White, R. R., Wren, J., Davis, H. R., Galassi, M., Starr, D., Vestrand, W. T., and Wozniak, P.: 2004, in H. Lewis and G. Raffi (eds.), *Advanced Software, Control, and Communication Systems for Astronomy*, Vol. 5496 of *Presented at the Society of Photo-Optical Instrumentation Engineers (SPIE) Conference*, pp 302–312

Wijers, R. A. M. J., Rees, M. J., and Mészáros, P.: 1997, *Mon. Not. R. Astron. Soc.* **288**, L51

Williams, R. J. and Mulherin, J.: 2001, in B. Paczynski, W.-P. Chen, and C. Lemme (eds.), *IAU Colloq. 183: Small Telescope Astronomy on Global Scales*, Vol. 246 of *Astronomical Society of the Pacific Conference Series*, pp 95–+

Winkler, C., Courvoisier, T. J.-L., Di Cocco, G., Gehrels, N., Giménez, A., Grebenev, S., Hermsen, W., Mas-Hesse, J. M., Lebrun, F., Lund, N., Palumbo, G. G. C., Paul, J., Roques, J.-P., Schnopper, H., Schönfelder, V., Sunyaev, R., Teegarden, B., Ubertini, P., Vedrenne, G., and Dean, A. J.: 2003, *Astron. Astrophys.* **411**, L1

Woosley, S. E.: 1993, *Astrophys. J.* **405**, 273

Woosley, S. E. and Bloom, J. S.: 2006, *Ann. Rev. Astron. Astrophys.* **44**, 507

Wozniak, P., Vestrand, W. T., Starr, D., Wren, J., Borozdin, K., Brumby, S., Casperson, D., Galassi, M., McGowan, K., and White, R.: 2002, *GRB Coordinates Network* 1757

Woźniak, P. R., Vestrand, W. T., Wren, J. A., White, R. R., Evans, S. M., and Casperson, D.: 2005, *Astrophys. J., Lett.* **627**, L13

Woźniak, P. R., Vestrand, W. T., Wren, J. A., White, R. R., Evans, S. M., and Casperson, D.: 2006, *Astrophys. J., Lett.* **642**, L99

Yi, T., Liang, E., Qin, Y., and Lu, R.: 2006, *Mon. Not. R. Astron. Soc.* **367**, 1751

Yost, S. A., Aharonian, F., Akerlof, C. W., Ashley, M. C. B., Barthelmy, S., Gehrels, N., Göğüş, E., Güver, T., Horns, D., Kızılŏlu, Ü., Krimm, H. A., McKay, T. A., Özel, M., Phillips, A., Quimby, R. M., Rowell, G., Rujopakarn, W., Rykoff, E. S., Schaefer, B. E., Smith, D. A., Swan, H. F., Vestrand, W. T., Wheeler, J. C., Wren, J., and Yuan, F.: 2007, *Astrophys. J.* **669**, 1107

Yost, S. A., Alatalo, K., Rykoff, E. S., Aharonian, F., Akerlof, C. W., Ashley, M. C. B., Blake, C. H., Bloom, J. S., Boettcher, M., Falco, E. E., Göğüş, E., Güver, T., Halpern, J. P., Horns, D., Joshi, M., Kızıloğlu, Ü., McKay, T. A., Mirabal, N., Özel, M., Phillips, A., Quimby, R. M., Rujopakarn, W., Schaefer, B. E., Shields, J. C., Skrutskie, M., Smith, D. A., Starr, D. L., Swan, H. F., Szentgyorgyi, A., Vestrand, W. T., Wheeler, J. C., and Wren, J.: 2006a, *Astrophys. J.* **636**, 959

Yost, S. A., Yuan, F., Swan, H., and Akerlof, C.: 2006b, *GRB Coordinates Network* 4488

Zeh, A., Klose, S., and Hartmann, D. H.: 2004, *Astrophys. J.* **609**, 952

Zeh, A., Klose, S., and Kann, D. A.: 2006, *Astrophys. J.* **637**, 889

Zerbi, F. M., Chincarini, G., Rodonó, M., Antonelli, A., Burderi, L., Campana, S., Conconi, P., Covino, S., Cutispoto, G., Ghisellini, G., Lazzati, D., Martinetti, E., Molinari, E., Sardone, S., Stella, L., and Vitali, F.: 2001, in E. Costa, F. Frontera, and J. Hjorth (eds.), *Gamma-ray Bursts in the Afterglow Era*, pp 434–+

Zhang, B.: 2007, *Chinese Journal of Astronomy and Astrophysics* **7**, 1

Zhang, B., Fan, Y. Z., Dyks, J., Kobayashi, S., Mészáros, P., Burrows, D. N., Nousek, J. A., and Gehrels, N.: 2006, *Astrophys. J.* **642**, 354

Zhang, B. and Kobayashi, S.: 2005, *Astrophys. J.* **628**, 315

Zhang, B., Kobayashi, S., and Mészáros, P.: 2003a, *Astrophys. J.* **595**, 950

Zhang, B. and Mészáros, P.: 2002, *Astrophys. J.* **566**, 712

Zhang, B. and Mészáros, P.: 2004, *International Journal of Modern Physics A* **19**, 2385

Zhang, B.-B., Liang, E.-W., and Zhang, B.: 2007, *Astrophys. J.* **666**, 1002

Zhang, W., Woosley, S. E., and MacFadyen, A. I.: 2003b, *Astrophys. J.* **586**, 356

Appendix A

Pinouts for Dynostar X3 to PC Serial Port Interface

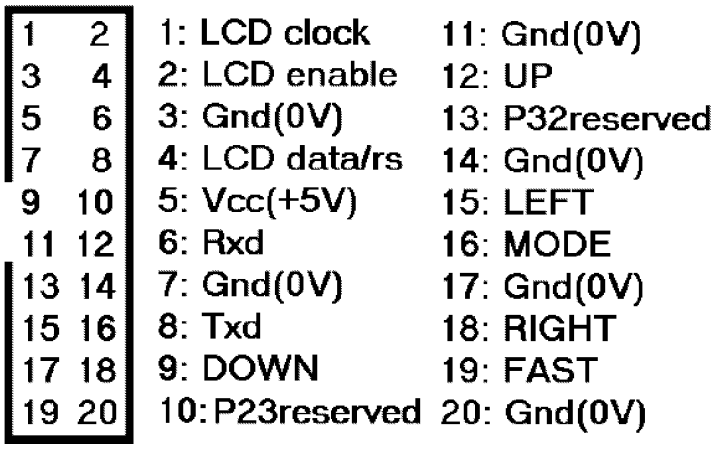

Figure A.1: Pinout for Dynostar–X3 20–pin connector. *From Boxdörfer (2003).*

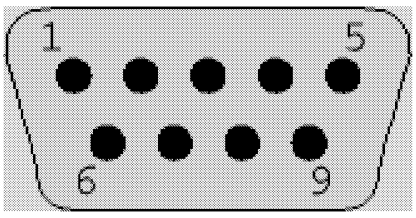

Pin	Description
1	**DCD** – Data Carrier Detect
2	**RXD** – Received Data
3	**TXD** – Transmitted Data
4	**DTR** – Data Terminal Ready
5	**GND** – Logic Ground
6	Data Set Ready
7	**RTS** – Request To Send
8	**CTS** – Clear To Send
9	Ring Detect

Figure A.2: Pinout for PC 9–pin RS–232 port. *From Sweet (2005).*

Appendix B

RTS2 Configuration Files for Watcher

rts2.ini (watcher1)

```
[database]
name = stars
[observatory]
altitude = 1400
latitude = -29.0389
longtitude = 26.4056
epoch_id = 3
day_horizont = 1 # Sun is below horizont, when its calculated altitude
night_horizont = -6.0 # Night starts, when sun gets below that value
evening_time = 1800 # Evening time - time to cool cameras in seconds
morning_time = 1800 # Time to cool off cameras in seconds
flat_sun_min = -6.0
flat_sun_max = -5.0
soap = 81
min_alt = 20
model_step_type = -2
[centrald]
morning_off = false
morning_standby = false
reboot_on = no
[grbd]
port = 5198
server = "-"
seplimit = 0.1
[swift]
min_horizon = 20
```

```
[imgproc]
astrometry = "/etc/rts2/img_process"
astrometry_timeout = 300
imageglob = "/images/002/que/*/*.fits"
obsprocess = "/etc/rts2/obsprocess"
darkprocess = "/etc/rts2/darkprocess"
flatprocess = "/etc/rts2/flatprocess"
[C0]
xplate = 0.84
yplate = 0.84
rotang = 354.5
xoa = 512
yoa = 512
flip = 1
flatmin = 20
flatmax = 3000
darks = "1 5 10 20 30 40 60 120"
filter = "B V R I C"
blocked_by = "FW0 F0 T0"
script = "F 2 E 60"
[T0]
blocked_by = "C0"
```

apogee.ini (watcher1)

```
[system]
Interface = PCI
Base = 0x0
Cable = LONG
Data_Bits = 14
Sensor = CCD
Mode = 0x1
Test = 0x4
Shutter_Speed = Normal
Shutter_Bits = 0x00
MaxBinX = 8
MaxBinY = 63
Guider_Relays = False
[geometry]
Columns = 1040
```

```
Rows = 1034
ImgCols = 1024
ImgRows = 1024
BIC = 9
BIR = 7
SkipC = 6
SkipR = 2
HFlush = 8
VFlush = 50
[temp]
Control = True
Target = -15.0
Cal = 165
Scale = 2.1
[ccd]
Sensor = KAF-1001e
Color = False
Noise = 10
Gain = 8.0
PixelXSize = 24
PixelYSize = 24
```

devices (watcher1)

```
dome dublin DOME -s /usr/local/bin/execSms -O -M jfrench@bermuda.ucd.ie,
gmelady@bermuda.ucd.ie, lorraine.hanlon@ucd.ie, MeintjPJ.SCI@mail.uovs.ac.za,petr@kubanek.net
focusd robofocus F0 -f /dev/ttyS4 -x C0 -p 10060
filterd ifw FW0 -f /dev/ttyS1 -F "B:V:R:I:C"
```

devices (watcher2)

```
camd    apogee  C0      -c -10 -W FW0 -F F0 -r 354.5
teld    paramount  T0   -f /dev/ttyS1 -m /etc/rts2/model.dat -D -2550000
```

services (watcher1)

```
soapd SOAP
grbd GRBD
selector SEL
imgproc  IMGP
executor EXEC
```

centrald (watcher1)

```
centrald
--server localhost
```

centrald (watcher2)

```
centrald
--server watcher1
```

Appendix C

Paramount ME Configuration File

```
********************** Axis 0 (RA) Control version 2.5.19 ********************
Index angle: 267
Base rate: 43067265
Maximum speed: 1040000000
Acceleration: 400
Minimum position limit: -4960000
Maximum position limit: 1120000
Sensor (from sync): 5
Guide: 672926
PEC ratio: 10
Maximum position error: 16000
EMF constants: 72
Home velocity high: 660000000
Home velocity medium: 110000000
Home velocity low: 3900000
Home direction, sense: 1
Home mode, required, Joystick, In-out-in: 1794
Home index offset: 0
PEC cutoff speed: 0
Maximum voltage: 15
Maximum gain: 150
Home sense 1: 1
Home sense 2: 0
Cur pos: 187762
********************** Axis 1 (DEC) Control version 2.5.19 *******************
Index angle: 1786
Base rate: 0
```

```
Maximum speed: 1040000000
Acceleration: 400
Minimum position limit: -5460000
Maximum position limit: 1700000
Sensor (from sync): 4
Guide: 438102
PEC ratio: 10
Maximum position error: 16000
EMF constants: 72
Home velocity high: 660000000
Home velocity medium: 110000000
Home velocity low: 3900000
Home direction, sense: 1
Home mode, required, Joystick, In-out-in: 1794
Home index offset: 0
PEC cutoff speed: 0
Maximum voltage: 15
Maximum gain: 150
Home sense 1: 1
Home sense 2: 0
Cur pos: -1370298
```

Appendix D

Configuration File for Meteo Weather Station Tools

All the configuration information used by the meteo weather station tools to communicate with the station and with the database are stored in an XML file, which also describes all the graphs that are produced from the data. Full details on configuration options can be found in the `meteo.xml` man page. The current configuration in use on Watcher's weather station is stored in `/usr/local/etc/meteo.xml` on watcher1, and is shown below.

```
<meteo>
  <!--
    database configuration
  -->
  <database>
    <hostname>watcher1</hostname>
    <dbname>meteo</dbname>
    <user>meteo</user>
    <password>meteopass</password>
    <!--<writer>meteoupdate</writer>
    <writerpassword>m57cwrt</writerpassword> -->
    <writer>mtp</writer>
    <writerpassword>mtpass</writerpassword>
    <msgqueue>/var/lib/meteodb-queue</msgqueue>
    <updatefile>/var/log/meteoupdate.log</updatefile>
    <prefix>meteo</prefix>
  </database>
```

```
  <!--
    station configuration
  -->
  <station name="Boyden">
    <url>file:///dev/ttyS0</url>
    <type>VantagePro</type>
    <speed>19200</speed>
    <sensors>
      <sensor name="console">
        <field>temperature</field>
        <field>humidity</field>
        <field>barometer</field>
        <field>battery</field>
        <field>sunrise</field>
        <field>sunset</field>
      </sensor>
      <sensor name="iss">
        <field>temperature</field>
        <field>humidity</field>
        <field>rain</field>
        <field>rainrate</field>
        <field>wind</field>
        <field>transmitter</field>
      </sensor>
      <sensor name="leaf1">
        <field>wetness</field>
        <field>temperature</field>
      </sensor>
      <sensor name="leaf2">
         <field>temperature</field>
      </sensor>
    </sensors>

    <averages>
      <sensor name="console">
<average name="temperature" base="temperature" operator="avg"/>
<average name="temperature_min" base="temperature" operator="min"/>
<average name="temperature_max" base="temperature" operator="max"/>
<average name="humidity" base="humidity" operator="avg"/>
<average name="humidity_min" base="humidity" operator="min"/>
```

```
<average name="humidity_max" base="humidity" operator="max"/>
<average name="barometer" base="barometer" operator="avg"/>
<average name="barometer_min" base="barometer" operator="min"/>
<average name="barometer_max" base="barometer" operator="max"/>
<average name="battery" base="battery" operator="avg"/>
<average name="sunrise" base="sunrise" operator="avg"/>
<average name="sunset" base="sunset" operator="avg"/>
      </sensor>
      <sensor name="iss">
<average name="temperature" base="temperature" operator="avg"/>
<average name="temperature_min" base="temperature" operator="min"/>
<average name="temperature_max" base="temperature" operator="max"/>
<average name="humidity" base="humidity" operator="avg"/>
<average name="humidity_min" base="humidity" operator="min"/>
<average name="humidity_max" base="humidity" operator="max"/>
<average name="wind" base="wind" operator="wind"/>
<average name="windgust" base="windgust" operator="max"/>
<average name="rain" base="rain" operator="sum"/>
<average name="rainrate" base="rainrate" operator="avg"/>
<average name="transmitter" base="transmitter" operator="avg"/>
      </sensor>
      <sensor name="leaf1">
<average name="wetness" base="wetness" operator="avg"/>
<average name="wetness_min" base="wetness" operator="min"/>
<average name="wetness_max" base="wetness" operator="max"/>
<average name="temperature" base="temperature" operator="avg"/>
<average name="temperature_min" base="temperature" operator="min"/>
<average name="temperature_max" base="temperature" operator="max"/>
      </sensor>
      <sensor name="leaf2">
<average name="temperature" base="temperature" operator="avg"/>
<average name="temperature_min" base="temperature" operator="min"/>
<average name="temperature_max" base="temperature" operator="max"/>
      </sensor>

    </averages>
  </station>
  <!--
    Graph configurations
  -->
```

```
  <graphs lockfile="/tmp/lockfile" running="4" queued="10">
    <graph name="Boyden.temperature-new" offset="0"
height="300" width="600" bgcolor="#ffffff" fgcolor="#000000">
      <leftlabel align="center">Temperature grad C</leftlabel>
      <rightlabel align="center">relative Humidity %</rightlabel>
      <leftaxis type="dynamic" maxname="tt" minname="dd" min="-100" max="100"
origin="0" maxtickcount="20"
first="-100"
last="100" step="1" format="%.1f" ticks="yes" gridlines="yes"/>
      <rightaxis min="0" max="100" first="0" last="100" step="20" format="%3.0f"
        ticks="yes" gridlines="no"/>
      <graphwindow llx="55" lly="19" urx="555" ury="293"/>
      <channels>
<query>
  <select name="t">Boyden.iss.temperature</select>
  <select name="tmax">Boyden.iss.temperature_max</select>
  <select name="tmin">Boyden.iss.temperature_min</select>
  <select name="h">Boyden.iss.humidity</select>
  <select name="hmax">Boyden.iss.humidity_max</select>
  <select name="hmin">Boyden.iss.humidity_min</select>
  <select name="cloud_top">Boyden.leaf1.temperature</select>
  <select name="cloud_top_min">Boyden.leaf1.temperature_min</select>
  <select name="cloud_top_max">Boyden.leaf1.temperature_max</select>
  <select name="cloud_bottom">Boyden.leaf2.temperature</select>
  <select name="cloud_bottom_min">Boyden.leaf2.temperature_min</select>
  <select name="cloud_bottom_max">Boyden.leaf2.temperature_max</select>
  <data name="tt">
    <function name="floor" limit="-50">
      <function name="ceil" limit="50">
<value name="t"/>
      </function>
    </function>
  </data>
  <data name="dewpointmin">
    <function2 name="dewpoint">
      <value name="hmin"/>
      <value name="tmin"/>
    </function2>
  </data>
  <data name="dewpointmax">
```

```
    <function2 name="dewpoint">
      <value name="hmax"/>
      <value name="tmax"/>
    </function2>
  </data>
  <data name="dewpoint">
    <function2 name="dewpoint">
      <value name="h"/>
      <value name="t"/>
    </function2>
  </data>
  <data name="dd">
    <function name="floor" limit="-50">
      <value name="dewpoint"/>
    </function>
  </data>
</query>

<!-- draw graphs for the datasets as specified in the previous tags -->
<channel color="#aaaaff" type="range" scale="left"
  namelower="dewpointmin" nameupper="dewpointmax"/>
<channel color="#0000ff" type="curve" scale="left" name="dewpoint"/>
<channel color="#ffaaaa" type="range" scale="left"
  namelower="tmin" nameupper="tmax"/>
<channel color="#654321" type="curve" scale="left" name="tt"/>
<channel color="#65ff21" type="curve" scale="left" name="cloud_bottom"/>
<channel color="#ff4321" type="curve" scale="left" name="cloud_top"/>
<channel color="#dddddd" type="nodata" name="t"/>
      </channels>
    </graph>

    <!-- Temperature graph -->
    <graph name="Boyden.temperature" offset="0"
height="144" width="600" bgcolor="#ffffff" fgcolor="#000000">
      <leftlabel align="center">Temperature Out (deg C)</leftlabel>
      <leftaxis type="static" min="-5" max="30"
first="-5" last="30" step="5" format="%.0f"
ticks="yes" gridlines="yes"/>
      <graphwindow llx="55" lly="19" urx="555" ury="139"/>
      <channels>
```

```
<query>
  <select name="t">Boyden.iss.temperature</select>
  <select name="tmin">Boyden.iss.temperature_min</select>
  <select name="tmax">Boyden.iss.temperature_max</select>
  <select name="h">Boyden.iss.humidity</select>
  <select name="hmin">Boyden.iss.humidity_min</select>
  <select name="hmax">Boyden.iss.humidity_max</select>
  <data name="dewpoint">
    <function2 name="dewpoint">
      <value name="h"/>
      <value name="t"/>
    </function2>
  </data>
  <data name="dewpointmax">
    <function2 name="dewpoint">
      <value name="hmax"/>
      <value name="tmax"/>
    </function2>
  </data>
  <data name="dewpointmin">
    <function2 name="dewpoint">
      <value name="hmin"/>
      <value name="tmin"/>
    </function2>
  </data>
</query>
<channel color="#d2d2ff" type="range" scale="left"
  nameupper="dewpointmax" namelower="dewpointmin"/>
<channel color="#6464ff" type="curve" scale="left" name="dewpoint"/>
<channel color="#ffb4b4" type="range" scale="left"
  nameupper="tmax" namelower="tmin"/>
<channel color="#b40000" type="curve" scale="left" name="t"/>
<channel color="#e6e6e6" type="nodata" name="t"/>
      </channels>
    </graph>

    <!-- inside Temperature graph -->
    <graph name="Boyden.temperature_inside" offset="0"
height="144" width="600" bgcolor="#ffffff" fgcolor="#000000">
      <leftlabel align="center">Temperature In (deg C)</leftlabel>
```

```
      <leftaxis type="static" min="-15" max="35"
first="-10" last="30" step="10" format="%.0f"
ticks="yes" gridlines="yes"/>
      <graphwindow llx="55" lly="19" urx="555" ury="139"/>
      <channels>
<query>
  <select name="t">Boyden.console.temperature</select>
  <select name="tmin">Boyden.console.temperature_min</select>
  <select name="tmax">Boyden.console.temperature_max</select>
  <select name="h">Boyden.console.humidity</select>
  <select name="hmin">Boyden.console.humidity_min</select>
  <select name="hmax">Boyden.console.humidity_max</select>
  <data name="dewpoint">
    <function2 name="dewpoint">
      <value name="h"/>
      <value name="t"/>
    </function2>
  </data>
  <data name="dewpointmax">
    <function2 name="dewpoint">
      <value name="hmax"/>
      <value name="tmax"/>
    </function2>
  </data>
  <data name="dewpointmin">
    <function2 name="dewpoint">
      <value name="hmin"/>
      <value name="tmin"/>
    </function2>
  </data>
</query>
<channel color="#d2d2ff" type="range" scale="left"
  nameupper="dewpointmax" namelower="dewpointmin"/>
<channel color="#6464ff" type="curve" scale="left" name="dewpoint"/>
<channel color="#ffb4b4" type="range" scale="left"
  nameupper="tmax" namelower="tmin"/>
<channel color="#b40000" type="curve" scale="left" name="t"/>
<channel color="#e6e6e6" type="nodata" name="t"/>
<channel color="#ff0000" type="sun" station="Boyden"/>
      </channels>
```

```
    </graph>

    <!-- Pressure -->
    <graph name="Boyden.pressure" offset="0"
height="144" width="600" bgcolor="#ffffff" fgcolor="#000000">
      <leftlabel align="center">Pressure (hPa)</leftlabel>
      <leftaxis type="static" min="800" max="1050"
first="800" last="1050" step="50" format="%.0f"
ticks="yes" gridlines="yes"/>
      <graphwindow llx="55" lly="19" urx="555" ury="139"/>
      <channels>
<query>
  <select name="p">Boyden.console.barometer</select>
  <select name="pmin">Boyden.console.barometer_max</select>
  <select name="pmax">Boyden.console.barometer_min</select>
</query>
<channel color="#d2d2ff" type="range" scale="left"
  nameupper="pmax" namelower="pmin"/>
<channel color="#7f7fff" type="curve" scale="left" name="p"/>
<channel color="#e6e6e6" type="nodata" name="p"/>
      </channels>
    </graph>

    <!-- Wind -->
    <graph name="Boyden.wind" offset="0"
height="144" width="600" bgcolor="#ffffff" fgcolor="#000000">
      <leftlabel align="bottom">Speed (m/s)</leftlabel>
      <rightlabel align="top">Azimut (deg)</rightlabel>
      <leftaxis type="static" min="0" max="25"
first="0" last="15" step="5" format="%.0f"
ticks="yes" gridlines="yes"/>
      <rightaxis type="static" min="-540" max="360"
first="0" last="360" step="180" format="%.0f"
ticks="yes" gridlines="yes"/>
      <graphwindow llx="55" lly="19" urx="555" ury="139"/>
      <channels>
<query>
  <select name="azi">Boyden.iss.winddir</select>
  <select name="v">Boyden.iss.wind</select>
  <select name="vmax">Boyden.iss.windgust</select>
```

```
</query>
<channel type="windbackground" scale="right"
  northcolor="#e0e0ff" southcolor="#ffe0e0"
  westcolor="#e0ffe0" eastcolor="#ffffc8"
  letters="SWNE" />
<channel color="#6464ff" type="curve" scale="right" name="azi"/>
<channel color="#006400" type="histogram" scale="left" name="vmax"/>
<channel color="#00ff00" type="histogram" scale="left" name="v"/>
<channel color="#ffffff" type="lowdata" name="vmax" limit="0.1"/>
<channel color="#e6e6e6" type="nodata" name="azi"/>
      </channels>
    </graph>

    <!-- Radiation -->
    <graph name="Boyden.radiation" offset="3600"
height="144" width="600" bgcolor="#ffffff" fgcolor="#000000">
      <leftlabel align="center">Solar Radiation (M/m2)</leftlabel>
      <rightlabel align="center">UV index</rightlabel>
      <leftaxis type="static" min="0" max="1200"
first="0" last="1200" step="200" format="%.0f"
ticks="yes" gridlines="yes"/>
      <leftaxis interval="86400" type="static" min="0" max="600"
first="0" last="600" step="100" format="%.0f"
ticks="yes" gridlines="yes"/>
      <rightaxis type="static" min="0" max="12"
first="0" last="12" step="2" format="%.0f"
ticks="yes" gridlines="no"/>
      <rightaxis interval="86400" type="static" min="0" max="6"
first="0" last="6" step="1" format="%.0f"
ticks="yes" gridlines="no"/>
      <graphwindow llx="55" lly="19" urx="555" ury="139"/>
      <channels>
<query>
  <select name="solar">Boyden.iss.solar</select>
  <select name="uv">Boyden.iss.uv</select>
</query>
<channel color="#c8b400" type="histogram" scale="left" name="solar"/>
<channel color="#6400c8" type="curve" scale="right" name="uv"/>
<channel color="#e6e6e6" type="nodata" name="solar"/>
      </channels>
```

```
    </graph>

    <!-- Rain -->
    <graph name="Boyden.rain" offset="0"
height="144" width="600" bgcolor="#ffffff" fgcolor="#000000">
      <leftlabel align="center">Precipitation (mm)</leftlabel>
      <rightlabel align="center">Total rain (mm)</rightlabel>
      <leftaxis interval="300" type="static" min="0" max="6"
first="0" last="6" step="1" format="%.0f"
ticks="yes" gridlines="yes"/>
      <leftaxis interval="1800" type="static" min="0" max="10"
first="0" last="10" step="2" format="%.0f"
ticks="yes" gridlines="yes"/>
      <leftaxis interval="7200" type="static" min="0" max="20"
first="0" last="20" step="5" format="%.0f"
ticks="yes" gridlines="yes"/>
      <leftaxis interval="86400" type="static" min="0" max="40"
first="0" last="40" step="10" format="%.0f"
ticks="yes" gridlines="yes"/>

      <leftaxis type="static" min="0" max="30"
first="0" last="30" step="10" format="%.0f"
ticks="yes" gridlines="yes"/>
      <rightaxis type="dynamic" minname="totalrain" maxname="totalrain"
origin="0" maxtickcount="10" step="10" ticks="yes" gridlines="no"
format="%3.0f" />
      <graphwindow llx="55" lly="19" urx="555" ury="139"/>
      <channels>
<query>
  <select name="rain">Boyden.iss.rain</select>
  <data name="totalrain">
    <function name="accumulate">
      <value name="rain"/>
    </function>
  </data>
</query>
<channel color="#0000ff" type="histogram" scale="left" name="rain"/>
<channel color="#00ffff3f" type="histogram" scale="right" name="totalrain"/>
<channel color="#f3f3f33f" type="nodata" name="rain"/>
      </channels>
```

```
    </graph>

    <!-- humidity graph -->
    <graph name="Boyden.humidity" offset="0"
height="344" width="600" bgcolor="#ffffff" fgcolor="#000000">
      <leftlabel align="center">relavite Humdity (%)</leftlabel>


      <leftaxis type="static" min="0" max="100"
first="0" last="100" step="5" format="%.0f"
ticks="yes" gridlines="yes"/>

     <graphwindow llx="55" lly="19" urx="555" ury="339"/>
      <channels>
<query>
  <select name="h">Boyden.iss.humidity</select>
  <select name="hmin">Boyden.iss.humidity_max</select>
  <select name="hmax">Boyden.iss.humidity_min</select>
</query>
<channel color="#d2d2ff" type="range" scale="left"
  nameupper="hmax" namelower="hmin"/>
<channel color="#7f7fff" type="curve" scale="left" name="h"/>
<channel color="#e6e6e6" type="nodata" name="h"/>
      </channels>
    </graph>


    <!-- humidity_inside graph -->
    <graph name="Boyden.humidity_inside" offset="0"
height="144" width="600" bgcolor="#ffffff" fgcolor="#000000">
      <leftlabel align="center">relavite Humdity (%)</leftlabel>
      <leftaxis type="static" min="0" max="100"
first="0" last="100" step="20" format="%.0f"
ticks="yes" gridlines="yes"/>
      <graphwindow llx="55" lly="19" urx="555" ury="139"/>
      <channels>
<query>
  <select name="h">Boyden.console.humidity</select>
  <select name="hmin">Boyden.console.humidity_max</select>
  <select name="hmax">Boyden.console.humidity_min</select>
```

```
</query>
<channel color="#d2d2ff" type="range" scale="left"
  nameupper="hmax" namelower="hmin"/>
<channel color="#7f7fff" type="curve" scale="left" name="h"/>
<channel color="#e6e6e6" type="nodata" name="h"/>
      </channels>
    </graph>

    <!-- wetness -->
    <graph name="Boyden.wetness" offset="0"
height="144" width="600" bgcolor="#ffffff" fgcolor="#000000">
      <leftlabel align="center">Wetness (index: 0-25)</leftlabel>
      <leftaxis type="static" min="-1" max="17"
first="0" last="15" step="5" format="%.0f"
ticks="yes" gridlines="yes"/>
      <graphwindow llx="55" lly="19" urx="555" ury="139"/>
      <channels>
<query>
  <select name="wet">Boyden.leaf1.wetness</select>
  <select name="wetness_min">Boyden.leaf1.wetness_max</select>
  <select name="wetness_max">Boyden.leaf1.wetness_min</select>
</query>
<channel color="#d2d2ff" type="range" scale="left"
  nameupper="wetness_max" namelower="wetness_min"/>
<channel color="#7f7fff" type="curve" scale="left" name="wet"/>
<channel color="#e6e6e6" type="nodata" name="wet"/>
      </channels>
    </graph>



    <!-- cloud -->
    <graph name="Boyden.cloud" offset="0"
height="300" width="600" bgcolor="#ffffff" fgcolor="#000000">
      <leftlabel align="bottom">Temp (deg)</leftlabel>
      <rightlabel align="center">Difference</rightlabel>
      <leftlabel align="center">Cloud Sensor (deg)</leftlabel>

      <leftaxis type="dynamic" minname="cloud_bottom_min" maxname="cloud_top_max" min="-5" max="40"
maxtickcount="20" first="0" last="40" step="1" format="%.0f"
```

```
ticks="yes" gridlines="no"/>

      <rightaxis type="dynamic" minname="cloud_diff_min" maxname="cloud_diff_max"
        maxtickcount="20" step="1" format="%.0f"
        ticks="yes" gridlines="yes"/>

      <graphwindow llx="55" lly="19" urx="555" ury="295"/>
     <channels>
<query>
  <select name="cloud_top">Boyden.leaf1.temperature</select>
  <select name="cloud_top_min">Boyden.leaf1.temperature_min</select>
  <select name="cloud_top_max">Boyden.leaf1.temperature_max</select>
  <select name="cloud_bottom">Boyden.leaf2.temperature</select>
  <select name="cloud_bottom_min">Boyden.leaf2.temperature_min</select>
  <select name="cloud_bottom_max">Boyden.leaf2.temperature_max</select>
  <data name="cloud_diff">
    <diff>
      <value name="cloud_bottom"/>
      <value name="cloud_top"/>
    </diff>
  </data>
          <data name="cloud_diff_max">
    <diff>
      <value name="cloud_bottom_max"/>
      <value name="cloud_top_min"/>
    </diff>
  </data>
          <data name="cloud_diff_min">
            <diff>
              <value name="cloud_bottom_min"/>
              <value name="cloud_top_max"/>
            </diff>
          </data>

</query>
<channel color="#6464ff" type="range" scale="left"
  nameupper="cloud_top_max" namelower="cloud_top_min"/>
<channel color="#b40000" type="range" scale="left"
  nameupper="cloud_bottom_max" namelower="cloud_bottom_min"/>
<channel color="#9933ff" type="curve" scale="right" name="cloud_diff"/>
```

```
<channel color="#e6e6e6" type="nodata" name="cloud_diff"/>
<channel color="#ff0000" type="sun" station="Boyden"/>
      </channels>

       </graph>

    <!-- cloud 2 -->
    <graph name="Boyden.cloud2" offset="0"
height="300" width="600" bgcolor="#ffffff" fgcolor="#000000">
      <leftlabel align="bottom">Temp (deg)</leftlabel>
      <rightlabel align="center">Difference</rightlabel>
      <leftlabel align="center">Cloud Sensor (deg)</leftlabel>

      <leftaxis type="dynamic" minname="cloud_bottom_min" maxname="cloud_top_max" min="-5" max="40"
maxtickcount="20" first="0" last="40" step="1" format="%.0f"
ticks="yes" gridlines="no"/>

      <rightaxis type="dynamic" minname="cloud_diff" maxname="cloud_diff"
        maxtickcount="20" step="1" format="%.0f"
        ticks="yes" gridlines="yes"/>

      <graphwindow llx="55" lly="19" urx="555" ury="295"/>
     <channels>
<query>
  <select name="cloud_top">Boyden.leaf1.temperature</select>
  <select name="cloud_top_min">Boyden.leaf1.temperature_min</select>
  <select name="cloud_top_max">Boyden.leaf1.temperature_max</select>
  <select name="cloud_bottom">Boyden.leaf2.temperature</select>
  <select name="cloud_bottom_min">Boyden.leaf2.temperature_min</select>
  <select name="cloud_bottom_max">Boyden.leaf2.temperature_max</select>
  <data name="cloud_diff">
    <diff>
      <value name="cloud_bottom"/>
      <value name="cloud_top"/>
    </diff>
  </data>
         <data name="cloud_diff_max">
    <diff>
      <value name="cloud_bottom_max"/>
      <value name="cloud_top_min"/>
```

```
    </diff>
  </data>
          <data name="cloud_diff_min">
            <diff>
              <value name="cloud_bottom_min"/>
              <value name="cloud_top_max"/>
            </diff>
          </data>

</query>
<channel color="#9933ff" type="curve" scale="right" name="cloud_diff"/>
<channel color="#e6e6e6" type="nodata" name="cloud_diff"/>
<channel color="#ff0000" type="sun" station="Boyden"/>
      </channels>

       </graph>

    <!-- console battery graph -->
    <graph name="Boyden.battery" offset="0"
height="144" width="600" bgcolor="#ffffff" fgcolor="#000000">
      <leftlabel align="center">Battery voltage (V)</leftlabel>
      <leftaxis type="static" min="3.9" max="4.1"
first="3.9" last="4.1" step="0.05" format="%.1f"
ticks="yes" gridlines="yes"/>
      <graphwindow llx="55" lly="19" urx="555" ury="139"/>
      <channels>
<query>
  <select name="b">Boyden.console.battery</select>
</query>
<channel color="#7f7fff" type="curve" scale="left" name="b"/>
<channel color="#e6e6e6" type="nodata" name="b"/>
      </channels>
    </graph>

    <!-- # of samples -->
    <graph name="Boyden.samples" offset="0"
height="144" width="630" bgcolor="#ffffff" fgcolor="#000000">
      <leftlabel align="center">Number of samples</leftlabel>
      <leftaxis interval="300" type="static" min="0" max="300"
first="0" last="300" step="100" format="%.0f"
```

```
ticks="yes" gridlines="yes"/>
      <leftaxis interval="1800" type="static" min="0" max="3000"
first="0" last="3000" step="500" format="%.0f"
ticks="yes" gridlines="yes"/>
      <leftaxis interval="7200" type="static" min="0" max="30000"
first="0" last="30000" step="5000" format="%.0f"
ticks="yes" gridlines="yes"/>
      <rightlabel align="center">Total number of samples</rightlabel>
      <rightaxis interval="300" type="static" min="0" max="300000"
first="0" last="300000" step="100000" format="%.0f"
ticks="yes" gridlines="yes"/>
      <rightaxis interval="1800" type="static" min="0" max="300000"
first="0" last="300000" step="50000" format="%.0f"
ticks="yes" gridlines="yes"/>
      <rightaxis interval="7200" type="static" min="0" max="3000000"
first="0" last="3000000" step="500000" format="%.0f"
ticks="yes" gridlines="yes"/>
      <graphwindow llx="55" lly="19" urx="555" ury="139"/>
      <channels>
<query>
  <select name="s">Boyden.iss.samples</select>
  <data name="totals">
    <function name="accumulate">
      <value name="s"/>
    </function>
  </data>
</query>
        <channel color="#afafff" type="histogram" scale="right" name="totals"/>
<channel color="#ff0f0f" type="curve" scale="left" name="s"/>
<channel color="#e6e6e6" type="nodata" name="s"/>
      </channels>
    </graph>

  </graphs>
</meteo>
```

Appendix E

UPS Configuration Files and Scripts

ups.conf

```
[watcher-ups]
driver = newhidups
port = auto
desc = "Watcher network"
```

upsd.conf

```
ACL all 0.0.0.0/0
ACL localhost 127.0.0.1/32
ACL watcher2 196.21.180.40/32
ACCEPT localhost
ACCEPT watcher2
REJECT all
```

upsmon.conf

```
RUN_AS_USER nut
MONITOR watcher-ups@localhost 1 watcher1-ups upsw1mon master
MINSUPPLIES 1
SHUTDOWNCMD /usr/local/ups/bin/ups-shutdown
NOTIFYCMD "/usr/local/ups/sbin/upssched"
POLLFREQ 5
POLLFREQALERT 5
HOSTSYNC 15
DEADTIME 15
POWERDOWNFLAG /etc/killpower
NOTIFYMSG ONLINE "UPS \%s is on mains power (watcher)."
```

```
NOTIFYMSG ONBATT "UPS \%s is on battery power."
NOTIFYMSG LOWBATT "UPS \%s is on low battery power."
NOTIFYFLAG ONLINE WALL+EXEC
NOTIFYFLAG ONBATT WALL+EXEC
NOTIFYFLAG LOWBATT WALL
RBWARNTIME 43200
NOCOMMWARNTIME 300
FINALDELAY 5
```

upssched.conf

```
CMDSCRIPT /usr/local/ups/bin/upssched-cmd
PIPEFN /var/run/upssched/upssched.pipe
LOCKFN /var/run/upssched/upssched.lock
AT ONBATT watcher-ups@localhost EXECUTE upsonbatt
AT ONLINE watcher-ups@localhost EXECUTE upsonline
```

upsd.users

```
[watcher1-ups]
password = upsw1mon
allowfrom = localhost
actions = SET
instcmds = ALL
upsmon master
[watcher2-ups]
password = upsw2mon
allowfrom = watcher2
actions = SET
instcmds = ALL
upsmon slave
```

ups-shutdown

```
#!/bin/bash

# Email status of UPS.
/usr/local/ups/bin/upsc watcher-ups@localhost | mail -s
"Watcher-ups at low battery, shutting down Watcher system"
 jfrench@bermuda.ucd.ie, gmelady@bermuda, gary.melady@gmail.com, petr@kubanek.net
```

```
# Put rts2 central server to "off"
/usr/local/bin/rts2-weathertimeout

# Wait for 6 minutes to allow roof to fully close.
# (should take less than 4 min)
sleep 360

# Shut down system.
/sbin/shutdown -h +0
```

upssched-cmd

```
case $1 in
upsonbatt)
/usr/local/ups/bin/upsc watcher-ups@localhost | mail -s "Watcher on battery power"
gmelady, jfrench, gmelady@bermuda.ucd.ie, jfrench@bermuda.ucd.ie,
gary.melady@gmail.com, petr@kubanek.net
;;

upsonline)
/usr/local/ups/bin/upsc watcher-ups@localhost | mail -s "Watcher on mains power"
 gmelady, jfrench, gmelady@bermuda.ucd.ie, jfrench@bermuda.ucd.ie,
gary.melady@gmail.com, petr@kubanek.net
;;

*)
logger -t upssched-cmd "Unrecognized command: $1"
;;
esac
```

List of Publications

Refereed

1. S. Foley, S. McGlynn, S. McBreen, L. Hanlon, B. McBreen, J. French, G. Melady, R. O'Connor (2007). "Gamma–Ray Bursts detected by INTEGRAL", Proceedings of "*Swift* & GRBs: Unveiling the Relativistic Universe", *Il Nuovo Cimento C*, vol. 121, p.1055.

2. E. Winston, S. McBreen, A. J. Carr, B. McBreen, P. Duggan, L. Hanlon, J. French, L. Metcalfe (2005). "Gamma-ray Bursts and X-ray melting of material as a source of chondrules and planets", *Il Nuovo Cimento C*, vol. 28, p.653.

Submitted

1. A. J. Castro-Tirado, A. de Ugarte Postigo, J. Gorosabel, T. A. Fatkhullin, V. V. Sokolov, M. Jelnek, D. Sluse, P. Ferrero, D. A. Kann, S. Klose, M. Bremer, J. M. Winters, D. Nuernberger, D. Perez-Ramrez, M.A. Guerrero, J. French, G. Melady, L. Hanlon, B. McBreen, F. J. Aceituno, R. Cunniffe, P. Kubánek, S. Vítek, S. Schulze, A. C. Wilson, R. Hudec, J. M. Gonzalez-Perez, T. Shahbaz, S. Guziy, L. Pavlenko, E. Sonbas, S. Trushkin, N. Bursov, N. A. Nizhelskij, L. Sabau-Graziati (2008). "Optical and near–infrared flares from SWIFT J195509+261406: a "transient Soft Gamma–Ray Repeater in our Galaxy?", submitted to *Nature*.

2. C. C. Thöne, D. A. Kann, G. Jóhannesson, J. H. Selj, A. Jaunsen, J. P. U. Fynbo, K. S. Baliyan, C. Bartolini, I. F. Bikmaev, J. S. Bloom, R. A. Burenin, B. E. Cobb, S. Covino, P. A. Curran, H. Dahle, J. French, S. Ganesh, G. Greco, A. Guarnieri, L. Hanlon, J. Hjorth, M. Ibrahimov, G. L. Israel, P. Jakobsson, B. L. Jensen, U. G. Jorgensen, I. M. Khamitov, D. Malesani, N. Masetti, J. Naranen, E. Pakstiene, D. A. Perley, A. Piccioni, G. Pizzichini, A. Pozanenko, D. Nanni, V. Rumyantsev, D. Starr, R. A. Sunyaev, F. Terra, P. M. Vreeswijk, A. C. Wilson (2008). "Photometry and Spectroscopy of GRB 060526: A thorough study of the afterglow and host of a high redshift gamma–ray burst", submitted to *Astronomy and Astrophysics*.

In preparation

1. J. French, L. Hanlon, Petr Kubánek, Martin Jelínek, B. McBreen, G. Melady, S. McBreen, G. Jóhannesson, C. Thöne, A. Kann, P. Meintjes M. Hoffmann, H. Calitz (2008). "Early optical observations of GRB 060526 with the Watcher robotic telescope", to be submitted to *Astronomy and Astrophysics*.

2. J. French, L. Hanlon, B. McBreen, G. Melady, Petr Kubánek, Martin Jelínek, S. McBreen, P. Meintjes M. Hoffmann, H. Calitz, A. J .Castro–Tirado, A. de Ugarte Postigo (2008). "The Watcher robotic telescope", to be submitted to *PASP*.

3. Martin Jelínek, A. J .Castro–Tirado, A. de Ugarte Postigo, S. McBreen, J. Gorosabel, J. French, L. Hanlon, G. Jóhannesson, S. Guzyi, M. Bremer, F. J. Aceituno, F. Hoyos, B. Cobb, Petr Kubánek, S. Vítek, R. Cunniffe, L. Sabau–Graziati and others (2008). "A causal relation between an intense X–ray flare and a refreshed shock observed in GRB 060904b", to be submitted to *Astronomy and Astrophysics*.

Non-Refereed

1. J. French, L. Hanlon, B. McBreen, S. McBreen, N. Smith, A. Giltinan, P. Meintjes M. Hoffmann, L. Moran (2004). "Watcher: A Telescope for Rapid Gamma–Ray Burst Follow-Up Observations", Proceedings of *Gamma–Ray Bursts: 30 Years of Discovery*, AIP Conference Proceedings, Vol. 727, p.741-744

2. Petr Kubánek, Martin Jelínek, Stanislav Vítek, Antonio de Ugarte Postigo, Martin Nekola, John French (2006). "RTS2: a powerful robotic observatory manager", *Advanced Software and Control for Astronomy*, Proceedings of the SPIE, vol. 6274, pp.62741V.

3. S. McGlynn, S. McBreen, L. Hanlon, B. McBreen, S. Foley, J. French, G. Melady, A. von Kienlin and R. Preece (2006). "Observations of Gamma-Ray Bursts with INTEGRAL", *Gamma-Ray Bursts in the Swift Era*, volume 836 of *AIP Conference Series*, pp.165–168

4. L. Moran, L. Hanlon, A. von Kienlin, B. McBreen, S. McBreen, *S. McGlynn*, J. French, R. Preece, Y. Kaneko, O. R. Williams, K. Bennett and R. M. Kippen (2004). "Preliminary INTEGRAL Analysis of GRB 040106", Proceedings of the *5th INTEGRAL Workshop on the INTEGRAL Universe*, ESA SP Vol. 552, pp.653–657

5. S. McBreen, L. Moran, B. McBreen, L. Hanlon, J. French, M. Conway (2004). 'Similarities in the temporal properties of gamma-ray bursts and soft gamma-ray repeaters", Proceedings of *Gamma–Ray Bursts: 30 Years of Discovery*, AIP Conference Proceedings, Vol. 727, p.61-64

6. L. Moran, L. Hanlon, B. McBreen, R. Preece, Y. Kaneko, O.R. Williams, K. Bennett, R. Marc Kippen, A. Von Kienlin, V. Beckmann, S. McBreen, J. French (2004). "INTEGRAL Spectrometer Analysis of GRB 030227 & GRB 030131", Proceedings of *Gamma–Ray Bursts: 30 Years of Discovery*, AIP Conference Proceedings, Vol. 727, p.225-228

7. I have also published 18 Gamma-Ray Burst Coordinates Network (GCN) notices on Watcher GRB follow-up observations (11 of these as first author): GCN Numbers – 7718, 7619, 7316, 6586, 6562, 6538, 6528, 6500, 6233, 5615, 5566, 5510, 5492, 5257, 5247, 5199, 5165, 4960.

In Preparation

1. P. Kubánek, M. Jelínek, J. French, M. Prouza, S. Vítek, A. J .Castro–Tirado, V. Reglero (2008). "The RTS2 Protocol", to be submitted to *Astronomical Telescopes and Instrumentation*, Proceedings of the SPIE.